

A METHOD FOR THE DEVELOPMENT OF AN EFFECTIVE FLOW
DIVERTING DEVICE FOR TREATMENT OF CEREBRAL ANEURYSMS

A DISSERTATION
SUBMITTED TO THE FACULTY OF THE GRADUATE SCHOOL
OF THE UNIVERSITY OF MINNESOTA
BY

Ricky Chow

IN PARTIAL FULFILLMENT OF THE REQUIREMENTS
FOR THE DEGREE OF
DOCTOR OF PHILOSOPHY

Eph Sparrow, PhD
September 2013

ACKNOWLEDGEMENTS

The author is extremely grateful for the following people who have provided emotional guidance, financial support, experimental resources, learning opportunities, and academic insights at various stages of his career. The research presented in this dissertation would have suffered without the contributions of every individual listed below.

To my family: If not for your encouragement, I would not have pursued a career in the medical device industry.

Albert Chow, Lina Chow, Kenny Chow

To Professor Tranquillo's group: My appointment as your lab scientist after moving from Toronto allowed me to develop my tissue engineering expertise, ignite my scientific curiosity, and pursue my Master's degree.

Bob Tranquillo, Zeeshan Syedain, Katie Ahmann, Justin Weinbaum, Sandy Johnson, Naomi Ferguson

To Professor Durfee and my colleagues at Lake Region Medical: The author's work on flow diverters started as in the New Product Design and Business Development course. Guidance by Professor Durfee led to the continuation of the project at Lake Region Medical. Prototyping of devices with colleagues greatly enriched this research.

Will Durfee, Joe Fleischhacker, Mark Fleischhacker, Kate Roehl, Pete Herman, John Schreiner, Gary Campbell, Andrew Senn, Arne Rimmereide, John Zimmerman, Galen Houk, Andy Mork, Nick Nimchuk, Tommy Acompanado, Mike Price, Denise Edoh

To Professor Sparrow's group: My original goal was to complete a Master's degree and focus on a career in industry. The thought of pursuing a PhD would not have crossed my mind if not for your patience, encouragement, and commitment to my growth as an engineer.

Eph Sparrow, Reza Rama-Zani, John Gorman, Kent Underland, Blaine Hatab

To Professor Divani's group and associates: One of the three pillars of this research (the *in vivo* studies) would have been severely stunted if not for your dedication, insights, and equipment.

Afshin Divani, Islam Shehata, John Ballard, Amanda Murphy, Jessica Nordberg

To Professor Sheng's group: One of the three pillars of this research (the *in vitro* studies) would have been extremely difficult if not for your dedication, insights, and equipment.

Jian Sheng, Mostafa Toloui

To my MS and PhD committee members: My work was favorably influenced by your experience and suggestions while serving as my MS and/or PhD committee members:

Eph Sparrow, Will Durfee, Paul Iaizzo, Afshin Divani, Victor Barocas, Art Erdman

ABSTRACT

Intracranial aneurysms are malformations that occur in the complex network of blood vessels supplying oxygen and nutrients to the brain. Weakening of the blood vessel wall leads to a bulge that ruptures in more than 30 000 Americans every year. Prognosis is very poor. Patients often die or suffer a greatly reduced quality of life.

Two predominant methods for treating aneurysms are (1) surgical clipping, where part of the skull is temporarily removed and a metallic clip is placed to circumvent the aneurysm neck, and (2) coiling, where metallic coils are snaked through the blood vessels and packed into the aneurysm.

For large aneurysms or those with poorly defined necks, a new class of medical device has recently emerged as a more effective treatment than coiling. A flow diverter is placed inside the parent vessel, spanning the aneurysm neck. The diverter's braided structure keeps most of the blood from entering the aneurysm. The risk of rupture is eliminated when stagnant pools of blood thrombose inside the aneurysm, cutting the aneurysm off from the rest of the circulatory system.

However, complications related to the presence of flow diverters are observed clinically. Aneurysms with incomplete clot formation after placement of the flow diverter are still at risk of rupture. The high metallic content of the device presents a risk of in-stent thrombosis and require a lifetime of anti-coagulants for its management. Subarachnoid hemorrhage after placement of the flow diverter is observed, but the underlying mechanism is not well understood. Therefore, a greater understanding of the fluid mechanics underlying flow diversion is needed to facilitate the design of the next generation of flow diverters.

Research was pursued in three parallel synergistic paths. (1) Benchtop experiments using a technique called particle imaging velocimetry (PIV) were used to characterize the flow diversion accorded by the Pipeline Embolization Device (PED, designed by Covidien) in a variety of geometries. (2) The computational fluid dynamic (CFD) simulation methods were verified with PIV results, and then applied towards a wider range of vessel geometries to predict how the PED will perform at various locations of the human neurovasculature. (3) Animal studies were pursued to develop surgical techniques for device evaluation in the future.

The implementation of PIV was found to be a labor and computationally intensive process. Previous researchers who have used PIV to experimentally investigate the flow diverting effect of the device occasionally interrogated the fluid domain at several planes, but typically only at the center plane bisecting the aneurysm. This limited information was found to be insufficient for verification of CFD simulations or to calculate bulk properties such as flow rate of fluid entering the aneurysm. Evaluation of intraaneurysmal

flow was also found to be problematic after placement of the flow diverter. The significantly reduced flow highlighted the difference in densities between the seeded reflective particles and the flowing fluid. Particles also accumulated on the glass model wall in regions of low flow. These complications introduced challenges to the PIV measurement technique.

Detailed sets of PIV results were collected in three flow domains by interrogating the flow at parallel planes 400 μm apart. The flow rates of fluid entering the aneurysm before (Q_{UT}) and after (Q_T) placement of the flow diverters were calculated. CFD simulations were conducted with the openings, or pores, of the PED modeled as an array of diamond shaped pores connecting the aneurysm to the parent artery. Since the deployed shape of the PED was variable and depended on the deployment technique, simulations with different diamond pore dimensions were conducted. The Q_T and Q_{UT} values predicted from CFD were in reasonable agreement with the PIV results.

CFD simulations were then conducted in an array of idealized blood vessel geometries that typified a portion of the vessel curvatures found in the human neurovasculature. It was discovered that the performance of the PED varied depending on the curvature of the parent vessel, the location of the aneurysm along the curve, and the geometry of the aneurysm neck. The claim of “85% reduction in circulation” made by Covidien (who designed the PED) is a somewhat ambiguous statement. An ~85% reduction in vorticity was observed on the center planes of the aneurysms evaluated in this research effort, but the reduction in flow rate entering the aneurysm was on average only around 65%, and dipped as low as 50% in the most tortuous bends. However, the shapes of the deployed PED, the vessel geometries, and inlet conditions examined in this thesis may have been different than those used to substantiate Covidien’s marketing claim. The term “circulation” was also not defined in Covidien’s literature. Further research is needed to identify the source of this discrepancy.

The present research also provides insight into the fluid mechanics of blood entering aneurysms created in a rabbit model. Residence time was defined as the volume of the aneurysm divided by the flow rate of blood entering the aneurysm. Blood velocities acquired using an ultrasound probe were used as input to CFD simulations. The varying volumes of the aneurysms and the varying angles of the aneurysms relative to their parent arteries led to residence times that varied from rabbit to rabbit. Knowledge of the initial flow conditions is important for an apples to apples comparison of new flow diverter designs. More animal studies combined with clinical data of the PED are needed to determine the minimum threshold in flow reduction, the minimum residence time, or some other metric that will predict healing of the aneurysm.

In summary, a comprehensive platform of evaluation techniques was developed and implemented for use in optimizing the design of the next generation of flow diverters. The reduction in flow entering the aneurysm after placement of the PED was found to be less than the claimed “reduction in circulation” and presents an opportunity for a flow diverter that restricts flow more severely. Moving from a metallic braid to a polymeric stent graft platform would allow for easier manipulation of flow diversion characteristics while taking into account other design requirements such as device stiffness, force required to advance it through the catheter, radiopacity, thrombogenicity, stent migration, and others. A better understanding of the underlying mechanism by which flow diverters heal aneurysms will lead to wider adoption and on-label use (officially approved by the European Commission and the Food and Drug Administration) of this class of device as a first-line treatment for all aneurysms.

TABLE OF CONTENTS

CHAPTER	PAGE
LIST OF TABLES	VIII
LIST OF FIGURES	X
LIST OF ABBREVIATIONS	XX
1.0 INTRODUCTION	1
1.1 CEREBRAL ANEURYSMS AND CURRENT TREATMENT METHODS	2
1.2 RESEARCH GOALS	6
2.0 LITERATURE REVIEW AND BACKGROUND INFORMATION	9
2.1 PHYSIOLOGY OF CEREBRAL NEUROVASCULATURE	10
2.2 DISTRIBUTION OF ANEURYSM SIZES, SHAPES, ORIENTATIONS, AND LOCATIONS	15
2.3 DESCRIPTION OF RELEVANT FLUID MODELS AND NON-DIMENSIONAL NUMBERS	21
2.4 PUBLISHED LITERATURE ON <i>IN SILICO</i> CFD SIMULATIONS	24
2.5 PUBLISHED LITERATURE ON <i>IN VITRO</i> BENCHTOP EXPERIMENTS	37
2.6 PUBLISHED LITERATURE ON <i>IN VIVO</i> ANIMAL EXPERIMENTS AND CLINICAL TRIALS	48
3.0 <i>IN VITRO</i> EXPERIMENTS	53
3.1 SPECIFIC AIMS OF <i>IN VITRO</i> EXPERIMENTS	54
3.2 DEVELOPMENT OF <i>IN VITRO</i> EXPERIMENTAL TECHNIQUES	56
3.3 INTRAANEURYSMAL FLOW IN UNTREATED AND TREATED GLASS MODELS	68
3.4 DISCUSSION OF BENCHTOP EXPERIMENTS	84
4.0 <i>IN SILICO</i> SIMULATIONS	88
4.1 SPECIFIC AIMS OF <i>IN SILICO</i> SIMULATIONS	89
4.2 APPLICATION OF COMMERCIALY AVAILABLE SOFTWARE	91
4.3 VERIFICATION OF CFD RESULTS BY MEANS OF PIV RESULTS	105
4.4 EFFECT OF FLOW DIVERTING DEVICES IN IDEALIZED GEOMETRIES	136
4.5 DISCUSSION OF COMPUTER SIMULATIONS	153

CHAPTER	PAGE
5.0 <i>IN VIVO</i> EXPERIMENTS	159
5.1 SPECIFIC AIMS OF <i>IN VIVO</i> EXPERIMENTS	160
5.2 DEVELOPMENT OF AN IMPROVED RABBIT ANEURYSM MODEL	162
5.3 PREDICTED TEST CONDITIONS IN THE RABBIT ANEURYSM MODEL	178
5.4 DISCUSSION OF ANIMAL STUDIES	185
6.0 CONCLUDING REMARKS AND NEXT STEPS	190
7.0 REFERENCES AND BIBLIOGRAPHY	197
A.0 APPENDIX A: SUPPLEMENTAL FIGURES AND TABLES FROM PIV EXPERIMENTS	213
B.0 APPENDIX B: SUPPLEMENTAL FIGURES AND TABLES FROM CFD SIMULATIONS	232
C.0 APPENDIX C: SUPPLEMENTAL FIGURES AND TABLES FROM THE ANIMAL STUDIES	256

LIST OF TABLES

TABLE	DESCRIPTION	PAGE
1-1	Published prospective studies of flow diversion of intracranial aneurysms.	6
2-1	Summary of vessel diameters compiled from the literature search.	12
2-2	Partial collection of velocities and velocity profiles from the literature search.	13
2-3	Partial collection of velocities and velocity profiles from the literature search.	14
2-4	Distribution of ruptured aneurysm locations treated at Abbott Northwestern Hospital in Minneapolis, MN.	17
2-5	Distribution of aneurysms located at bifurcating vessels that were treated at Massachusetts General Hospital.	18
2-6	Comparison of aspect ratio between ruptured and unruptured aneurysms.	18
2-7	Comparison of various shape indices between ruptured and unruptured aneurysms.	20
2-8	Description of various blood viscosity models.	21
2-9	Effect of fluid model on WSS experienced inside the aneurysm.	29
2-10	Association of qualitative intraaneurysmal flow metrics and rupture of aneurysms.	30
2-11	Fluid mixtures used in PIV experiments of different researchers	40
2-12	Geometric dimensions of elastase induced aneurysms	51
2-13	Occlusion rates of PED prototypes implanted in the rabbit aneurysm model.	52
3-1	Dimensions of glass models used in PIV experiments	69
4-1	Mesh parameters for untreated aneurysms	112
4-2	Mesh parameters for treated aneurysms	112
4-3	Flow rate of blood entering the aneurysm in the treated and untreated cases for different mesh densities	113
4-4	Characteristics of pores for the flow diverter modeled with a 1mil wire	117
4-5	Characteristics of pores for the flow diverter modeled with a 2 mil wire	117
4-6	Characteristics of offset pores for the flow diverter modeled with a 2 mil wire	123
4-7	Characteristics of offset pores for the flow diverter modeled with a 2 mil wire	124
4-8	Geometric parameters of the idealized flow domains	137

TABLE	DESCRIPTION	PAGE
5-1	Summary of aneurysms created at the abdominal aorta	165
5-2	Summary of aneurysms created at the root of the RCCA while developing the aneurysm creation technique	168
5-3	Summary of aneurysms created at the root of the RCCA	176
5-4	Blood velocity and vessel diameter measurements acquired using an ultrasound probe	179
5-5	Flow rate of blood in various vessels	180
5-6	Boundary conditions in CFD simulations inside flow domains derived from CT scans of rabbits	181
5-7	The predicted flow rates of blood entering the aneurysms and residence times	182

LIST OF FIGURES

FIGURE	DESCRIPTION	PAGE
1-1	Rough distribution of aneurysms found in the human neurovasculature.	2
1-2	Angiogram illustrated an aneurysm on the basilar artery. Conventional treatment methods: clipping and coiling.	3
1-3	The Silk device from Balt Extrusion	4
1-4	The Pipeline Embolization Device (PED) from Covidien	4
1-5	The Flow Reduction Endoluminal Device (FRED) from Microvention	5
1-6	Irregularities in the size of holes in the flow diverter.	7
2-1	Normal range of physiological wall shear stress.	10
2-2	Blood vessels of the human neurovasculature.	11
2-3	Distribution of aneurysms by location, dome size, and neck size.	15
2-4	Distribution of aneurysms by dome size.	16
2-5	Distribution of aneurysms by location.	16
2-6	Risk of aneurysm rupture for different sized aneurysms	17
2-7	Comparison of size and aspect ratio between ruptured and unruptured aneurysms.	19
2-8	Definition of undulation index.	19
2-9	The apparent viscosity of various blood viscosity models plotted against strain rate.	22
2-10	Description of idealized geometries with varying bend radius and wall shear experienced at the distal wall.	25
2-11	Description of idealized geometries with varying circumferential offsets.	25
2-12	Description of idealized geometries with complex curvature upstream of the aneurysm.	26
2-13	Streamlines of flow in a posterior communicating aneurysm at a 150bpm pulse	27
2-14	Comparison of velocity isosurfaces of intraaneurysmal flow at three different pulse rates.	27
2-15	Comparison of intraaneurysmal flow after simplification of the upstream vessel segment.	28
2-16	Description of geometries and pulsatile inlet flow for evaluating effect of fluid model on wall shear stress.	29
2-17	Treatment of a human intracranial aneurysm using the Medtronic S670 stent	31
2-18	Various metal braided flow diverter designs and formation of thrombus inside rabbit aneurysms.	31

FIGURE	DESCRIPTION	PAGE
2-19	Treatment of a rabbit aneurysm with the PED	32
2-20	Definition of a braided flow diverter in a computer simulation.	32
2-21	Streamlines of fluid entering the aneurysm after placement of the braided flow diverter.	33
2-22	Definition of fluid domain and stents.	33
2-23	The effects of two different stents on intraaneurysmal flow in idealized geometries.	34
2-24	The effects of two different stents on intraaneurysmal flow in patient derived geometries.	34
2-25	The definition of different flow diverter designs	35
2-26	The relative change in residence times in the straight parent artery and the curved parent artery geometries	35
2-27	Flow into perforating vessels after placement of a flow diverter	36
2-28	Reconstruction of the neurovasculature from a CT scan of a resin cast model.	37
2-29	Various rigid vascular models.	38
2-30	Various compliant vascular models.	39
2-31	A compliant vascular model.	39
2-32	Measurement of intraaneurysmal flow with a Doppler guidewire	41
2-33	Angiogram of aneurysm treated with coils.	42
2-34	Dye entering aneurysms before and after placement of a stent	42
2-35	Quantitative analysis of dye entering the aneurysm before and after placement of a flow diverter	43
2-36	Experimental PIV set up	44
2-37	Intraaneurysmal flow measured using PIV	44
2-38	Intraaneurysmal flow measured using PIV throughout the cardiac cycle	45
2-39	Comparison of CFD simulation and PC-MRI measurement of flow	46
2-40	PC-MRI measurement of flow inside the human patient	47
2-41	Microsurgical steps to create a bifurcating aneurysm in a rabbit	48
2-42	Direct and angiographic visualized o the bifurcating aneurysm created in a rabbit.	49
2-43	Illustration of conventional method for creating elastase induced aneurysms in a rabbit	50
2-44	Illustration of conventional method for creating elastase induced aneurysms in a rabbit	50
2-45	Typical fluoroscopic view of aneurysms.	51

FIGURE	DESCRIPTION	PAGE
2-46	Angiographic view of an aneurysm after placement of a PED prototype	52
3-1	Flowchart of PIV experiments	55
3-2	Flowchart of flow loop used in PIV experiments	56
3-3	Illustration of flow meter and pressure meter readings	57
3-4	Fixture used to hold the glass model	58
3-5	Planar-concave and planar-convex lens assembly for light sheet generation	59
3-6	Schematic of PED in its crimped, or compacted, form on the delivery wire	60
3-7	Bard Dimension Articulating Stone Basket / Grasper	60
3-8	Picture of various components of the PIV experimental set up	61
3-9	Cartoon of PIV experimental set up	62
3-10	Comparison of raw to enhanced image for PIV analysis	63
3-11	Image enhancement flowchart	64
3-12	Example of histogram equalization enhancement of a sample image.	64
3-13	Enhanced images after different levels of thresholding.	65
3-14	Illustration of displacement vector generation	66
3-15	Assembly of PIV data in TecPlot	67
3-16	Front, side, and isometric views of the fluid domain inside the glass models	69
3-17	Front, side, and isometric views of the fluid domain inside the glass models	70
3-18	Front, side, and isometric views of the fluid domain inside the glass models	71
3-19	Difference between (F) and (R) suffix on flow domains with offset aneurysms	71
3-20	Front, side, and isometric views of the fluid domain inside the glass models	72
3-21	Flowchart of PIV experiments	73
3-22	Definition of V_N vector	74
3-23	Velocity contour diagrams are extracted of the three planes illustrated here	75
3-24	PIV planar and normal velocity contours for RC-SOD147-6	76
3-25	PIV planar and normal velocity contours for RC-SOD147-12(F/R)	76
3-26	Normal velocity across necks for RC-SOD147-6 and -12(F/R)	77
3-27	Normal velocity across necks for RC-SOD147-1, -2, and -3	78
3-28	PIV planar and normal velocity contours for RC-SOD147-1, -2, and -3	78
3-29	Normal velocity across necks for RC-SOD147-7(F/R)	79
3-30	PIV planar and normal velocity contours for RC-SOD147-7(F/R)	79

FIGURE	DESCRIPTION	PAGE
3-31	Normal velocity across necks for RC-SOD147-8(F/R)	80
3-32	PIV planar and normal velocity contours for RC-SOD147-8(F/R)	81
3-33	Normal velocity across necks for RC-SOD147-9(F/R)	81
3-34	PIV planar and normal velocity contours for RC-SOD147-9(F/R)	82
3-35	Normal velocity across necks for RC-SOD68-1 and -3	83
3-36	PIV planar and normal velocity contours for RC-SOD68-1 and -3	83
3-37	Accumulation of particles on wall of glass model	85
3-38	PIV in the parent artery is precluded by the opaque flow diverter	87
4-1	Flow chart of CFD research	90
4-2	Glass models packaged for CT scans	92
4-3	Image slice from hospital grade CT scan	92
4-4	Image slice from industrial grade μ CT scan	93
4-5	Orientation of images in Mimics	94
4-6	Definition of glass model wall	95
4-7	Definition of flow domain within glass models	96
4-8	Wall smoothing of reconstructed flow domain	96
4-9	Adjustments to flow domain to ease flow analysis in post processing	97
4-10	Pore patterns of Chapter 4.3 and 4.4	98
4-11	5 steps for modeling pores in ANSYS Design Modeler	99
4-12	Creation of virtual cells on the surface of the flow domain	100
4-13	Mesh density inside flow domain	101
4-14	Dense mesh deployed at the diamond shaped pores of the flow diverter	101
4-15	User interface in CFX-Pre	102
4-16	User interface in CFX-Post	103
4-17	Flowchart of data files in CFD simulations	104
4-18	Flow domains inside RC-SOD147-6 and -12	105
4-19	Location of inlet in RC-SOD147-12(F) and (R)	106
4-20	Simulation plan for verification of CFD simulations using PIV results	107
4-21	Location of midplane bisecting the aneurysm	108
4-22	Definition of normal velocity vector and flow entering the aneurysm	108

FIGURE	DESCRIPTION	PAGE
4-23	Flow rate of blood entering the untreated aneurysms with different Re numbers and flow models	111
4-24	Velocity contours at midplane bisecting the aneurysm for three different Re numbers	111
4-25	Comparison of flow rate entering the aneurysm with different mesh densities	114
4-26	Close up view of elements spanning the diamond shaped pores of the flow diverter	115
4-27	Close up view of flow through pores of the flow diverter with different mesh densities	115
4-28	Description of 0%, 50%, and 100% stretched pores	116
4-29	Image of pores from a flow diverter modeled as 1 mil wires	118
4-30	Image of pores from a flow diverter modeled as 2 mil wires	119
4-31	Q_T and Q_T/Q_{UT} in three different flow domains with various values of pore stretching and wire diameters	121
4-32	Image of offset pores from a flow diverter modeled as 2 mil wires	122
4-33	Image of offset pores from a flow diverter modeled as 2 mil wires	123
4-34	Q of treated aneurysms with original and offset diamond pores	124
4-35	Locations of PIV planes in RC-SOD147-6	125
4-36	Locations of PIV planes in RC-SOD147-12	126
4-37	Location of V_N sample lines from PIV results	126
4-38	Location of V_N sample planes from CFD results	127
4-39	Comparison of contour plots from CFD simulations and PIV experiments in RC-SOD147-6	128
4-40	Comparison of contour plots from CFD simulations and PIV experiments in RC-SOD147-12(F)	129
4-41	Comparison of contour plots from CFD simulations and PIV experiments in RC-SOD147-12(R)	130
4-42	Q_T/Q_{UT} comparison between CFD and PIV	131
4-43	Q_T comparison between CFD and PIV	131
4-44	Close up view of PED deployed in various glass models	133
4-45	Curvature and positioning of pores in CFD model	134
4-46	Composite image comparing the deployed shapes of the PED in the glass model from PIV vs. CFD	134
4-47	The different upstream segments for idealized domains D and E are shown	138

FIGURE	DESCRIPTION	PAGE
4-48	Explanation of different geometric parameters in the idealized domains	139
4-49	Inlet flow profiles at two different pulse rates	139
4-50	Comparison of pores modeled in Chapters 4.3 and 4.4	140
4-51	Flowchart of simulations conducted in idealized geometries	140
4-52	Illustration of where flow metrics of interest were extracted	142
4-53	Time averaged Q_T/Q_{UT} ratios for different idealized flow domains, steady vs. pulsatile inlet	143
4-54	Peak Q_T/Q_{UT} ratios throughout the cardiac cycle for different idealized flow domains	144
4-55	Time averaged maximum velocities in the midplane bisecting the idealized aneurysms, steady vs. pulsatile inlet	144
4-56	Time averaged spatial average velocities in the midplane bisecting the idealized aneurysms, steady vs. pulsed inlet	145
4-57	Time averaged spatial average WSS at the neck of the idealized aneurysms, steady vs. pulsatile inlet	145
4-58	Time averaged Q_T/Q_{UT} ratios for different idealized flow domains, planar vs. perp curve inlet	147
4-59	Time averaged maximum velocities in the midplane bisecting the idealized aneurysms, planar vs. perp curve inlet	147
4-60	Time averaged spatial average velocities in the midplane bisecting the aneurysms, planar vs. perp curve inlet	148
4-61	Time averaged spatial average WSS at the neck of the idealized aneurysms, planar vs. perp curve inlet	148
4-62	Time averaged Q_T/Q_{UT} ratios for different idealized flow domains, 60 vs. 150 BPM	150
4-63	Peak Q_T/Q_{UT} ratios throughout the cardiac cycle for different idealized flow domains, 60 vs. 150 BPM	151
4-64	Time averaged maximum velocities in the midplane bisecting the idealized aneurysms, 60 vs. 150 BPM	151
4-65	Time averaged spatial average velocities in the midplane bisecting the idealized aneurysms, 60 vs. 150 BPM	152
4-66	Time averaged spatial average WSS at the neck of the idealized aneurysms, 60 vs. 150 BPM	152
4-67	Summary of Q_T and Q_T/Q_{UT} in idealized domains with different upstream segments	154

FIGURE	DESCRIPTION	PAGE
4-68	Q_T and Q_T/Q_{UT} in experimentally derived and idealized flow domains	155
4-69	Comparison of flow domains derived from the glass models and their idealized analogues.	156
4-70	Summary of max and average V_T/V_{UT} in domains with different upstream segments	157
5-1	Flow chart of animal research pursued	161
5-2	Creation of aneurysms on the abdominal aorta through the abdominal cavity	162
5-3	Creation of aneurysms on the abdominal aorta through the side	163
5-4	Use of a soft rapid prototyped cavity mold to contain the elastase	164
5-5	Use of a felt tipped “marker” to apply the elastase	164
5-6	Exposed site at the root of the RCCA for creation of aneurysms in the conventional technique	166
5-7	Measurement of vessel diameter in Ultrasound B-Mode	170
5-8	Measurement of blood velocity using Ultrasound PWD mode	170
5-9	Orientation of ultrasound probe to monitor flow inside an aneurysm	171
5-10	Measurement of intraaneurysmal flow	171
5-11	Representative image of aneurysms anchored to nearby tissue with an intact RCCA	172
5-12	Representative image of aneurysms anchored to nearby tissue with a severed RCCA	173
5-13	Representative image of aneurysms not anchored to nearby tissue with a severed RCCA	173
5-14	Angiograms of group 1 aneurysms	174
5-15	3D reconstruction of group 1 aneurysms	174
5-16	Angiograms of group 3 aneurysms	175
5-17	3D reconstruction of group 3 aneurysms	175
5-18	Blood flow in artery before aneurysm creation, after aneurysm creation, and at followup surgery	180
5-19	Calculation of Q in rabbit models	182
5-20	Flow inside aneurysm of rabbit 34	183
5-21	Flow inside aneurysm of rabbit 38	183
5-22	Flow inside aneurysm of rabbit 41	184
5-23	Flow inside aneurysm of rabbit 43	184
5-24	Aneurysm created in rabbit 20	186
5-25	Residence times in ideal aneurysms of Chpt 4.4 and rabbit aneurysms of Chpt 5.3	188

FIGURE	DESCRIPTION	PAGE
6-1	Comparison of Q_T/Q_{UT} and Avg V_T/V_{UT} metrics	192
6-2	Calculation of recirculation metric	192
6-3	Summary of vorticity in idealized aneurysms	193
6-4	Reconstruction of PED shape using μ CT with $\sim 17\mu\text{m}$ resolution	194
6-5	Comparison of virtual and actual angiograms	195
6-6	Illustration of polymeric stent-graft	195
A-1	Planar velocity contours for RC-SOD147-6	214
A-2	Planar velocity contours for RC-SOD147-12(F)	215
A-3	Planar velocity contours for RC-SOD147-12(R)	216
A-4	Planar velocity contours for RC-SOD147-1	217
A-5	Planar velocity contours for RC-SOD147-2	218
A-6	Planar velocity contours for RC-SOD147-3	219
A-7	Closeup view of PED deployed in RC-SOD147-1, -2, and -3	220
A-8	Planar velocity contours for RC-SOD147-7(F)	221
A-9	Planar velocity contours for RC-SOD147-7(R)	222
A-10	Planar velocity contours for RC-SOD147-8(F)	223
A-11	Planar velocity contours for RC-SOD147-8(R)	224
A-12	Planar velocity contours for RC-SOD147-9(F)	225
A-13	Planar velocity contours for RC-SOD147-9(R)	226
A-14	Closeup view of PED deployed in RC-SOD147-7	227
A-15	Closeup view of PED deployed in RC-SOD147-8	228
A-16	Closeup view of PED deployed in RC-SOD147-9	228
A-17	Closeup view of PED deployed in RC-SOD68-1 and -3	229
A-18	Planar velocity contours for RC-SOD68-1	230
A-19	Planar velocity contours for RC-SOD68-3	231
B-1	Planar velocity contours for RC-SOD147-6 with different inlet turbulence intensities	233
B-2	Planar velocity contours for RC-SOD147-12(F/R) with different inlet turbulence intensities	234
B-3	Planar velocity contours for untreated RC-SOD147-6 and -12(F/R) with different mesh densities	235

FIGURE	DESCRIPTION	PAGE
B-4	Planar velocity contours for treated RC-SOD147-6 and -12(F/R) with different mesh densities	236
B-5	Close-up velocity contours of fluid flowing through the diamond shaped pores with different mesh densities	237
B-6	Intraaneurysmal flow for flow diverter modeled as 1 mil wires, $Re = 387$	238
B-7	Intraaneurysmal flow for flow diverter modeled as 1 mil wires, $Re = 580$	239
B-8	Intraaneurysmal flow for flow diverter modeled as 1 mil wires, $Re = 773$	240
B-9	Intraaneurysmal flow for flow diverter modeled as 2 mil wires, $Re = 387$	241
B-10	Intraaneurysmal flow for flow diverter modeled as 2 mil wires, $Re = 580$	242
B-11	Intraaneurysmal flow for flow diverter modeled as 2 mil wires, $Re = 773$	243
B-12	Intraaneurysmal flow for flow diverter modeled as 2 mil wires, centered and offset pores at 100% stretch	244
B-13	Intraaneurysmal flow for flow diverter modeled as 2 mil wires, centered and offset pores at 250% stretch	245
B-14	Idealized flow domains A to D	246
B-15	Idealized flow domains E to H	247
B-16	Idealized flow domain I	248
B-17	Time dependent Q_T and Q_{UT} in straight inlet domains with 3mm RoC	249
B-18	Time dependent Q_T and Q_{UT} in straight inlet domains with 4mm RoC	249
B-19	Time dependent Q_T and Q_{UT} in straight inlet domains with 6mm RoC	250
B-20	Time dependent Q_T and Q_{UT} in planar curve inlet domains with 3mm RoC	251
B-21	Time dependent Q_T and Q_{UT} in planar curve inlet domains with 4mm RoC	251
B-22	Time dependent Q_T and Q_{UT} in planar curve inlet domains with 6mm RoC	252
B-23	Time dependent Q_T and Q_{UT} in perpendicular curve inlet domains with 3mm RoC	252
B-24	Time dependent Q_T and Q_{UT} in perpendicular curve inlet domains with 4mm RoC	253
B-25	Time dependent Q_T and Q_{UT} in perpendicular curve inlet domains with 6mm RoC	253
B-26	Time dependent Q_T and Q_{UT} in straight inlet domains with 3mm RoC, 150 BPM	254
B-27	Time dependent Q_T and Q_{UT} in straight inlet domains with 4mm RoC, 150 BPM	254
B-28	Time dependent Q_T and Q_{UT} in straight inlet domains with 6mm RoC, 150 BPM	255

FIGURE	DESCRIPTION	PAGE
C-1	Fusiform aneurysm in rabbit 012 at followup	257
C-2	Saccular aneurysm in rabbit 014 at followup	257
C-3	Saccular aneurysm in rabbit 015 at followup	257
C-4	Saccular aneurysm in rabbit 016 at followup	258
C-5	Saccular aneurysm in rabbit 017 at followup	258
C-6	Saccular aneurysm in rabbit 020 at followup	259
C-7	Saccular aneurysm in rabbit 025 at followup	259
C-8	Saccular aneurysm in rabbit 026 at followup	260
C-9	Saccular aneurysm in rabbit 028 at followup	260
C-10	Saccular aneurysm in rabbit 030 at followup	261
C-11	Saccular aneurysm in rabbit 031 at followup	261
C-12	Saccular aneurysm in rabbit 032 at followup	262
C-13	Saccular aneurysm in rabbit 035 at followup	262
C-14	Saccular aneurysm in rabbit 038 at followup	263
C-15	Saccular aneurysm in rabbit 041 at followup	263
C-16	Saccular aneurysm in rabbit 042 at followup	263
C-17	Saccular aneurysm in rabbit 043 at followup	264

LIST OF ABBREVIATIONS

ACA	Anterior cerebral artery
ACommA	Anterior communicating artery
BA	Basilar artery
CAD	Computer aided design
CAE	Computer aided engineering
CCA	Common carotid artery
CFD	Computational fluid dynamics
CT	Computational tomography, an imaging modality
DSA	Digital subtraction angiography, an imaging modality
ECA	External carotid artery
FDA	Food and Drug Administration
FDM	Fused deposition modeling, a method of RPM
FRED	Flow Reduction Embolization Device
ICA	Internal carotid artery
IVUS	Intravascular ultrasound
MCA	Middle cerebral artery
MFAA	Mass flow absolute average
MRI	Magnetic resonance imaging, an imaging modality
PCA	Posterior cerebral artery
PCommA	Posterior communicating artery
PED	Pipeline Embolization Device
PIV	Particle imaging velocimetry
PMA	Pre-market approval (for FDA class III medical devices)
PTV	Particle tracking velocimetry
OCT	Optical coherence tomography
Q	Volumetric flow rate entering the aneurysm
Q _T	Volumetric flow rate entering the treated aneurysm after placement of a flow diverter
Q _{UT}	Volumetric flow rate entering the untreated aneurysm before placement of a flow diverter
Q _T /Q _{UT}	Fraction of flow rate entering the treated aneurysm; metric for device effectiveness
RPM	Rapid prototype manufacturing
SLA	Stereolithography, a method of RPM
SLS	Selective laser sintering, a method of RPM
SST-GT	Shear stress transport, gamma theta transition model for characterizing fluid behavior
VA	Vertebral artery

CHAPTER 1: INTRODUCTION

1.1. CEREBRAL ANEURYSMS

INCIDENCE OF STROKE AND CEREBRAL ANEURYSMS

Stroke describes a scenario where normal blood flow to a patient's brain is interrupted. The cause may be a blockage (an ischemic stroke) or a rupture (hemorrhagic stroke) of the neurovascular system. Stroke is a significant cause of death and disability of the American population, third after heart disease and cancer. More than 600 000 new cases occur each year, with 10 – 25% of cases of the hemorrhagic type. While oxygenated blood can still be delivered to the brain, a leakage or rupture can lead to a slow buildup or a sudden increase in intracranial pressure. This pressure compresses nearby blood vessels and brain matter, leading to ischemia and cell death. [1]

The parts of the neurovasculature at high risk of leakage or rupture typically occur at vessel bifurcations and sharp bends. This is due to the hemodynamic stress imposed on vessel tissue as blood is split into multiple streams or turned in a new direction. Aneurysms can be considered as bulges or sacs that form as a result of this abnormal stress. Figure 1-1 estimates the distribution of cerebral aneurysms.

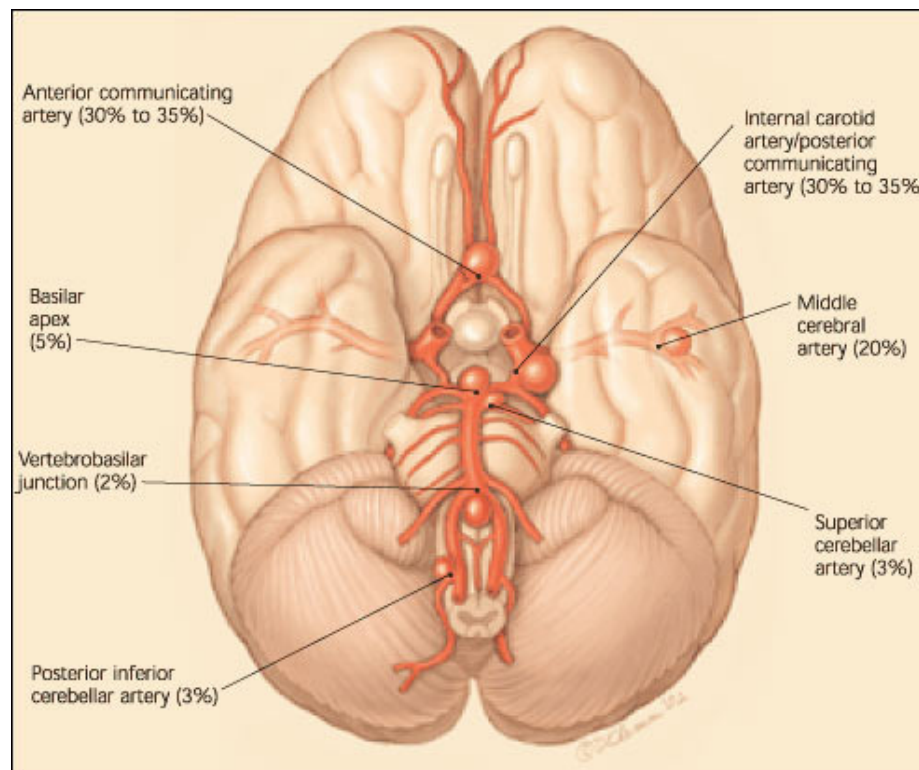


Figure 1-1.The distribution of cerebral aneurysms is shown. The bulges in the blood vessel symbolize aneurysms. [2]

CONVENTIONAL TREATMENT OF INTRACRANIAL ANEURYSMS

Cerebral aneurysms can be detected by three common imaging systems: angiography, computed tomography (CT), and magnetic resonance imaging (MRI). In all three cases, an abnormal structure in the neurovascular can be observed (Figure 1-2A). Depending on the size and location of the aneurysm, physicians historically have had three options upon discovery of an aneurysm: open craniotomy and clipping (Figure 1-2B), endovascular coiling (Figure 1- 2C), or do nothing if the risk of complications during treatment is too high.

Open craniotomy and clipping is a mature technique that carries the risk of long recovery times and infection. It is unsuitable for hard to reach aneurysms as physicians must gently work beside brain tissue to deploy the clip across the neck of the aneurysm. The greatest benefit of the clipping technique is that the aneurysm is completely sealed off, eliminating the risk of leakage and rupture.

Coiling is an endovascular technique that carries a smaller risk of infection and shorter recovery time than clipping. A catheter is snaked through the patient's arterial system from a femoral entry point to the aneurysm site. Platinum or polymer coils are deployed into the aneurysm cavity, inducing thrombosis and "solidification" of the aneurysm. While coiling is an excellent alternative to clipping, long term complications due to insufficient packing of the coils and risk of loose thrombotic material migrating downstream from the aneurysm has demanded research into other endovascular methods of treating intracranial aneurysms.

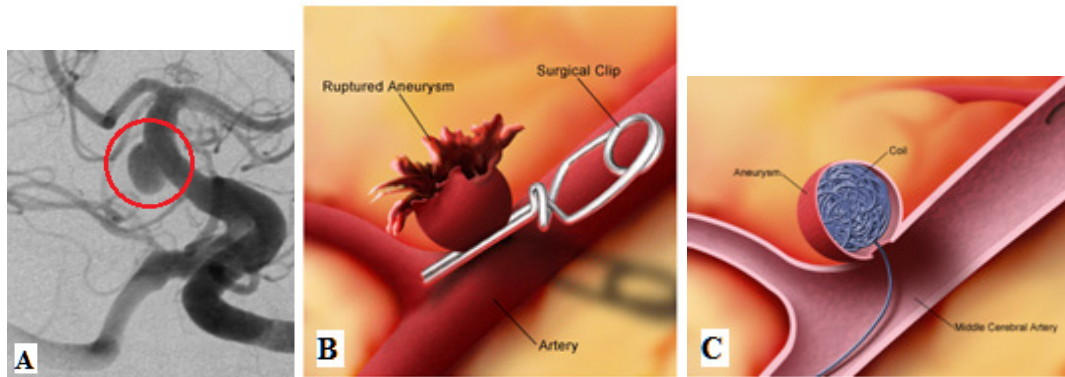


Figure 1-2A. An angiogram showing a basilar artery aneurysm (circled in red) [3] **1-2B:** An aneurysm can be treated by opening the skull and placing a clip across the aneurysm neck [4]. **1-2C:** An aneurysm can also be treated by inserting platinum or polymer coils into the aneurysm cavity [5].

EMERGENCE OF FLOW DIVERTERS

In the last few years, a new class of endovascular devices has become commercially available for the treatment of large and wide-necked aneurysms. Due to their large volume, large aneurysms can be difficult and expensive to fill with coils. Due to the lack of a well defined neck, coils would prolapse back into parent artery and create a risk of thrombosis and ischemic stroke. Flow diverters address both of these deficiencies by inducing thrombus formation inside the aneurysm by significantly reducing blood flow entering the aneurysm. [6]

The first device available on the market is the Silk by Balt Extrusion in 2008. It is a braided stent woven from many individual metallic wires, as illustrated in Figure 1-3. The second device commercially available device is the Pipeline Embolization Device, or PED, which received PMA approval from the United States Federal Drug Administration in March of 2011. It is also a braided stent, as illustrated in Figure 1-4, but with a slightly different deployment mechanism than the Silk. A third device that will be commercially available soon is the Flow Reduction Embolization Device by Microvention, or FRED, which promises to offer superior deliverability. As shown in Figure 1-5, the FRED is still a braided stent, but radiopaque markers are present at the ends of the stent, allowing for robust manipulation of the device while placing it across an aneurysm in the neurovasculature.

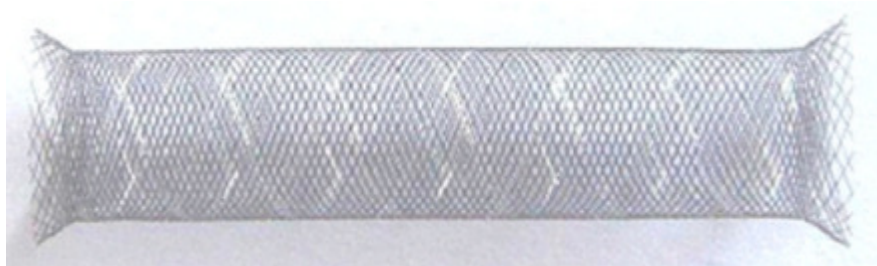


Figure 1-3. The Silk flow diverter by Balt Extrusion. It is a braided structure woven from many individual metallic fibers. [7]

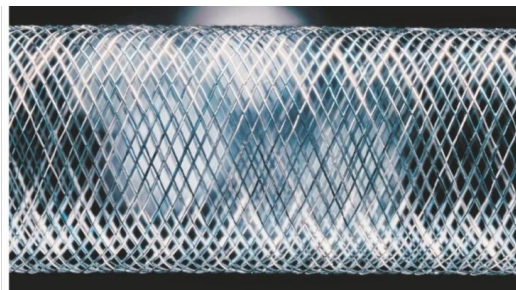


Figure 1-4. A close-up of the Pipeline Embolization Device by Covidien. It is also a braided structure woven from many individual metallic filars. Some of the filars are radiopaque to allow physicians to visualize the placement of the device across the aneurysm. [8]

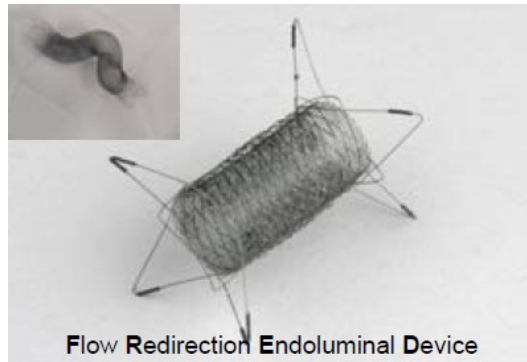


Figure 1-5.The Flow Redirection Endoluminal Device from Microvention. It also relies on a braided structure to diverter flow. However, the constrained ends engage with a more reliable delivery wire, which leads to a more robust and simpler deployment experience for the doctor. [9]

1.2. RESEARCH GOALS

Flow diverters have demonstrated their superiority over coiling in the treatment of large and wide necked aneurysms. [10, 11] However, problems have become more common as the PED moved out of the clinical trial phase and into general use. Complications of hemorrhaging have been reported. Aneurysms are not always occluded six months after implantation (Table 1-1). It is difficult to ascertain the exact level of flow reduction since the shape of the woven mesh is highly variable when deployed and dependent on operator skill. [10]

Table 1-1.Published prospective studies of flow diversion for intracranial aneurysms. [10]

Author and Year	No. of Patients	No. of Aneurysms	Recurrence (%)	Location			Size			Device	Occlusion Rate (Complete)		
				AC (%)	PC (%)	S (%)	L (%)	G (%)	3 mo (%)		6 mo (%)	12 mo (%)	
Lylyk et al, 2009	53	63	37	87	13	52	35	13	PED	56	93	95	
Byrne et al, 2010	70	70	N/A	71	29	26	53	21	SFD	N/A	49	N/A	
Lubicz et al, 2010	29	34	29	85	15	53	35	12	SFD		69	N/A	
Szikora et al, 2010	18	19	5	95	5	26	53	21	PED	N/A	95	N/A	
Nelson et al, 2011	31	31	39	94	6	64.5	29	6.5	PED	N/A	93	N/A	

Six patients of the Lylyk et al series and 9 patients of the Szikora et al series have been included in the PITA trial (Nelson et al 2011).

AC indicates anterior circulation; DN, de novo; G, giant; L, large; N/A, not available; PC, posterior circulation; PED, pipeline embolization device; R, ruptured; REC, recurrence; S, small; SFD, SILK flow diverter; UR, unruptured.

Not all of the data that Chestnut Medical (then eV3, then Covidien) provided to the FDA as part of their submission package for pre-market approval, or PMA, was made public. Therefore, it is not known if Chestnut Medical had done an extensive study (computational or experimental) on the flow diverting behavior of their device within the range of geometry and flow combinations present in the human neurovasculature. Academic researchers, particularly Juan Cebral at George Mason University, have simulated and published the flow diverting behavior of PED-like devices in patient derived geometries [12]. However, such data are not useful for deriving threshold values, such as the maximum flow rate entering the aneurysm that can still lead to thrombus formation, when geometric variables, such as aneurysm neck size, are not well characterized or examined in a controlled manner.

The lack of understanding of the performance characteristics of currently available flow diverters and of the minimum threshold of flow diversion needed to induce healing of the aneurysm prevents the optimization of the device. While a complete elimination of flow entering the aneurysm would be the perfect scenario, striving towards this situation comes with a heavy price. The dimensions of the diamond shaped pores formed by the braided structure of the current generation of flow diverters are affected by tortuous bends. Along the curve which defines the outer edge of the diverter, the braided structure opens up, leading to larger pores and reduced flow reduction efficacy. Along the inner curve, the braided structure compresses, leading to smaller pores, as shown in Figure 1-6. The neurovasculature is lined with very small vessels, on

the order of 100 μ m to 1mm in diameter, which may be occluded by this compressed braided structure, leading to lacunar strokes.

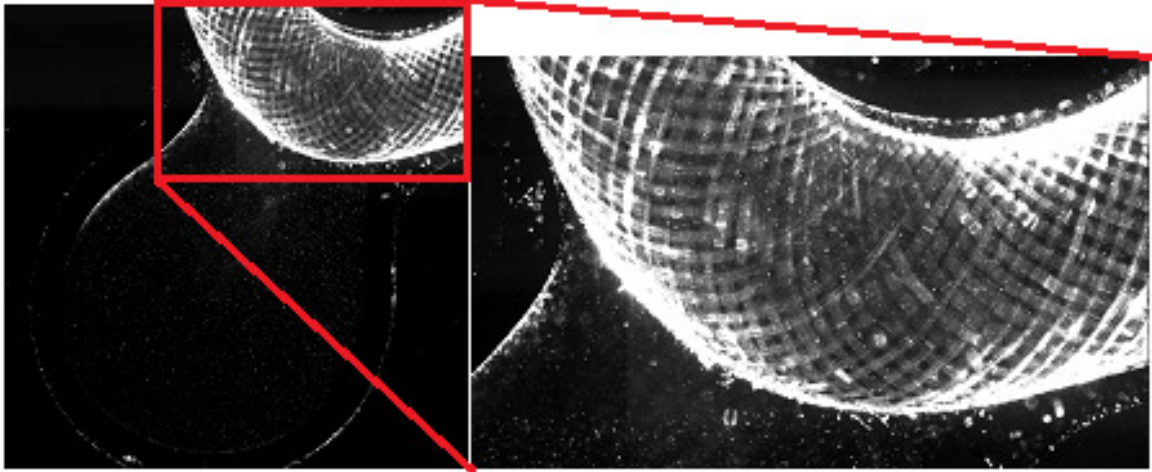


Figure 1-6. Non-uniformities in pore dimensions are seen in the flow diverter. The displayed images are from particle imaging velocimetry (PIV) experiments performed in this research, which will be described later. A close-up view of the flow diverter is shown on the right. Along the inner curve, the braided structure is collapsed, leading to smaller diamond-shaped pores which may occlude flow entering nearby perforating vessels. Along the outer curve, the braided structure is expanded, leading to larger diamond-shaped pores which are less effective in diverting flow than if the flow diverter was in a less curved blood vessel.

The exposed metal of the flow diverter braids can also trigger a thrombogenic or inflammatory response. It is currently managed with anti-coagulant and anti-platelet medications. It is estimated that around 30 – 35% of the surface area is occupied by metal, whereas typical neurovascular stents have around 5%. [10]. Therefore, if the flow diversion performance window and minimal level of flow diversion required are known, it is possible that the braided structure can be loosened to incorporate less metal and reduce the likelihood that thrombus will form inside the lumen of the device and cause an ischemic stroke.

In order to design the next generation of flow diverters, this PhD research was conducted with four main objectives:

1. Develop and implement experimental techniques to verify computer simulation models for analyzing intraaneurysmal flow.
2. Determine the performance of commercially available flow diverters in a range of flow domains that represent the human neurovasculature.

3. Explore methods for improving the standard model of aneurysm creation in rabbits to better understand the minimum threshold of flow reduction needed to induce thrombus formation and healing of the aneurysm.
4. Identify design directions and formulate the experimental plan for optimizing the pore pattern for the next generation of flow diverters.

The research will be presented in three main blocks:

1. Bench top experiments using a technique called particle imaging velocimetry (PIV) to characterize the flow diversion behavior of the Pipeline Embolization Device (PED).
2. Verification of computational fluid dynamic (CFD) models of the PED, and CFD predictions of device effectiveness in vessel geometries and blood flows common to the neurovasculature.
3. Development of an improved aneurysm model in rabbits through external application of elastase and manipulation of the vessel stump.

**CHAPTER 2: LITERATURE REVIEW AND BACKGROUND
INFORMATION**

2.1. PHYSIOLOGY OF THE CEREBRAL NEUROVASCULATURE

INTRODUCTION

This chapter discusses the following subjects:

- Range of normal wall shear stress (WSS) for healthy vessels
- Overview of the neurovascular anatomy
- Neurovascular vessel diameters
- Neurovascular flow rates

RANGE OF NORMAL WSS FOR HEALTHY VESSELS

The normal range of wall shear stress experienced at healthy arterial walls is 10 to 70 dynes / cm² or 1 to 7 Pa in healthy vessels, as illustrated in Figure 2-1. This range of WSS keeps the endothelial cells quiescent and non-thrombogenic. Shear stresses below this range lead to an atherosclerotic phenotype of endothelial cells. Shear stresses above this range damage formed blood elements and trigger remodeling of the underlying smooth muscle cell layer in the blood vessel [13].

Both are reasonable physiological responses when it is realized that blood flowing past a sclerotic blockage experiences an increased velocity, thus raising WSS beyond the “normal” range. When the smooth muscle cell layer of the blood vessel thins out, the vessel diameter increases, the blood velocity decreases, and WSS lowers down to the “normal” range. However, as the smooth muscle cell layer continuously remodels itself, non-uniformities occur that result in aneurysms. The thinner vessel wall is also more susceptible to rupture and hemorrhaging.

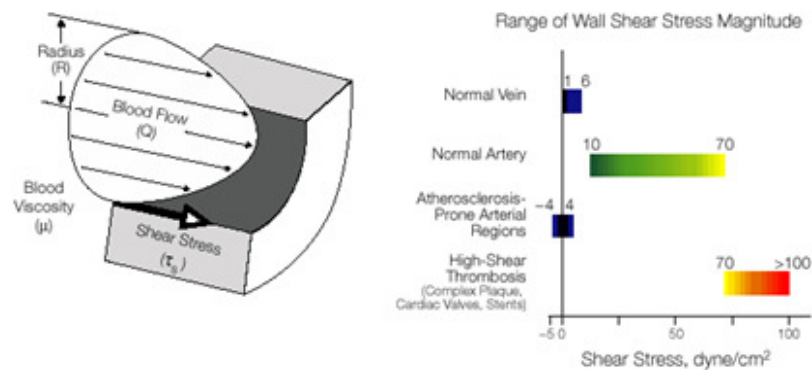


Figure 2-1. The normal range of wall shear stress experienced by the human artery is between 10 – 70 dynes / cm². Stresses beyond this range lead to remodeling of the vessel wall in an attempt to return to the normal range. [13]

OVERVIEW OF THE NEUROVASCULAR ANATOMY

The human neurovasculature is fed by four major vessels, the left/right internal carotid arteries (ICA) and the left/right vertebral arteries. The two vertebral arteries merge into the basilar artery (BA). The anterior communicating artery (ACommA) and posterior communicating arteries (PCommA) intersect ICAs and the BA to form a structure called the Circle of Willis (CoW). While the CoW is not fully formed in all individuals, it allows the neurovasculature to compensate (to an extent) for injuries or blockages of any of the feeder vessels via retrograde flow of blood. Figure 2-2A illustrates a side view of the anterior circulation (supplied by the ICA). Figure 2-2B illustrates a flattened view of the anterior circulation (supplied by the left and right ICA) and the posterior circulation (supplied by the left and right VA). Figures 2-2C and D illustrate the different segments of the ICA. It is particularly tortuous in the upper regions (C4 – C7), leading to complex blood flow and formation of aneurysms.

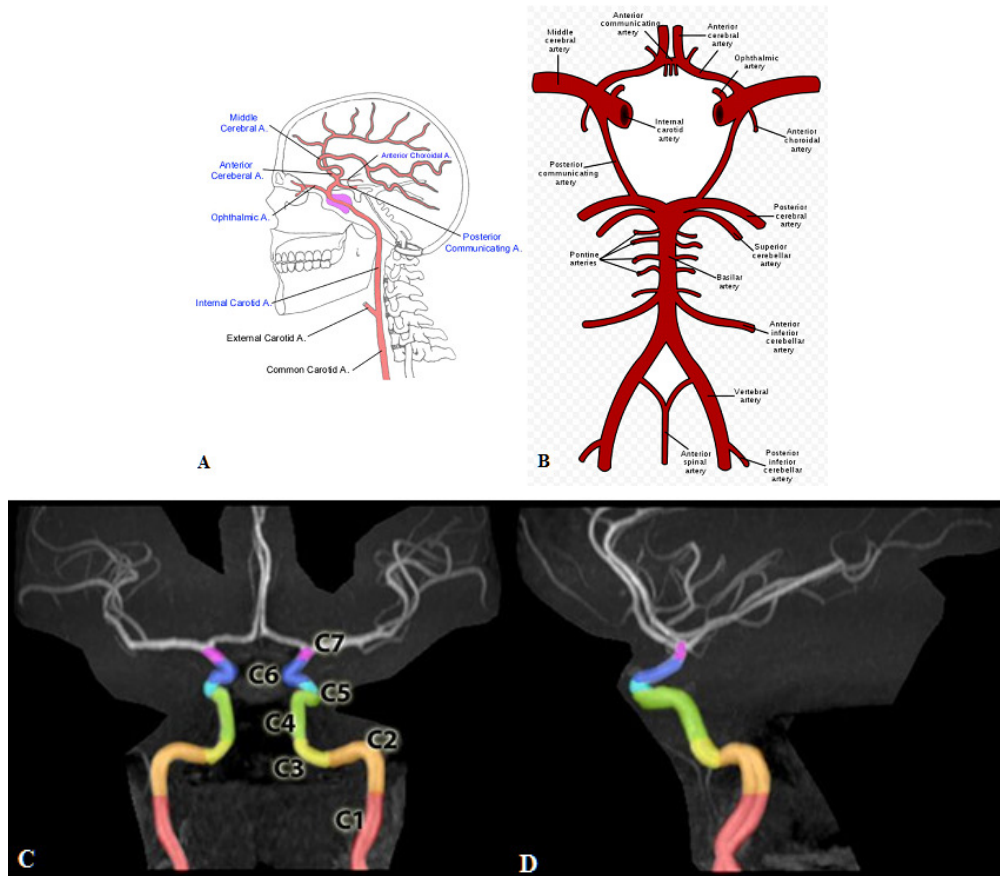


Figure 2-2A. The anterior portion of the neurovasculature is shown. [14] **2-2B.** The feeder vessels supplying the Circle of Willis are shown. The CoW can be visualized as the ring formed by the ACommA and PCommAs as they join up the ICAs and BA. [15] **2-3C.** The different segments of the ICA are shown. C1: Cervical. C2: Petrous. C3: Lacerum. C4: Cavernous. C5: Clinoid. C6: Ophthalmic / supraclinoid. C7: Communicating / terminal. **2-3D.** A side view of the ICA [16]

NEUROVASCULAR VESSEL DIAMETERS

During the course of anatomical and blood flow studies, researchers have reported a range of diameters for a number of different vessels in the neurovasculature. Some sources provide average diameters +/- the standard deviation. Others list out individual measurements. Table 2-1 is a summary of diameters found in the literature search.

Table 2-1. Internal diameters (ID) of different vessels. ACA: Anterior cerebral artery. ACommA: Anterior communicating artery. BA: Basilar artery. ICA: Internal carotid artery. MCA: Middle cerebral artery. PCA: Posterior cerebral artery. PCommA: Posterior communicating artery. VA: Vertebral artery.

Vessel	Internal Diameter [mm]	Reference	Internal Diameter [mm]	Reference
ACA	2.34 (avg)	[17]	1.78 +/- 0.41	[21]
ACA	2.0, 2.3, 2.3, 3.4	[18]	2.3 +/- 0.1	[22]
ACA	2.6	[19]		
ACommA	1.48 (avg)	[17]	2.45 +/- 0.45	[23]
ACommA	2.3, 2.3	[18]	1.2 +/- 1	[22]
ACommA	2.0 +/- 1.5	[19]	2.5 (avg)	[25]
ACommA	1.13 +/- 0.28	[21]	1.4 +/- 0.3	[27]
BA	3.24 (avg)	[17]	3.05 +/- 0.15	[22]
BA	3 (avg)	[18]	3.2 (avg)	[24]
ICA	4 (avg)	[17]	3.6 +/- 0.1	[22]
ICA	4.2, 4.2	[18]	4.9	[26]
ICA	4.2 +/- 0.4	[19]	4.72 +/- 0.26	[20]
MCA	2.86 (avg)	[17]	2.7 +/- 0.1	[22]
MCA	2.7, 2.7	[18]	1.6	[27]
MCA	1.9 +/- 0.6	[19]		
PCA	2.2, 2.2, 2.2, 2.2	[18]		
PCommA	2, 2	[18]		

NEUROVASCULAR FLOW RATES

Blood flow rates are typically reported while the patient is at rest. Researchers variously report velocities as average values, max/min values, or simply show velocity vs. time plots. An approximate upper and lower bound for velocities can be found from the literature despite variation due to equipment and patient differences.

Table 2-2. Partial collection of velocities and velocity profiles from the literature search. Velocity profiles from Devault [18] contain the predicted outflow (red line), mean (blue line), mean +/- standard deviation (green line), and mean +/- two standard deviations (dashed green line).

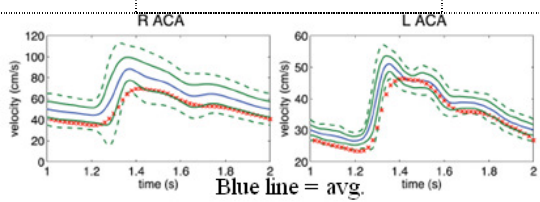
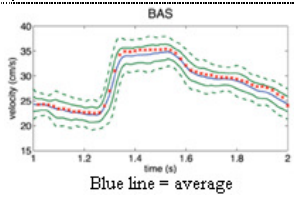
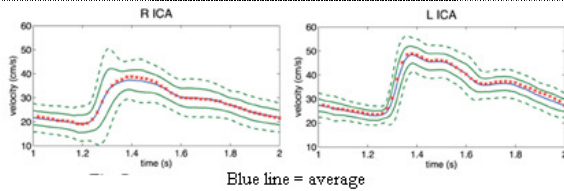
Vessel	Min [cm/s]	Avg [cm/s]	Max [cm/s]	Reference
ACA				[18]
ACA		32.6		[20]
ACA		53 +/- 7		[29]
ACA-A1		69 +/- 5, 116 +/- 53		[30]
BA				[18]
BA		43.2		[20]
ICA				[18]
ICA		35 +/- 7		[29]
ICA-C1		73 +/- 11		[30]

Table 2-3. Partial collection of velocities and velocity profiles from the literature search. Velocity profiles from Devault [18] contain the predicted outflow (red line), mean (blue line), mean +/- standard deviation (green line), and mean +/- two standard deviations (dashed green line).

Vessel	Min [cm/s]	Avg [cm/s]	Max [cm/s]	Reference
MCA	65		80	[31]
MCA		60		[32]
MCA				[18]
MCA	60		65	[24]
MCA		55.5 +/- 3.7		[33]
MCA		69 +/- 14		[34]
MCA		43.3		[20]
MCA		61 +/- 3		[35]
MCA		65 +/- 6		[29]
MCA-MI				[36]
PCA				[18]
PCA		58.4		[20]
PCA		46 +/- 7		[29]

2.2. DISTRIBUTION OF ANEURYSM SIZES, SHAPES, ORIENTATIONS, AND LOCATIONS

Obtaining a distribution of aneurysm sizes sorted by their locations in the neurovasculature was much more difficult and simply the distribution of aneurysm sizes. Researchers measure, record, and present aneurysm sizes differently. Some researchers describe aneurysms as dimension A * dimension B. Others simply give one dimension, which the author presumes is the diameter of a sphere which approximates the volume of the aneurysm. A number of researchers describe both a neck size and a dome diameter.

Figure 2-3 summarizes the dimensions of aneurysms in various locations of the neurovasculature from manuscripts that describe both the neck and the dome geometries. [37, 38, 39, 40, 41]. Unfortunately, the selection of these aneurysms was not random. They were selected for a particular procedure or study, such as the use of a stent to prevent coils from escaping the aneurysm. The Wiebers manuscript [42] presented a random selection of aneurysms (~ 6000 unruptured aneurysms) but only one dimension was described. (see Figure 2-4)

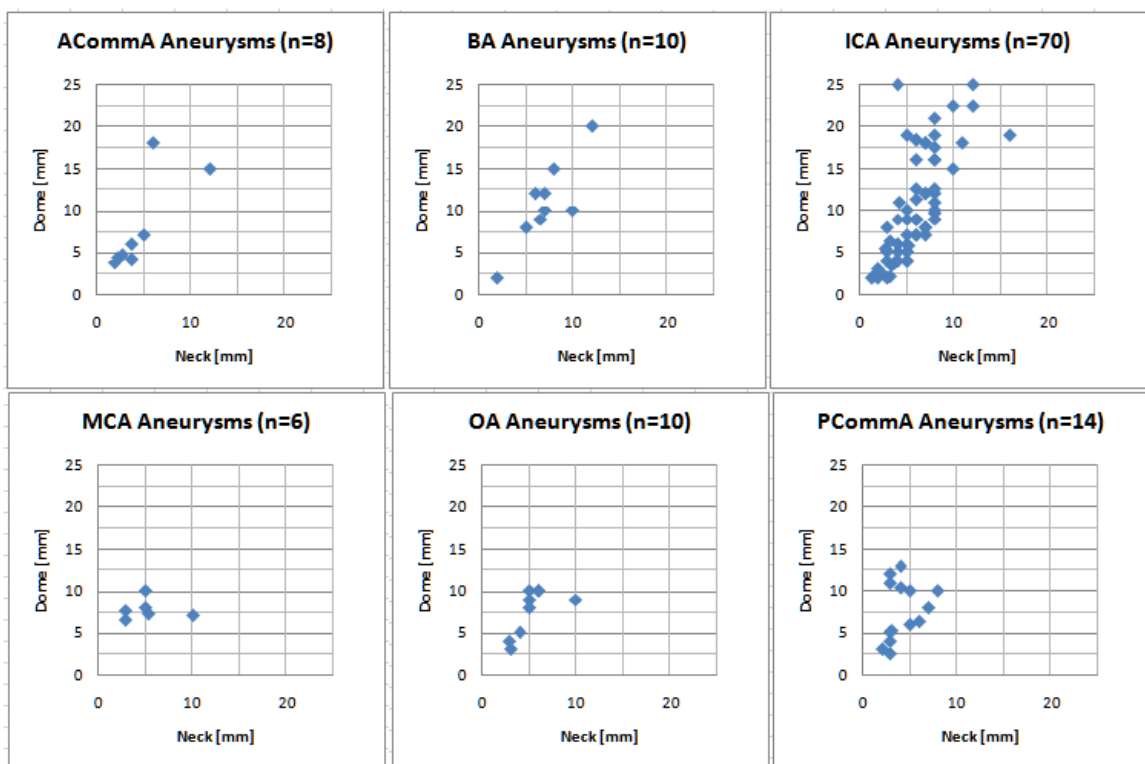


Figure 2-3. Information from researchers who described both the neck size and the aneurysm size in their studies. Due to the small and non-random sample size from the manuscripts, the data should be regarded as qualitative. [37, 38, 39, 40, 41]

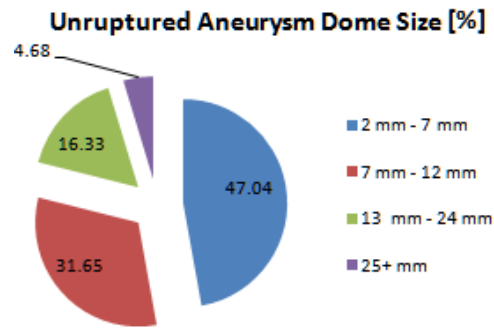


Figure 2-4. Weiber et al. examined almost 6000 unruptured intracranial aneurysms and sorted them based on size. [42]

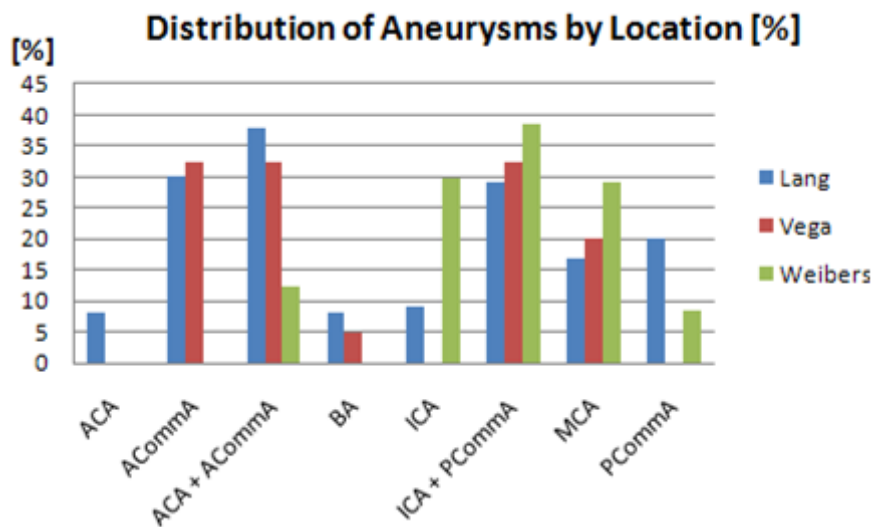


Figure 2-5. Comparison of distribution of aneurysm locations between Lang [44], Vega [2], and Wiebers [42]

Wiebers et al. [42] were interested in answering two questions:

1. What is the probability of a ruptured aneurysm being a certain size?
2. What is the probability of future rupture of a given sized aneurysm discovered before rupture?

By following patients for an extended amount of time (~6 years), Weiber concluded that aneurysms smaller than 7 mm were at low risk of rupture in the future. Aneurysms between 7 – 12 mm in size slowly accumulated risk over time. Aneurysms larger than 12 mm quickly accumulated risk over the first several years (Figure 2-6). [42]

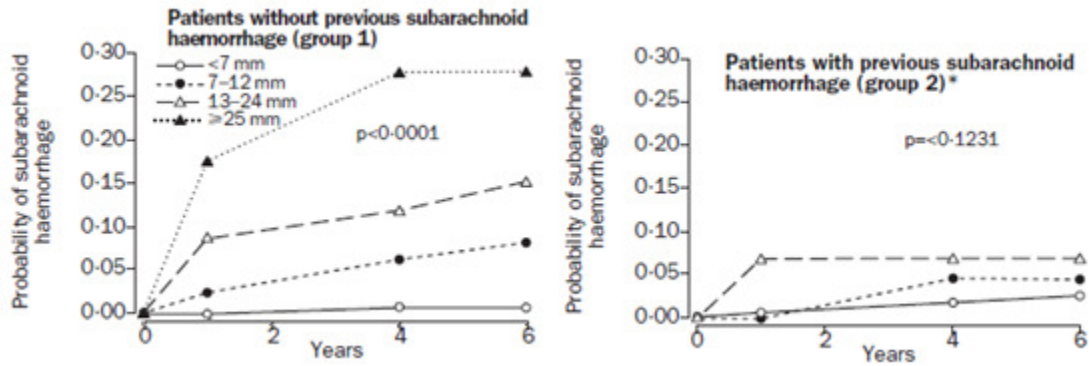


Figure 2-6. The risk of rupture in untreated aneurysms was largely dependent on size in patients without a previous history of subarachnoid hemorrhaging. [42]

Delgado and Tubman [45] examined the 1681 aneurysms treated at Abbott Northwestern Hospital from June 1995 to January 2012 and reported the spatial and size distribution of ruptured aneurysms (Table 2-4). Carter et al. [46] reported the size and location of unruptured and ruptured aneurysms located at bifurcations that were treated at Massachusetts General Hospital from 1991 to 2003 (Table 2-5). Tables 2-4, 2-5, and Figure 2-3 serve as a guide as to the size of aneurysms that are possible for a given region of the neurovasculature. Each region of the neurovasculature has its own distinct range of parent vessel diameters and radii of curvature at bends. These combinations guide the selection of flow domains of interest when evaluating flow diverter designs.

Table 2-4. Distribution of ruptured aneurysm locations treated at Abbott Northwestern Hospital (Minneapolis, MN), sorted by maximum aneurysms sac dimension. [45]

Aneurysm location	≤5 mm	%	6-9 mm	%	≥10 mm	%	Total	%
All	297	48.5	210	34.3	106	17.3	613	100
Anterior circulation	204	51.3	120	30.2	74	18.6	398	64.9
ACOM	131	58.5	67	29.9	26	11.6	224	36.5
MCA	35	42.2	26	31.3	22	26.5	83	13.5
ICA	24	34.3	24	34.3	22	31.4	70	11.4
Posterior circulation	93	43.3	90	41.9	32	14.9	215	35.1
PCOM	53	44.2	56	46.7	11	9.2	120	19.6
Basilar	16	33.3	17	35.4	15	31.3	48	7.8
PICA	14	63.6	5	22.7	3	13.6	22	3.6

Table 2-5. Distribution of aneurysms located at bifurcating vessels that were treated at Massachusetts General Hospital. [46]

	Unruptured (n)	Mean size	Ruptured (n)	Mean size	Totals
Basilar	88	11.8	105	9.6	193
Ophthalmic	124	8.5	21	13.1	145
MCA	258	8.2	140	8.7	398
Anterior commissure	143	7.7	283	7.4	426
Posterior commissure	115	7.2	200	7.9	315
Distal	26	6.2	32	5.7	58
ICA bifurcation	50	8.8	21	11.1	71
PICA	15	7.1	52	7.1	67
Totals	819	8.4	854	8.2	1673

Ujiie et al. [47] were interested in determining if the aspect ratio (AR) of aneurysms was a factor in predicting rupture. As Table 2-6 illustrates, the AR is defined as the depth of the aneurysm bulb divided by the neck width. Approximately 200 aneurysms were examined and statistically significant differences in the AR were observed between unruptured vs. ruptured aneurysms at all locations within the neurovasculature. As Figure 2-7 illustrates, Weir et al. [48] also observed in 774 aneurysms that a higher AR was more prone to rupture, whereas size was not a significant predictor of rupture.

Table 2-6. The aspect ratios (depth / neck width) and sizes of aneurysms were compared. Statistically significant values of aspect ratios were observed between unruptured vs. ruptured aneurysms. [47]

Site of Aneurysm and Status	Mean Aspect Ratio	t Statistic	Mean Size (mm)	t Statistic
Anterior communicating artery				
<i>Ruptured</i>	2.6 ± 0.92	0.000394	7.2 ± 2.36	NS
<i>Unruptured</i>	1.5 ± 0.42		5.1 ± 2.55	
Middle cerebral artery				
<i>Ruptured</i>	2.6 ± 0.79	0.00024	9.2 ± 3.44	NS
<i>Unruptured</i>	1.6 ± 0.63		6.9 ± 3.27	
Internal carotid artery-posterior communicating artery				
<i>Ruptured</i>	2.4 ± 0.51	0.0000	9.0 ± 2.48	0.007
<i>Unruptured</i>	1.4 ± 0.34		5.8 ± 3.32	
Other				
<i>Ruptured</i>	3.1 ± 0.86	0.000458	8.9 ± 1.83	0.001
<i>Unruptured</i>	1.4 ± 0.50		5.1 ± 3.10	

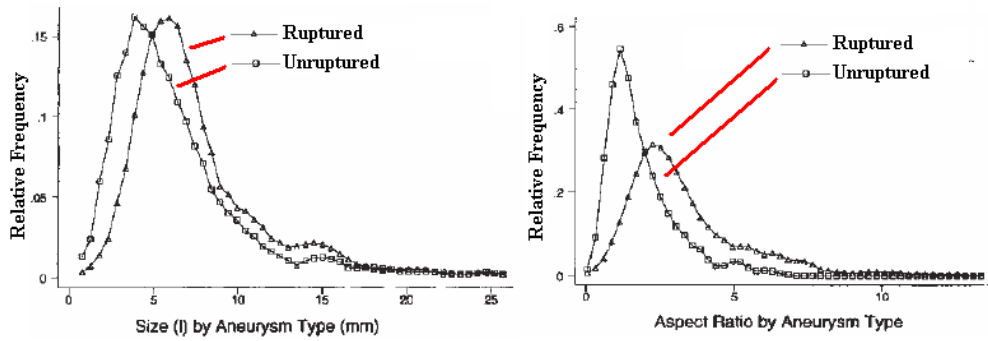


Figure 2-7. Size is not a significant predictor of aneurysm rupture, but aneurysms with higher aspect ratio are more prone to rupture. [48]

The increasing popularity of 3D imaging modalities, such as MRI, spurred Raghavan et al. [49] to develop shape indices to describe the shapes of aneurysms. That study examined 27 aneurysms (18 unruptured, 9 ruptured) and concluded that two indices in particular were significant between unruptured and rupture aneurysms. The undulation index (UI) is based on the difference between the volume of an aneurysm and that of a convex hull (see figure 2-8) superimposed over it. The non-sphericity index (NSI) is based on the difference between the surface of an aneurysm and that of a sphere. As indicated in Table 2-7, ruptured aneurysms had statistically significant higher values of UI and NSI.

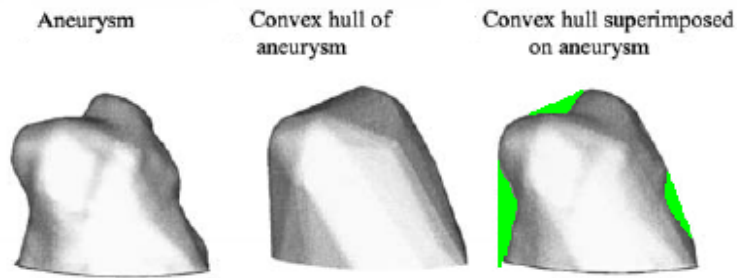


Figure 2-8. To calculate the Undulation Index (UI), a convex hull is superimposed on the aneurysm volume. The difference (shown in green) is an indicator of the degree of undulations on the aneurysm. [49]

Table 2-7. Raghavan et al. formulated six different indices to describe the shape of the aneurysm. This was made possible with the growing popularity of 3D imaging systems such as MRI which do not mask the subtleties of aneurysm shapes. The Undulation Index and Non-Sphericity Index were found to be statistically higher for ruptured aneurysms. [49]

Shape Index	Low	Medium	High
Undulation index (UI)			
Aspect ratio (AR)			
Ellipticity index (EI)			
Non-sphericity index (NSI)			
Conicity parameter (CP)			
Bottleneck factor (BF)			

Index	Unruptured Aneurysm	Ruptured Aneurysm	p Value	AUC†
age	57 ± 13	56 ± 19	0.857	0.44
sex (% female)	89	67	0.296	—
volume (V)	84 ± 59	146 ± 219	0.264	0.48
max diameter (D _{max})	4.81 ± 1.37	4.87 ± 1.86	0.918	0.45
surface area (S)	83 ± 41	122 ± 128	0.243	0.53
height (H)	5.13 ± 1.54	6.55 ± 3.80	0.175	0.60
neck diameter (D _n)	4.25 ± 1.38	3.79 ± 1.58	0.443	0.42
undulation index (UI)	0.071 ± 0.039	0.137 ± 0.066	0.003	0.80
aspect ratio (AR)	1.27 ± 0.40	1.85 ± 0.79	0.016	0.72
ellipticity index (EI)	0.131 ± 0.047	0.185 ± 0.052	0.011	0.76
nonsphericity index (NSI)	0.156 ± 0.058	0.233 ± 0.061	0.004	0.83
conicity parameter (CP)	0.199 ± 0.194	0.152 ± 0.222	0.579	0.40
bottleneck factor (BF)	1.156 ± 0.171	1.387 ± 0.492	0.082	0.60
mean curvature norm (MLN)	0.333 ± 0.057	0.384 ± 0.057	0.038	0.72
gaussian curvature norm (GLN)	2.051 ± 0.868	2.699 ± 0.899	0.083	0.69

* Values are presented as the means ± standard deviations.
† Represents predictive capability of an index. An AUC of 0.05 indicates an index with zero predictability.

2.3. DESCRIPTION OF RELEVANT FLUID MODELS AND NON-DIMENSIONAL NUMBERS

Blood is a suspension of erythrocytes (red blood cells), leukocytes (white blood cells), thrombocytes (platelets), and dissolved blood plasma proteins and minerals. In low shear flows, non-Newtonian behavior is observed due to the aggregation and viscoelastic behavior of the formed blood elements. Johnston et al. [50, 51] have summarized in Table 2-8 the typical values and models used to describe blood viscosity by different researchers. The apparent blood viscosities at different strain rates for the different blood models are plotted in Figure 2-9. When blood is simulated as a Newtonian fluid, the dynamic viscosity is typically rounded up to $\mu = 0.0035 \text{ Pa} \cdot \text{s}$.

Table 2-8. Various blood viscosity models summarized by Johnston et al. $1 \text{ P} = 1 \text{ poise} = 0.1 \text{ Pa} \cdot \text{s}$. [50, 51]

Blood model	Effective viscosity μ
Newtonian model	$\mu = 0.0345 \text{ P}$
Carreau model (Cho and Kensey, 1991)	$\mu = \mu_{\infty} + (\mu_0 - \mu_{\infty})[1 + (\lambda\dot{\gamma})^2]^{(n-1)/2}$, where $\lambda = 3.313\text{s}$, $n = 0.3568$, $\mu_0 = 0.56 \text{ P}$ and $\mu_{\infty} = 0.0345 \text{ P}$
Walburn-Schneck model (Walburn and Schneck, 1976)	$\mu = C_1 e^{C_2 H} [e^{C_4 (TPMA/H^2)}] (\dot{\gamma})^{-C_3 H}$, where $C_1 = 0.00797$, $C_2 = 0.0608$, $C_3 = 0.00499$, $C_4 = 14.585 \text{ l g}^{-1}$, $H = 40\%$ and $TPMA = 25.9 \text{ g l}^{-1}$
Power Law (Cho and Kensey, 1991)	$\mu = \mu_0 (\dot{\gamma})^{n-1}$, where $\mu_0 = 0.035$ and $n = 0.6$
Casson model (Fung, 1993)	$\mu = [(\eta^2 J_2)^{1/4} + 2^{-1/2} \tau_y^{1/2}]^2 J_2^{-1/2}$, where $ \dot{\gamma} = 2\sqrt{J_2}$, $\tau_y = 0.1(0.625H)^3$ and $\eta = \eta_0(1 - H)^{-2.5}$ with $\eta_0 = 0.012 \text{ P}$ and $H = 0.37$
Generalised Power Law model (Ballyk et al., 1994)	$\mu = \lambda \dot{\gamma} ^{n-1}$, $\lambda(\dot{\gamma}) = \mu_{\infty} + \Delta\mu \exp\left[-\left(1 + \frac{ \dot{\gamma} }{a}\right) \exp\left(\frac{-b}{ \dot{\gamma} }\right)\right]$, $n(\dot{\gamma}) = n_{\infty} - \Delta n \exp\left[-\left(1 + \frac{ \dot{\gamma} }{c}\right) \exp\left(\frac{-d}{ \dot{\gamma} }\right)\right]$, where $\mu_{\infty} = 0.035$, $n_{\infty} = 1.0$, $\Delta\mu = 0.25$, $\Delta n = 0.45$, $a = 50$, $b = 3$, $c = 50$ and $d = 4$

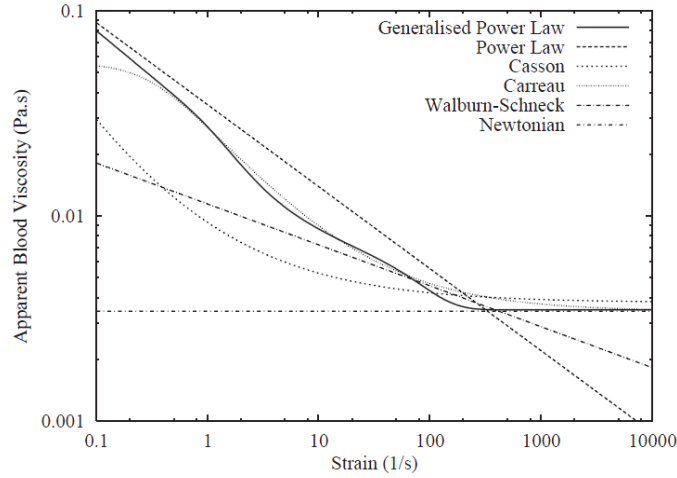


Figure 2-9. The apparent blood viscosity is plotted against the strain rate for the different blood models described by Johnston. [50]

The simulations and experiments conducted in this body of research examine the incompressible flow of a Newtonian fluid in a rigid wall environment. Background research, largely from computation studies, indicated that the majority of fluid behavior was captured by this simplified scenario. The Navier-Stokes equation of interest (Equation 2-1 in vector form, Equation 2-1B in repeated subscript form) and the equation for conservation of mass (Equation. 2-2) are shown. Application of these equations along with the appropriate boundary conditions allow for the characterization of flow inside a domain of interest. In the computer simulations, the value for the residual number is imposed by the user. Simulations are considered to be converged when the residual value, which refers to slight imbalances of momentum and mass within the flow domain due to solver inaccuracies, is reached. A value of 10^{-6} was imposed.

$$\rho \left(\frac{\partial \mathbf{v}}{\partial t} + \mathbf{v} \cdot \nabla \mathbf{v} \right) = -\nabla p + \mu \nabla^2 \mathbf{v} + \mathbf{f} \quad (\text{Eq. 2 - 1})$$

$$\rho \frac{\partial u_i}{\partial t} + u_j \frac{\partial u_i}{\partial x_j} = -\frac{\partial p}{\partial x_i} + \mu \frac{\partial^2 u_i}{\partial x_j \partial x_j} + f_i \quad (\text{Eq. 2 - 1B})$$

$$\frac{\partial \rho}{\partial t} + \nabla \cdot (\rho \mathbf{v}) = 0 \quad (\text{Eq. 2 - 2})$$

While the human vasculature is an intricately complex network of blood vessels, blood flow can still be considered, in its simplest model, as flow in a pipe. The Reynolds number Re defined in Equation 2-3 is a dimensionless number that quantifies the relative importance of inertial forces and viscous forces. Re is composed of the fluid density, dynamic viscosity, velocity, and characteristic dimension of the flow domain. In pipe flow, the dimension of interest is typically the pipe diameter.

$$Re = \frac{\text{Inertial Forces}}{\text{Viscous Forces}} = \frac{\text{Density} * \text{Velocity} * \text{Characteristic Length}}{\text{Dynamic Viscosity}} = \frac{\rho * V * D}{\mu} \quad (\text{Eq. 2 - 3})$$

The heart pumps blood in a pulsatile manner. The Womersley number α defined in Equation 2-4 is a dimensionless number that quantifies the relative importance of transient inertial forces and viscous forces in a laminar and incompressible flow. The Womersley number is composed of the fluid density, angular frequency of the oscillating flow, the characteristic dimension of the flow domain, and the dynamic viscosity. In pipe flow, the characteristic dimension is typically the pipe diameter.

$$\alpha^2 = \frac{\text{Transient Inertia Forces}}{\text{Viscous Forces}} = \frac{\text{Density} * \text{Ang Freq} * \text{Char. Length}^2}{\text{Dynamic Viscosity}} = \frac{\rho * \omega * L^2}{\mu} \quad (\text{Eq. 2 - 4})$$

If flows in different domains have a similar Reynolds number and a similar Womersley number, the fluid structures within the domain will look very similar. This concept is known as dynamic similarity. This allows for greater flexibility in an experimental procedure when the need for certain parameteric values, such as the size of a glass model, can be compensated for by adjusting the values of other parameters such as fluid velocity or properties of the working medium.

Depending on the relative magnitudes of inertial forces and viscous forces, the fluid may behave in a laminar manner, a turbulent manner, or somewhere in between. Turbulent flow is time-dependent and chaotic. The Reynolds Averaged Navier Stokes (RANS) equations, which form the basis of turbulent flow modeling, are founded on Reynolds decomposition, where the flow is subdivided into a time-averaged and a fluctuating component as indicated in Equation 2-5. Substitution of the decomposition into Equation 2-1B, the steady Navier-Stokes equation for an incompressible Newtonian fluid, yields Equation 2-6.

$$u_i(t) = \bar{u}_i + u'_i(t), \text{ assumes } \overline{u'_i} = 0 \quad (\text{Eq. 2 - 5})$$

where u = flow variable such as velocity, \bar{u} = time average, u' = fluctuation, i can be substituted for j and k

$$\rho \bar{u}_j \frac{\partial \bar{u}_i}{\partial x_j} = \rho \bar{f}_i + \frac{\partial}{\partial x_j} \left[-\bar{p} \delta_{ij} + \mu \left(\frac{\partial \bar{u}_i}{\partial x_j} + \frac{\partial \bar{u}_j}{\partial x_i} \right) - \overline{\rho u'_i u'_j} \right] \quad (\text{Eq. 2 - 6})$$

Change in mean momentum = mean body force + stress from pressure field + viscous stresses + Reynolds Stress

The last term on the right hand side of Equation 2-6 is called the Reynolds stress term. Many models for describing the Reynolds stress have been developed. Simulations based on either the k- ϵ or k- ω turbulence models are common. The SST-gamma theta model was used by the author because the turbulence intensity term in the model approaches zero at low Reynolds numbers. This allows for the emergence of turbulent behavior locally where appropriate. Other models impose turbulence throughout the entire flow domain.

2.4. PUBLISHED LITERATURE ON *IN SILICO* CFD SIMULATIONS

INTRODUCTION

The computational fluid dynamic analysis of the neurovasculature is an intensely studied subject, particularly since the development of commercial software packages, such as ANSYS and ABACUS, and the concomitant rapid increase in computational power available to engineers in the form of workstations and supercomputers.

Many different research groups have focused on the analysis of cerebral aneurysms. The most commonly invoked assumptions include the modeling of blood as a Newtonian fluid, the vessel wall modeled as a rigid member, and the fluid flow as steady. The non-Newtonian behavior of blood is largely absent due to the participating shear rates and Reynolds numbers, except in the case of very small vessels and in isolated regions of aneurysms. A rigid wall is typically used since fluid-structural interactions produce differences that are of second order compared to major influences such as the parent vessel geometry [52, 53, 54]. A steady flow is accepted as a reasonable first approximation of the solution. However, more contemporary manuscripts show researchers taking advantage of increasingly powerful computers to simulate pulsatile inlets and examine time dependent flow metrics such as oscillatory shear indices [55].

This chapter discusses the following subjects:

- Variation of flow domain geometry
- Assessing the effect of non-Newtonian behavior on intraaneurysmal flow
- Predicting the risk of aneurysm rupture
- Analysis of stents and flow diverters

VARIATION OF FLOW DOMAIN GEOMETRY

Idealized aneurysms are geometrically simple and are typically constructed by combining spheres and curved blood vessels with constant radii of curvature. As illustrated in Figure 2-10, Hoi et al. began studying intraaneurysmal fluid behavior at the most basic level by varying the parent artery radius of curvature and the neck opening length in an idealized aneurysm. As the radius of curvature decreased, the wall shear on the distal neck increased. [56]

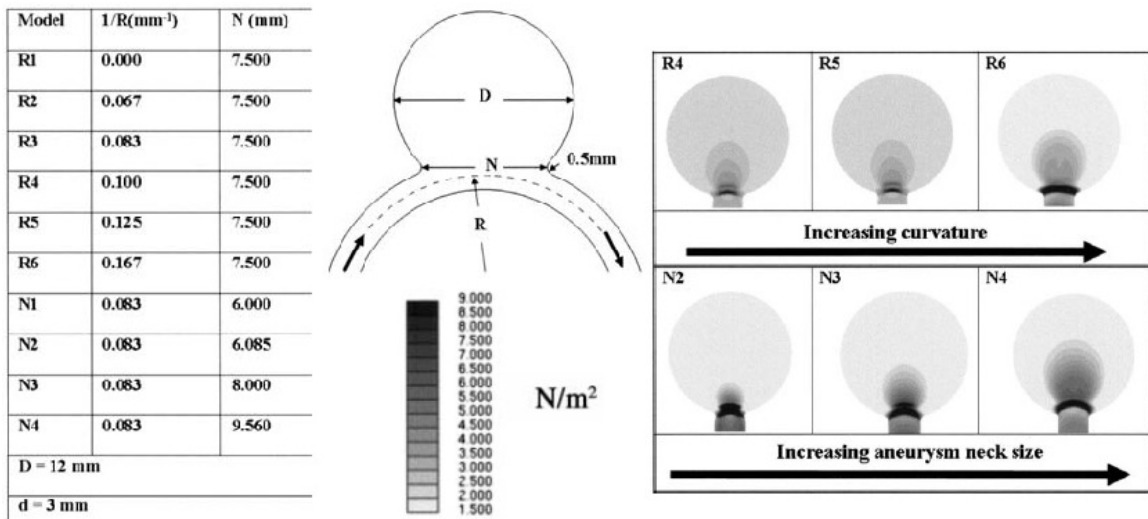


Figure 2-10. Hoi and collaborators simulated flow in an idealized aneurysm, varying radii of curvature and neck sizes [56]

Liou et al. complicated the idealized aneurysm model by introducing an offset to the aneurysm plane, as illustrated in Figure 2-11. The fluid flow was more complex as asymmetrical flows altered the amount of fluid entering the aneurysm and the WSS experienced by the aneurysm neck. They concluded that aneurysms offset by 45 degrees were at the highest risk of rupture based on pressure, followed by aneurysms offset by 90, 0, and 135 deg [57].

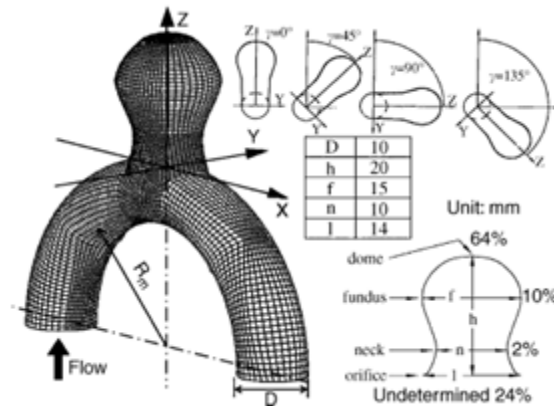


Figure 2-11. Building on Hoi's idealized aneurysm model, Liou et al. offset the symmetry plane of the aneurysm to explore the impact of radius of curvature and neck size on wall shear stress and flow patterns. [57]

Sato et al. introduced another variable into the idealized aneurysm model by decoupling the upstream and downstream segments of the parent artery, such that these segments no longer lie on a single plane, as

illustrated in Figure 2-12. They also introduced a greater number of parameters to describe the aneurysm shape. Unfortunately, results were presented from a very limited subset of the possible combinations in upstream/downstream offset angle, dome height, orifice width, inlet flow speeds, etc. [58]. However, the concept of different radii of curvature planes between the upstream and downstream segments was an interesting addition. The three-dimensional tortuosity present in the neurovasculature makes the Sato simulations more realistic than those of Liou.

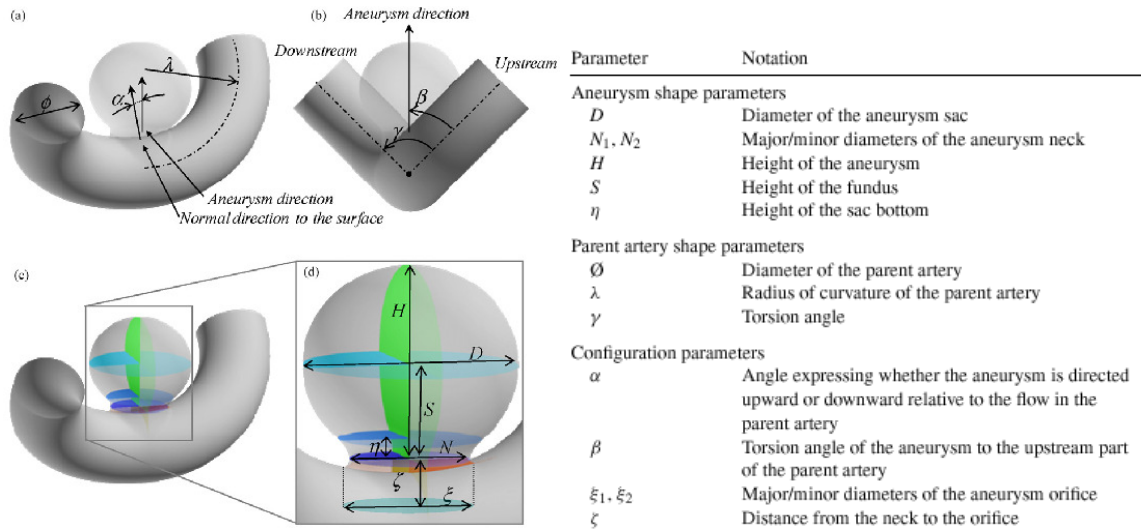


Figure 2-12. Sato's decoupling of the radius of curvature planes between the upstream and downstream segments parent vessel more closely mimics the complex and tortuous nature of the human neurovasculature. [58]

Jiang et al. moved even farther away from the idealized aneurysm model and conducted a CFD analysis in flow domains reconstructed from MRI data of a real patient. In Figure 2-13, the fluid flow in the posterior communicating artery is shown by means of streamlines for a 150 bpm pulse rate along different times in the cardiac cycle. In Figure 2-14, velocity isosurfaces for 60 bpm, 100 bpm, and 150 bpm are compared at early diastole of the cardiac cycle [36]. It illustrates how the penetration of high velocity fluid into the aneurysm is dependent on the activity level of the patient. The velocity profiles at the three different pulse rates are also shown.

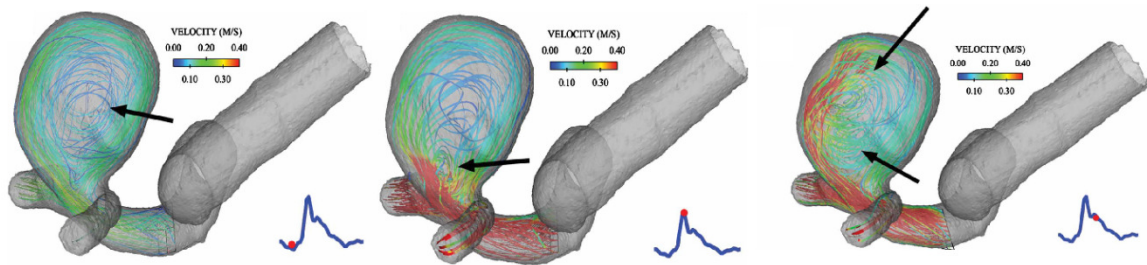


Figure 2-13. Fluid flow in a posterior communicating artery aneurysm was simulated with a 150 beats per minute pulsatile inlet profile. The streamlines of blood entering the aneurysm are shown after three different points in the cardiac cycle, as illustrated by the red dot only the blue velocity profile [36].

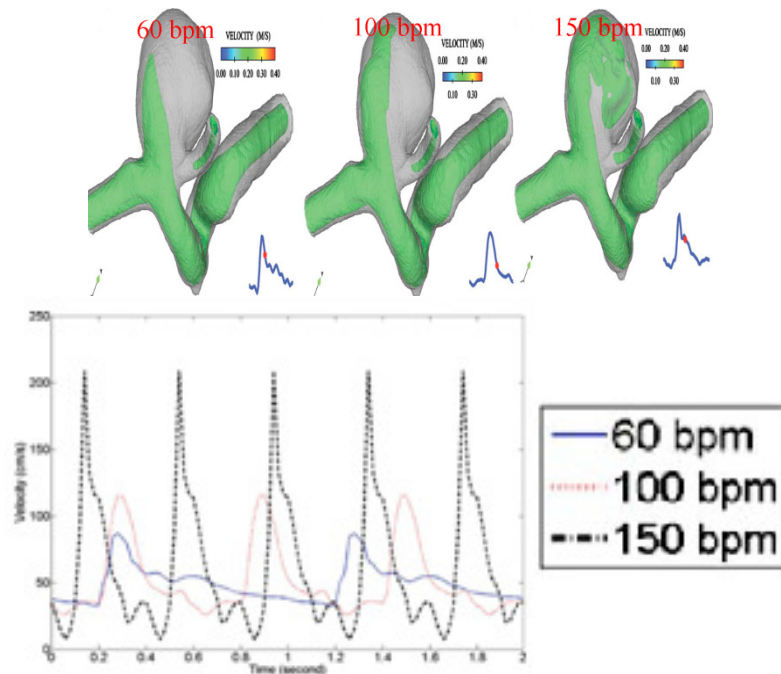


Figure 2-14. Comparison of velocity isosurfaces show that intraaneurysmal flow at early diastole is dependent on the pulse rate. The velocity profiles at the three different pulse rates are shown. [36].

Due to the intense computational demands of simulating pulsatile flow, Castro et al. examined the effect of truncating and simplifying the parent artery upstream of the aneurysm. While the simulations could be completed quicker, the streamlines flowing into the aneurysms were altered. As such, the altered shapes and locations of impact zones might have led to erroneous conclusions regarding where aneurysms are at most risk for rupture. [59]. Figure 2-15 illustrates two examples of truncating the upstream vessel geometry and associated changes in WSS distribution and streamlines of blood entering the aneurysm.

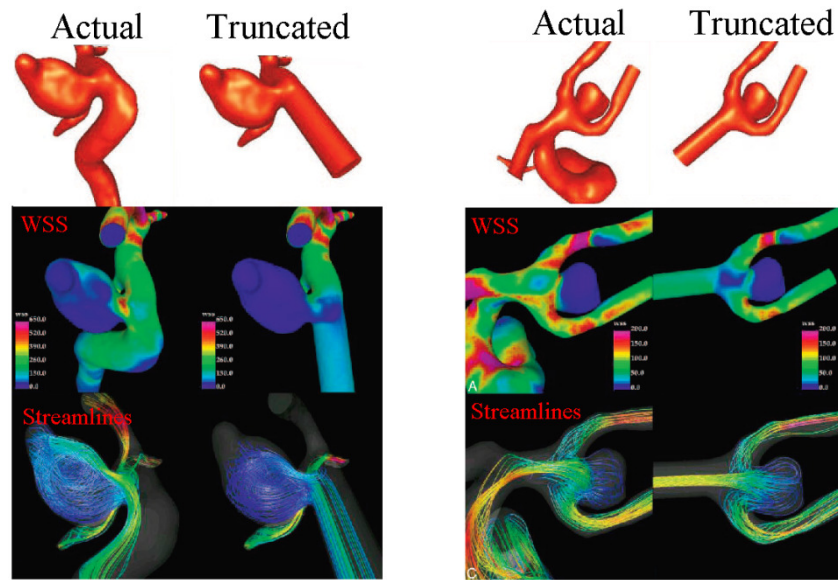


Figure 2-15. Castro et al. compared intraaneurysmal hemodynamics between unaltered parent arteries vs. simplified and truncated vessels. Two examples of truncation are shown on the left and the right. The changes in shape and location of impact zones are dependent on the tortuosity of the unaltered upstream domains. [59]

ASSESSING THE EFFECT OF NON-NEWTONIAN BEHAVIOR ON INTRAANEURYSMAL FLOW

Blood is a non-Newtonian fluid due to the presence of formed blood elements such as red blood cells, white blood cells, and platelets. The shear rates typically present in healthy blood vessels are high enough such that blood can be reasonably simulated as a Newtonian fluid. However, in isolated regions, such as inside the aneurysm sac, there are regions of very low flow and shear rates. Consequently, previous researchers have investigated the effects of accounting for non-Newtonian behavior when shear rates are below 100 / s.

Fisher et al. studied the non-Newtonian behavior of blood when aneurysms are included in the pulsatile flow domain. Idealized geometries of aneurysms were positioned on a curved blood vessel, a straight vessel, and at a bifurcation, as illustrated in Figure 2-16. The WSSs predicted by a Newtonian model were compared to those predicted by the Casson, Carreau, and Power Law models. Fisher found that the non-Newtonian models predicted significant differences in the WSS compared to the Newtonian model, particularly when comparing the minimum WSS in the aneurysm and the WSSs present during the diastole phase of the cardiac cycle. [60] However, the geometries of the parent vessel and the aneurysm had a much greater impact on WSS and therefore are of greater interest than tuning the non-Newtonian model for blood, as summarized in Table 2-9.

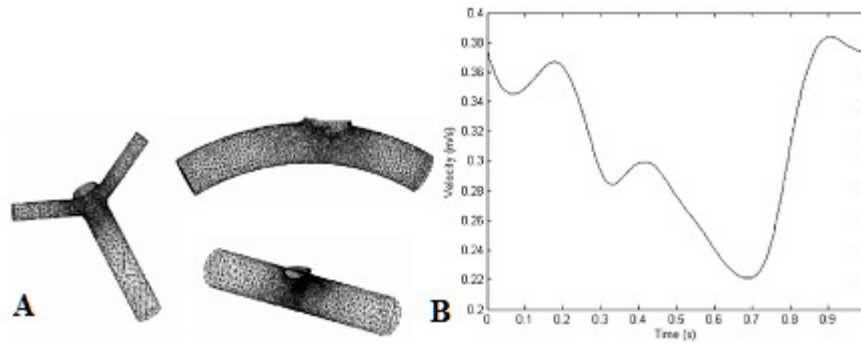


Figure 2-16A. Base geometries of the fluid domain examined by Fisher et al. **2-16B.** The inlet flow velocity used as a function of time. [60]

Table 2-9. Comparison of fundus WSS, minimum WSS, maximum WSS, and average WSS for the various viscosity models of blood. Bolded values were taken during systole phase of the cardiac cycle. Non-bolded values were taken from the diastole phase. Differences were observed between the non-Newtonian and Newtonian models for blood. However, even greater differences were observed for different parent artery geometries and are therefore of greater interest than tuning the non-Newtonian model for blood [60]

Morphology	Model	Fundus WSS (N/m ²)	Min WSS (N/m ²)	Max WSS (N/m ²)	Average WSS over aneurysm surface (N/m ²)
7 mm sphere at bifurcation	Newtonian	0.054	0.004	12.120	0.645
	Casson	0.036 (-33.3%)	0.003 (-25%)	12.400 (2.3%)	0.656 (1.7%)
	Carreau A	0.059 (63.7%)	0.007 (75%)	11.930 (-1.6%)	0.664 (2.9%)
	Carreau B	0.045 (-23.7%)	0.004 (0%)	10.440 (-13.9%)	0.661 (2.5%)
	Power law	0.055 (22.2%)	0.088 (120%)	12.100 (-0.16%)	0.663 (2.8%)
	Newtonian	0.028	0.002	4.023	0.233
	Casson	0.014 (-50%)	0.001 (-50%)	3.310 (-17.7%)	0.209 (-10.3%)
	Carreau A	0.020 (-28.6%)	0.003 (50%)	3.650 (-9.3%)	0.234 (0.43%)
	Carreau B	0.006 (-78.6%)	0.001 (-50%)	2.848 (-29.2%)	0.213 (-8.6%)
	Power law	0.022 (-21.4%)	0.003 (50%)	3.781 (-6.0%)	0.238 (2.1%)
High AR at bifurcation	Newtonian	0.022	0.009	9.725	0.643
	Casson	0.010 (-54.5%)	0.008 (-11.1%)	9.783 (0.6%)	0.638 (-0.8%)
	Carreau A	0.027 (22.7%)	0.018 (100%)	9.663 (-0.6%)	0.655 (1.9%)
	Carreau B	0.018 (-18.2%)	0.015 (66.7%)	8.711 (-10.4%)	0.637 (-0.9%)
	Power law	0.027 (22.7%)	0.018 (100%)	9.816 (0.9%)	0.659 (2.5%)
	Newtonian	0.007	0.005	3.919	0.268
	Casson	0.001 (-85.7%)	0.001 (-80%)	2.685 (-31.5%)	0.198 (-26.1%)
	Carreau A	0.002 (-71.4%)	0.002 (-60%)	2.774 (-29.2%)	0.206 (-23.1%)
	Carreau B	0.0007 (-90%)	0.0006 (-88%)	2.463 (-37.1%)	0.192 (-28.3%)
	Power law	0.005 (-28.6%)	0.004 (-20%)	2.963 (-24.4%)	0.217 (-19.0%)
4 mm sidewall on curved vessel	Newtonian	0.454	0.073	6.571	0.657
	Casson	0.477 (5.1%)	0.110 (50.7%)	7.206 (9.7%)	0.719 (9.4%)
	Carreau A	0.491 (8.1%)	0.125 (71.2%)	6.742 (2.6%)	0.707 (7.6%)
	Carreau B	0.542 (19.4%)	0.205 (180.8%)	6.054 (-7.9%)	0.750 (14.2%)
	Power law	0.501 (10.4%)	0.134 (83.6%)	6.770 (3%)	0.710 (8.1%)
	Newtonian	0.185	0.042	2.925	0.274
	Casson	0.197 (6.5%)	0.050 (19%)	2.674 (-8.6%)	0.298 (8.8%)
	Carreau A	0.214 (15.7%)	0.092 (119%)	2.555 (-12.6%)	0.309 (12.8%)
	Carreau B	0.245 (32.4%)	0.101 (140.5%)	2.238 (-23.5%)	0.346 (26.3%)
	Power law	0.230 (24.3%)	0.099 (135.7%)	2.549 (-12.8%)	0.317 (15.7%)
4 mm sidewall on straight vessel	Newtonian	0.056	0.045	2.078	0.157
	Casson	0.056 (0%)	0.046 (2.22%)	2.232 (7.4%)	0.177 (12.7%)
	Carreau A	0.08 (46.4%)	0.072 (60%)	2.046 (-1.5%)	0.198 (26.1%)
	Carreau B	0.079 (41.1%)	0.075 (66.7%)	2.090 (0.6%)	0.200 (27.4%)
	Power law	0.081 (44.6%)	0.062 (37.8%)	1.987 (-4.4%)	0.188 (19.7%)

PREDICTING THE RISK OF ANEURYSM RUPTURE

Cebral et al. [61] conducted CFD simulations of 210 aneurysms derived from human patients. Two observers blinded to the clinical history of the aneurysms rated the intraaneurysmal flows based on four qualitative metrics:

- **Flow complexity:** A “simple” pattern consists of a single recirculation zone or vortex structure inside the aneurysm.
- **Flow stability:** A “stable” flow indicates flow patterns that persist during the cardiac cycle.
- **Concentration of inflow jet entering the aneurysm:** A “concentrated” jet penetrates relatively deep into the aneurysm sac and are thin or narrow in the main flow direction.
- **Size of the flow impingement zone:** A “small” impingement zone indicates that the area of the aneurysm wall experiencing an elevated WSS due to impact of the inflow stream is less than 50% of the area of the aneurysm.

It was statistically demonstrated (see Table 2-10) that unstable, complex intraaneurysmal flow with a concentrated jet impinging on a small portion of the aneurysm wall was associated with a higher likelihood of rupture.

Table 2-10. CFD simulations were conducted in 210 aneurysms. The intraaneurysmal flow was then qualitatively evaluated based on flow complexity, flow stability, concentration of the jet entering the aneurysm, and the size of the impingement zone on the aneurysm wall. The 210 aneurysms were then sorted based on their clinical history and value for each of the four metrics. For example, under flow complexity, 62 unruptured and 14 ruptured aneurysms had simple flow. 65 unruptured and 69 ruptured aneurysms had complex flow. [61]

	Unruptured	Ruptured	χ^2	P	OR
Flow complexity					
Simple	62	14	22.190	<.0001	4.701
Complex	65	69			
Flow stability					
Stable	59	20	10.694	.0018	2.733
Unstable	68	63			
Inflow concentration					
Diffuse	85	28	22.252	<.0001	3.975
Concentrated	42	55			
Impingement size					
Large	62	20	12.890	.0006	3.005
Small	65	63			

ANALYSIS OF STENTS AND FLOW DIVERTERS

As researchers began understanding and visualizing intraaneurysmal hemodynamics through the use of CFD, clinicians began reporting case studies where a stent across the aneurysm neck may lead to coagulation of blood within the aneurysm. The clot reduces both the flow rate of blood entering the aneurysm as well as the WSS at nearby walls, reducing the risk of rupture [6, 62, 63, 64, 65]. Figure 2-17 illustrates the treatment of a human intracranial aneurysm using a S670 stent, which is a coronary stent not designed for flow diversion (Medtronic). Figure 2-18 illustrates various metal braid flow diverter designs and the formation of thrombus inside the rabbit aneurysm model. Figure 2-19 illustrates the eradication of the aneurysm angiographically in the rabbit model after placement of a flow diverter.



Figure 2-17A. The Medtronic S670 stent used by Benndorf. **2-17B.** Two overlapping stents (S670, white arrows) were placed in a human patient across the neck of an aneurysm (black arrow). **2-17C.** 4 weeks after stent placement, the aneurysm was nearly obliterated with a small region of extravasation (black arrow) proximal to the aneurysm. [62]

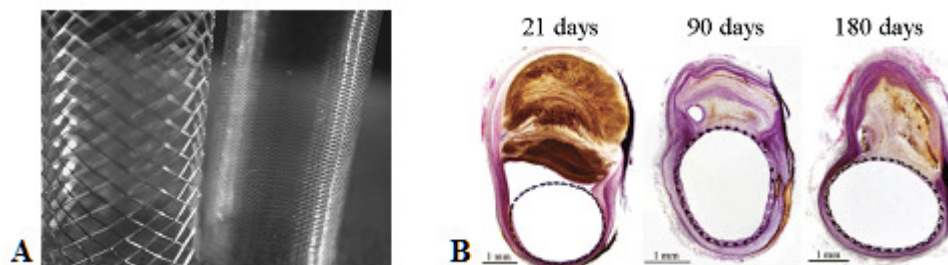


Figure 2-18A. Sadasivan et al. prototyped stents with reduced porosity to restrict the flow of blood into the aneurysm. The Wallstent is shown on the left. A prototype of ~70% porosity is shown on the right. **2-18B.** A followup study at 21 days (left), 90 days (middle) and 180 days (right) demonstrate the formation of a mature thrombus within the aneurysm. [63]

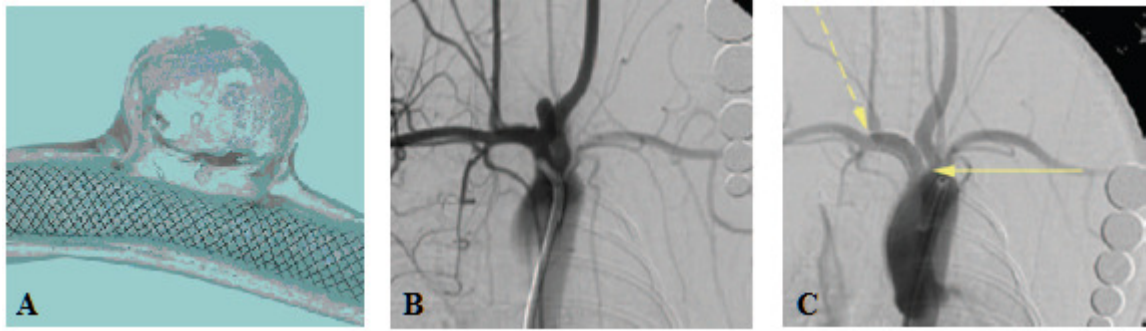


Figure 2-19A. The Pipeline by Covidien is a commercially pursued neurovascular stent specifically designed to disrupt flow entering the aneurysm to promote coagulation and aneurismal wall healing. **2-19B.** The Pipeline device is placed across an aneurysm created in the aortic arch of a rabbit. **2-19C.** A 6 month followup shows that the aneurysm has been sealed. The yellow arrows denote the ends of the Pipeline device. [6]

This has inspired researchers to understand the effect of stent struts placed at the aneurysm neck. Stuhne et al. placed a helical stent across the neck of an aneurysm in a straight vessel. A periodic simulation demonstrated that the disrupted flow caused by the struts may be simulated by a coarse mesh. However, a fine mesh at the struts is needed to visualize the shear stress experienced by formed blood elements as they flow through the stent. Figure 2-20 illustrates the geometric model and numerical mesh in the CFD simulation and Figure 2-21 illustrates streamlines inside the aneurysm at different times in the cardiac cycle. [66]

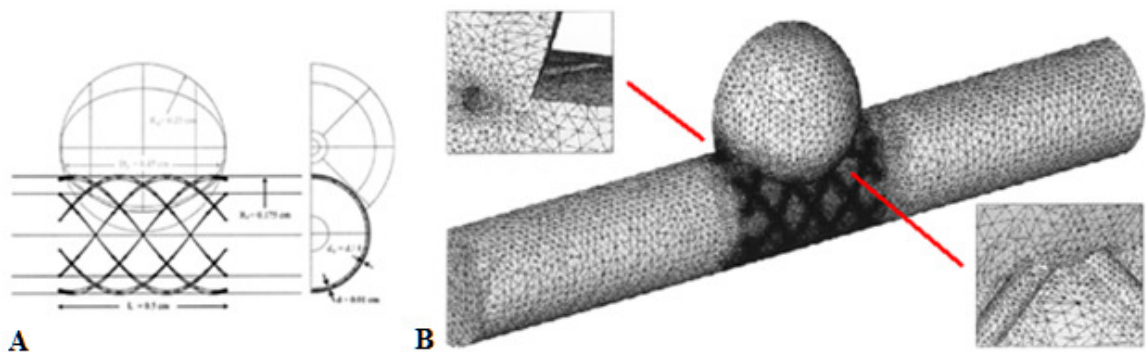


Figure 2-20A. An idealized geometry with a helical stent was generated by Stuhne et al. **2-20B.** A mesh was generated by a commercial software package (ICEM CFD). Stuhne et al. compared the WSS distribution between different levels of mesh refinement at the struts. [66]

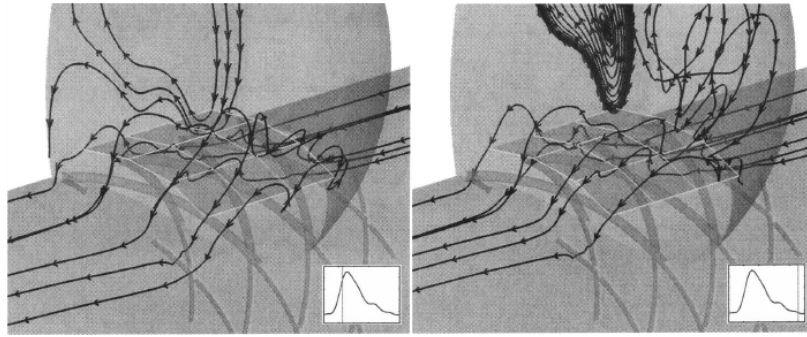


Figure 2-21. In a straight parent artery, there is typically very little flow entering the aneurysm. The stent struts act as a flow disperser, causing blood to enter and exit out of the aneurysm. Sample streamlines seeded from the aneurysm neck are shown at two points of the cardiac cycle. [66]

Kim et al. built upon Hoi et al.'s research (they were actually part of the same research group at the State University of New York, which also created the Asymmetrical Vascular Stent) and Stuhne's research by placing a stent in an idealized model with a curved parent artery and a patient-derived model. Kim et al. demonstrated that a tighter radius of curvature led to increased flow into the aneurysm. Kim also demonstrated that differences in WSS distributions can be observed when the aneurysm neck is covered by stents with different strut designs [67]. Figure 2-22 illustrates the geometric models of the aneurysms and the stents. Figures 2-23 and 2-24 illustrate the velocities and wall shear stress observed in the different domains and stent configurations.



Figure 2-22A. Geometries of idealized and patient specific aneurysms used in Kim's simulations. **2-22B.** The cell designs of the Tristar stent and the Wallstent. [67]

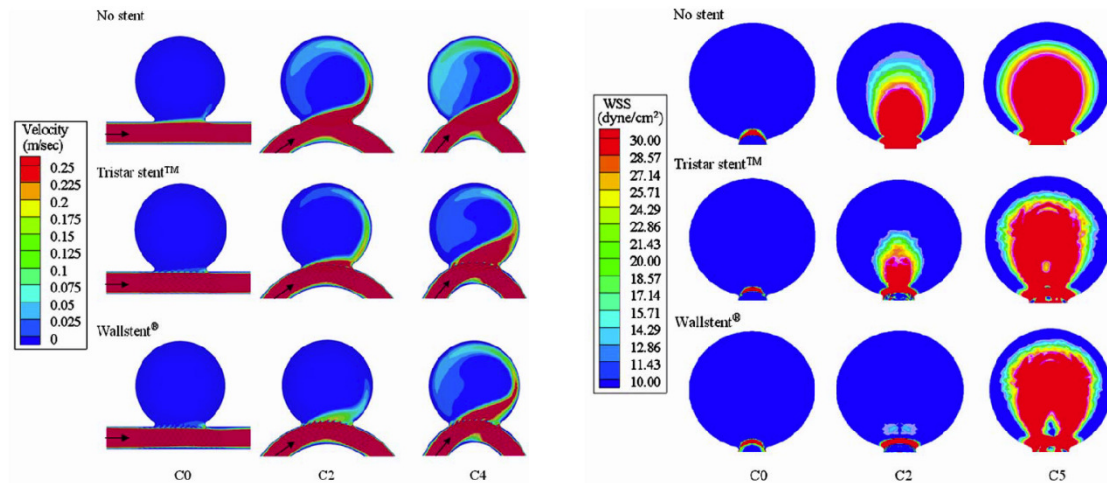


Figure 2-23. The effects of two different stents (a Tristar stent and a Wallstent) in varying vessel radii of curvature (C2: RoC = 15 mm, C4: RoC = 9 mm, C5 = 6mm) were simulated in the idealized aneurysm model. The inlet speed was held constant. Due to the different cross sectional profiles of the stents, different flow dispersion effects were observed. Velocity profiles are shown on the left. WSS on the right. [67]

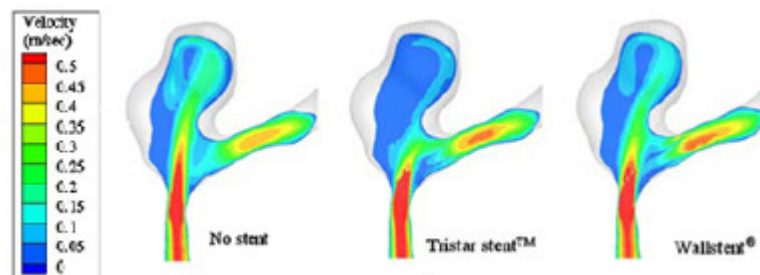


Figure 2-24. The effects of two different stents (A Tristar stent and a Wallstent) in a patient-specific aneurysm model. Due to the different cross sectional profiles of the stents, different flow diffusion effects were observed. [67]

Seshadhri et al. systematically varied the flow domain and device [68] as summarized in Figure 2-25. It was concluded that the device with the lowest porosity (Silk) always led to the largest hemodynamic modification. However, since the neck size was tied to the aneurysm bulb diameter, it was difficult to discern the individual contributions to flow metrics such as residence time of blood inside the aneurysm. Also, only relative changes in residence time were reported (see Figure 2-26 for aneurysms treated with the SILK device), thus making it difficult to determine if the flow diverters had reduced flow to a similar absolute value.

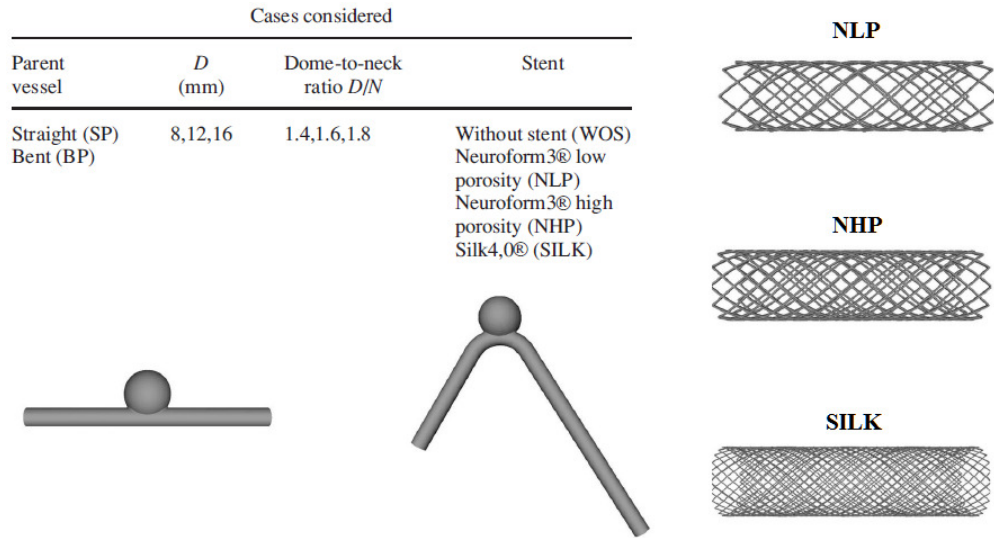


Figure 2-25. The simulation parameters pursued by Seshadhri as shown. D = diameter of aneurysm dome. [68]

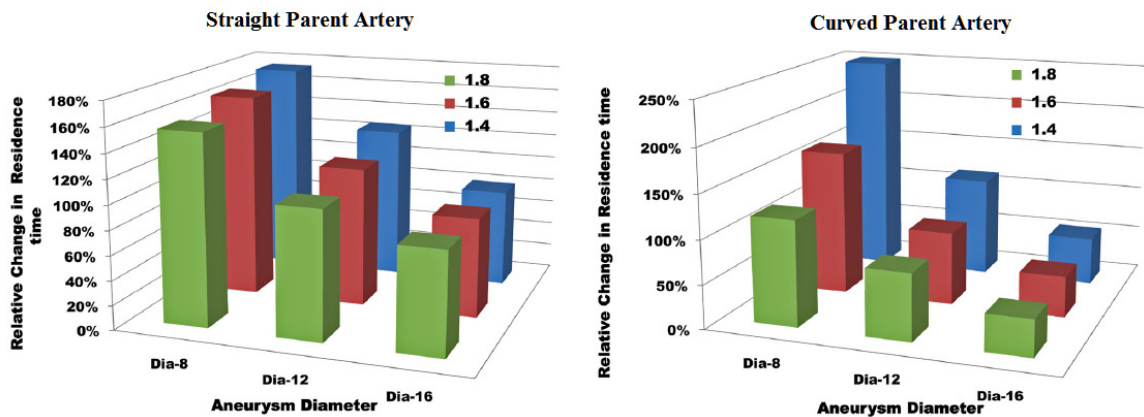


Figure 2-26. The relative change in residence time of blood inside the aneurysm after treatment of with the SILK device is summarized for the flow domains with a straight parent artery and a curved parent artery. [68]

Flow diverters currently available or are on the path to regulatory approval are based on a braided structure (PED, SILK, FRED, NeuroEndoGraft). Due to the dense weave, the likelihood of one of the metal filars lying on top of a perforating vessel is very high. Appanaboyina et al. [69] simulated the flow across the braided structure into a $300\mu\text{m}$ vessel. It was presented that a 90% occlusion of a perforator with a sharp connection (bottom row of Figure 2-27) led to a maximum reduction of only 7% in flow. However, the braided structure collapses along the inner curve of a bend. Perforating vessels of interest can be as fine as $100\mu\text{m}$ in diameter. Thrombus formation on the filars of the device further reduces the open area through which blood can flow. Therefore, further studies are needed to assess the risk for causing lacunar strokes.

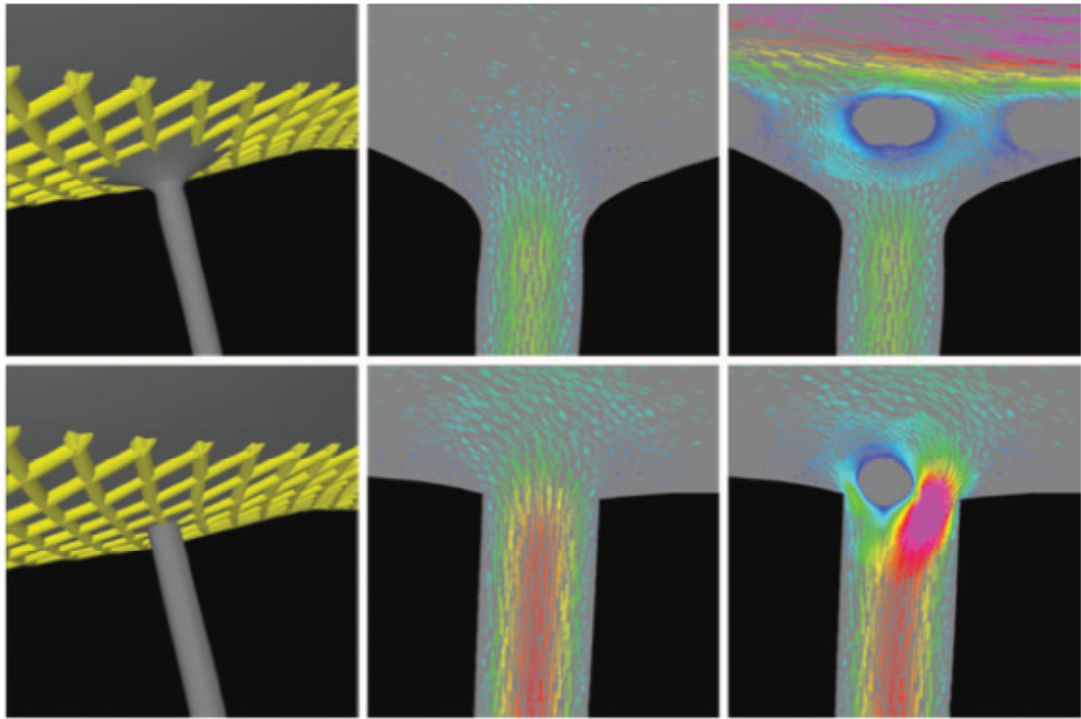


Figure 2-27. Flow through a PED-like flow diverter into a 300µm perforating vessel was simulated. It was determined that since the vast majority of resistance for flow entering the perforator comes from the distal vascular bed, the additional resistance of the flow diverter had little effect on the flow rate. However, the flow diverter collapses along the inner curve of a bend. The smaller openings combined with smaller perforating vessels (down to 100µm in diameter) present a risk for lacunar strokes. [69]

2.5. PUBLISHED LITERATURE ON *IN VITRO* BENCHTOP EXPERIMENTS

MODELING THE VASCULAR PATHWAY

The most basic method for modeling or designing an *in vitro* neurovascular pathway is to build it out of simple primary shapes such as spheres, ellipsoids, vessels with a circular cross sections, vessels with uniform radii of curvature, etc. The simple geometry allows for a very easy time when using a CAD package, such as Pro/E or Solidworks, or when working in a machine shop to construct an *in vitro model*.

However, pathways constructed with primary shapes miss out on complex features such the irregular shapes of aneurysms, variations in vessel cross-sectional shapes, bifurcations, and difficult to describe path lines. There are numerous methods for obtaining, visualizing, and processing actual human neurovasculatures. 3D models can be derived from CT, MRI, or DSA scans using commercial programs such as Mimics or 3D Doctor. These 3D models can then be imported directly into CFD or idealized by tracing the pathlines and lofting circular cross sections.

Based on the author's experience, tracing the pathlines and lofting cross sections allow for sensitivity simulations to be conducted. For example, the vessel diameters may be adjusted. Radii of curvature may be changed. The upstream and downstream portions of the vasculature may be truncated. Figure 2-28 illustrates the conversion of the reconstructed geometry in Mimics to an idealized geometry in Solidworks.

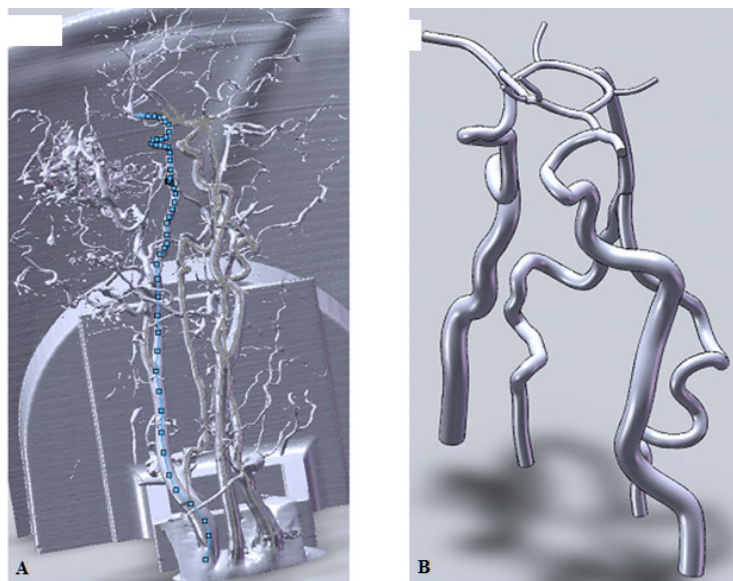


Figure 2-28A. A CT scan of the neurovasculature was imported into Solidworks. The pathline for the right ICA (blue line) is shown. **2-28B.** The Circle of Willis and truncated segments of the feeder vessels were created in Solidworks by lofting circular cross sections along pathlines.

CONSTRUCTING *IN VITRO* MODELS

Rigid Models

Rigid models may be constructed using techniques such as CNC (computer-numerically-controlled) machining out of rigid materials such as steel. The complexity of the model that can be constructed is dependent on the skill of the machinist and/or programmer. Figure 2-29A illustrates one such mold.

Rigid models may also be constructed in a glass blowing facility. Due to inaccuracies in the glass blowing process, a CT scan should be conducted to obtain the geometry of final flow domain. CFD simulations should then be conducted based on the fluid domain from the CT scan. Hoi et al. [70] found that discrepancies between simulated and benchtop flow characteristics can be due to deviations in the glass model. Figure 2-29B illustrates a glass blown neurovascular model with aneurysms.

Lastly, models may be “printed” using 3D manufacturing techniques such as stereolithography (SLA), selective laser sintering (SLS) or fused deposition modeling (FDM). CAD files may be sent to companies such as Stratasys (www.stratasys.com/) which possess the necessary equipment and raw materials to prototype rigid models. Figure 2-29C illustrates one such model.

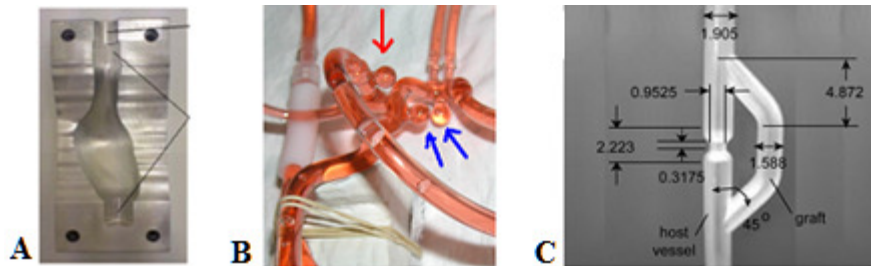


Figure 2-29A. An aneurysm model was CNC machined into a steel block for casting wax cores. [71] A similarly complex flow domain can conceivably be machined in a clear plastic block for flow studies. **2-29B.** A flow loop consisting of a glass model with aneurysms (red and blue arrows) is shown. Red dye was added to water to show the flow domain bound by the blown glass. **2-29C.** A phantom model mimicking a stenotic vessel with a bypass graft is shown. The model was constructed using the SLA technique. Dimensions shown are in millimeters. [72]

Compliant Models

To better mimic the elastic behavior of blood vessels in the body, there are two major approaches in constructing compliant models. A number of researchers encapsulate the flow domain with a thin layer of elastic material (see Figure 2-31). Other researchers encapsulate the flow domain in a block of elastic material (see Figure 2-30). Both methods rely on the use of the lost material technique (typically wax, low melt alloy, etc.).

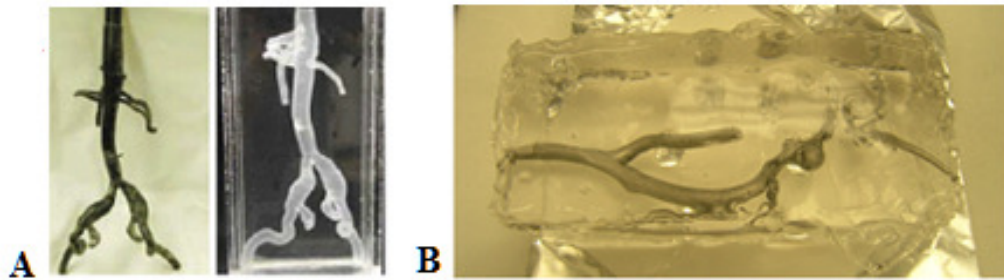


Figure 2-30A.An example of a “compliant vessel” model constructed by dip coating a water dissolvable core material (black) in silicone (translucent).[73] **2-30B.**An example of a “compliant block” model constructed by casting a silicone block over a low melt alloy core.

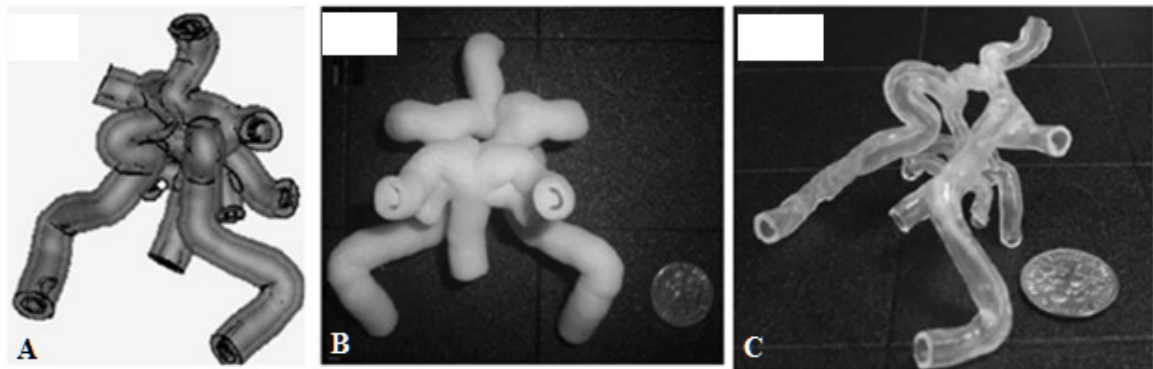


Figure 2-31A.A vessel mold is drafted in a CAD package. **2-31B.** The mold is prototyped in ABS using the fused deposition method. **2-31C.** Silicone is injected in the mold. The ABS plastic is then removed with a solvent, leaving behind a compliant vessel for flow studies. [74]

FLUID MIXTURES

Researchers are concerned with the following parameters when selecting the appropriate fluid for *in vitro* studies: viscosity, density (for neutral buoyancy of particles for PIV/PTV studies), non-Newtonian behavior, and refractive index (to minimize distortion when viewing through a transparent model). Depending on the equipment used and the purpose of the experiment, a range of different formulations (summarized in Table 2-11) are used when performing *in vitro* studies.

Table 2-11. The fluid mixtures used in PIV experiments of different researchers are summarized.

Ref	Mixture and Properties
[75]	33% glycerol; Newtonian fluid, viscosity = 3.695 Pa-s at 20°C
[76]	60% glycerol; density = 1156 kg/m ³ , refractive index of 1.413, kin. viscosity = 8.3 mm ² /s at 23°C
[77]	40% ethylene glycol, ?% lycopodium powder; density = 1030 kg/m ³ , viscosity = 2.5 cp at 25°C,
[78]	46% glycerin, 14% NaCl; refractive index of 1.41
[79]	50% glycerol, 0.5% NaCl
[80]	?% thiocyanate, 0.13% Separan AP-30; Power Law non-Newtonian behavior achieved
[70]	60% glycerine; ~10 – 20 μm fluorescent beads for PIV measurements
[81]	60% glycerin; viscosity = 10.8 cp
[82]	58% glycerine, 42% physiological saline solution; density = 1148 kg/m ³ , viscosity = 11.42cP
[83]	60% glycerin; density = 1157 kg/m ³ , viscosity = 15.2 cP
[84]	25% glycerin; density = 1059 kg/m ³ , viscosity = 2.45 cP
[85]	58% glycerine, 42% physiological saline solution; density = 1148 kg/m ³ , viscosity = 11.42cP
[86]	40% glycerol; Newtonian, viscosity = 2.2 cP 0.01% Separan AP45, 0.04% Separan AP30, 4% IPA, 0.01% MgCl ₂ ; non-Newt., vis. = 2 – 8 cP
[87]	60% glycerine; refractive index = 1.45, kinematic viscosity = 4.0 cP at 25°C

While the fluid properties in CFD simulations may be adjusted to match whatever was used for *in vitro* experiments, past researchers typically try to match dimensionless numbers to physiological values. For example, when the flow domain has to be adjusted, such as tripling the vessel diameter to enable easier visualization in PIV experiments, viscosity is also increased to maintain physiological values of the Reynolds number.

Other flow parameters, such as the Womersley number, are manipulated by computer controls at the inlet pump to achieve the appropriate flow velocity and pulsatility profiles.

FLOW ASSESSMENT TECHNIQUES

Doppler Guidewires

Doppler guidewires are commercially available and typically used to assess flow in coronary and peripheral arteries. Bennedorf et al. [88] assessed intraneurysmal flow in human patients using the Smart Wire (probe and ultrasound generator) by Cardiometrics, and demonstrated that a difference in overall fluid velocity can be observed when sampling the dome, aneurysm neck, and parent vessel regions of interest, as illustrated in Figure 2-32. However, complex flow behavior is not detectable using the Doppler technique.

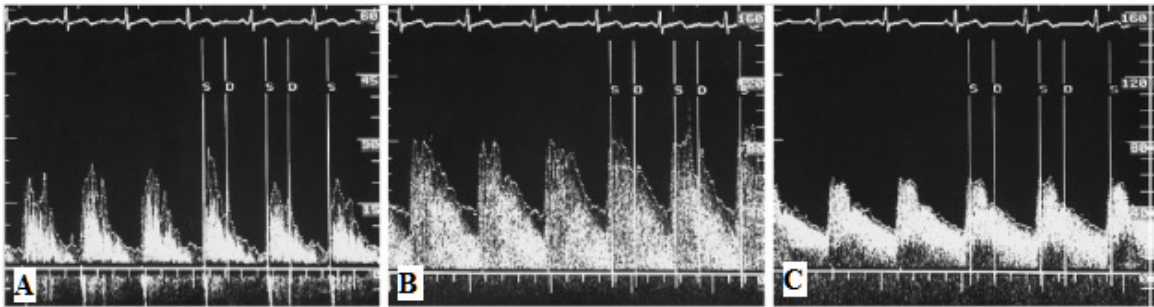


Figure 2-32A. Flow near the dome of the aneurysm. **2-32B.** Flow near the aneurysm neck. **2-32C.** Flow in the parent artery just outside the aneurysm. Note the differences in flow magnitudes as well as the pulsatility indices. [88]

Dye Uptake and Washout Assessed With Optical Dye or Radiopaque Dye under Angiography

When coils are deployed in aneurysms, physicians typically inject radiopaque dye from an upstream location to assess the effectiveness of the procedure. Researchers are able to use this established technique when assessing flow in *in vitro* models. Regular dye (such as food dye) may be used when assessing flow with a regular camera. Radiopaque dye (laden with iodine) may be used when assessing flow under angiography. The dye density may be correlated to a grayscale/RGB value when using an image processing program such as ImageJ. The dye uptake and washout rates may then be compared between different flow conditions and locations of the AVS. Figure 2-33 illustrates the exclusion of dye angiographically after coils are placed inside the aneurysm. Figure 2-34 illustrates the update of dye into aneurysms with different bend radii before and after placement of a stent. Figure 2-35 illustrates an example of grayscale intensity comparisons at the aneurysm before and after misplacement of a flow diverter.

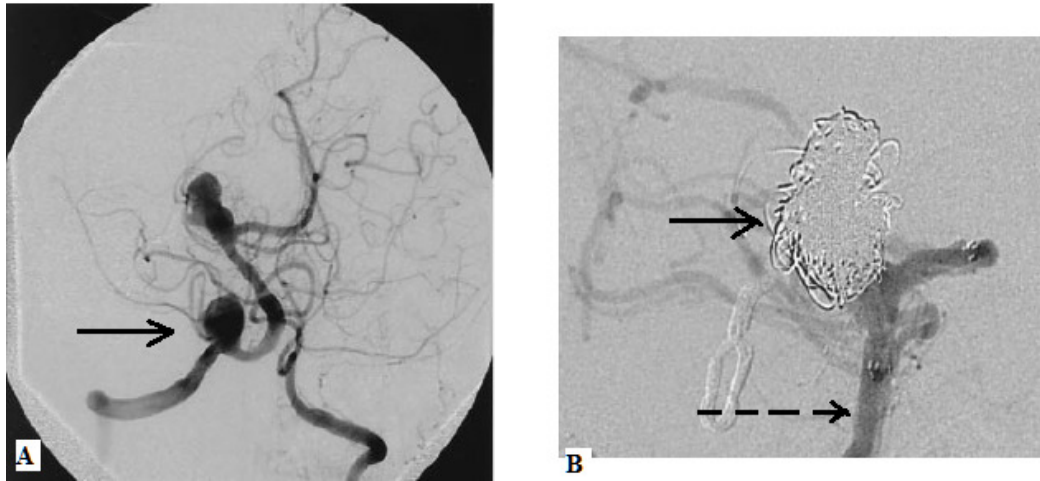


Figure 2-33A. An aneurysm (solid arrow) is present near the right vertebral artery. **2-33B.** The placement of platinum coils (solid arrow) is preventing flow from entering the aneurysm, as indicated by the dye in the parent vessel (dashed arrow) [38]

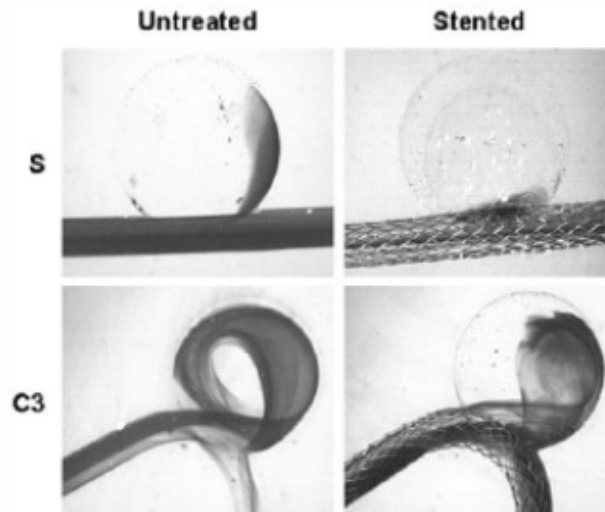


Figure 2-34. Dye is injected upstream of the aneurysm in these two models. S: straight vessel. C3: radius of curvature = 9 mm. A region of interest (ROI) may be defined inside the aneurysm bulb to quantify the grayscale density value due to the dye entering the aneurysm. [83]

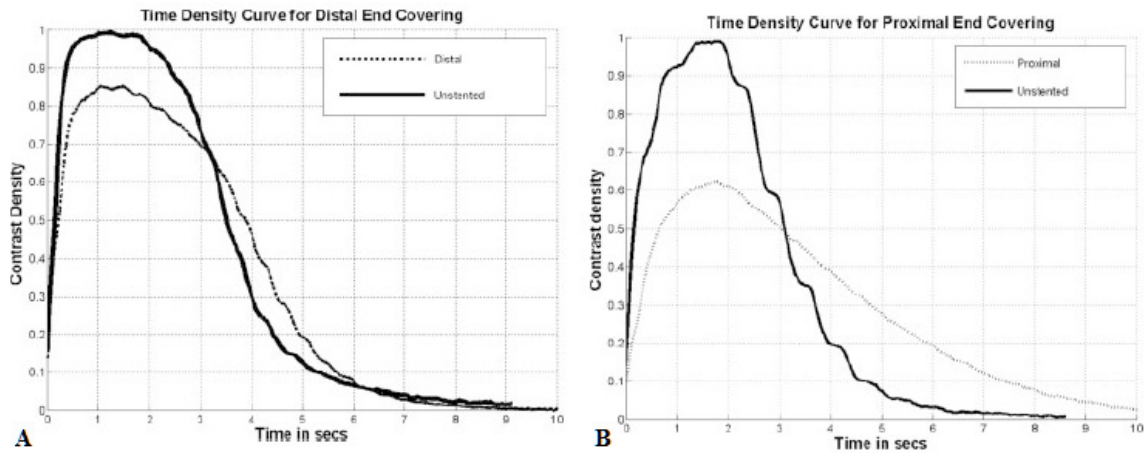


Figure 2-35A. Intraaneurysmal time density curve of a misplaced flow diverter with a distal opening. **2-35B.** Intraaneurysmal time density curve of a misplaced flow diverter with a proximal opening. Note that the dye uptake and washout rates are slower when the AVS is present. [84]

PIV / PTV

Particle imaging and particle tracking velocimetry (PIV, PTV respectively) are two techniques commonly used when understanding the finer intricacies of flow fields is desired. PIV can be briefly described as the comparison of successive images taken in close temporal proximity. Particles seeded in the flowing medium show up at slightly different locations on successive images. Analysis algorithms are commercially available to track the movement of these particles over time to calculate velocity within the flow domain. The typical PIV system uses a laser sheet to illuminate a plane of particles, thus describing flow on a plane of interest within the flow domain. Newer and much more complicated systems are able to conduct 3D PIV which determines flow in all three dimensions. PTV is a modified form of PIV. The most obvious difference is a much lower density of seeded particles to allow for identification and tracking of individual particles within the flow field.

Figure 2-36 illustrates the experimental set up used by Canton et al. and a sample image of the aneurysm of interest. Figure 2-37 illustrates the acquisition of velocity fields inside an aneurysm before and after placement of a flow diverter. Results from CFD were compared to PIV. Figure 2-38 illustrates the velocities fields measured using PIV inside the aneurysm before and after placement of the flow diverter along the cardiac cycle.

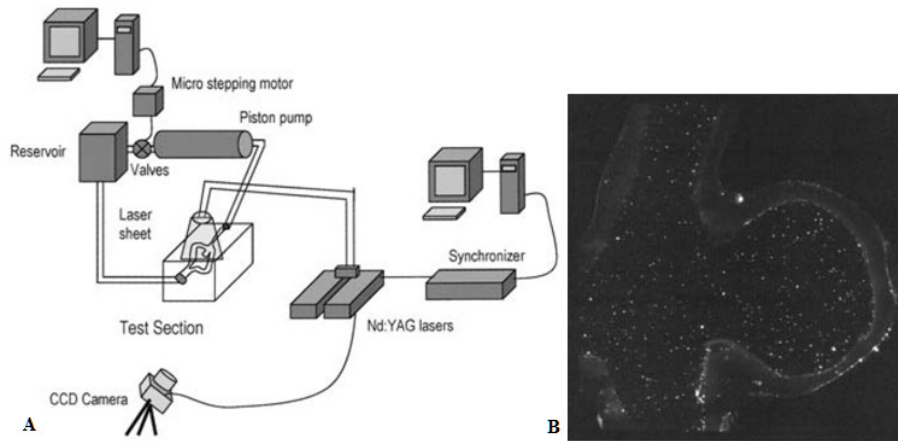


Figure 2-36A. The PIV system used by Canton et al. is shown. Note that the Nd-YAG lasers create a laser sheet to illuminate a plane of particles which are seeded in the flow domain. **2-36B.** An example of an image captured by the CCD camera. Analysis of particles in successive images allow for calculation of particle velocities on the plane illuminated by the laser sheet. [77]

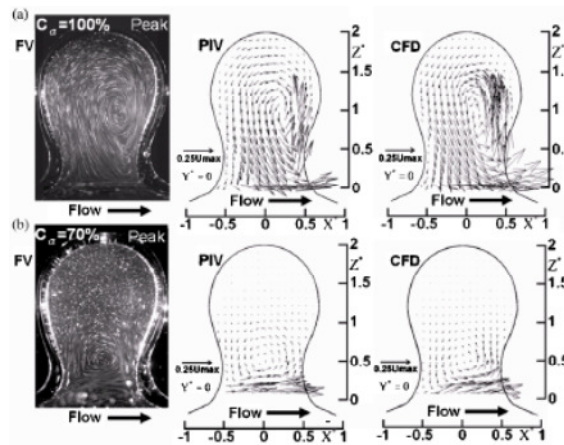


Figure 2-37. Flow within an aneurysm is compared between the unstented ($C = 100\%$) and stented ($C = 70\%$) scenarios. “FV” shows the view of the fluid as seen by the camera in the PIV system. “PIV” shows the velocity vector diagram as calculated by the PIV analysis program. “CFD” shows the vector diagram predicted from CFD simulations. [89]

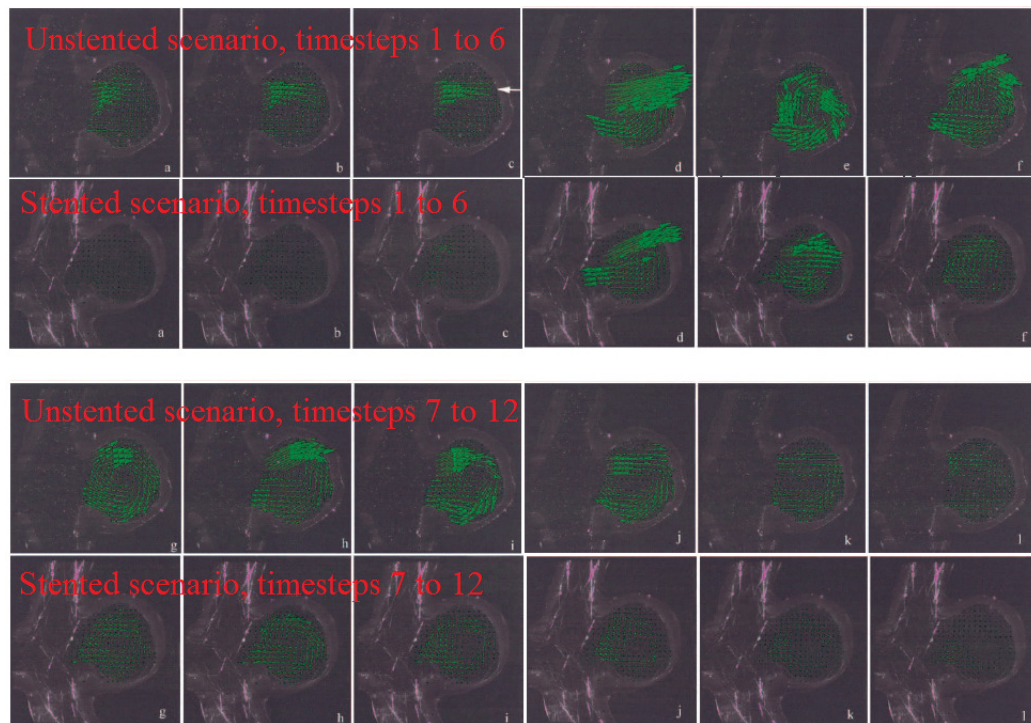


Figure 2-38. Intraaneurysmal flow was compared between the unstented and stented scenarios for the entire cardiac cycle using the PIV technique. Note that despite the high porosity of the stent (Neuroform by Boston Scientific), flow was significantly reduced. [77]

MRI / PC-MRI

Magnetic resonance imaging (MRI) and phase contrast magnetic resonance imaging (PC-MRI) are two flow visualization techniques that may be applied to *in vitro* as well as *in vivo* models. The major benefit lies in the physicians' familiarity of this imaging modality, which makes the eventual proof of flow diverter efficacy much easier. However, the cost of purchasing and/or operating a MRI is orders of magnitude higher than a PIV/PTV system. Magnetic objects are also prohibited, which makes the design of *in vitro* flow systems more difficult.

Regardless, researchers in the field have already utilized MRI/PC-MRI to study neurovascular and intraaneurysmal flow. Some have also begun comparing flow fields predicted or measured by CFD vs. PIV/PTV vs. MRI/PC-MRI. Figure 2-39 illustrates a comparison between CFD (labeled as FEA) and PC-MRI of velocity profiles at different locations in the flow domain and two points along the cardiac cycle. Figure 2-40 illustrates the flow inside the neurovasculature captured using PC-MRI.

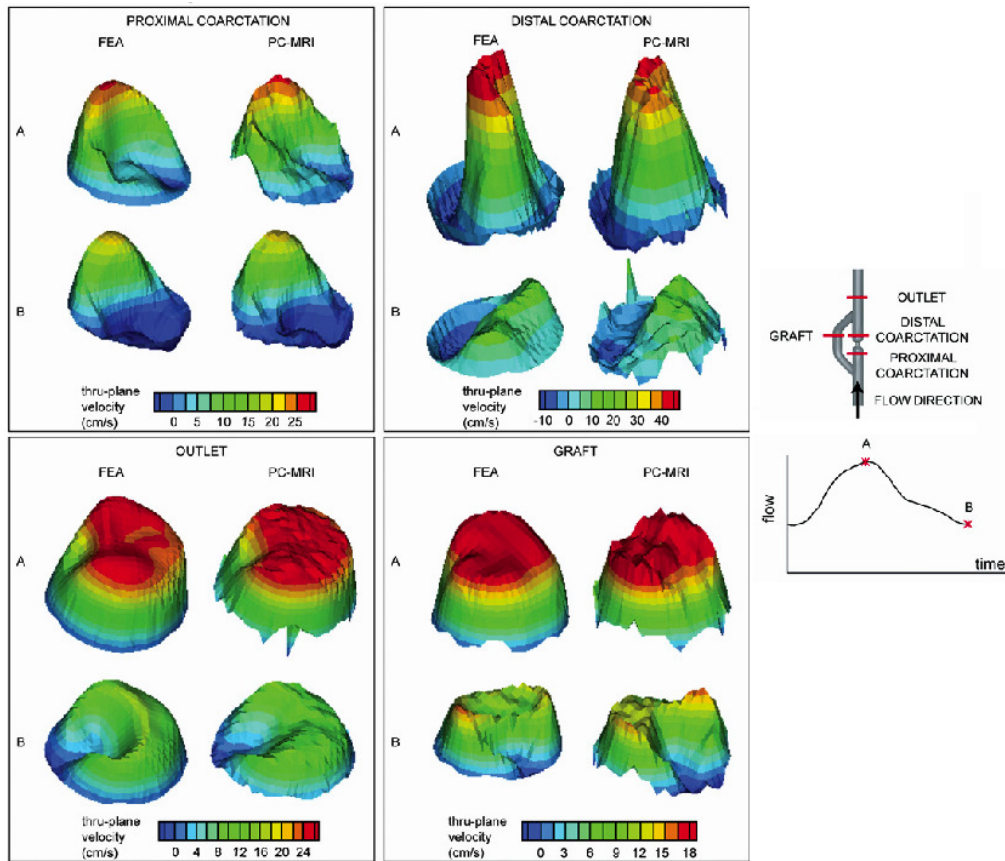


Figure 2-39. Through-plane velocities at various locations of the flow domain are compared between values predicted by CFD (labeled as FEA – finite element analysis) vs. measured by PC-MRI and at two different time points in the cardiac cycle (A: peak, B: late deceleration). [72]

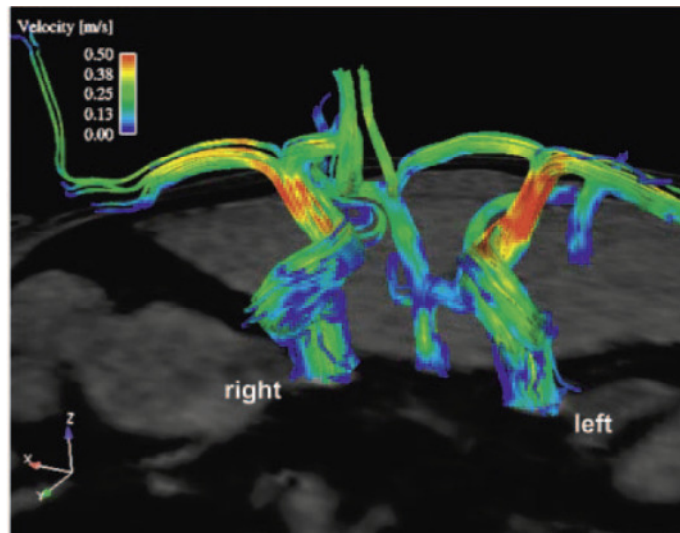


Figure 2-40. Flow sensitized MRI is capable of capturing and visualizing the intricate behavior of blood flow as it navigates the tortuous neurovasculature. [90] This refinement allows for a researcher or clinician to not only compare intraaneurysmal flow predicted by CFD vs. measured by MRI, but also allows for the confirmation of flow alteration after an AVS has been deployed across the neck of the aneurysm.

2.6. PUBLISHED LITERATURE ON *IN VIVO* ANIMAL AND CLINICAL TRIALS

The two most common methods for creating saccular aneurysms similar to those found in the human neurovasculature are the vein pouch model and the elastase induced aneurysm model.

In general, the vein pouch aneurysm model involves harvesting a vein elsewhere in the animal, punching a hole in the desired parent vessel, then suturing on a segment of the vein onto the hole to form an aneurysm. Sherif et al. [91] presented a vein pouch model where the aneurysm was positioned on a bifurcating geometry. The right common carotid artery (RCCA) was crossed over to an opening made in the left common carotid artery (LCCA). A segment of the jugular vein was sutured along with the RCCA to form an aneurysm similar to those found at the basilar artery tip or at other bifurcating structures. Figure 2-41 illustrates the suturing order on the posterior side and the anterior side of the anastomosis. Figure 2-42 illustrates how the aneurysm appears from the naked eye and under fluoroscopy.

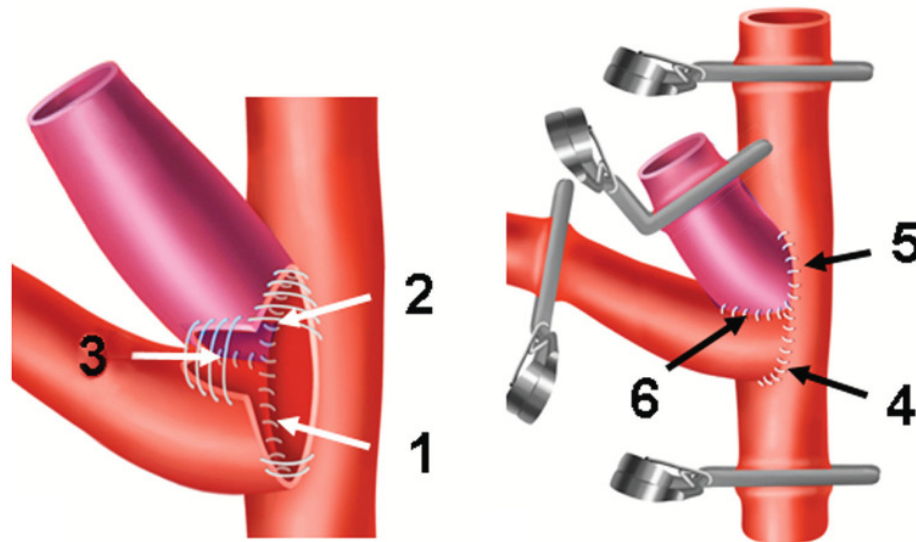


Figure 2-41. The microsurgical steps during the creation of the venous pouch arterial bifurcation aneurysm model are listed. **Left.** From the posterior aspect, the suture order is 1. RCCA to LCCA. 2. Venous pouch to LCCA. 3. Venous pouch to RCCA. **Right.** From the anterior aspect, the suture order is 4. RCCA to LCCA. 5. Venous pouch to LCCA. 6. Venous pouch to RCCA. [91]

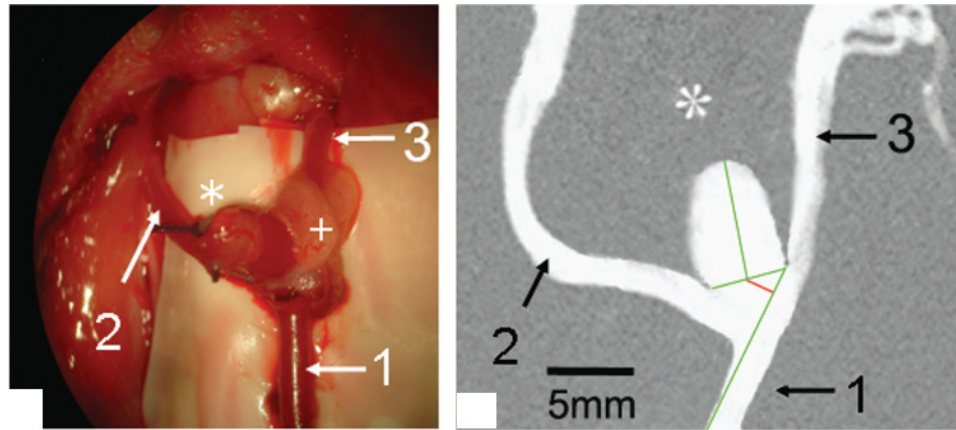


Figure 2-42. The aneurysm seen by the naked eye (**left**) and under fluoroscopy (**right**) is shown. 1 points to the proximal LCCA. 2 points to the RCCA that was brought over and sutured to the LCCA. 3 points to the distal LCCA. The asterisk points to the dome of the aneurysm. [91]

The elastase induced, or elastase digested arterial sac aneurysm (EDASA), model creates an aneurysm by breaking down the elastin in the vessel wall. In the typical rabbit model, the RCCA is tied off a couple millimeters distal to the origin at the brachiocephalic artery to form the initial pouch. Elastase that is applied before or after the RCCA is ligated weakens the tissue to form an aneurysm. This is the more popular and published method for creating aneurysms largely due to lower mortality rates and requires a lower level of surgical expertise compared to vein pouch model.

Figure 2-43 illustrates the predominant method for creating elastase induced aneurysms. The RCCA is accessed through an incision at the neck. An introducer sheath is inserted into the RCCA. A balloon catheter is then inflated at the root near the brachiocephalic artery. An elastase/contrast medium mixture is injected into the RCCA through a microcatheter to expose the vessel intravascularly to elastase. After a predetermined exposure time and/or dosage, the balloon is deflated. The RCCA is ligated some distance from the origin. The incision is then closed up and the rabbit brought out of anesthesia. [92] Figure 2-44 illustrates how the ligated, or tied, RCCA forms the aneurysm and what it looks like fluoroscopically. [93]

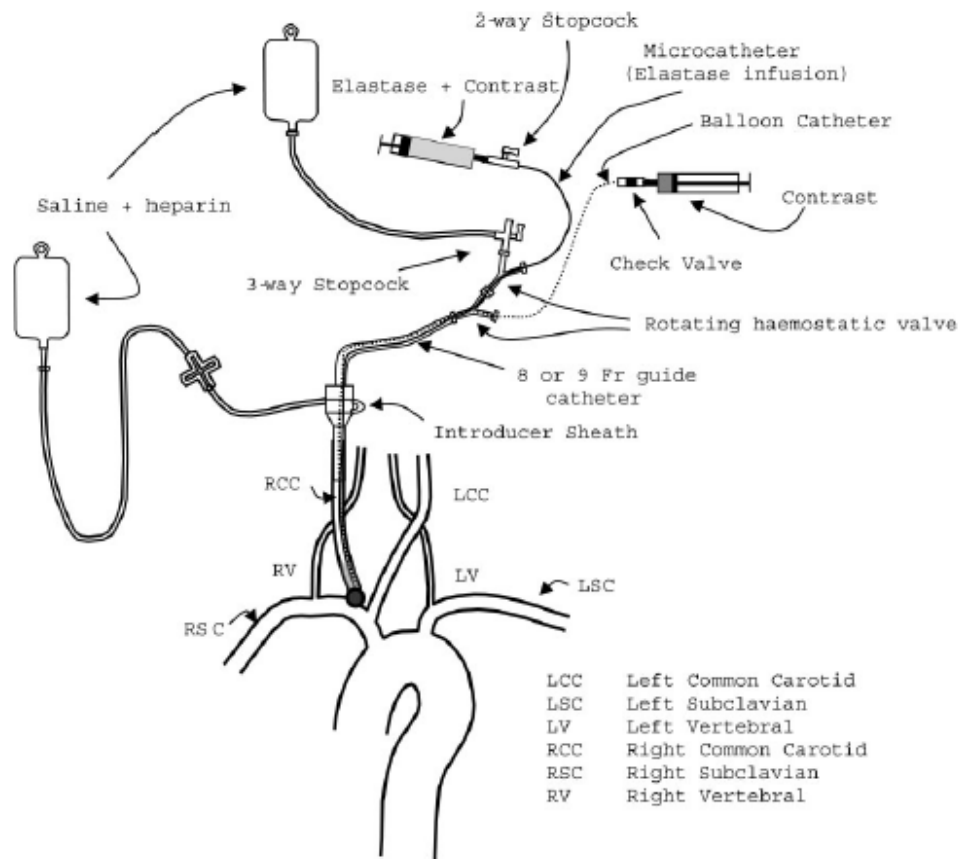


Figure 2-43.The devices used in the predominant method for creating elastase induced aneurysms are shown.[92]

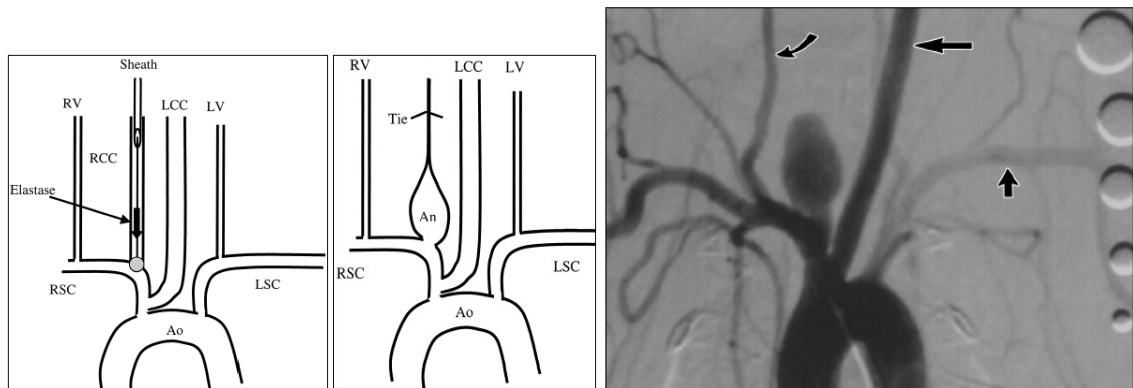


Figure 2-44.Aneurysms were created in the rabbit right subclavian artery and remained patent at the 6 month timepoint. [93]

The placement of the balloon catheter and the ligation on the RCCA affects the volume of the aneurysm and the dome to neck ratio. In one study, Ding et al. [94] pursued two treatment groups. In group 1, the entire balloon was inserted into the subclavian and brachiocephalic arteries. In group 2, only part of the

balloon was inserted into the subclavian and brachiocephalic arteries. The rest of the balloon was kept in the RCCA. Figure 2-45 illustrates the typical fluoroscopic view of the aneurysms in group 1 on the left and group 2 on the right. Table 2-12 summarizes the differences in various geometric features between the two groups.

Table 2-12. The average +/- standard deviation values for width, neck diameter, aneurysm dome to neck ratio, and height of aneurysms in groups 1 and 2 from Ding et al. are shown. In group 1, the balloon was entirely in the subclavian and brachiocephalic arteries. In group 2, part of the balloon was in the RCCA, likely shielding what became the aneurysm neck from the enzymatic effects of elastase. [94]

	Group 1 (n = 62)	Group 2 (n = 28)	P Value
Width (mm)	3.8 ± 1.0	3.3 ± 0.9	<.05
Neck diameter (mm)	3.4 ± 1.2	2.3 ± 0.9	<.001
Dome: neck ratio	1.2 ± 0.4	1.7 ± 0.7	<.005
Height (mm)	8.0 ± 1.7	7.5 ± 2.2	>.05

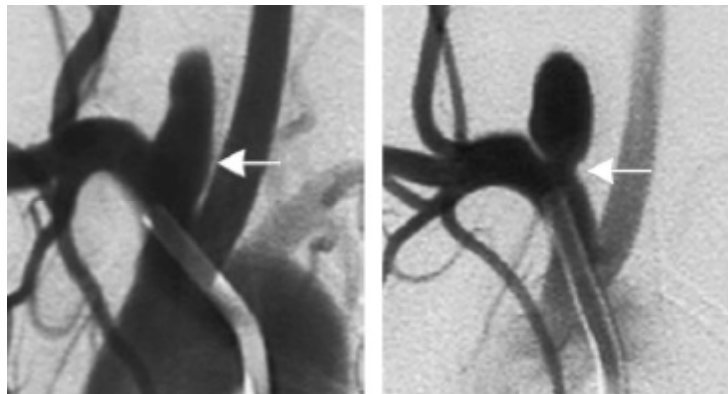


Figure 2-45. A typical aneurysm from group 1 is shown on the **left**. A typical aneurysm from group 2 is shown on the **right**. [94]

Kallmes et al. [6, 95] evaluated PED prototypes in the elastase induced aneurysm model. The PED-1 configuration was a 32-strand braid that achieved approximately 30% area coverage when fully expanded. The PED-2 configuration was a 48-strand braid that achieved approximately 35% area coverage. Table 2-13 summarizes the occlusion rates at 1 month, 3 month, and 6 month followup. Figure 2-46 illustrates an example of an occluded aneurysm at followup.

Table 2-13. The occlusion rates of the PED-1 and PED-2 prototypes at 1 month, 3 months, and 6 months after implantation. [6, 95]

	PED-1			PED-2		
	1 month	3 months	6 months	1 month	3 months	6 months
Incomplete Occlusion	1 / 6	0 / 5	1 / 6	0 / 6	0 / 6	0 / 6
Near Occlusion	2 / 6	3 / 5	1 / 6	1 / 6	0 / 6	0 / 6
Complete Occlusion	3 / 6	2 / 5	4 / 6	5 / 6	6 / 6	6 / 6

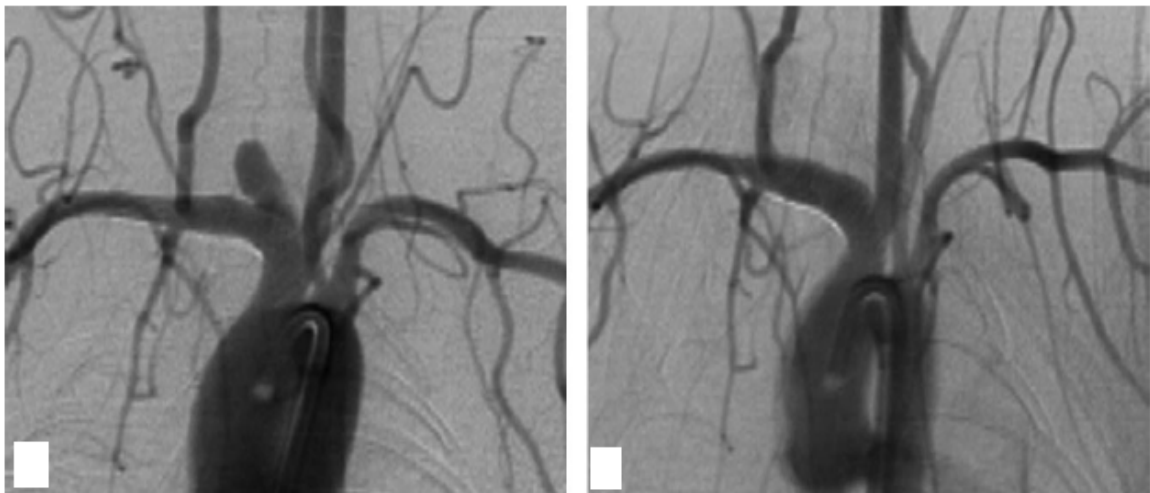


Figure 2-46. Dye was observed entering the aneurysm immediately after placement of the PED-2 prototype in most cases (**left**). At followup, 17 of 18 aneurysms were completely occluded (**right**). [6, 95]

CHAPTER 3: *IN VITRO* EXPERIMENTS

3.1. SPECIFIC AIMS OF *IN VITRO* EXPERIMENTS

The main objectives of benchtop experimental studies were to:

1. Characterize the intraaneurysmal flow prior to and after placement of a Pipeline Embolization Device (PED)
2. Develop an understanding of the variability in pore dimensions and wall apposition of the PED
3. Obtain a sufficiently populated dataset for verification of select CFD simulations
4. Identify the limitations of an experimental approach for characterizing intraaneurysmal flow

In order to achieve these objectives, equipment and methods for conducting PIV experiments were assembled and implemented. The majority of the initial tools were provided by Professor Jian Sheng. Modifications were performed to extract data from flow domains specific to this research. Figure 3-1 summarizes the research plan and associated sub-chapters for the PIV work.

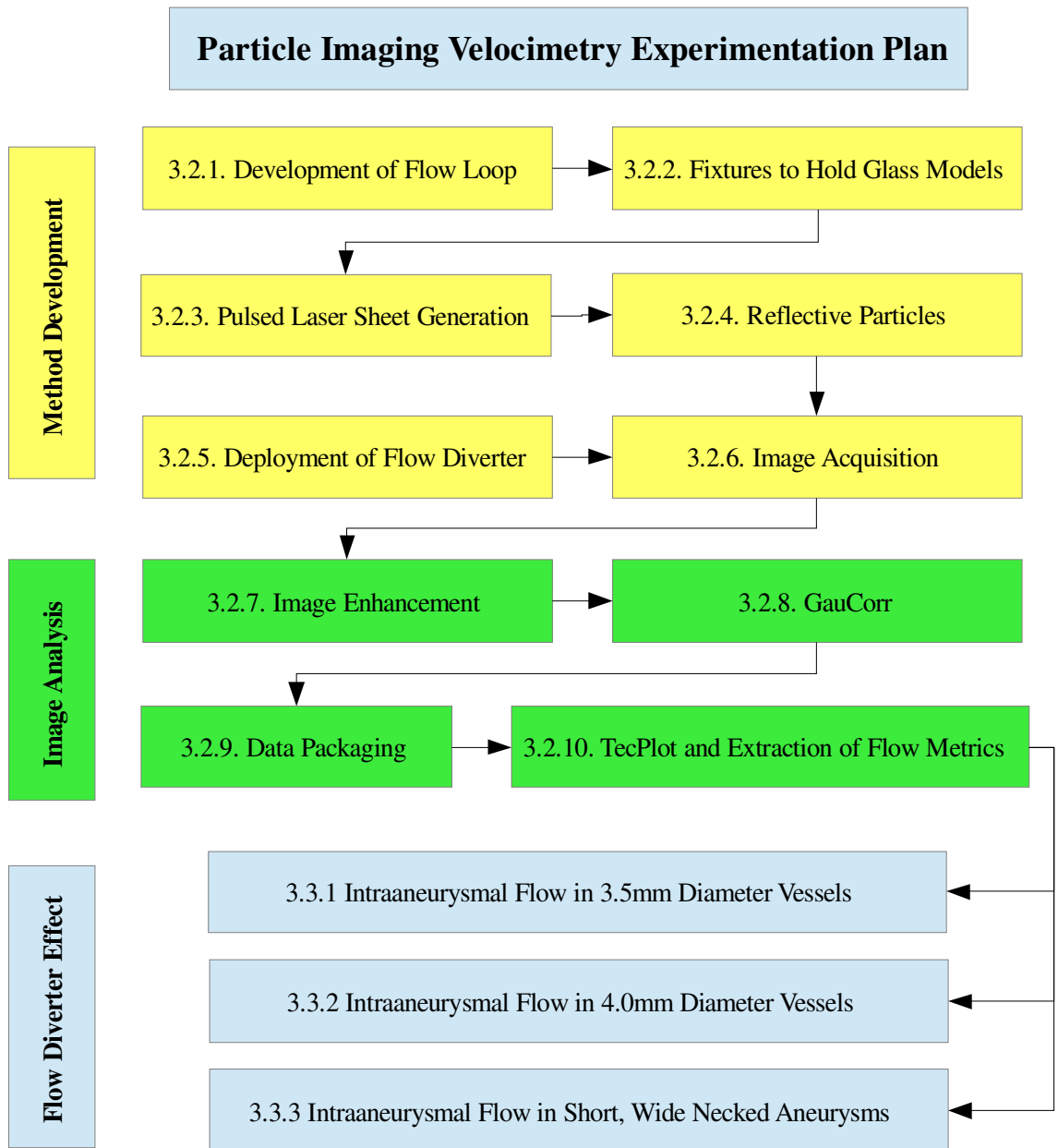


Figure 3-1. The experimental research consisted of developing the image acquisition methods, writing the image analysis algorithms, and understanding the flow diverting effect of the PED in a variety of flow domains. The subchapter numbers are shown.

3.2. DEVELOPMENT OF *IN VITRO* EXPERIMENTAL TECHNIQUES

3.2.1. Development of Flow Loop

Commercially available components were used where available. The *in vitro* experiments were performed under steady flow. A peristaltic pump (Cole Parmer, EW-77910-20) was placed in line with a pulse dampener (Cole Parmer, EW-07596-20), water heater (Hydor ETH 300), pressure sensors (Omega, PX309-005A5V), a flow sensor (Cole Parmer, EW-32818-38), and custom glass blown models from Farlow Scientific. A ~2L reservoir was constructed out of polycarbonate to store excess working fluid, making the flow loop an open system. Appropriately sized Tygon tubing (Cole Parmer) and luer barb fittings (Qosina) were used to connect the different components. A DATAQ 718B data acquisition unit and DI-5B43-05 input modules were used to collect the pressure and flow data. A schematic of the flow path is shown in Figure 3-2.

The pair of pressure sensors bracketing the pulse dampener confirmed that the fluctuations generated by the peristaltic pump were reduced, as shown in Figure 3-3, to a level closer to the signal noise inherent to the sensors.

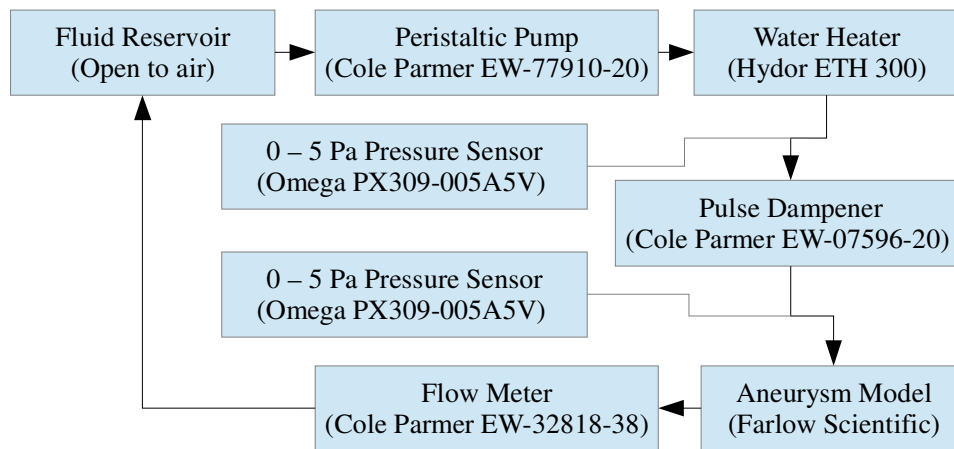


Figure 3-2. The flow loop is composed of the commercially available equipment shown above.

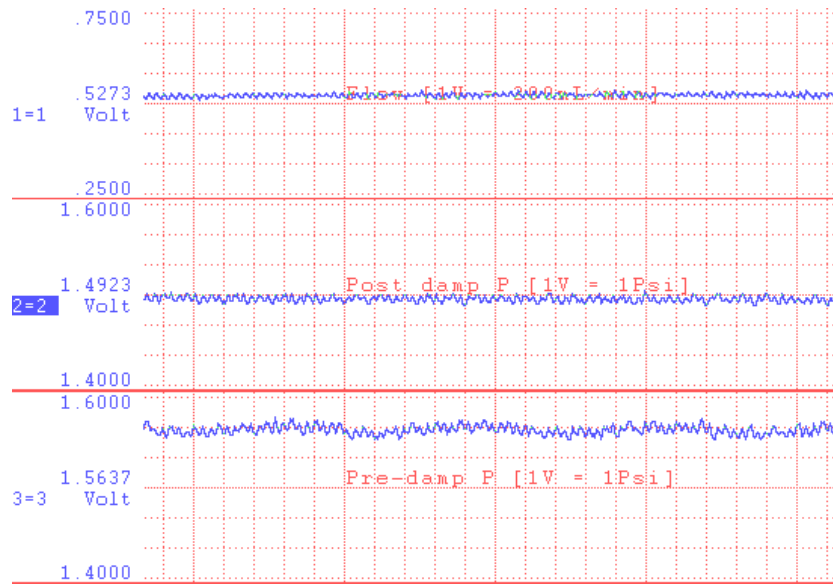


Figure 3-3. The DATAQ data acquisition unit recorded the flow through the aneurysm model (top trace) and the pressures before (bottom trace) and after the pulse dampener (middle trace). The smoothness of the post-dampener pressure trace illustrates how the small perturbations inherent to the peristaltic pump were largely removed.

3.2.2. Fixtures to Hold the Glass Models

Glass models were ordered from Farlow Scientific with specified vessel diameters, radii of curvature, and aneurysm sizes. Due to time and lab space considerations, the laser sheet, described in Chapter 3.2.3, was kept stationary. The glass models were mounted in rapid prototyped fixtures connected to rotational and translational stages. The rapid-prototyped fixture is shown in Figure 3-4. That fixture was then mounted on a freely rotatable stage (Misumi RTRS40-R), a z-axis stage (Misumi ZLFG40), and an x-axis stage (Misumi XSGA60) to allow for fine adjustments to the orientation of the laser sheet relative to the glass model. The fixture components were rapid prototyped out of ABS plastic in the Mechanical Engineering Student Shop using Stratasys equipment.

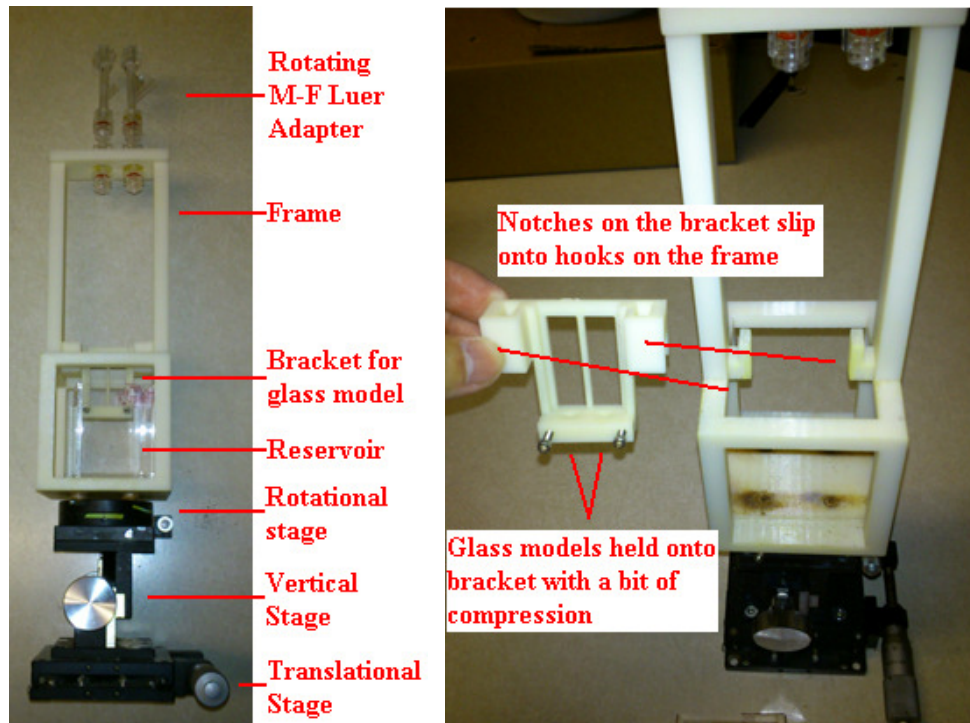


Figure 3-4. The fixture for holding the glass models consists of the frame, collars to hold the rotating female-male luer adapters to the frame, the rotating female-male luer adapters (Qosina #20023), a polycarbonate box for matching the index of refraction on the exterior surface of the glass models, and brackets to hold the glass model in place.

3.2.3. Pulsed Laser Sheet Generation

The laser generator was a Litron Lasers Nano S PIV unit, which emits light at the 532nm wavelength (green light). Timing of the two laser pulses for generating the image pairs was controlled by a BNC Model 575 Pulse Generator. Two pairs of planar concave and convex lenses from Edmund Optics were mounted orthogonally in series to turn the laser dot emitted by the Litron laser into a laser sheet. The spacing of the four lenses, shown in Figure 3-5, were manually adjusted until the desired height and thickness of the laser sheet when it arrived at the glass model, specifically the aneurysm, was approximately 0.5mm thick.

The laser power was manually adjusted until the images captured by the camera showed a sufficiently dense distribution of reflections from the seeded particles. In certain scenarios, more particles were added to the flowing medium to better visualize the flow. Due to the nature of the CCD (charge coupled device) camera, to be discussed in Chapter 3.2.6, laser power was kept at the minimal level necessary. The sensor in the camera can be overwhelmed if too much laser energy is reflected into the camera, causing permanent damage.

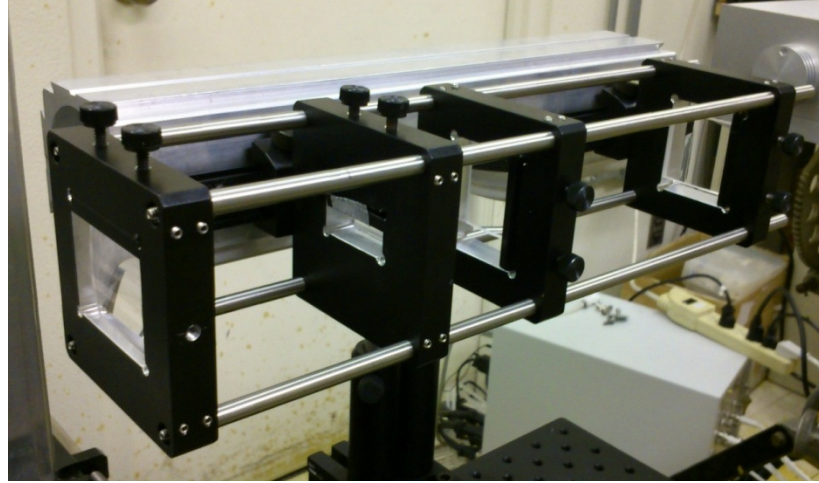


Figure 3-5. Two pairs of planar concave and planar convex lenses were mounted in a series of brackets (black squares) on adjustable rails (four circular rods) to turn the laser dot into a laser sheet. The spacing between the four lenses was manually adjusted until the desired laser sheet height and thickness was achieved in the target area, i.e. the aneurysm.

3.2.4. Reflective Particles

Hollow glass spheres ($\rho = 1.1 \text{ kg/m}^3$) approximately $8 - 12 \mu\text{m}$ in diameter from TSI Inc. were seeded in an approximately 60% w/w sodium iodide solution, mixed to achieve an index of refraction of approximately 1.472 to match the refractive index of the glass aneurysm models. The kinematic viscosity of the solution was approximately $1.98 * 10^{-6} \text{ kg / (m*s)}$ [96]. For the Stokes number, the characteristic time of the flow field was calculated using the mean velocity at the inlet of the glass model (at 100 mL/min) and the diameter of the aneurysm. As shown in Equation 3-4, the Stokes number is extremely small, indicating that these hollow glass spheres accurately follow the streamlines of the fluid flow, and therefore are a suitable seeding particle for analyzing flow inside the different glass models.

$$Stokes = \frac{\tau_{CHARACTERISTIC RESPONSE TIME OF PARTICLE}}{\tau_{CHARACTERISTIC TIME OF FLOW FIELD}} = \frac{\tau_P}{\tau_F} \quad (Eq. 3 - 1)$$

$$\tau_P = d_{PARTICLE}^2 \frac{\rho_{PARTICLE}}{18\mu} = (1 * 10^{-5} \text{m})^2 * \frac{1.1 \text{ kg}}{\text{m}^3} * \frac{\text{m} * \text{s}}{18 * 1.98 * 10^{-6} \text{ kg}} = 3.1 * 10^{-6} \text{s} \quad (Eq. 3 - 2)$$

$$\tau_F = \frac{\text{Aneurysm diameter}}{\text{Mean velocity entering glass model at 100 mL/min}} = \frac{1 \text{ cm}}{17 \text{ cm/s}} = 5.8 * 10^{-2} \text{s} \quad (Eq. 3 - 3)$$

$$Stokes = 5.3 * 10^{-5} \quad (Eq. 3 - 4)$$

3.2.5. Deployment of Flow Diverter

The deployment mechanism of the Pipeline Embolization Device is rather complex. The device is not easily reloaded onto the delivery wire after deployment. As shown in Figure 3-6, the distal end of the device is normally trapped underneath a coil. In a clinical procedure, the device is advanced to the aneurysm via a microcatheter and partially deployed to anchor the device. The distal end is then released from the delivery wire by rotating the delivery wire. The device is then fully deployed by continuing to retract the microcatheter.

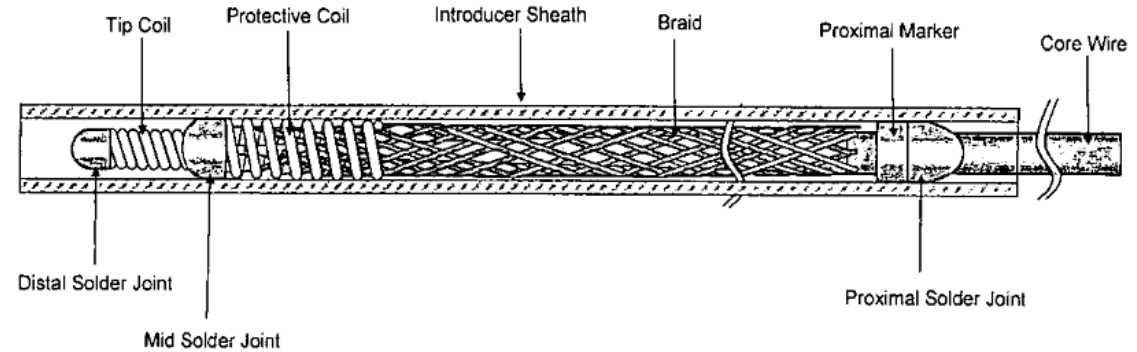


Figure 3-6. The Pipeline Embolization Device is packaged with its distal end trapped underneath a coil on the delivery wire. [97]

Due to the lack of equipment to reload the Pipeline Embolization Device back onto the delivery wire, a kidney stone remover (Bard Dimension Articulating Stone Basket/Grasper, Figure 3-7) was used to place the flow diverter across the aneurysm neck. The kidney stone remover was first advanced through the glass model. One end of the PED was trapped inside the basket. The PED was then dragged through the glass model until it spanned the aneurysm neck. The basket was then released and the kidney stone remover taken out of the glass model. The glass model, with the PED in place, was then connected into the flow loop for PIV testing.

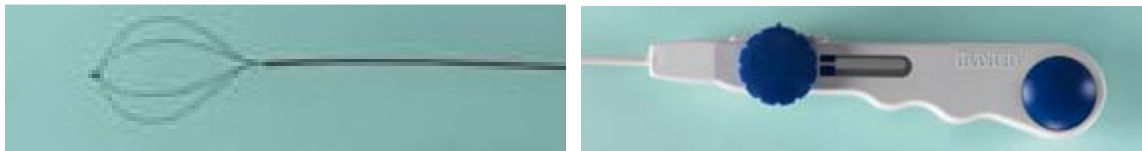


Figure 3-7. The Bard Dimension Articulating Stone Basket/Grasper basket (left) and manipulating handle (right) are shown (not to scale). When the blue knob of the handle is retracted, the basket collapses. In order to place the flow diverter across the aneurysm neck, one end of the flow diverter is trapped inside the basket and dragged into position. When the flow diverter is at the desired location, the basket is relaxed and removed from the glass model. The glass model was then reattached to the flow loop for PIV testing. [98]

3.2.6. Image Acquisition

The PIV images were acquired with an Imperx IPX-4M15-LMFN camera, set to output black and white 2048 * 2048 pixel images. A Nikon Nikkor AF Micro 105mm 1:2.8D lens assembly allows for adjustment of the magnification level. The camera and lens assembly is oriented orthogonally to the laser sheet and mounted on an x-y translational stage to focus the image on a plane illuminated by the laser sheet. Figure 3-8 is a photograph of the equipment. Figure 3-9 is a schematic diagram summarizing all of the components of the PIV experimental set up.

In order to interrogate the flow at different planes within the glass model, the translational stage holding the glass model fixture was manipulated to have the laser sheet illuminate at a different location. The translational stage for the camera was then also manipulated to focus the image.

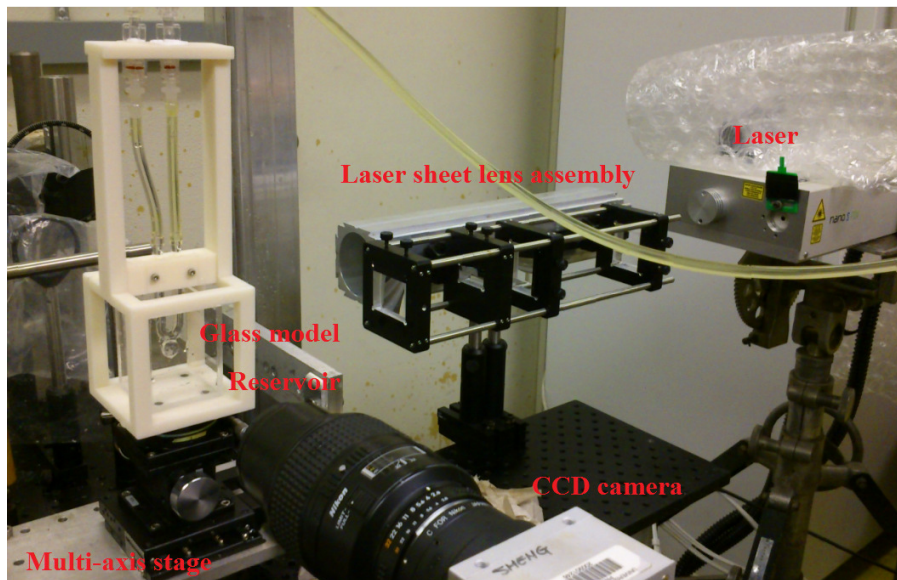


Figure 3-8. Several components of the PIV set up are shown. Note that the camera is oriented approximately orthogonally to the laser sheet illuminating the glass model. The reservoir outside of the glass model is also filled with sodium iodide in order to match the glass model's index of refraction at both the interior and exterior surfaces.

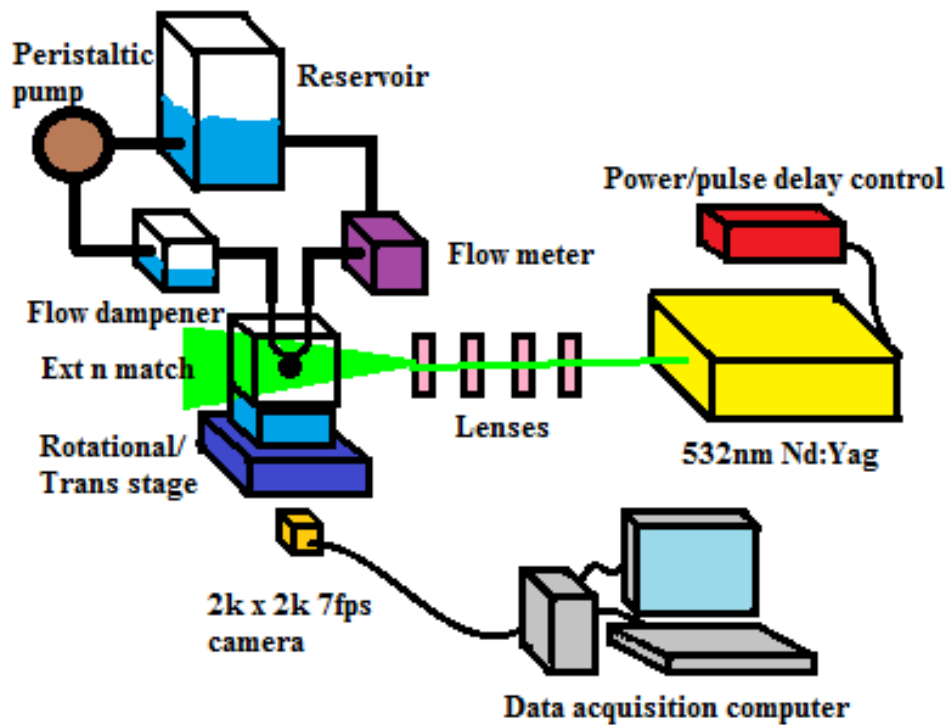


Figure 3-9. A schematic diagram summarizing all of the components of the PIV experimental set up. The green laser beam emitted from the Nd-Yag laser is transformed into a laser sheet to illuminate planes of interest in the glass model.

3.2.7. Image Enhancement

The images captured by the camera are enhanced because the orientation of the camera relative to the illumination plane captures only a small fraction of the energy reflected off of the particles, rendering the particles difficult to differentiate from the background noise. By enhancing the image to strengthen the signal of the particles, the particle tracking algorithms are much more precise. Engineering judgment is exercised to determine the appropriate level of image enhancement. Incorrect levels end up bringing background noise into the images, leading to incorrect calculations of fluid velocities. Figure 3-10 illustrates an image before and after enhancement.

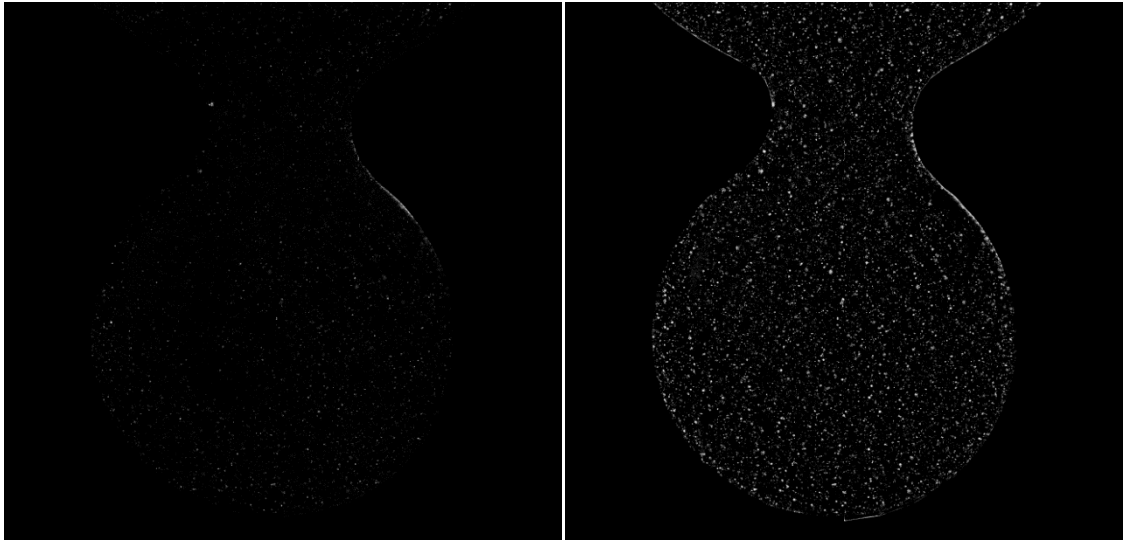


Figure 3-10. The raw (left) and enhanced (right) images are shown.

Figure 3-11 illustrates the steps taken to enhance the image. The background noise is first removed in ImageJ, an open source image manipulation program, based on a median filter algorithm. Based on trial and error with different filter settings, the grayscale value of a pixel was replaced by the median of grayscale value within a seven pixel radius. A mask was then manually applied to leave behind only the region of interest, namely the flow inside the glass model. This reduces computational time for GauCorr, described in Chapter 3.2.8, as it does not need to perform image analysis outside of the region of interest. A closed-source program developed at John Hopkins University and provided by Professor Sheng was then used to enhance the images via histogram equalization of pixels above a desired threshold of pixel grayscale values in the image. An example of image enhancement of a generic image is shown in Figure 3-12. Figure 3-13 illustrates how different grayscale threshold values lead to different concentrations of particles. Through trial and error, pixels at the bottom 92% of grayscale values were excluded and the remaining pixels equalized in the images sent to GauCorr.

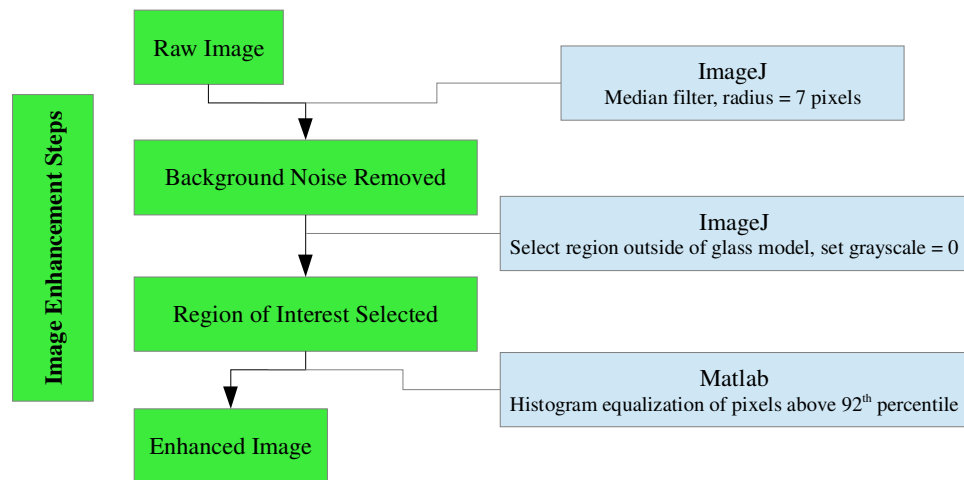


Figure 3-11. The steps taken to prepare the images for analysis are shown.

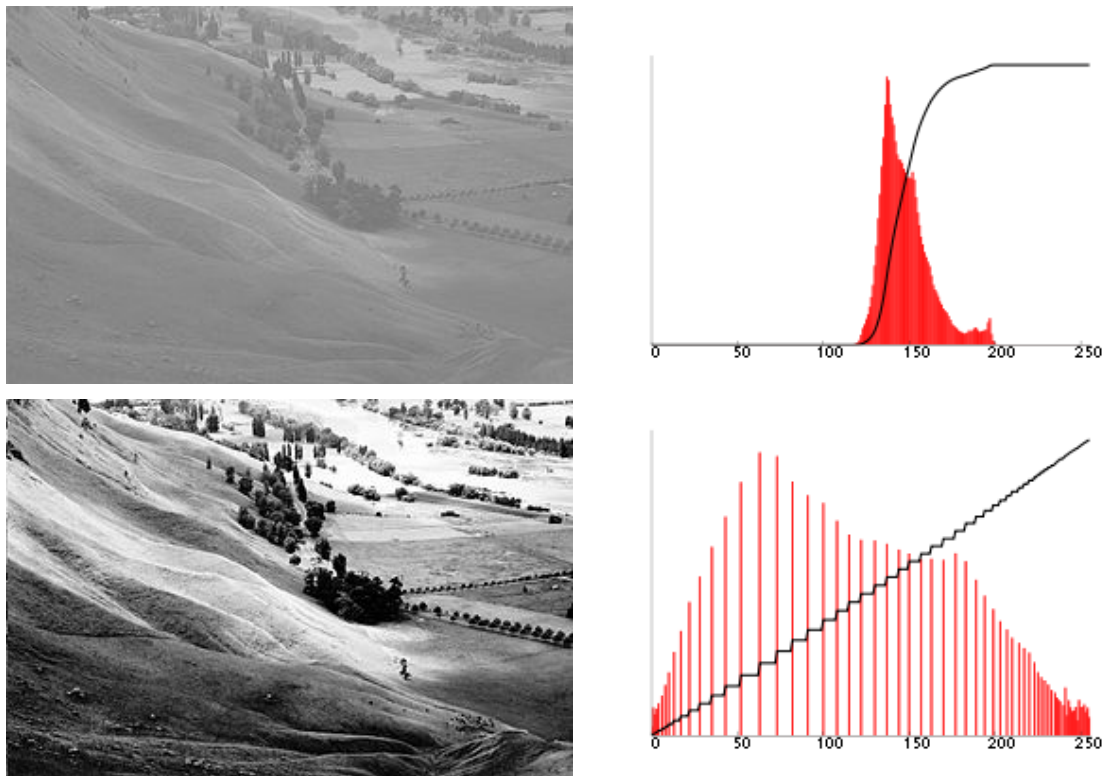


Figure 3-12. An example illustrating the effect of histogram equalization enhancement of an image is shown. The red bars in the histograms on the right illustrate the distribution of grayscale values within the image of its left. The black lines indicate the cumulative density function of the pixels. Good contrast between pixels of interest, i.e. those of the reflective particles, and the background noise leads to generation of a more accurate vector map. [99]

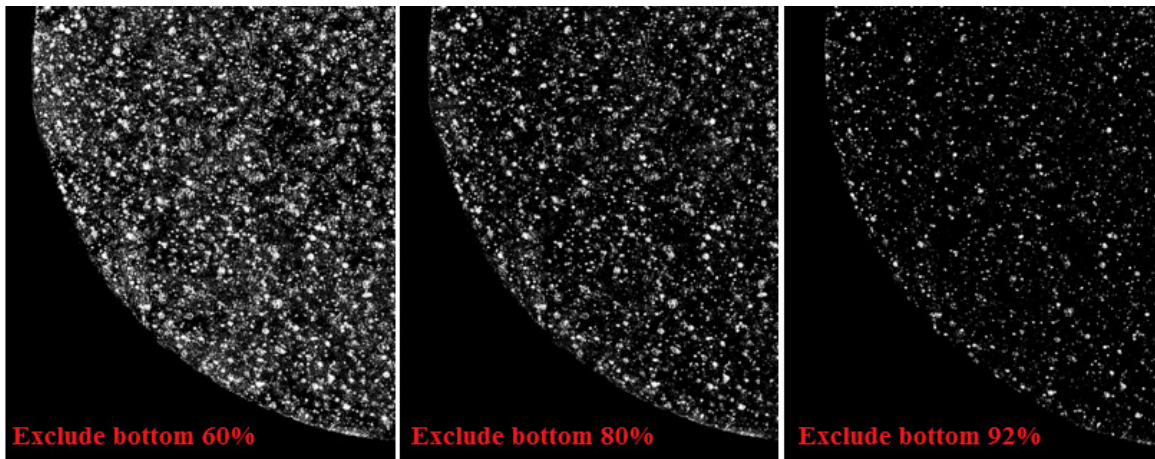


Figure 3-13. By filtering out pixels with grayscale values below a certain threshold, the histogram equalized images end up with different particle densities. If the threshold includes too many pixels at the bottom end of the grayscale distribution, random background noise ends up in the final image, introducing error into the displacement vector calculation. Engineering judgment was exercised to select the correct threshold.

3.2.8. GauCorr

GauCorr is a closed-source program developed at John Hopkins University and provided by Professor Sheng for analysis of image pairs. Alternative commercially available programs are sold by TSI and LaVision.

In its simplest form, vector maps generated by GauCorr and other programs are calculated by breaking down images into interrogation windows, locating the particles, and then calculating the most likely displacement vector of the particles between image pairs. As shown in Figure 3-14, particles are identified inside the interrogation window (red dashed square) at image A (red dots). A short time later, a second image is taken, image B, and the particles are represented as blue dots. GauCorr searches in the nearby area around the interrogation window to find a best match of the original pattern of particles within the interrogation window. The displacement vector between the original interrogation window and the window of best match (blue dashed square) is then collected with all the other vectors calculated elsewhere to build a map.

Selection of the correct interrogation window parameters as well as the quality of image pairs has a strong effect on the accuracy of vector map. Referring again to Figure 3-14, not all particles have the exact same displacement. If the window is not the correct size, the program has a difficult time determining which displacement vector is the correct one. If the program is allowed too large a distance to search for optimal

correlation, it may end up with an incorrect displacement vector as there may be a random pattern elsewhere in the fluid field that adequately matches the original pattern. Therefore, some error checking is programmed into GauCorr. One feature, for example, invokes continuity of fluid flow to limit the difference in velocity magnitude and direction between adjacent vectors.

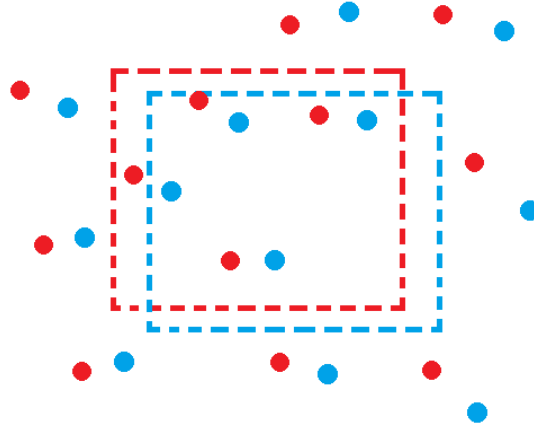


Figure 3-14. A schematic diagram illustrating the calculation of displacement vectors is shown. Particles from the first image are shown as red dots. Sometime later, a second image is taken and the particles are represented as blue dots in this figure. An interrogation window is defined in the first image, shown as the dashed red rectangle, and the particle pattern is defined. GauCorr then searches in the nearby region to find a pattern of blue particles that best matches the pattern of the red particles. In this example, the best pattern in the second image is represented by the dashed blue rectangle. The displacement vector between the dashed red and blue rectangles is returned as the displacement vector for fluid flow in this particular region of the domain.

3.2.9. Data Packaging

The displacement vector maps generated by GauCorr are 2D matrices of pixel displacement between image pairs. Manipulation of these matrices by including information such as the length scale of each pixel, the time duration between image pairs, and the location of the illumination plane inside the flow domain produce vector maps in 3D space with more conventional units, such as m/s for velocity. This manipulation was done in Matlab.

Due to small disturbances in the actual flow as well as slight inaccuracies in the image preparation and analysis process, velocity maps were generated from an average of 100 image pairs. Calculating the standard deviation of vectors also allowed for detection of unsteady regions within the flow domain.

3.2.10. TecPlot and Extraction of Flow Metrics

TecPlot is a commercially available data visualization and analysis program, analogous to the CFX-Post module of ANSYS's simulation suite. The packaged velocity vector maps are imported into Tecplot. Since the location of the illumination plane was included in the data matrix during the packaging step, a quasi-3D view of fluid flow inside the flow domain can be generated. Visualization of geometrical features, namely the locations of the distal and proximal ends of the aneurysm neck, allow for easier identification of where to integrate the normal velocity vector for calculating the flow rate of fluid entering the aneurysm.

Figure 3-15 illustrates one such assembly of velocity planes in TecPlot. Data at 24 planes spaced $400\mu\text{m}$ apart were collected, analyzed, and assembled. The outline of the aneurysm shape can be roughly estimated. The data processing ability of Tecplot allows for scrolling between planes to observe the penetration of the jet entering the aneurysm. Movies can also be generated for presentations using TecPlot.

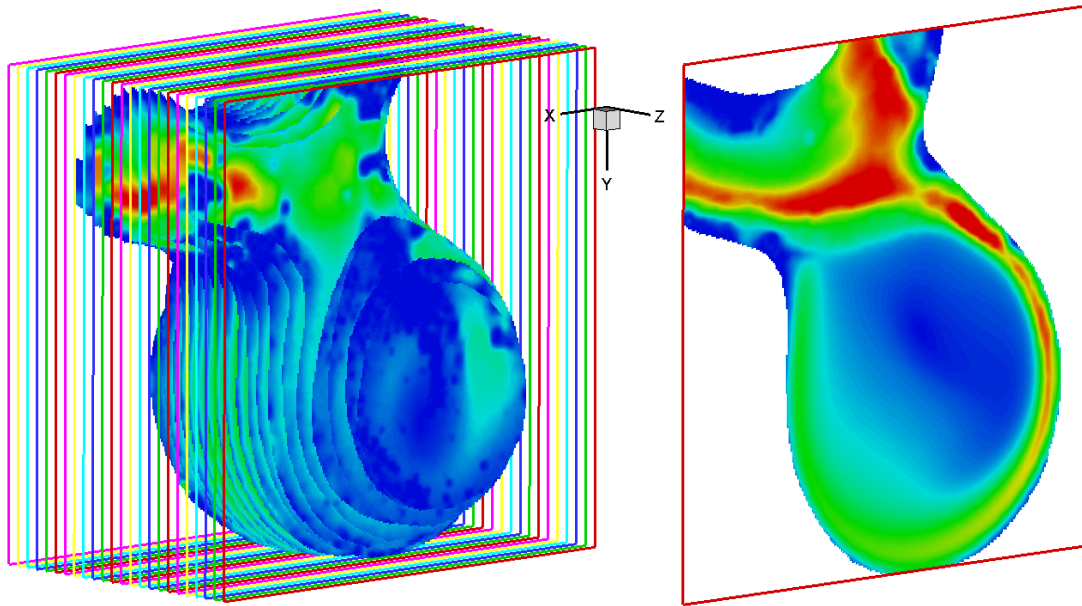


Figure 3-15. Left: The assembly of planar velocities on 24 planes spaced $400\mu\text{m}$ apart is shown. The different colored squares illustrate the 3D location of each plane. **Right:** The planar velocity in the center plane is shown.

3.3. INTRAANEURYSMAL FLOW IN UNTREATED AND TREATED GLASS MODELS

INTRODUCTION

This section of Chapter 3 discusses the research that was conducted to experimentally assess the flow diverting effect of the Pipeline Embolization Device (PED) in a matrix of glass models. The diameter of the parent artery, the curvature of the bend, and the placement of the aneurysm along the bend were varied to obtain a preliminary understanding of the effectiveness of the PED in a range of geometries found in the human neurovasculature.

METHOD

Flow Domains

Experimental data were collected for the domains listed in Table 3-1. The glass models were blown by a company in California named Farlow Scientific. The dimensions specified to the glass blowers are shown in the left side of Table 3-1. The actual dimensions, as measured from 3D reconstructions of CT scans of the glass models, are shown on the right side. Dimensions of interest include the parent artery diameter (PA), radius of curvature of the bend (RoC, defined as the distance from the bend center to centerline of the vessel), the location of the aneurysm (Deg, short for degree), the diameter of the aneurysm bulb (Anu), and the length of the aneurysm neck (Neck). Due to discrepancies between the requested geometries and the actual geometries, as well as irregularities in the shape of the glass blown aneurysms, it was decided that subsequent CFD simulations for verification must be conducted in the actual geometries. The creation of the computer models for simulations is described in Chapters 4.2.1 and 4.2.2.

The front, side, and isometric views of the fluid domain inside the glass models are shown in Figures 3-16, 3-17, 3-18, and 3-20. The RC-SOD68 series and RC-SOD147 series of glass models were manufactured at a different time during the duration of the project, partially explaining the markedly different aneurysm shapes. In addition to non-spherical aneurysms, there was also poor control over the dimensions of the aneurysm neck. Within the RC-SOD147 series, aneurysms located at the center of the bend (at 90 degrees) generally had narrower necks than aneurysms offset slightly to the side (60 degrees).

Table 3-1. The requested and actual dimensions of the glass models are shown.

Domain	Requested Dimensions					Actual Dimensions				
	PA [mm]	RoC [mm]	Deg	Anu [mm]	Neck [mm]	PA [mm]	RoC [mm]	Deg	Anu [mm]	Neck [mm]
RC-SOD68-1	3	6	90	10	5.42	3.44	6.4	90	9.5	7.5
RC-SOD68-3	4	6	90	10	7.84	3.92	6.0	90	8.4	6.3
RC-SOD147-1	4	4	90	10	7.34	4.09	3.4	90	10.5	5.1
RC-SOD147-2	4	6	90	10	7.84	4.10	6.2	90	9.2	5.0
RC-SOD147-3	4	8	90	10	8.11	4.15	7.8	90	10.0	5.9
RC-SOD147-6	3	6	90	10	5.42	3.42	6.0	90	9.8	3.8
RC-SOD147-7	4	4	60	10	7.32	4.15	4.3	63	9.9	5.5
RC-SOD147-8	4	6	60	10	7.86	4.08	5.9	65	10.0	4.7
RC-SOD147-9	4	8	60	10	8.09	4.10	7.6	63	9.8	5.9
RC-SOD147-12	3	6	60	10	5.45	3.42	5.8	65	9.9	6.1

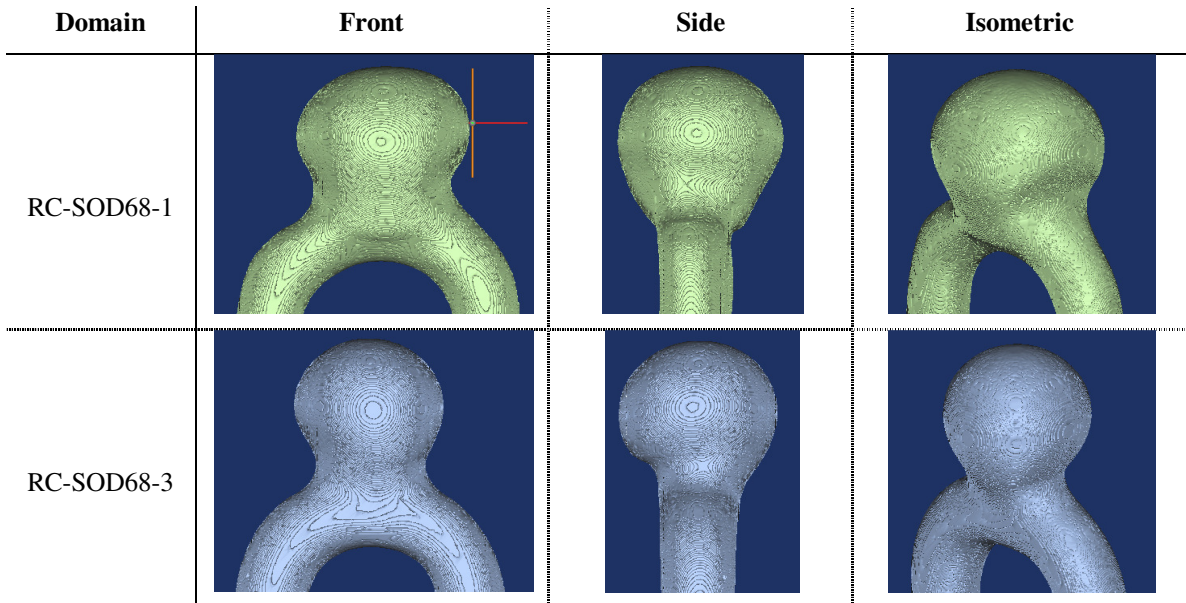


Figure 3-16. Images are not to scale and are meant to illustrate the irregularities and asymmetries in the shapes of the aneurysm neck and parent artery. The glass models of the RC-SOD68 series are shown.

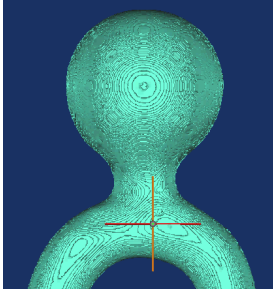
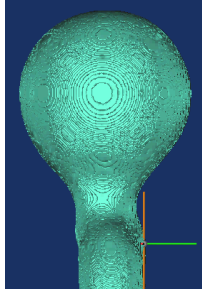
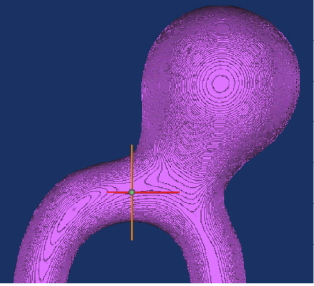
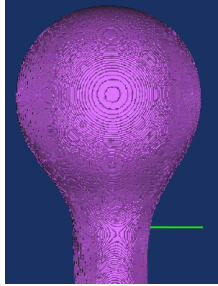
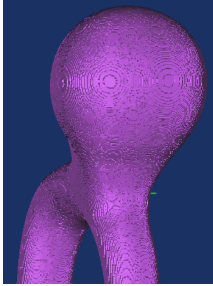
Domain	Front	Side	Isometric
RC-SOD147-6			
RC-SOD147-12			

Figure 3-17. Images are not to scale and are meant to illustrate the irregularities and asymmetries in the shapes of the aneurysm neck and parent artery. The glass models of the RC-SOD147 series with ~3.4 mm diameter vessels are shown.

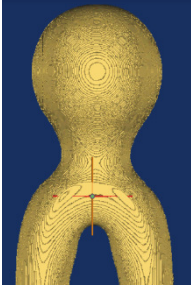
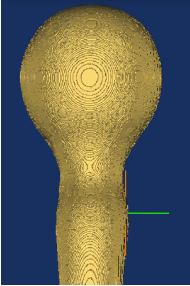
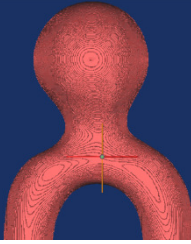
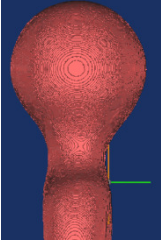
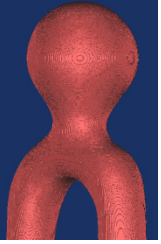
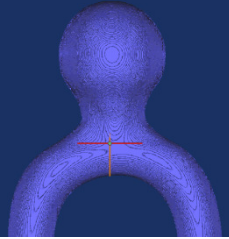
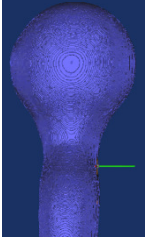
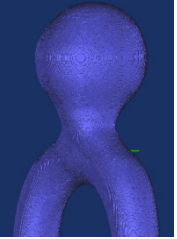
Domain	Front	Side	Isometric
RC-SOD147-1			
RC-SOD147-2			
RC-SOD147-3			

Figure 3-18. Images are not to scale and are meant to illustrate the irregularities and asymmetries in the shapes of the aneurysm neck and parent artery. The glass models of the RC-SOD147 series with ~4mm diameter vessels and aneurysms located in the middle of the bend are shown.

For flow domains with off-center aneurysms, the (F) suffix indicates that the aneurysm is biased away from the inlet. The (R) suffix denotes that the aneurysm is biased towards to the inlet. An illustration of RC-SOD147-12(F) and (R) is shown in Figure 3-19.

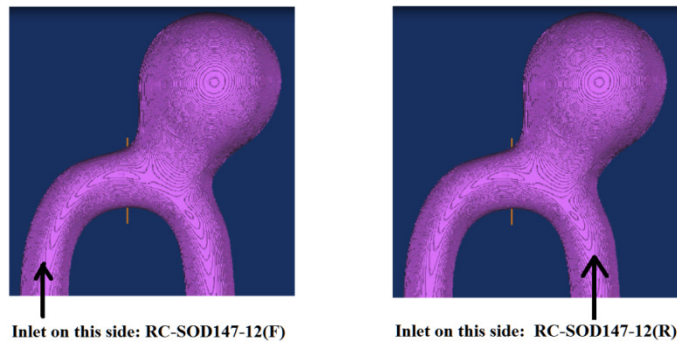


Figure 3-19. When the aneurysm is biased away from the inlet, it is referred to as RC-SOD147-12(F). When the aneurysm is biased towards from the inlet, it is referred to as RC-SOD147-12(R).

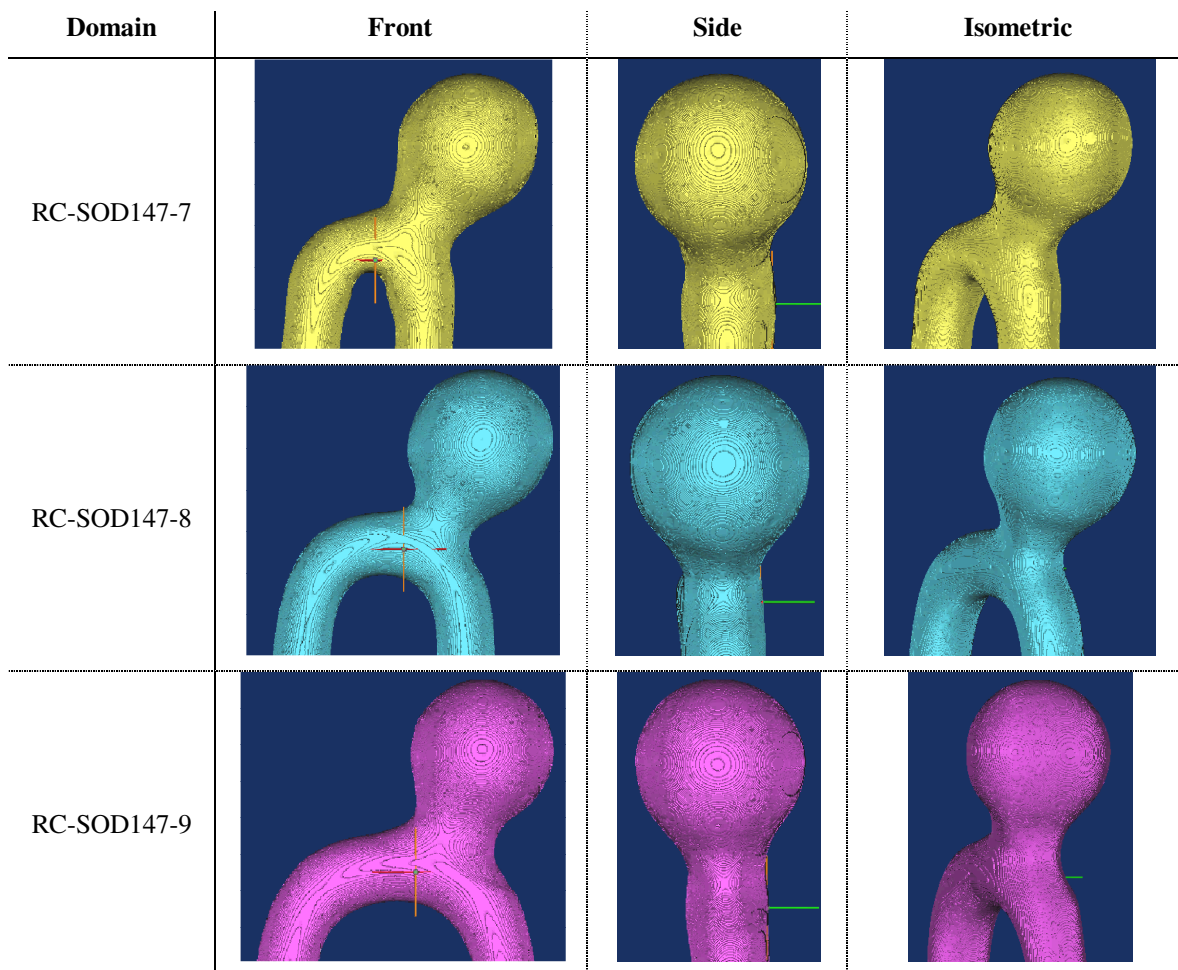


Figure 3-20. Images are not to scale and are meant to illustrate the irregularities and asymmetries in the shapes of the aneurysm neck and parent artery. The glass models of the RC-SOD147 series with ~4mm diameter vessels and aneurysms offset from the middle of the bend are shown.

Experimentation Plan

The PIV experiments were conducted with a steady flow of 100mL/min of sodium iodide solution pumped into the flow loop. The flow of fluid entering the aneurysm both before and after the placement of the flow diverter was examined. Results from the PIV experiments are summarized into three groups, as shown in Figure 3-21. The flow domains discussed in each chapter are as follows:

- Chapter 3.3.1
 - RC-SOD147-6, RC-SOD147-12(F), RC-SOD147-12(R)

- Chapter 3.3.2
 - RC-SOD147-1, RC-SOD147-2, RC-SOD147-3
 - RC-SOD147-7(F), RC-SOD147-7(R)
 - RC-SOD147-8(F), RC-SOD147-8(R)
 - RC-SOD147-9(F), RC-SOD147-9(R)

- Chapter 3.3.3:
 - RC-SOD68-1, RC-SOD68-3

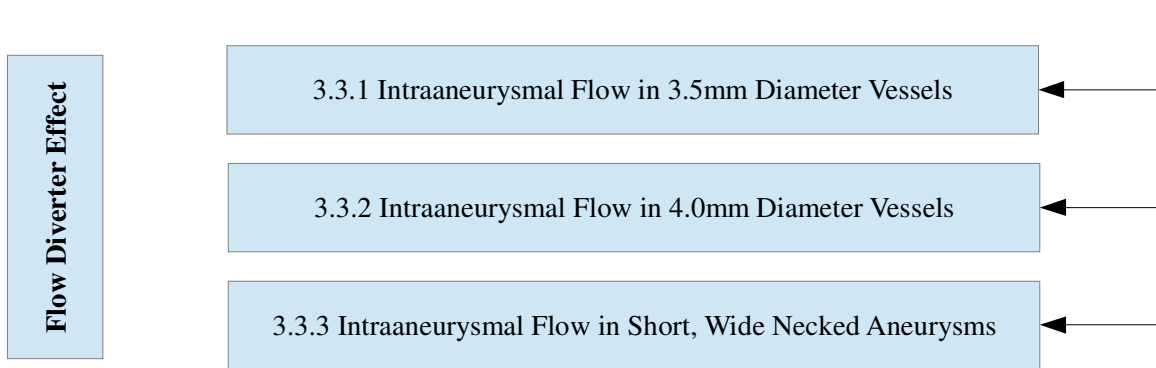


Figure 3-21. The effect of the flow diverter is summarized into three chapters.

Flow Metrics of Interest

The flow of fluid entering and exiting the aneurysm at the center plane approximately bisecting the aneurysm is compared before and after the placement of the flow diverter. The normal velocity vector, V_N , is described in Figure 3-22. Its value along the length of the neck is plotted, with a positive normal velocity indicating flow **into** the aneurysm. Color contour diagrams of the normal velocity are also shown, scaled from $-1/10^{\text{th}}$ of the inlet velocity (blue) to $+1/10^{\text{th}}$ of the inlet velocity (red) to better illustrate the structure of the jet.

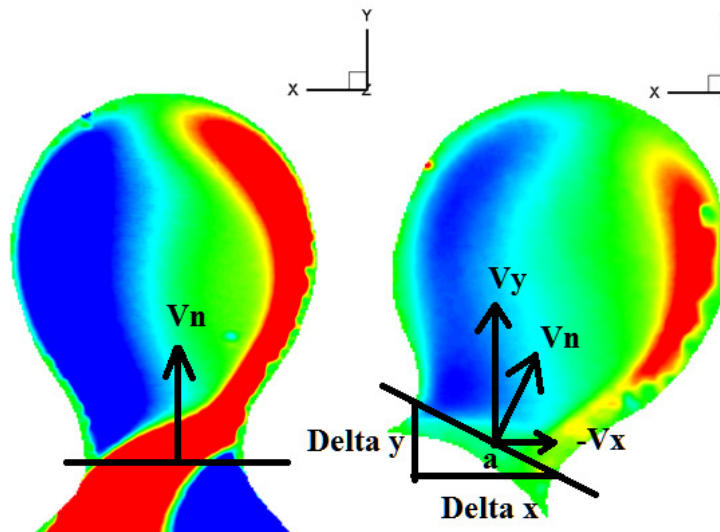


Figure 3-22. A line is defined across the neck of the aneurysm. The normal velocity vector is calculated to allow for calculation of fluid entering or exiting the aneurysm. The normal velocity vector (Eq. 3-6) is plotted along this line in chapters 3.3.1, 3.3.2, and 3.3.3.

$$a = \tan^{-1} \left(\frac{\text{delta } y}{\text{delta } x} \right) \quad (\text{Eq. 3 - 5})$$

$$V_N = V \cdot n = -V_x \sin(a) + V_y * \cos(a) \quad (\text{Eq. 3 - 6})$$

Color contour diagrams of the planar velocity magnitude, defined in Equation 3-7, on the center plane and on the planes 2 mm in front and behind the center plane are extracted. Figure 3-23 illustrates the locations of the three planes. The velocity contours in the untreated cases (without the flow diverter) are scaled from 0 m/s (blue) to the inlet velocity (red). The scales of the velocity contours in the treated cases (with the flow diverter) are from 0 m/s (blue) to 1/10th or 2/10th of the inlet velocity (red) to highlight the shape of the jet entering the aneurysm.

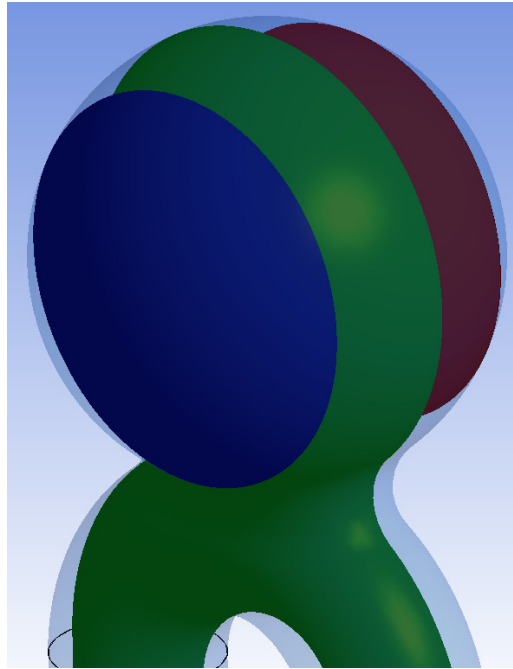


Figure 3-23. The locations of the three planes of interest are shown in an isometric view of an idealized geometry (faint blue outline). The plane approximately bisecting the aneurysm is indexed as the center plane (shown in green). Two more planes, 2 mm in front and behind the center plane (blue and red), are also examined. The velocity magnitude on these planes were plotted and shown in the appendix.

$$V_{PLANAR} = \sqrt{V_x^2 + V_y^2} \quad (Eq. 3 - 7)$$

OBSERVATIONS

3.3.1. Intraaneurysmal Flow in 3.5mm Diameter Vessels

Three flow domains with parent arteries of approximately 3.5mm in diameter were examined. The planar and normal velocity contour diagrams for the center plane are shown in Figures 3-24 and 3-25. The normal velocities across the neck of the aneurysm at the center plane are plotted in Figure 3-26. Representative images of the shapes of the flow diverters in the flow domains are in Appendix A.

Due to the narrow aneurysm neck of the -6 domain, fluid largely entered the aneurysm at the distal, or downstream, neck in the absence of the flow diverter. Placement of the flow diverter created a spot of flow entering at the proximal end and a spot exiting at the distal end. Furthermore, the penetration depth was significantly reduced. Whereas the jet entering the untreated aneurysm would circumnavigate the entire wall, the jet in the treated aneurysm penetrated only about halfway into the aneurysm before being dispersed into adjacent planes.

In RC-SOD147-12(F), the diverter caused the inlet jet to be shifted towards the proximal neck, but the cumulative flow rate (the area under the curve) was reduced. In RC-SOD147-12(R), the inlet jet was slightly hindered by the diverter. However, a strong jet still entered the aneurysm at the distal neck.

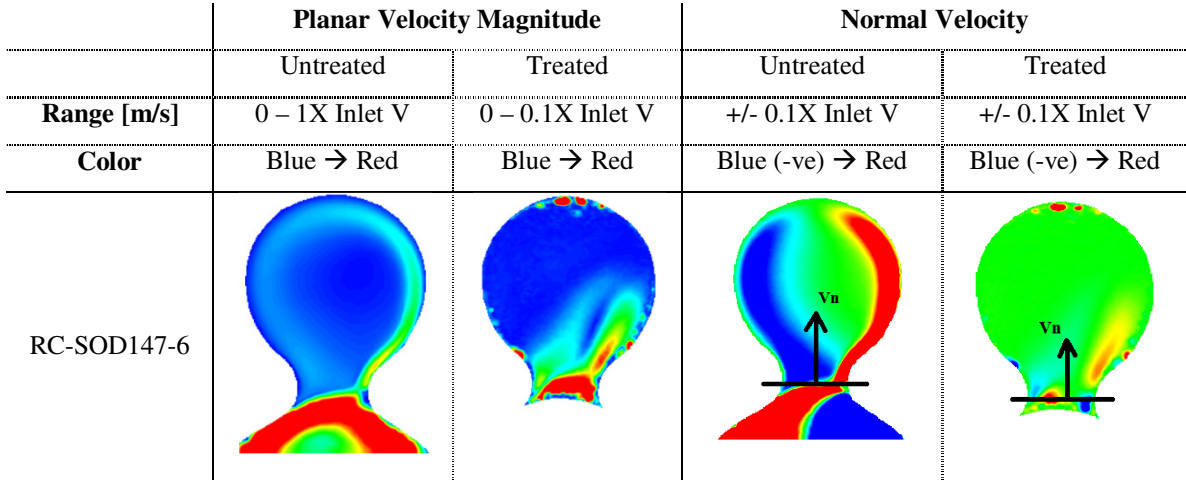


Figure 3-24. The planar and normal velocity contours are shown at the center plane of the RC-SOD147-6 domain.

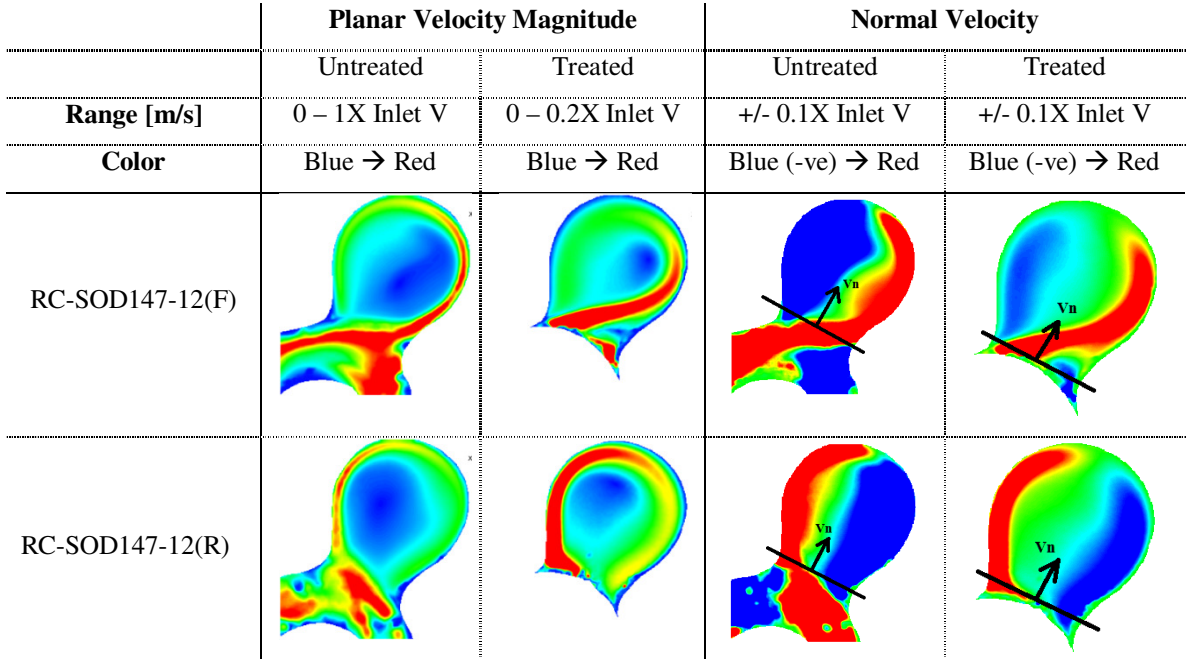


Figure 3-25. The planar and normal velocity contours are shown at the center plane of the RC-SOD147-12(F) and (R) domains.

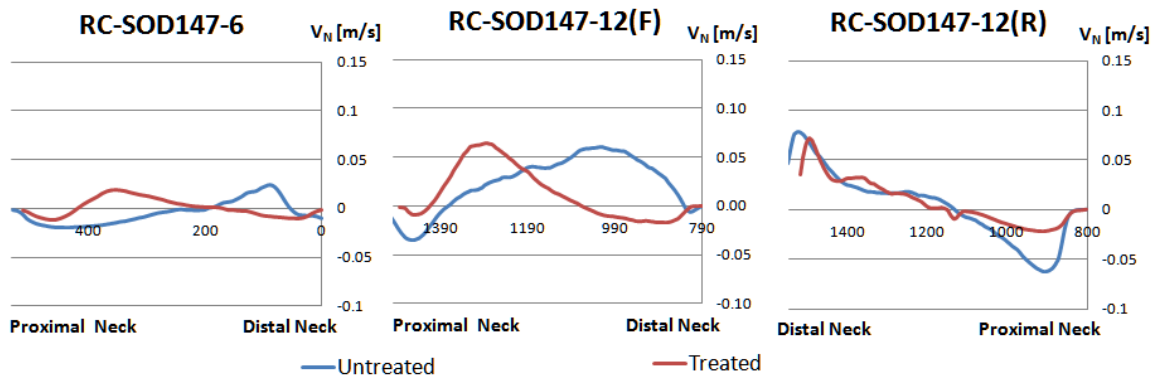


Figure 3-26. The normal velocities across the neck of the aneurysm at the center plane are shown for the three flow domains discussed in this chapter. The figures are aligned with the orientation of the planar velocity contours plots. For example, the distal neck is on the right side for RC-SOD147-6 for both the contour plot in Figure 3-24, and the normal velocity plot of this figure.

3.3.2. Intraaneurysmal Flow in 4.0mm Diameter Vessels

Nine flow domains with parent arteries of approximately 4mm in diameter were examined. The planar and normal velocity contour diagrams for the center plane are shown in Figures 3-28, 3-29, 3-31, and 3-33. The normal velocities across the neck of the aneurysm at the center plane are plotted in Figures 3-27, 3-30, 3-32, and 3-34. Representative images of the shapes of the flow diverters deployed in the glass models are displayed in Appendix A.

In RC-SOD147-1, the undiverted fluid enters the aneurysms in the proximal 75% of the neck along the center plane. This is likely because the curvature is so tight that the momentum of the incoming fluid carried it through the aneurysm neck. In RC-SOD147-2 and -3, Figure 3-27 illustrates that the majority of fluid entering the aneurysm neck has shifted towards the distal side. This is likely because the more gradual curvatures of these two domains have re-directed the incoming fluid into a more horizontal direction, thereby crossing the aneurysm neck further downstream.

In all three scenarios, the presence of the PED reduced the amount of fluid entering the aneurysm, as well as stunting the penetration of the jet. Instead of entering the aneurysm and maintaining a relatively high velocity jet along half to two-thirds of the circumference, the jet is only penetrating about half the height of the aneurysm.

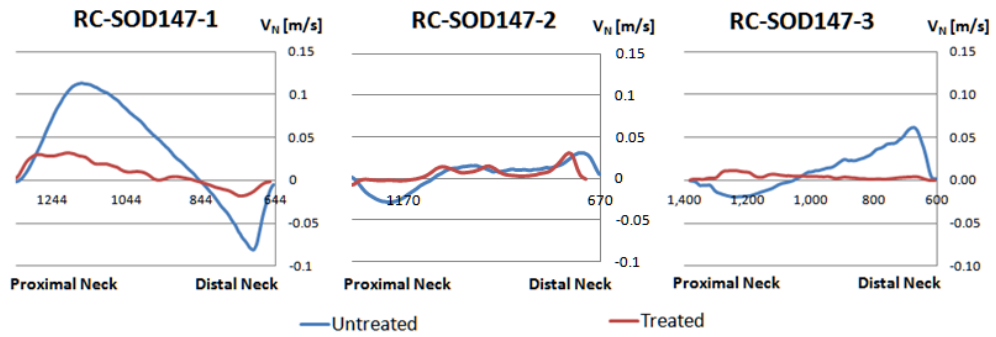


Figure 3-27. The normal velocities across the neck of the aneurysm at the center plane are shown for the three flow domains with aneurysms located in the middle of the bend. The figures are aligned with the orientation of the planar velocity contours plots. For example, the distal neck is on the right side for RC-SOD147-1 for both the contour plot in Figure 3-28, and the normal velocity plot of this figure.

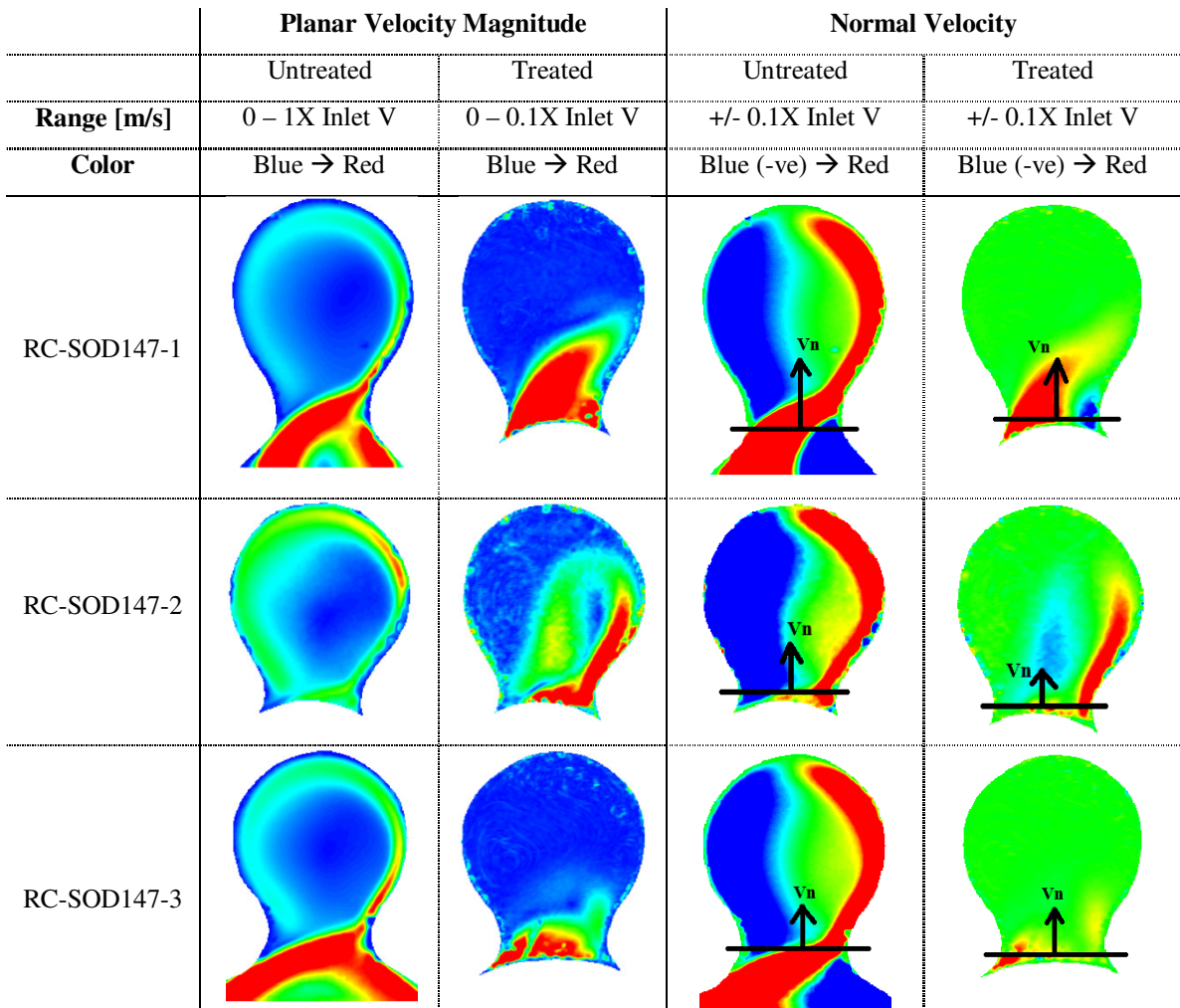


Figure 3-28. The planar and normal velocity contours are shown at the center plane.

In RC-SOD147-7, the incoming fluid is given little room to change directions due to the tightness of the curvature. Referring to Figure 3-30, fluid largely enters the aneurysm on the proximal side in the forward domain. In the reverse domain, the fluid's momentum carries it straight into the aneurysm along the distal side of the aneurysm neck. The PED greatly reduces the flow of fluid entering the aneurysm.

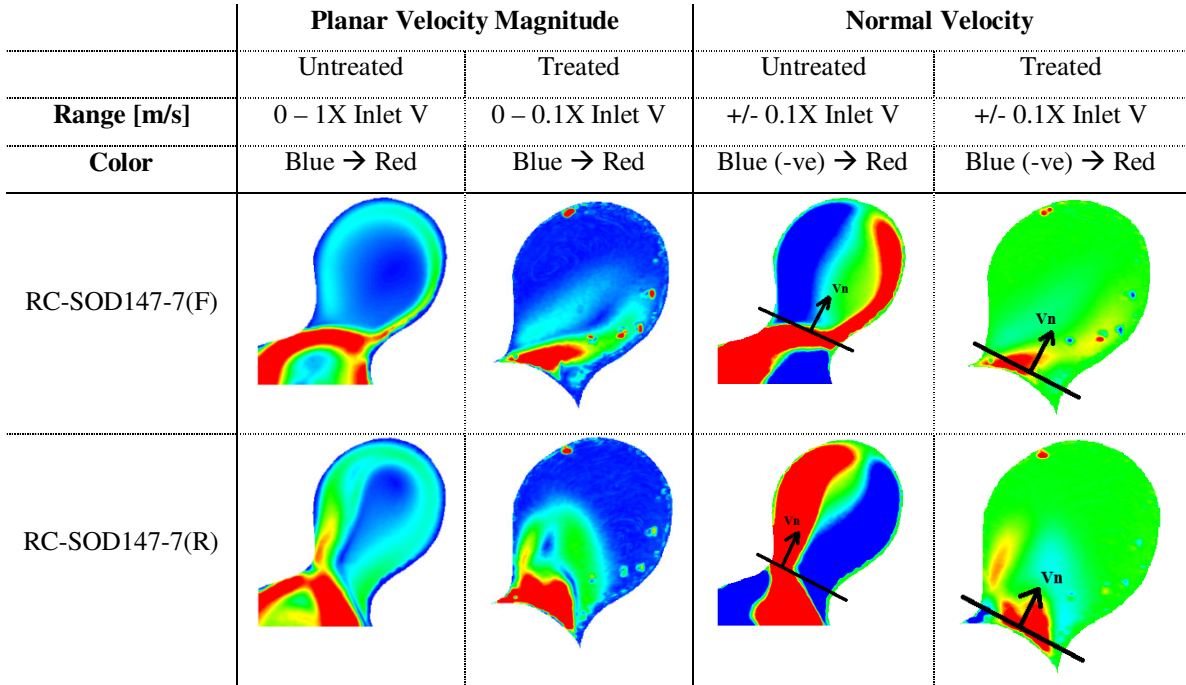


Figure 3-29. The planar and normal velocity contours are shown at the center plane of the RC-SOD147-7(F) and (R) domains.

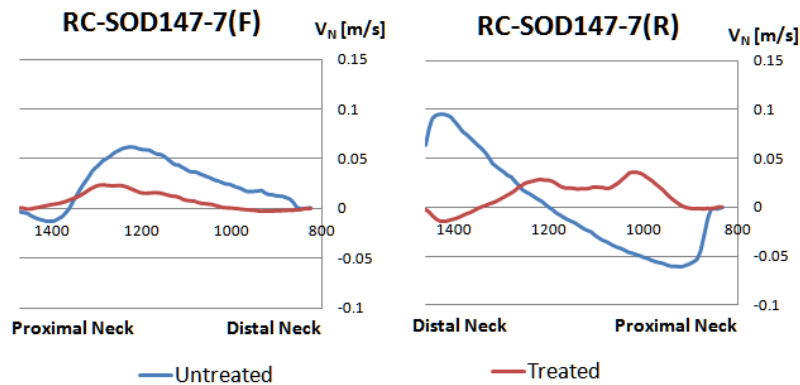


Figure 3-30. The normal velocities across the neck of the aneurysm at the center plane are shown for the two flow domains with a radius of curvature of approximately 4mm. The figures are aligned with the orientation of the planar velocity contours plots. For example, the distal neck is on the right side for RC-SOD147-7(F) for both the contour plot in Figure 3-29, and the normal velocity plot of this figure.

The flow entering the aneurysm in RC-SOD147-8 was lower than expected when compared to -7 and -9, which had radii of curvature that bracketing that of -8. Thus, the planar velocity contour diagrams were scaled to $\frac{1}{2}$ of the inlet velocity to illustrate the jet entering the aneurysm in the untreated case. Referring back to Figure 3-20 and Table 3-1, it can be observed that the neck of the aneurysm is smaller than those of RC-SOD147-7 and -9. Therefore, it is difficult to determine trends due to an increasing radius of curvature when the neck geometries are not kept constant. The normal velocity profiles from Figure 3-32 quantitatively show little effect with the placement of the flow diverter. However, Figure 3-31 illustrates that the presence of the flow diverter once again stunts the penetration of the fluid jet into the aneurysm.

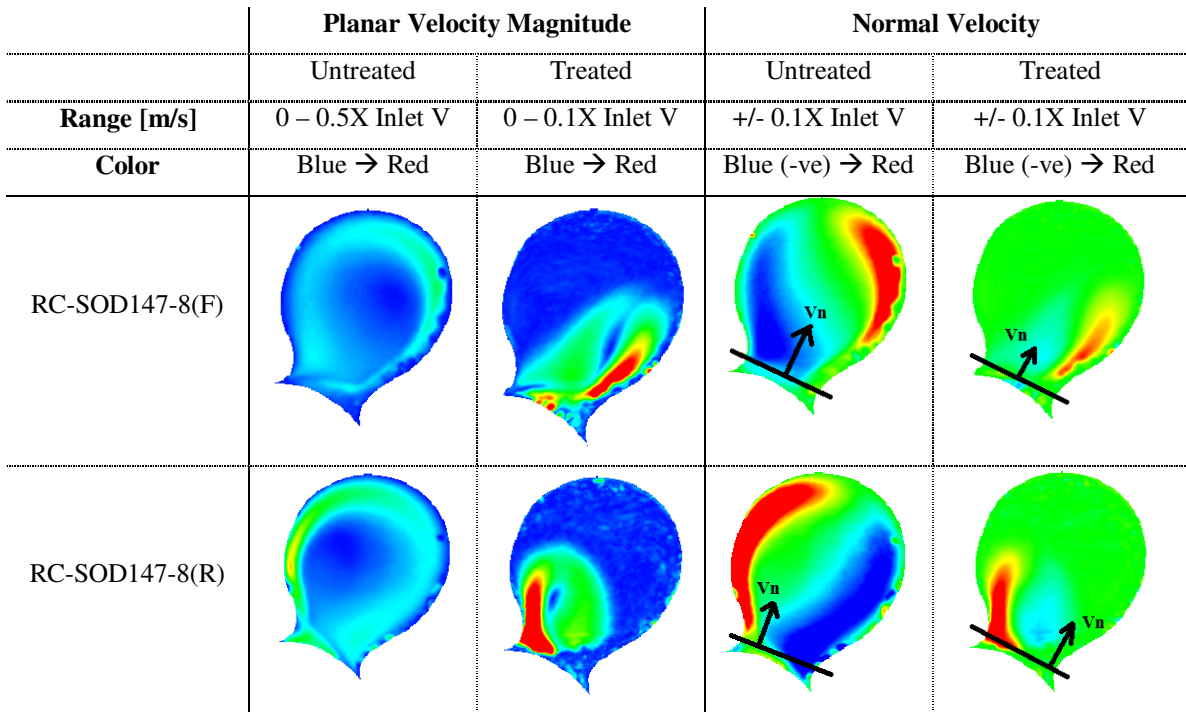


Figure 3-31. The planar and normal velocity contours are shown at the center plane of the RC-SOD147-8(F) and (R) domains.

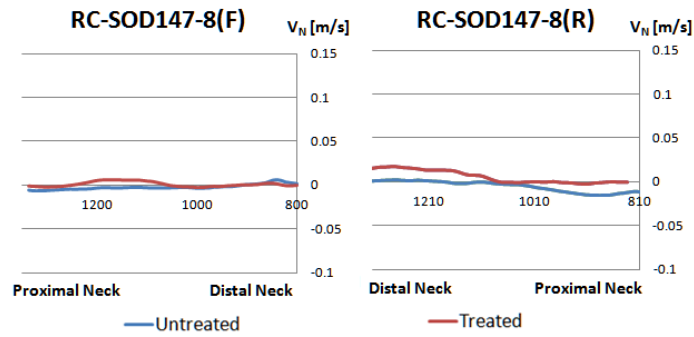


Figure 3-32. The normal velocities across the neck of the aneurysm at the center plane are shown for the two flow domains with a radius of curvature of approximately 6mm. The figures are aligned with the orientation of the planar velocity contours plots. For example, the distal neck is on the right side for RC-SOD147-8(F) for both the contour plot in Figure 3-31, and the normal velocity plot of this figure.

The large radius of curvature of the RC-SOD147-9 domain effectively redirected the momentum of the incoming fluid in the forward direction. The fluid was traveling in a near horizontal direction before impacting the distal neck. Interestingly, placement of the flow diverter appeared to have little effect in reducing normal velocities along the neck. Figure 3-33, however, illustrates that the jet inside the aneurysm is more dispersed after placement of the flow diverter. In the reverse direction, the placement of the flow diverter had a very significant effect, nearly eradicating all of the flow entering the aneurysm.

	Planar Velocity Magnitude		Normal Velocity	
	Untreated	Treated	Untreated	Treated
Range [m/s]	0 – 1X Inlet V	0 – 0.1X Inlet V	+/- 0.1X Inlet V	+/- 0.1X Inlet V
Color	Blue → Red	Blue → Red	Blue (-ve) → Red	Blue (-ve) → Red
RC-SOD147-9(F)				
RC-SOD147-9(R)				

Figure 3-33. The planar and normal velocity contours are shown at the center plane of the RC-SOD147-9(F) and (R) domains.

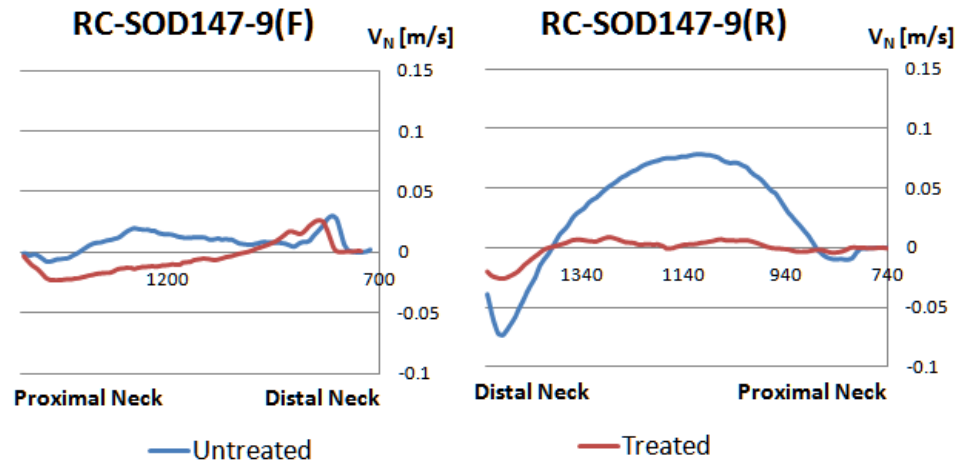


Figure 3-34. The normal velocities across the neck of the aneurysm at the center plane are shown for the two flow domains with a radius of curvature of approximately 8mm. The figures are aligned with the orientation of the planar velocity contours plots. For example, the distal neck is on the right side for RC-SOD147-9(F) for both the contour plot in Figure 3-33, and the normal velocity plot of this figure.

3.3.3. Intraaneurysmal Flow in Short, Wide Necked Aneurysms

The two glass models of the RC-SOD68 series were manufactured at a different time than the RC-SOD147 series. The neck length to parent artery diameter ratios for the glass models of the RC-SOD68 series were higher overall. The planar and normal velocity contour diagrams for the center plane are shown in Figures 3-35. The normal velocities across the neck of the aneurysm at the center plane are plotted in Figure 3-36. Representative images of the shapes of the flow diverters in flow domains are in Appendix A.

In RC-SOD68-1, a very strong jet of fluid entered the untreated aneurysm. The flow diverter placed in the parent artery protruded fairly deeply into the aneurysm due to the wide neck, but flow was nevertheless significantly reduced. In RC-SOD68-3, the presence of the flow diverter moved the location of the entering jet away from the distal aneurysm wall, relieving it of high wall shear stresses that increase the risk of aneurysm rupture.

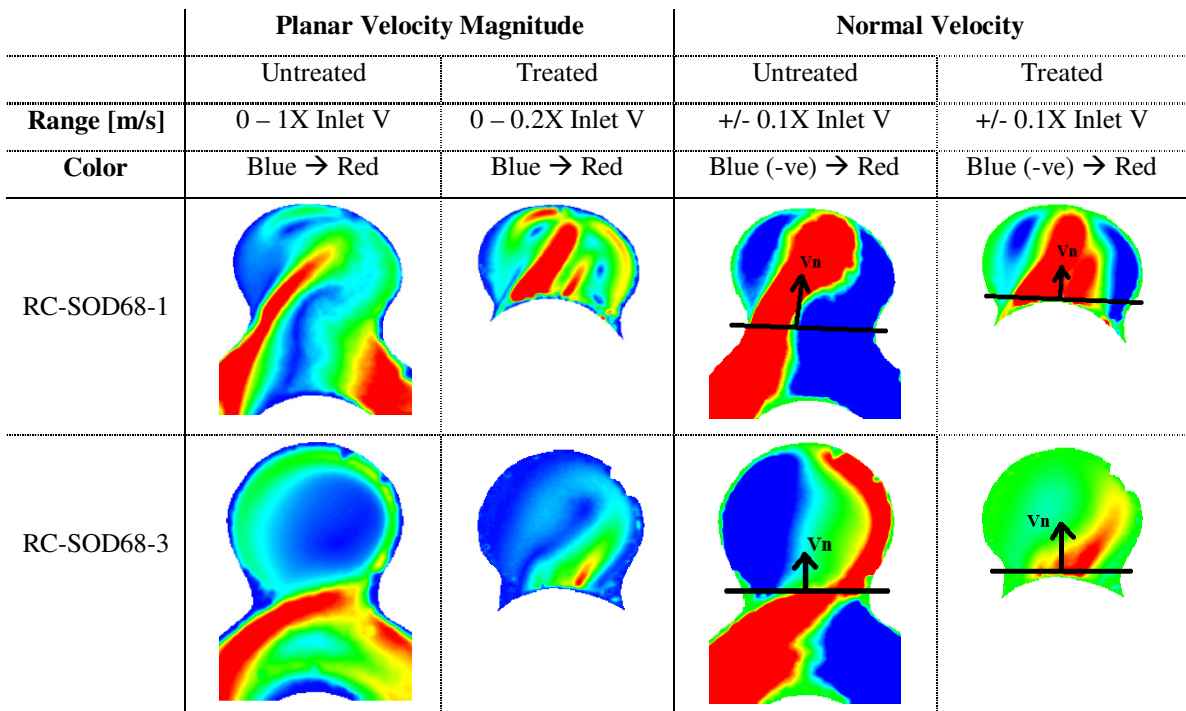


Figure 3-35. The planar and normal velocity contours are shown at the center plane of the RC-SOD68-1 and -3 domains.

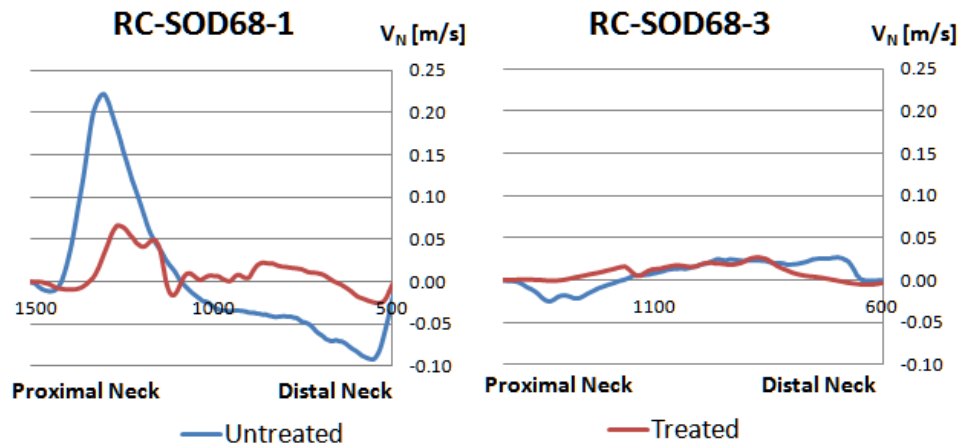


Figure 3-36. The normal velocities across the neck of the aneurysm at the center plane are shown for the two flow domains with relatively wide necks. The figures are aligned with the orientation of the planar velocity contours plots. For example, the distal neck is on the right side for RC-SOD68-1 for both the contour plot in Figure 3-35, and the normal velocity plot of this figure.

3.4. DISCUSSION OF BENCHTOP EXPERIMENTS

PIV is a labor and computationally intensive process. Unlike computer simulations where flow structures can be interrogated along any plane inside the solution domain with a post-processing program, a series of images need to be acquired at every single plane of interest for PIV. On average, computer simulation of steady flow in one domain may take one hour of labor for set up and four hours of computational time. Interrogation at each plane will take five minutes. Conversely, image acquisition at each plane for PIV takes 15 minutes of labor and three hours of computational time. If 10 – 15 planes of the flow domain are of interest, the efficiency of CFD rapidly becomes indisputable.

Balancing parameters of experimental design is difficult, particularly when actual sized devices are used as test articles. Two dimensional PIV, which was used in this body of research, is unable to account for out of plane motion. The thickness of the laser sheet is set to strike a balance between errors due to loss of particles if the laser sheet is too thin, and errors introduced by out of plane motion if the laser sheet is too thick. Errors are also introduced into the system due to inaccuracies of the camera and the rotational and translational stages that the glass models are mounted upon. The most straightforward solution in other experiments would be to enlarge the flow domain. In other words, aneurysm models scaled to a larger size allow for greater flexibility in the design of fixtures and other equipment configurations. However, manufacturing processes were not available for scaling up the flow diverter, or test article, of interest. Therefore, there was little flexibility in the experimental set up.

The density of the working fluid and the particles must be matched in future experiments. The background research discussed in Chapter 2 listed various fluid mixtures for conducting experimental studies. However, most are tailored towards matching the density and viscosity of blood, and not the density of the reflective particles. In the PIV experiments conducted in this body of research, the overriding concern was to match the index of refraction of the glass to the flowing fluid because the high degree of curvature meant index mismatches would lead to distortion of the laser sheet. In the typical PIV experiment of aneurysms, there is sufficient intraaneurysmal flow for the particles to track with the moving fluid. However, the flow diverter was so effective in most scenarios that the difference in densities started introducing errors into the measurements.

The significant reduction in flow rate by means of the Pipeline Embolization Device also leads to accumulation of reflective particles on the glass model wall, which obfuscates measurements.

Microscratches on the glass surface may lead to the accumulation of reflective particles over time, as illustrated in Figure 3-37. The reflective film diffuses the incoming laser sheet, leading to poorly illuminated particles inside the aneurysm. The film also reflects a lot of the laser energy into the camera, potentially damaging its internal circuitry.



Figure 3-37. The stagnant fluid inside the aneurysm after placement of the flow diverter leads to an accumulation of the reflective particles. The white film prevents particles inside the aneurysm from being illuminated by the laser sheet. The white film also reflects a lot of the laser energy directly into the camera, potentially damaging the internal circuitry. When measurements can no longer be reliably taken, the flow diverter is removed and the film dispersed with manual agitation. Since placement of the flow diverter is a time consuming process and the exact deployment configuration can not be re-established, measurements are taken as quickly as possible.

The irregularities in neck geometry and parent artery curvature reaffirm that using PIV for verification and CFD for establishing trends is the correct approach. As illustrated in the geometries reconstructed using Mimics, glass blown models do not faithfully represent the requested dimensions. While slight deviations from a spherical aneurysm bulb may have a minor effect on intraaneurysmal flow, the geometry of the aneurysm neck is of extreme importance. For example, results from RC-SOD147-6 and RC-SOD147-12 were meant to be compared with each other in order to determine the effect of the aneurysm location along the bend of the parent artery. Closer inspection of the glass models pointed to drastically different neck dimensions (3.8mm and 6.1mm respectively). Therefore, it is difficult to draw conclusions from changes in intraaneurysmal flow when multiple geometric parameters are varied at the same time.

Out-of-plane movement requires that verification of CFD simulations be based on PIV data collected across the entire neck and not just at the mid-plane or a few select planes. Examination of the PIV results indicated that there was a lot of fluid movement away from the center plane of the aneurysm. It appeared that fluid would predominantly enter the aneurysm near the center of the neck, and wash out of the aneurysm near the edges of the aneurysm neck. To better understand the effect of the flow diverter, simply comparing the flow profiles at the center plane of the aneurysm is not enough.

A broader metric, the total flow entering the aneurysm, also requires PIV data collected across the entire neck. This broader metric allows for a simpler determination of flow diverter effectiveness across a wider range of aneurysm and parent artery geometries.

Silicone models should be used for a more realistic wall apposition of the flow diverters. Silicone models may also allow for variation of just one geometric variable at a time. The walls of the blood vessel are not rigid. They slightly contract and expand with each heartbeat. The support structures surrounding the neurovasculature are also somewhat compliant. Vessels straighten out a bit when stents and flow diverters are deployed in the human vasculature. Therefore, future testing should be conducted in thin walled silicone models to mimic this behavior. The manufacturing method for silicone models also allows for better reproducibility. The core molds, as described in Figure 2-30A, are typically rapid prototyped before application of a silicone layer, thereby more faithfully reproducing the internal geometry. In contrast, glass blown aneurysms require some artisanal flair and are difficult to control and replicate.

Proper deployment mechanisms are also needed to ensure the pore shape is clinically relevant. When the Pipeline Embolization Device was dragged into place for the PIV experiments, the pores were stretched. The device was gently wiggled back and forth at the aneurysm to release any built up tension before releasing it from the kidney stone retriever. Inspection of the diamond shaped pores in the PIV images didn't reveal obvious signs of abnormal stretching. However, it is unknown how well the final shape mimics that of a device deployed conventionally by means of a catheter by a physician. One possible method for acquiring such information clinically could be through IVUS or OCT imaging of the flow diverter after it has been deployed across the aneurysm.

Even with resolution of all previously described experimental complications, assessment of intraluminal flow is not possible. The opaque metal filars block the laser sheet. The filars also block particles from being observed by the camera, as illustrated in Figure 3-38. Formation of a coherent fibrous layer on the surface of the flow diverter is the final stage of healing and is influenced by the flow of blood in the near vicinity of the braided mesh. Therefore, potential issues due to the design of the braid must be elucidated from computer simulations.

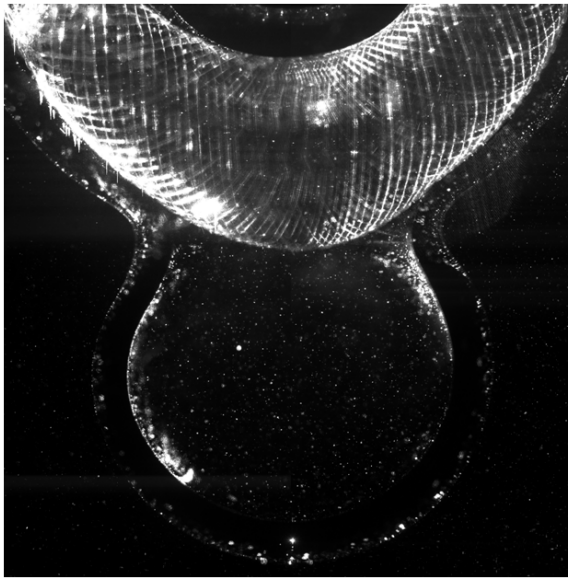


Figure 3-38. The opaque metallic filars of the flow diverter interfere with flow visualization inside the parent artery lumen.

CHAPTER 4: *IN SILICO* SIMULATIONS

4.1. SPECIFIC AIMS OF *IN SILICO* SIMULATIONS

The main objectives for the numerical simulation studies are to:

1. Develop a technique for modeling the complex geometry of the perforations (diamond shaped pores) of the Pipeline Embolization Device (PED) through which blood flows from the parent artery into the aneurysm.
2. Verify the perforation modeling technique using results from the PIV experiments.
3. Predict the effectiveness of the PED in a range of flow domains with idealized geometries.
4. Predict the effectiveness of the PED under exercise conditions.

In order to achieve these objectives, the simulation plan shown in Figure 4-1 was executed.

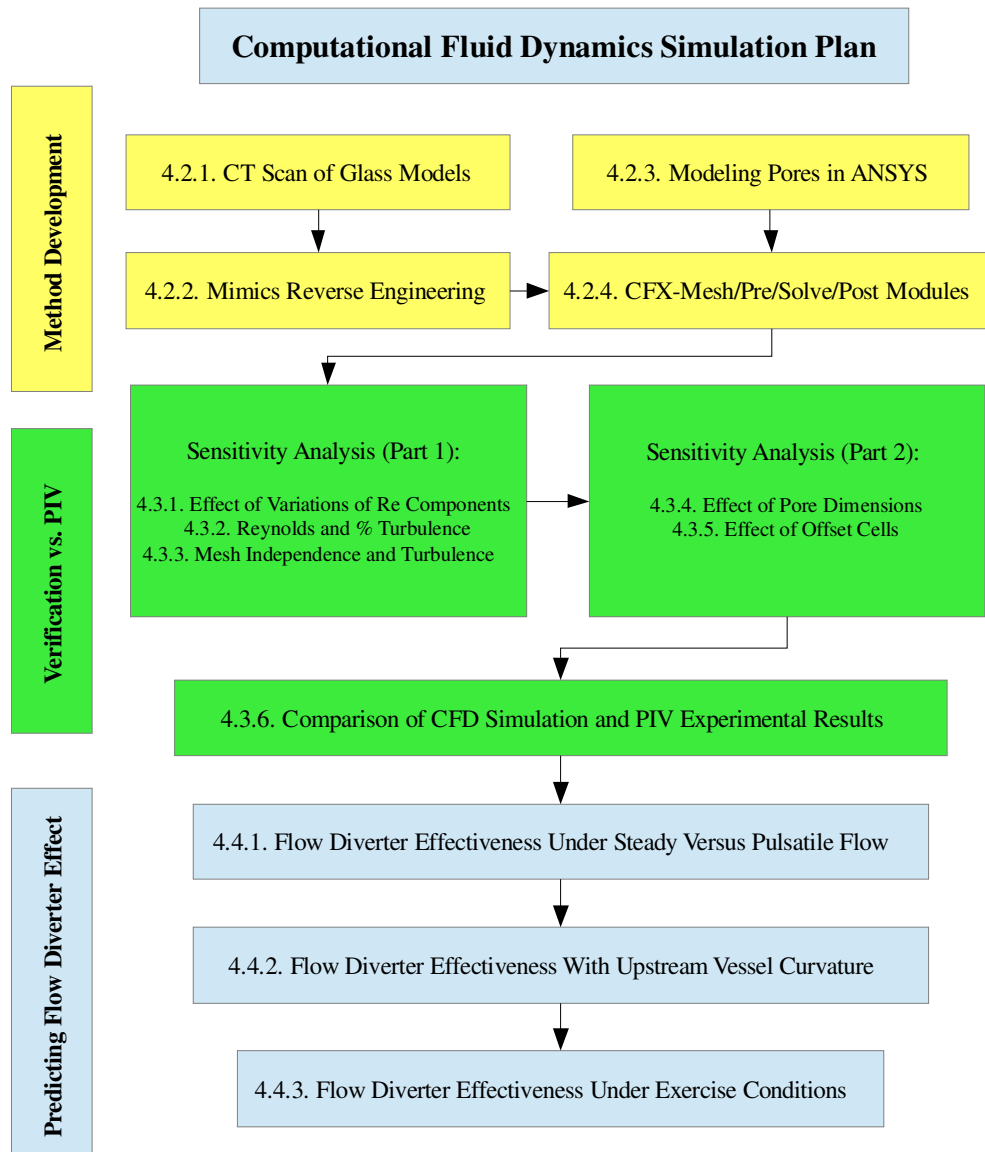


Figure 4-1. The simulation research consisted of learning how to use commercially available software to define the flow domain and flow diverter, to conduct a sensitivity analysis and verification using experimental data, and to predict the flow diverter performance in idealized geometries. The subchapter numbers in which these issues are discussed are shown.

4.2 APPLICATION OF COMMERCIALY AVAILABLE SOFTWARE

INTRODUCTION

Several commercially available software programs were used to conduct the computational fluid dynamics (CFD) simulations. Since the research was being applied towards the commercial development of a medical device, it was deemed unnecessary and more arduous to write and validate customized code in accordance with the various regulatory bodies, which would review the design dossier as part of the product approval process.

Idealized geometries with perfectly characterized dimensions were created using a computer assisted drafting (CAD) program called Solidworks. Actual geometries, such as those of the glass models used in the PIV experiments or of the aneurysms created in the rabbit model, were reconstructed from computed tomography, or CT, scans using the Mimics program by Materialize. Pores, or channels, through which fluid passes through the flow diverter into and out of the aneurysm were modeled in the Design Modeler module of the ANSYS computer aided engineering (CAE) program. The problem domain is then set up by combining the geometric and flow information in the CFX-Pre module of ANSYS. Post-processing was done with the CFX-Post module of ANSYS.

A more detailed explanation of how these different pieces of commercially available software are applied is in the following sections of Chapter 4.2. A flowchart summarizing the flow of data files is presented at the end.

4.2.1. CT Scan of Glass Models

The exact geometries of the glass models, previously described in the PIV experiments, were desired in order to accurately model the intraaneurysmal flow in the CFD simulations. Initially, the glass models were packaged together (see Figure 4-2) and scanned with equipment available at the Fairview Hospital on the University of Minnesota campus. The CT scanner's (Siemens Somatom Flash) finest resolution was 0.37 mm x 0.37 mm x 0.6mm. As shown in Figure 4-3, it was quickly determined that this scan resolution was insufficient to capture the curvature of the vessel circumference and the curvature of the aneurysm.

Therefore, the glass models were scanned at a company called North Star Imaging which offered industrial grade micro CT scans, or μ CT, with resolutions down to 50 μ m x 50 μ m x 50 μ m using a combination of longer irradiation times and stronger x-rays, which cannot be tolerated by living organisms. As shown in Figure 4-4, the much finer resolution allowed for an accurate reconstruction of the curvature.



Figure 4-2. The glass models were packaged together in order to reduce the number of scans necessary. Labels were placed on the glass models (not shown) to distinguish the inlet from the outlet.

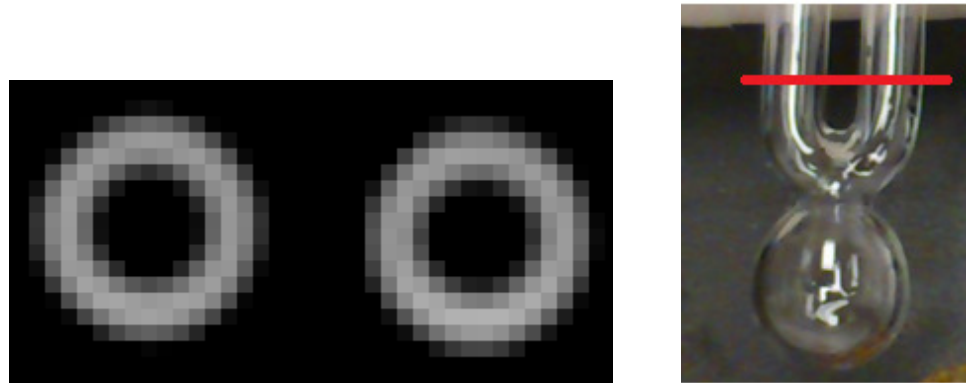


Figure 4-3. The CT scan generates a series of images or slices. The preferred orientation is the axial view, where the cross-sections of the upstream and downstream legs of the glass aneurysm are observed. A zoomed-in view of the scan performed at Fairview Hospital is shown on the left. The glass is radiopaque due to its slight lead content and shows up as white/gray. The two circles are the walls of the inlet and outlet legs of the glass model. The approximate location of the image on the left is illustrated by the red line on the right.



Figure 4-4. A slice of the μ CT scan performed at North Star Imaging is shown. The pixel size is significantly less than that from the hospital-grade scan done at Fairview Hospital. The slice thickness (distance between images) is also significantly reduced, from 600 μ m down to 50 μ m, allowing for better resolution and subsequent reconstruction of the curves of the aneurysm and the parent vessel.

4.2.2. Mimics Reverse Engineering by Materialize

Materialize provides a number of different software suites to convert the image sequences generated by various acquisition methods into solid models in a format that could be used for many purposes. These purposes include computer-aided engineering (via finite element analysis for solid mechanics or computational fluid dynamics for fluid mechanics), manufacturing of duplicate geometries, surface and volume calculations, and other applications. Computed tomography (CT) and magnetic resonance imaging (MRI) are two very common image acquisition techniques in the medical field. Due to cost and availability, CT was chosen to characterize the geometries of the glass models used in the PIV experiments and the aneurysms created in rabbits.

In the Mimics core module, the image stack from the CT scan is loaded. After identifying the spatial orientation of the scanned object (see Figure 4-5), the walls of the glass model are defined based on the brightness level of the pixels (see Figure 4-6). Reference to Figures 4-3 and 4-4 shows why the resolution of the scan is important. Large pixels with poorly defined edges demarking the edges of the wall lead to an inaccurate reconstruction of the highly curved aneurysm neck and parent vessels.

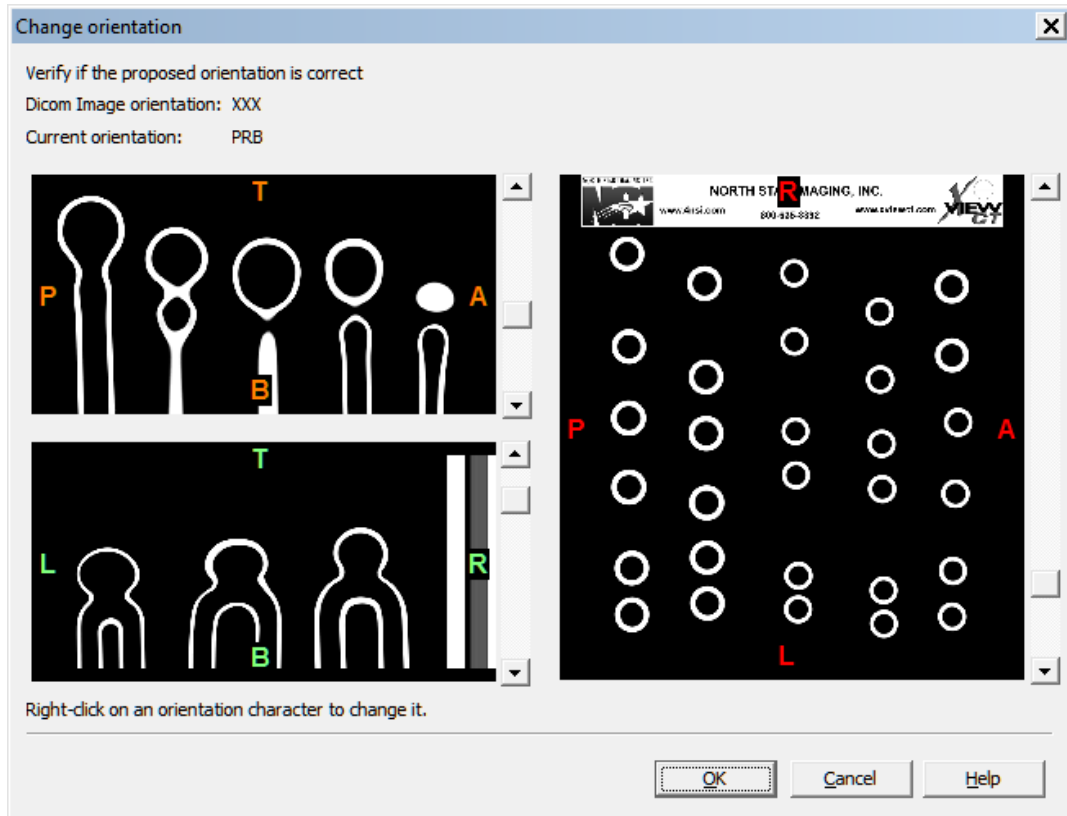
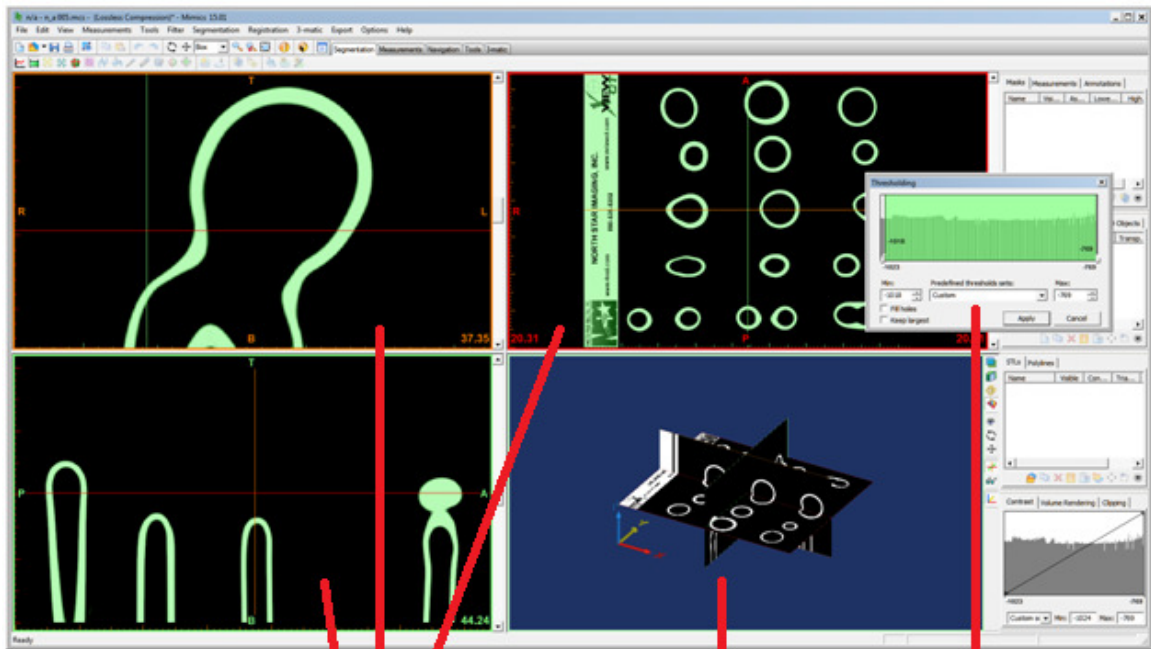


Figure 4-5. When the stack of images from a CT or MRI scan is imported into Mimics, the user is prompted to confirm the orientation of the scanned object by identifying the anterior (A), posterior (P), left (L), right (R), top (T), and bottom (B) orientations.



View of image stack from the x, y, and z orientations

3D rendering of intersecting planes

Range of grayscale values selected

Figure 4-6. A screenshot of the Mimics core module is shown with the image stack from the μ CT scan loaded. A green mask was defined with grayscale values a slightly above the minimum level to exclude the air (black).

After the walls of the glass model are defined, the cavities are designated as the flow domains (see Figure 4-7). The individual flow domains are then smoothed to remove the harsh edges caused by the extremely small pixel size from the μ CT scan (see Figure 4-8). Each individual flow domain is then exported into a separate Mimics module called Reverse Engineering. Another smoothing step is applied to further simplify the surface topology for less complex flow behavior at the wall. Minor adjustments to the orientation of the flow domains (see Figure 4-9) are then applied to make data analysis and comparison to the CFD results easier.

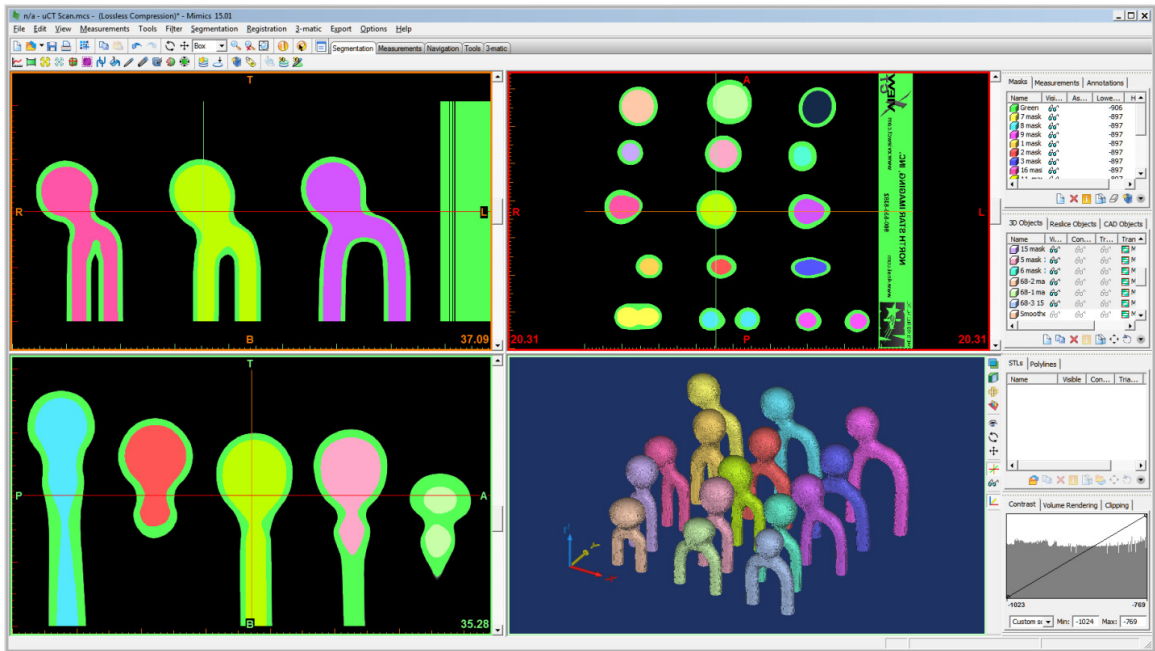


Figure 4-7. The cavities contained by the green mask, described in Figure 4-6, are individually filled and defined as the flow domain of the glass models. A 3D rendering of the twelve glass models is shown at the bottom right corner.

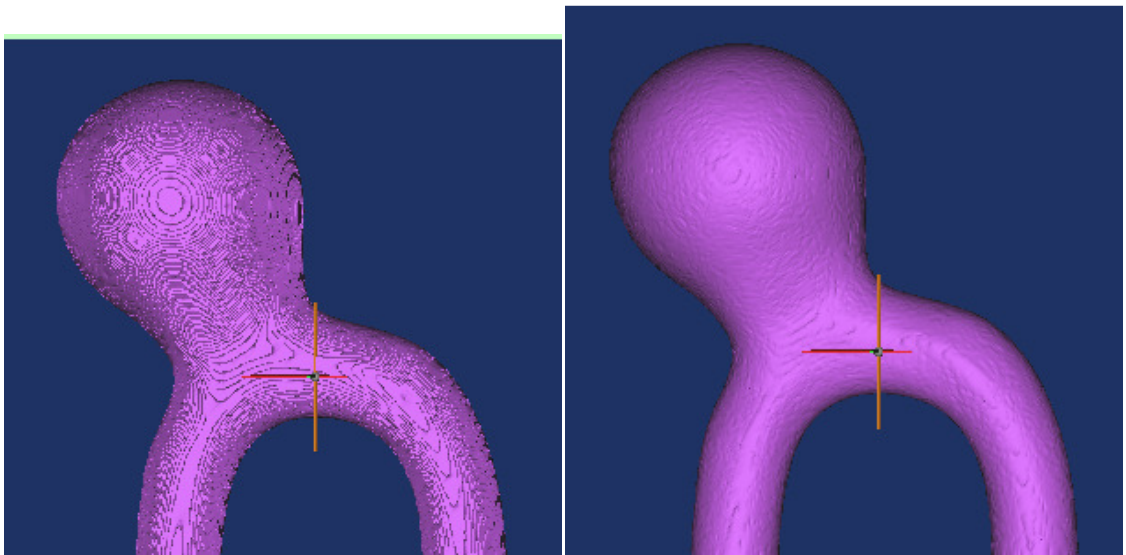


Figure 4-8. Due to the high resolution of the μ CT scan, sharp ridges are created in the 3D reconstruction of the flow domain, as shown at the left figure. Smoothing operations are applied to simplify the surface texture, as shown on the right figure, and to bring the computer generated geometry closer to reality, where the walls of the glass models are smooth.

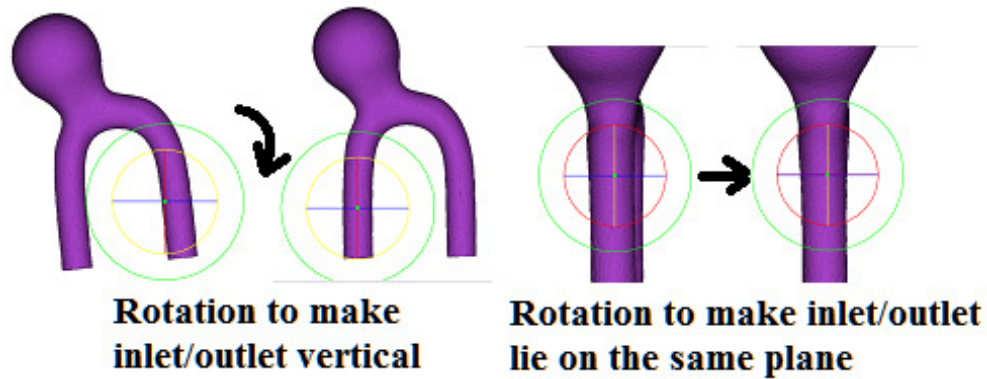


Figure 4-9. The glass models were packaged to minimize the rotational offset of the glass models with respect to the x, y, and z vectors. However, minor corrections were needed to make the after-simulation data analysis simpler. For example, the inlet and outlet legs would typically be several degrees away from vertical. Rotation allows for easier geometry generation of the inlet and outlet legs, which were not captured in the μ CT scan. The inlet and outlet legs would also typically be a degree or two away from lying flat on the XY plane. Rotation allows for easier definition of the plane bisecting the aneurysm for comparing velocity contour diagrams.

4.2.3. Modeling Pores in ANSYS Design Modeler

The flow diverter inside the glass model was modeled as an array of diamond shaped structures connecting the parent artery to the aneurysm. Briefly,

1. The glass model reconstructed in Mimics was imported into Design Modeler.
2. A thin slice of material was removed, temporarily separating the aneurysm from the parent artery.
3. Diamond shaped structures representing the pores of the flow diverter were arrayed across the aneurysm neck.
4. Excess diamonds were removed.
5. All individual components were merged into one for ease of defining the numerical mesh.

Figure 4-11 illustrates the five steps listed above. Slightly different merging methods for step five were used in chapters 4.3 and 4.4. After additional research, the perforation pattern of chapter 4.4 included partial diamonds at the edge of the neck surface, as illustrated in Figure 4-10.

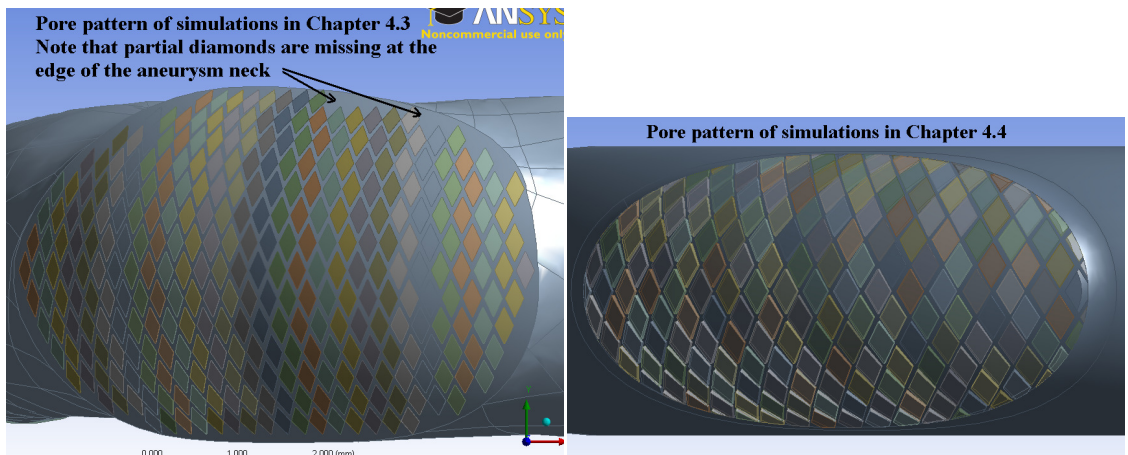


Figure 4-10. The pores near the edge of the aneurysm neck in the initial computer simulations, discussed in Chapter 4.3, were omitted (**left**). Additional research into geometry manipulation methods allowed for the inclusion of partial diamonds at the edge of the aneurysm neck and were applied towards simulations discussed in Chapter 4.4 (**right**).

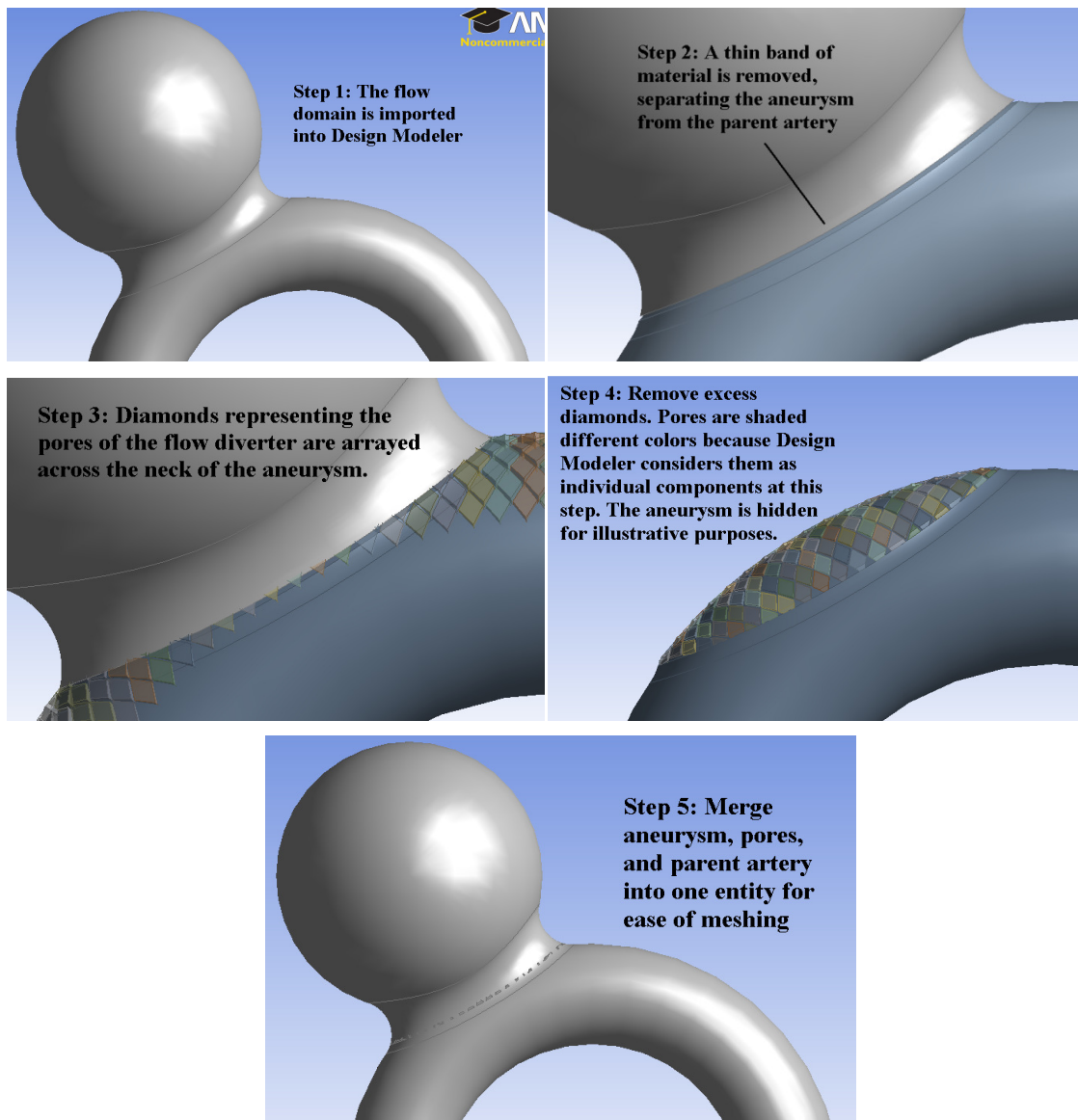


Figure 4-11. The 5 steps for modeling the flow diverter inside the fluid domain are shown.

4.2.4.1 Creation of the Numerical Mesh in the Flow Domain Using CFX-Mesh

The flow domain is imported into CFX-Meshing and the numerical mesh is generated. Briefly, the flow domain is divided into a large number of very small volumes, or elements. Relevant physical equations are balanced between neighboring elements. Since a fluid analysis is conducted, the three-dimensional Navier-Stokes equations expressing Newton's Second Law and the conservation of mass equation are discretized throughout the network of elements to create a highly coupled, non-linear set of algebraic equations.

The ‘quality’ of the mesh refers to whether the size and distribution of elements was deployed in such a manner that the movement of fluid is accurately calculated. A “mesh independence” study is typically conducted where numerical meshes of increasing density, or refinement, are solved. If little or inconsequential differences are observed, then the numerical mesh is considered to be good.

The reconstructed geometry of the glass models consisted of complex surfaces. Figure 4-12 illustrates how virtual cells were created by merging individual surfaces. Some accuracy in geometry was lost, but the creation of the numerical mesh was greatly simplified. Parameters such as maximum element size or inflation layers are then imposed, as illustrated in Figure 4-13. Special attention was paid to the diamonds connecting the aneurysm to the parent artery. Since the flow entering the aneurysm was of particular interest, the mesh needed to be of sufficient resolution to accurately calculate the flow of fluid through the flow diverter. Figure 4-14 illustrates one of the meshes created in the course of this research. The volume bounded by the black lines is an element.

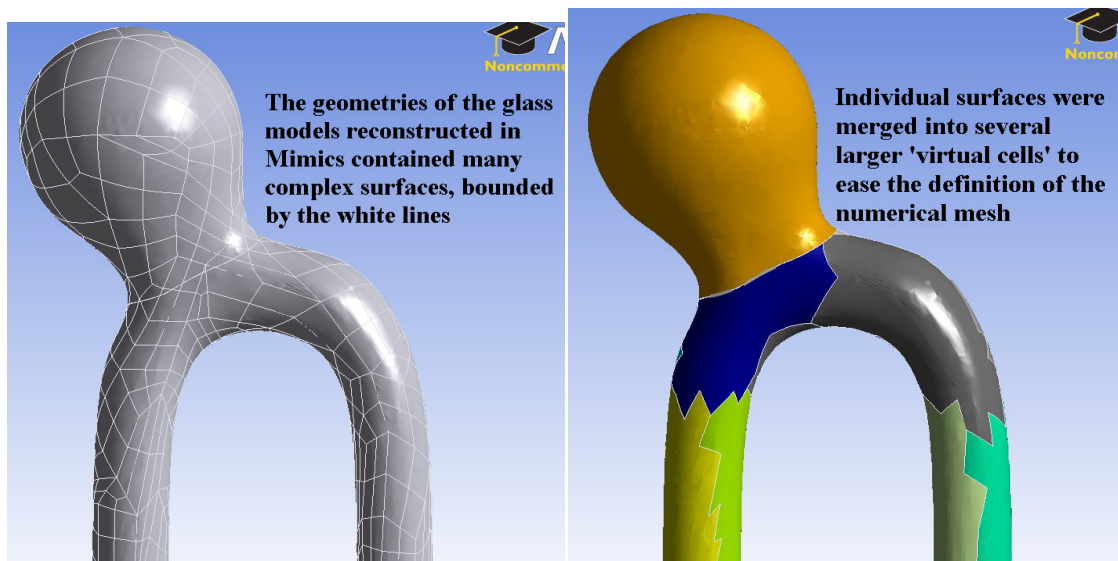


Figure 4-12. (Left) Geometries of the glass models reconstructed using Mimics contained many complex surfaces. Each individual surface was bounded by white lines. **(Right)** Virtual cells were created by merging surfaces to reduce the complexity of the numerical mesh.

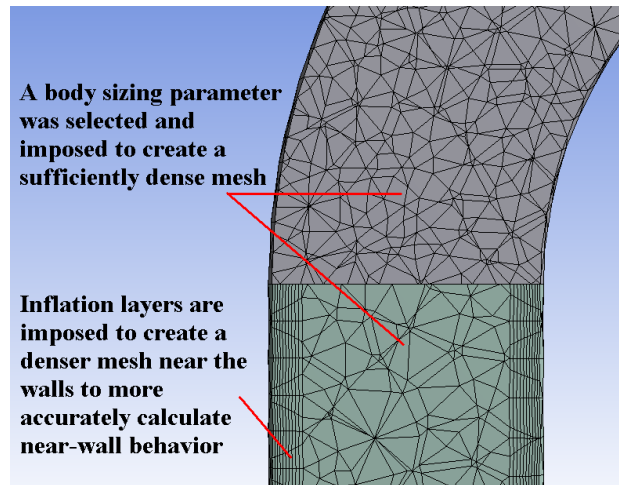


Figure 4-13. The density of the numerical mesh can be controlled by imposing inflation layers and body sizing. Judicious application of these size controls lead to computationally efficient meshes that are sufficiently dense only in locations of great interest or variability in fluid behavior.

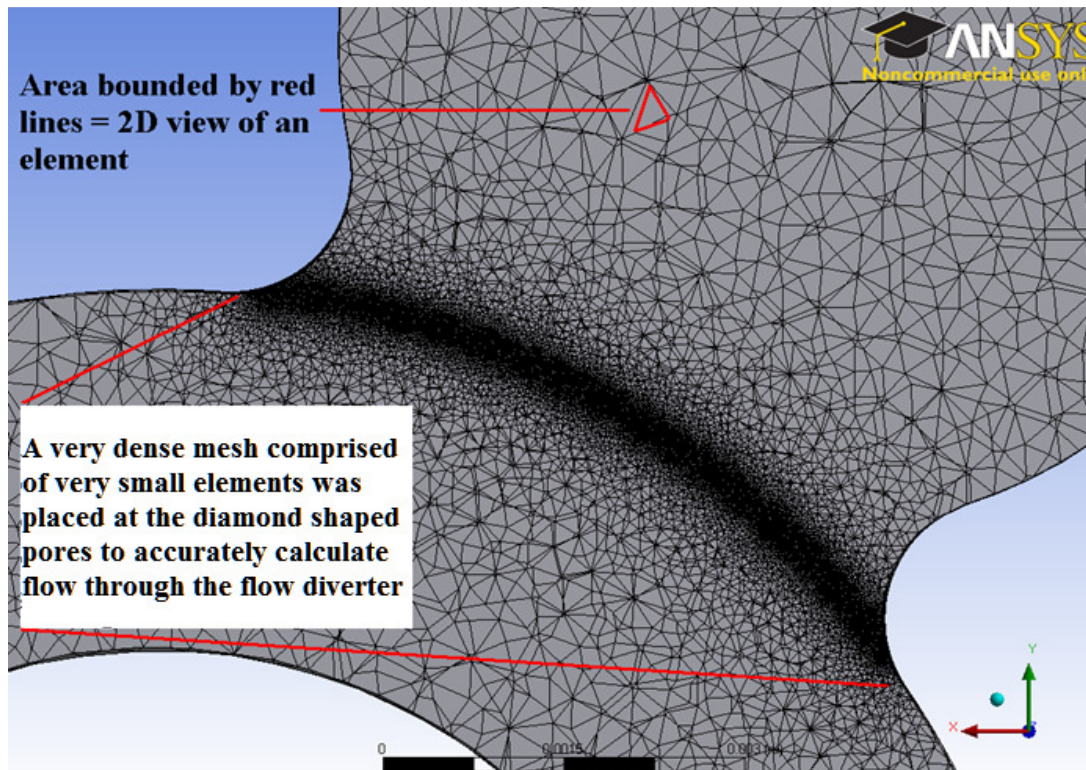


Figure 4-14. A very dense mesh is located at the aneurysm neck when a flow diverter is present in the model. The small elements allow for accurate calculation of fluid flow through the flow diverter into and out of the aneurysm.

4.2.4.2. Defining and Solving the Simulation in CFX-Pre and CFX-Solve

The following parameters are defined in CFX-Pre with values particular to a given simulation:

- The physical properties of the flowing medium (ex. the density and viscosity of blood)
- The type of simulation to be performed (ex. a transient simulation with solver steps every x seconds)
- The heat transfer model (ex. none) and turbulence model (ex. laminar) in the fluid domain
- The location and properties (ex. inflow rate) of the boundary conditions (inlet, outlet, and wall surfaces)
- The target root mean square (RMS) value of energy and momentum residuals, which are an indicator of the convergence (or error) of the solution
- The flow metrics of interest to be saved in the results file (ex. average wall shear stress on the aneurysm wall)

Figure 4-15 illustrates the interface in the CFX-Pre program for a particular simulation. A definition file (.def) is created by CFX-Pre. Solver parameters such as the number of CPU cores and distributed computing are defined in CFX-Solve. A results file (.res) is produced when the solution is converged.

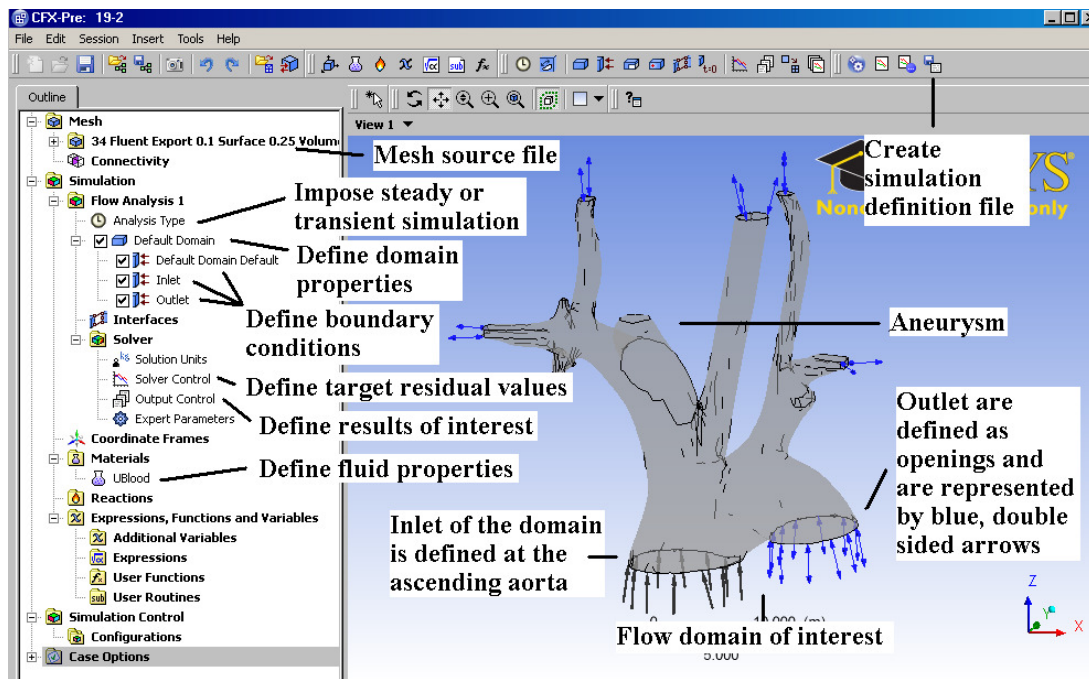


Figure 4-15. The interface in CFX-Pre is shown. The geometry of the rabbit aorta and artificial aneurysm from rabbit 34 is loaded for illustrative purposes. The locations for defining the different simulation parameters are labeled.

4.2.4.3. Extracting Figures and Flow Metrics of Interest in CFX-Post

CFX-Post is a post-processing program for visualizing fluid structures and calculating metrics of interest, such as the average fluid velocity on a plane. Figure 4-16 illustrates the interface in the CFX-Post program after the .res results files for a particular simulation was imported. Streamlines originating from the heart and streamlines crossing the neck of the aneurysm are shown.

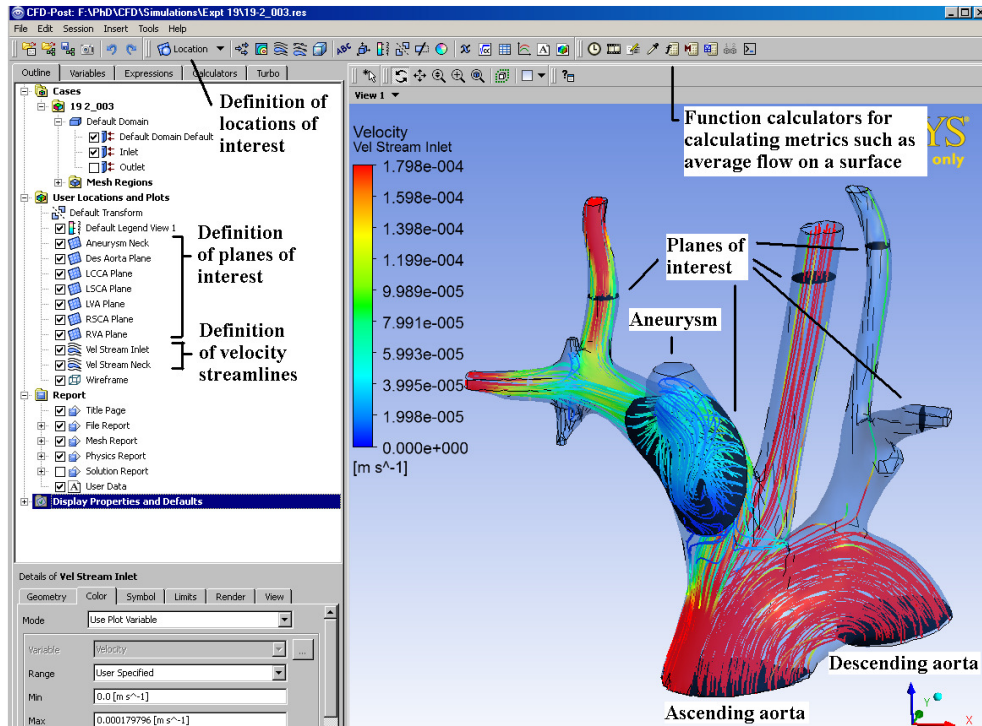


Figure 4-16. The interface in CFX-Post is shown. The geometry of the rabbit aorta and artificial aneurysm from rabbit 34 is loaded for illustrative purposes. The locations for defining the different simulation parameters are labelled.

SUMMARY

A summary of the inputs and outputs at various stages along the simulation process are presented in Figure 4-17.

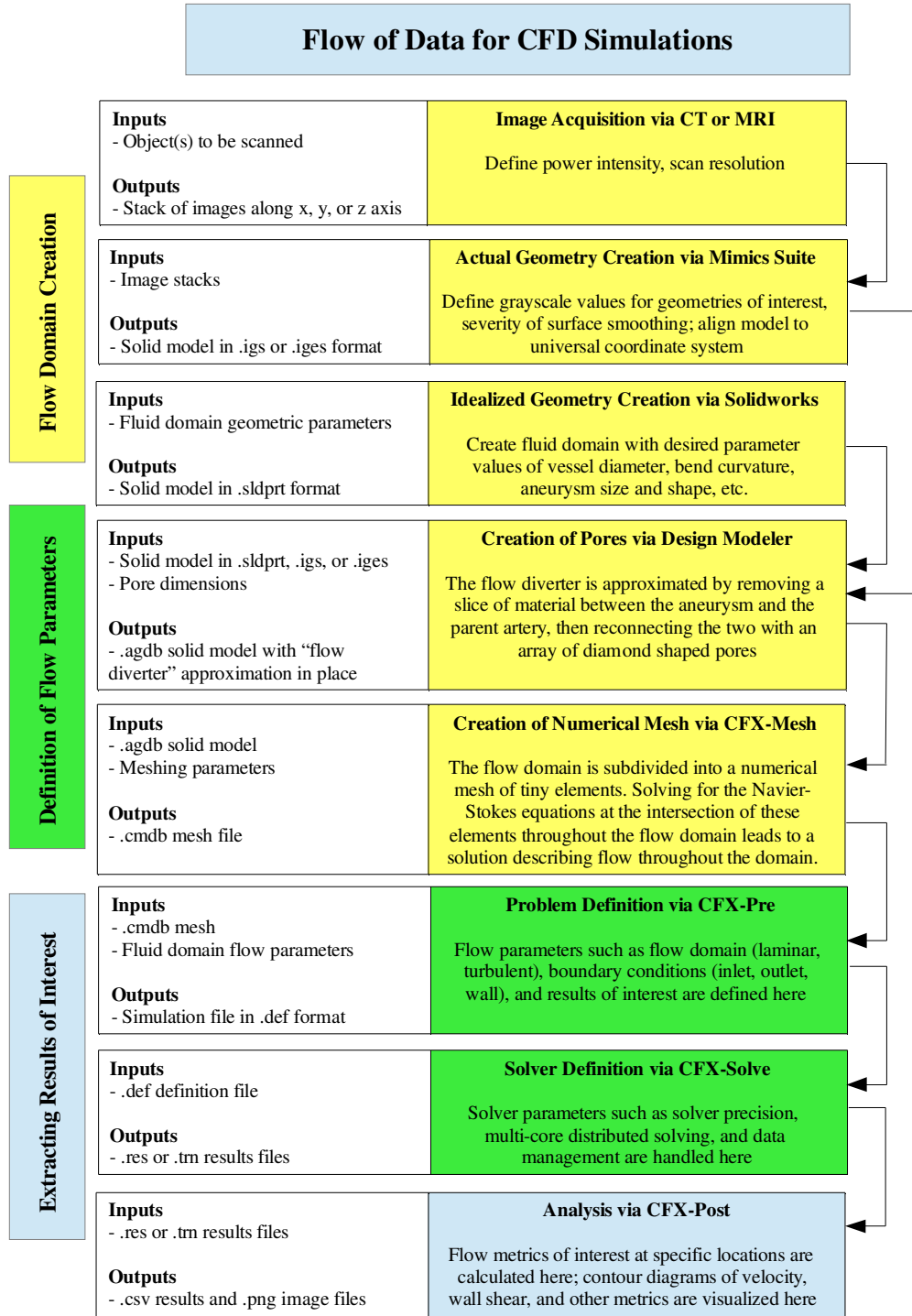


Figure 4-17. The flow of information in a CFD simulation is shown.

4.3 VERIFICATION OF CFD RESULTS BY MEANS OF PIV RESULTS

INTRODUCTION

This chapter discusses the research that was conducted to develop and verify the computation technique such that it is sufficiently accurate to predict the performance of the flow diverter. Two of the glass models from the PIV experiments were selected for this effort as they represented the “average” aneurysm and parent artery found in the neurovasculature. Computational simulations were conducted and results compared with those from the PIV experiments.

METHOD

Flow Domains

The two glass models selected for the verification work are RC-SOD147-6 and RC-SOD147-12. Figure 4-18 illustrates the shape of the parent arteries and aneurysms based on the 3D reconstruction of the microCT scan. Figure 4-19 illustrates that when the aneurysm is biased away from the inlet, the flow domain is named RC-SOD147-12(F). When the aneurysm is biased towards the inlet, the flow domain is name RC-SOD147-12(R). When an observation is present in both the forward and reverse cases, the flow domain may also be referred to as RC-SOD147-12(F/R).

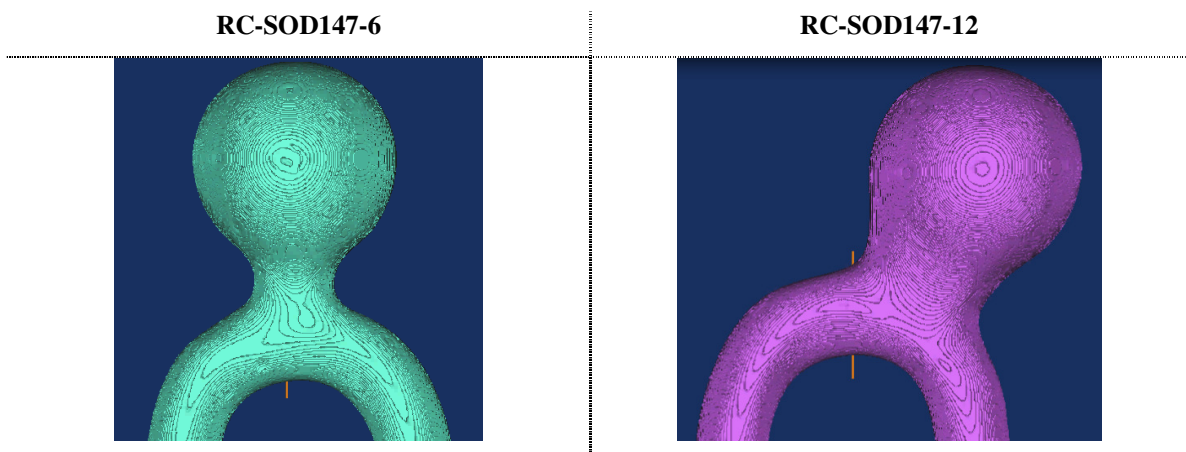


Figure 4-18. The 3D reconstructions of the flow domains inside glass models RC-SOD147-6 and RC-SOD147-12 are shown.

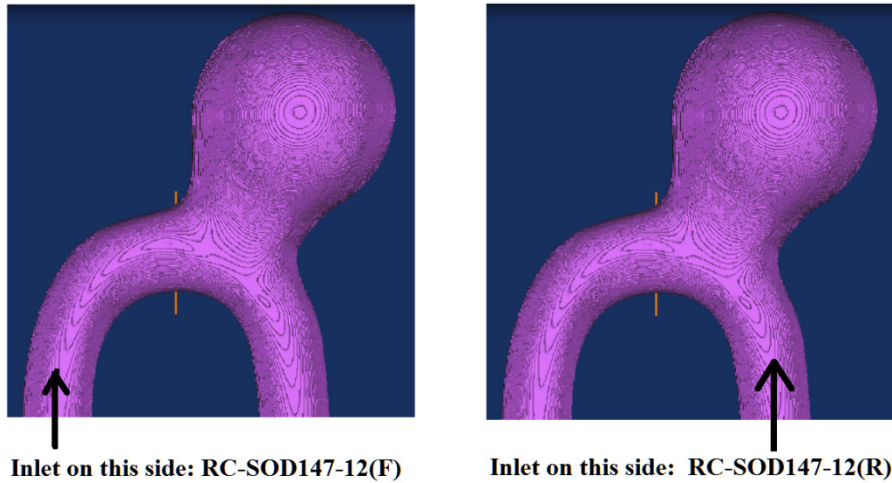


Figure 4-19. When the aneurysm is biased away from the inlet, it is referred to as RC-SOD147-12(F). When the aneurysm is biased towards from the inlet, it is referred to as RC-SOD147-12(R).

Simulation Plan

The verification excerpt of the CFD simulation plan is shown in Figure 4-20. It is broken up into three sections. The first section examines the effect of variables imposed on the flow domain, such as the turbulence model (if any), the fluid properties, and the precision of the numerical mesh. The second section examines the effect of variables that are more closely tied to the geometry of the flow diverter, namely the effect that pore dimensions have on the flow entering and exiting the aneurysm. Lastly, results from the CFD simulations will be compared to those obtained from the PIV experiments to determine if the simplifications and geometric models used in the simulations sufficiently capture the effect of the flow diverter. Heat transfer did not occur in the solution domain.

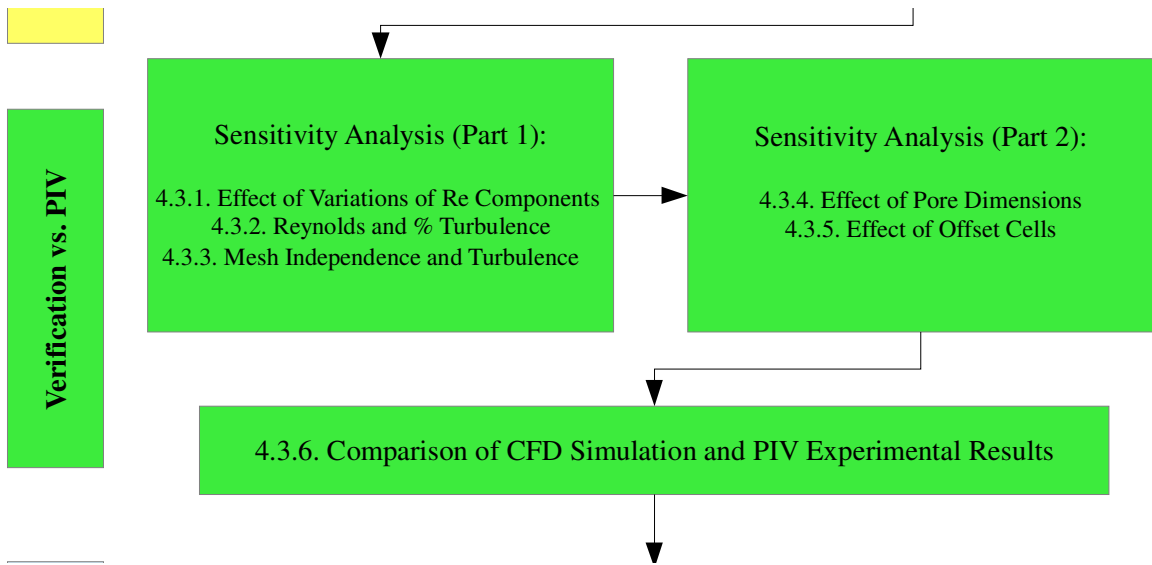


Figure 4-20. The verification excerpt is taken from the CFD simulation plan. Chapter 4.3 can be broken down into three components: sensitivity of fluid behavior due to parameters related to flow domain and the numerical mesh, sensitivity due to parameters related to the geometry of the flow diverter, and comparison of results from CFD simulations and PIV experiments.

Flow Metrics of Interest

Three primary results were of interest:

1. The velocity profile mapped at the plane approximately bisecting the aneurysm as shown in Figure 4-21.
2. The flow rate of fluid entering and exiting the aneurysms, calculated at planes roughly defined at the aneurysm necks, as illustrated in Figure 4-22.
 - The flow rate into the untreated aneurysm may be referred to as Q_{UT}
 - The flow rate into the treated aneurysm after placement of the flow diverter may be referred to as Q_T
3. The ratio of fluid entering the aneurysm before and after the placement of the flow diverter: Q_T/Q_{UT} .

These three metrics were deemed sufficient for obtaining a general understanding of the fluid flow entering the aneurysm, while providing a quantitative metric to compare the effectiveness of the flow diverter.

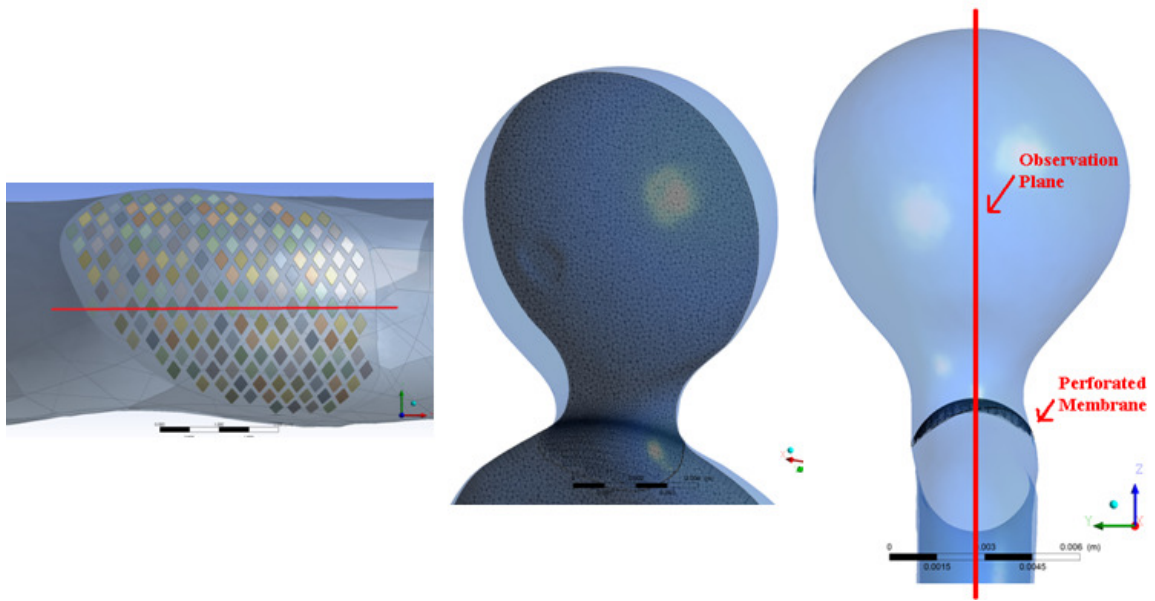


Figure 4-21. **Left:** A view of the pores (colored diamonds) that connect the parent artery (shaded gray, underneath pores) to the aneurysm (not shown). An observation plane is generated at the red line projected in and out of the page. **Middle:** An isometric view of the observation plane that approximately bisects the aneurysm. The thin black lines on the gray plane define the edges of elements that define the numerical mesh of the flow domain. **Right:** A side view of the observation plane that is commonly used to visualize the velocity contour approximately bisecting the aneurysm.

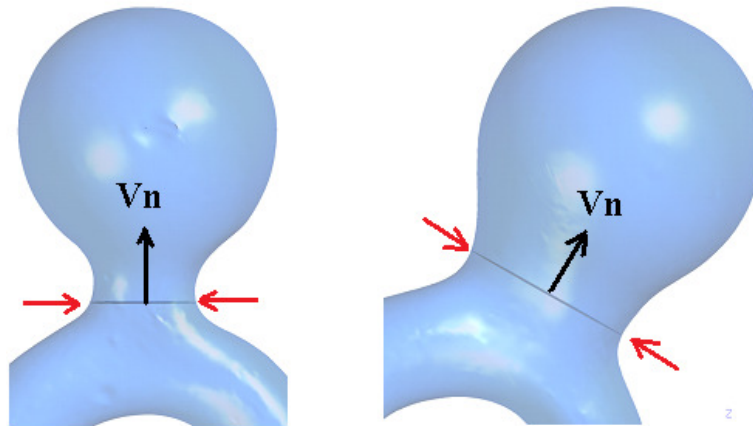


Figure 4-22. **Left:** The plane defined as the neck for RC-SOD147-6 is indicated by red arrows and appears as a gray line from this perspective. **Right:** The plane defined as the neck for RC-SOD147-12(F/R) is indicated by red arrows and appears as a gray line from this perspective.

$$2 * Q = \int |V_N| dA \quad (\text{Eq. 4 - 1})$$

$Q = \text{Flow into the aneurysm}$

$Q_{UT} = \text{Flow into untreated aneurysm}, Q_T = \text{Flow into aneurysm after a flow diverter}$

OBSERVATIONS

4.3.1: Effect of Parametric Variations of Re Components and Outlet Pressure on Flow into Aneurysms

The values of the components that make up the Reynolds number should have no effect on wall shear stress or flow patterns as long as the Reynolds number is the same. The outlet pressure should also have no effect. Equations 4-2 to 4-6 illustrate the derivation of the Reynolds number. Starting with the Navier-Stokes (N-S) equation for incompressible, steady flow:

$$\rho \left(\frac{\partial \mathbf{v}}{\partial t} + \mathbf{v} \cdot \nabla \mathbf{v} \right) = -\nabla p + \mu \nabla^2 \mathbf{v} + \mathbf{f} \quad (\text{Eq. 4 - 2})$$

Both sides are multiplied by $D/\rho V^2$:

$$\rho \left(\frac{\partial \mathbf{v}}{\partial t} + \mathbf{v} \cdot \nabla \mathbf{v} \right) * \frac{D}{\rho V^2} = (-\nabla p + \mu \nabla^2 \mathbf{v} + \mathbf{f}) \frac{D}{\rho V^2} \quad (\text{Eq. 4 - 3})$$

The following non-dimensionalized substitutions are defined:

$$\mathbf{v}' = \frac{\mathbf{v}}{V} \quad (\text{Eq. 4 - 4A})$$

$$p' = p \frac{1}{\rho V^2} \quad (\text{Eq. 4 - 4B})$$

$$\frac{\partial}{\partial t'} = \frac{D}{V} \frac{\partial}{\partial t'} \quad (\text{Eq. 4 - 4C})$$

$$\mathbf{f}' = \mathbf{f} \frac{D}{\rho V^2} \quad (\text{Eq. 4 - 4D})$$

$$\nabla' = D \nabla \quad (\text{Eq. 4 - 4E})$$

After substitution of the primed quantities, the non-dimensionalized version of Navier-Stokes looks like:

$$\frac{\partial \mathbf{v}'}{\partial t'} + \mathbf{v}' \cdot \nabla' \mathbf{v}' = -\nabla' p' + \frac{\mu}{\rho D V} \nabla'^2 \mathbf{v}' + \mathbf{f}' \quad (\text{Eq. 4 - 5})$$

And the Reynolds number is defined as the non-dimensional number in front of the viscosity term.

$$\frac{\partial \mathbf{v}'}{\partial t'} + \mathbf{v}' \cdot \nabla' \mathbf{v}' = -\nabla' p' + \frac{1}{Re} \nabla'^2 \mathbf{v}' + \mathbf{f}' \quad (\text{Eq. 4 - 6})$$

Therefore, while the CFD simulations will use the fluid properties of blood, which are different from that of the sodium iodide solution used in the PIV experiments, the flows should be comparable if similar Reynolds numbers are present. Since pressure shows up only as a derivative in the Navier Stokes equations, altering the outlet pressure will simply alter the datum pressure throughout the entire system and does not alter the fluid flow patterns.

4.3.2: Effect of Pipe-Based Re and % Inlet Turbulence in Untreated Glass Model Aneurysms

The effect of inlet velocity and turbulence intensity is discussed in this section. Three flow velocities at respective Reynolds numbers of 193, 387, and 580 were selected to approximate the low, medium, and high flow rates in the parent vessel along the cardiac cycle of a resting person. Due to these nominally laminar Reynolds numbers, it would be interesting to investigate how the SST-GT transitional model would respond when inlet turbulence intensities of 1% or 5% are imposed. The SST-GT model adapts by dampening the turbulence intensity term in the model at low Reynolds numbers. This allows for the emergence of turbulent behavior locally where appropriate.

The results are summarized in Figure 4-23. In general, the SST-GT model predicted 2.5% to 5% more flow entering the untreated aneurysms than the laminar model. Two exceptions were noted. In RC-SOD147-12(R), the turbulent simulations predicted slightly less flow entering the aneurysm than did the laminar simulation. In RC-SOD147-12(F), the turbulent models predicted about 17% more flow than the laminar model. Small differences, at less than 2%, were observed between the flow rates corresponding to specified values of 1% and 5% turbulence intensities at the flow inlet section.

With reference to Figure 4-24, the shape and penetration depth of the jet entering the aneurysm differ among the three flow speeds, each of which has a unique Reynolds number. Contour plots corresponding to the other turbulence intensities and flow domains can be found in Appendix B.

These observations suggest that it would be prudent to extract the ratio of fluid entering the aneurysm in the treated case (Q_T) divided by the untreated (Q_{UT}) case from simulations where the same inlet turbulence intensity and Reynolds number are imposed.

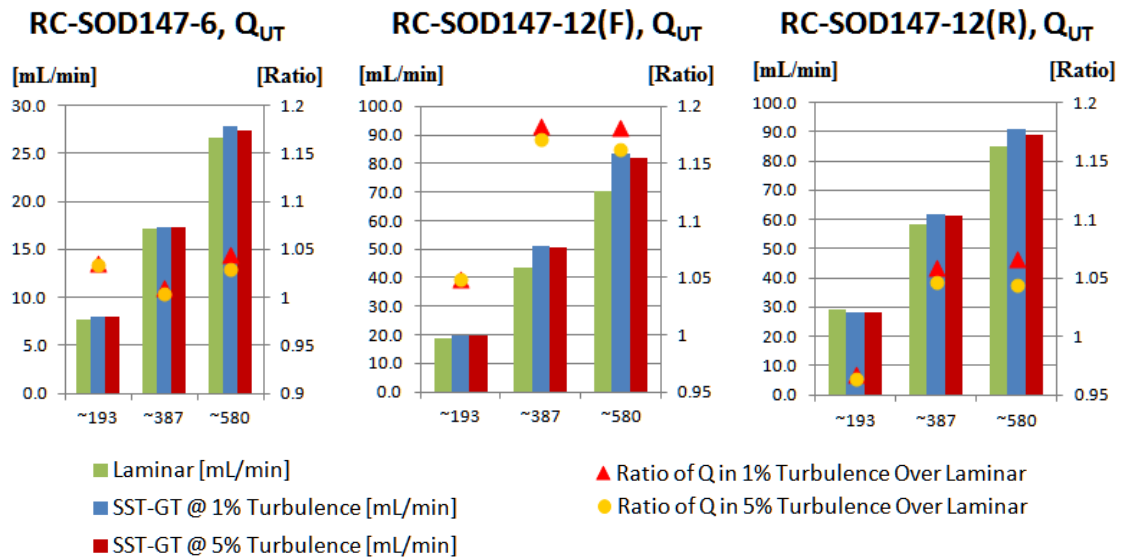


Figure 4-23. The flow rate of blood entering the aneurysm is shown for three different flow domains (RC-SOD147-6, -12(F) and -12(R)), three different inlet turbulence intensities (laminar, 1, and 5%), and three different dimensionless flow speeds. A difference in flow rate entering the aneurysm was observed between the laminar case and the 1% SST-GT turbulence case. A smaller difference was observed between the 1% and 5% SST-GT turbulence cases. In subsequent simulations, the Q_T/Q_{UT} ratio should be calculated using the same turbulence intensity.

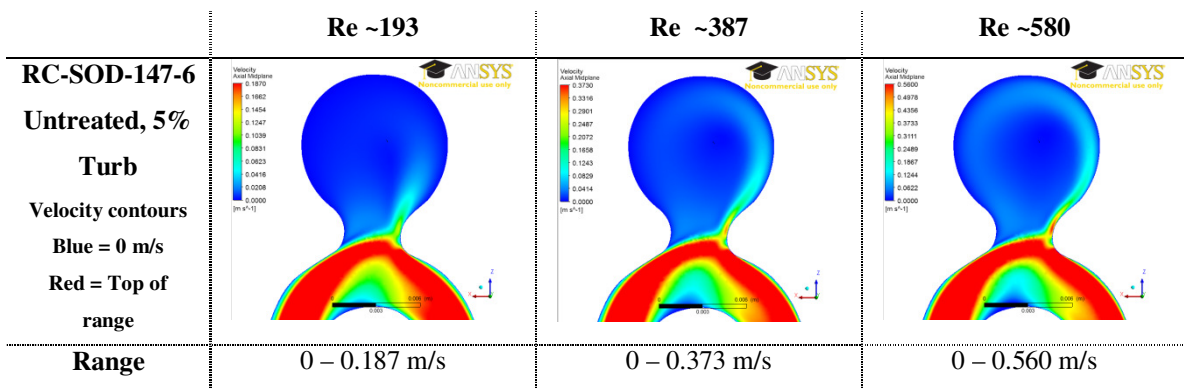


Figure 4-24. Despite scaling the velocity color contour plots by Reynolds number, differences in jet penetration into the aneurysm are evident.

4.3.3: Mesh Independence and Effect of Flow Regime in Glass Model Aneurysms

The effect of numerical mesh density and flow regime on the volumetric flow rate of fluid entering the aneurysms is discussed in this section. The parameters that characterize the different meshes are defined in Tables 4-1 and 4-2. The respective laminar and the SST-GT @ 5% turbulence regimes were examined.

Table 4-1. The distinguishing mesh parameters of the four different mesh densities for the **untreated** aneurysms examined.

Mesh Parameters	Coarse	Normal	Fine	Ultrafine
Default element (min)	$5 * 10^{-5}$ m	$3.89 * 10^{-5}$ m	$3 * 10^{-5}$ m	$2 * 10^{-5}$ m
Default element (max)	$9 * 10^{-3}$ m	$7.79 * 10^{-3}$ m	$7 * 10^{-3}$ m	$5 * 10^{-3}$ m
# of Nodes in Untreated Aneurysms				
RC-SOD147-6	612 885	651 044	704 204	733 252
RC-SOD147-12(F/R)	723 996	794 415	875 172	946 675

Table 4-2. The distinguishing mesh parameters of the four different mesh densities for the **treated** aneurysms examined.

Mesh Parameters	Coarse	Normal	Fine	Ultrafine
Default element (min)	$5 * 10^{-5}$ m	$3.89 * 10^{-5}$ m	$3 * 10^{-5}$ m	$3 * 10^{-5}$ m
Default element (max)	$9 * 10^{-3}$ m	$7.79 * 10^{-3}$ m	$7 * 10^{-3}$ m	$7 * 10^{-3}$ m
Body sizing @ Parent Vessel	$6 * 10^{-4}$ m	$4 * 10^{-4}$ m	$2 * 10^{-4}$ m	$2 * 10^{-4}$ m
Body sizing @ Pores	$4 * 10^{-5}$ m	$2 * 10^{-5}$ m	$1.5 * 10^{-5}$ m	$1.4 * 10^{-5}$ m
# of Nodes in Treated Aneurysms				
RC-SOD147-6	178 210	651 044	980 218	1 435 345
RC-SOD147-12(F/R)	268 266	794 415	1 296 860	1 732 030

Midplane velocity profiles can be found in Appendix B. The midplane is described in Figure 4-21.

The volumetric flow rates of blood entering the aneurysms are presented in Table 4-3 and Figure 4-25. Attention will first be turned to the untreated case. The flow rate of fluid entering the untreated aneurysm, Q_{UT} , fluctuated by about 5% based on the mesh density. The additional computational time required for the ultrafine mesh density did not lead to any appreciable differences. Therefore, the untreated aneurysms should be meshed at the fine density.

Mesh refinement had a more noticeable effect on the flow rate of fluid entering the treated aneurysm, Q_T . In particular, the Q_T/Q_{UT} ratio changed greatly for RC-SOD147-12(R). This may be due to the nearly perpendicular incident angle of the inlet jet, which may be more sensitive to the resolution of the numerical elements characterizing flow through the pores. Little to no differences in Q_T were observed between the fine and ultrafine mesh densities. Therefore, the treated aneurysms should be meshed at the fine density to reduce computational time.

Table 4-3. Upper part of the table: flow rate of blood entering the aneurysm in the untreated case. Lower part of the table: flow rate of blood entering the aneurysm after it is treated by the flow diverter. The numbers in parentheses represent the fraction of the flow rate entering the aneurysm in the presence of the flow diverter divided by that in the absence of the flow diverter (Q_T/Q_{UT}).

	SteadyInlet@Re~580 (Laminar Flow)				SteadyInlet@Re~580 (SST-GT Flow)			
Untreated	Coarse	Normal	Fine	Ultrafine	Coarse	Normal	Fine	Ultrafine
...147-6	--	27.6 mL/min	25.8	25.6	27.0	27.4	26.0	25.8
...147-12(F)	--	81.6	79.7	81.3	81.3	82.0	80.1	82.1
...147-12(R)	--	94.0	91.7	93.6	89.0	88.8	86.9	88.6
Treated	Coarse	Normal	Fine	Ultrafine	Coarse	Normal	Fine	Ultrafine
...147-6	--	8.7 mL/min (32%)	8.6 (34)	8.1 (31)	10.9 (40)	9.4 (34)	8.6 (33)	8.3 (32)
...147-12(F)	--	8.0 (9.8)	8.1 (10)	8.1 (10)	10.4 (13)	8.8 (11)	7.8 (9.7)	7.8 (9.7)
...147-12(R)	--	17.5 (19)	10.7 (12)	10.7 (12)	21.0 (24)	20.0 (23)	13.8 (16)	13.8 (16)

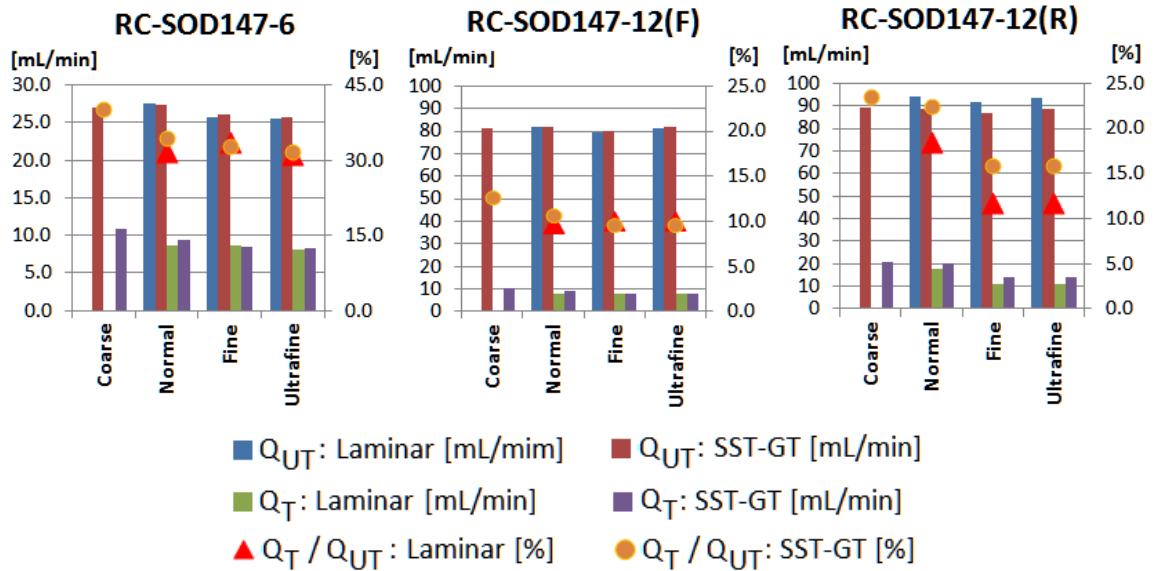


Figure 4-25. The volumetric flow rates (Q) of blood entering untreated and treated aneurysms are plotted above. The left y-axis is scaled for blood entering the aneurysm in [mL/min]. The right y-axis is scaled for the percentage of flow entering the aneurysm in the treated case divided by the flow in the untreated case in [%]. The five different mesh density and fluid regime combinations are presented in the x-axis.

The details of the numerical mesh at the flow diverter are illustrated in Figures 4-21. When examining the numerical mesh projected on the plane described in Figure 4-21 near the pores, it is rather evident when looking at Figure 4-26 that the normal mesh does a rather poor job in connecting the parent artery to the aneurysm bulb. In many cases, no nodes are present within the pore. Accordingly, the fluid flow rushing through the pores looks very different between a normal mesh and a fine mesh. As shown in Figure 4-27, small jets of fluid are visible immediately past the flow diverter before being dissipated inside the aneurysm when a fine mesh is used. The struts of the diverter also behave as expected by shielding against the incoming flow and forming low velocity regions, or wakes, immediately behind it. These jets and wakes areas are present in both the laminar and SST-GT fluid models.

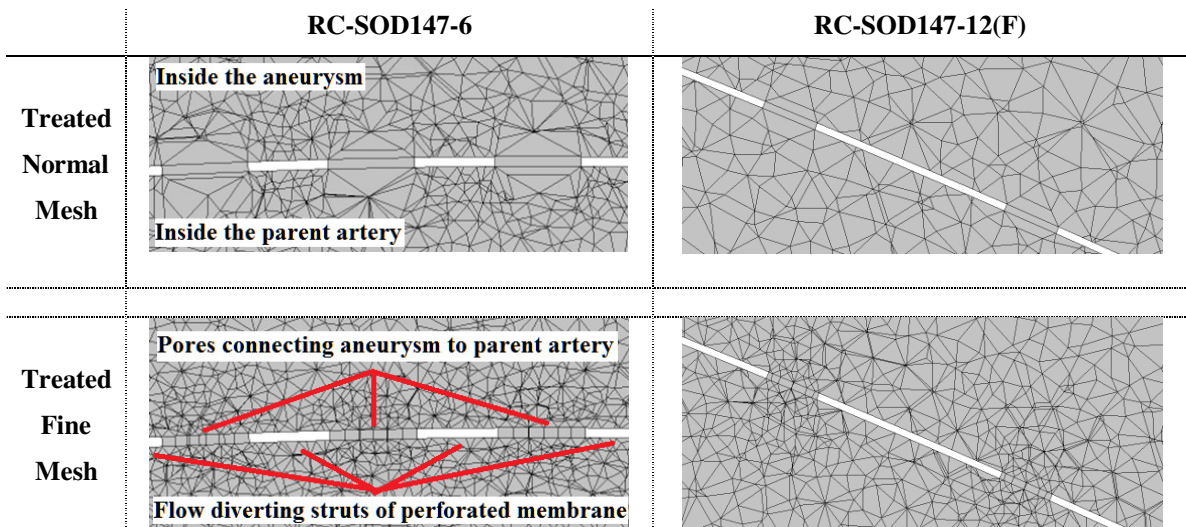


Figure 4-26. The numerical mesh (shaded gray) characterizing fluid flow at the perforated membrane is shown on a plane approximately bisecting the flow domain, as described in Figure 4-21. The region above the flow diverting struts of the perforated membrane (white spaces) is inside the aneurysm. The region below the membrane struts is in the parent artery. Note that when the “normal mesh” settings were used, no nodes (located at the intersection of the black lines) were observed inside the pores. In the images of the fine mesh above, it can be observed that approximately six elements (shaded gray area bounded by black lines) span the pore when the flow domain is cut open at this observation plane.

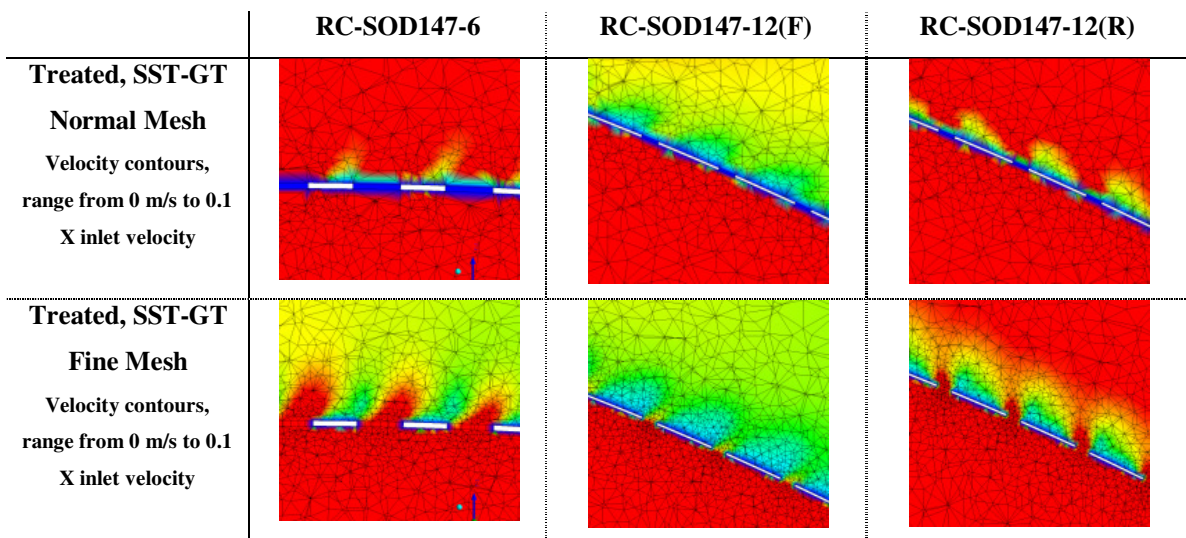


Figure 4-27. The flow through the perforated membrane with a normal mesh is noticeably different than with a fine mesh. Jets of high velocity fluid (shaded red) and wakes (low velocity flow regions shaded green and blue) behind the membrane struts (white spaces) are present as it would be intuitively expected in this scenario. The laminar cases can be found in the appendix on Appendix B.

4.3.4: Effect of Pore Dimensions

The effect of pore dimensions on the ratio of flow rate of entering the aneurysm before and after the placement of a flow diverter is discussed in this chapter. Three parameters were studied: the pore dimensions (0, 50, and 100% stretch of the original pore width), Reynolds numbers (387, 580, and 773), and flow domains (RC-SOD147-6, RC-SOD147-12(F) and RC-SOD147-12(R)).

Different pore dimensions were of interest because the braided structure of the Pipeline Embolization Device used in the PIV experiments is highly susceptible to varying pore dimensions. The pore dimensions are dependent on the technique used to place the device across the aneurysm because the crossing points of the filars are not fixed. Stretches of 50% and 100%, described in Figure 4-28, were chosen for the simulations to understand the changes in flow diversion effect in preparation for verification of CFD simulations using PIV data.

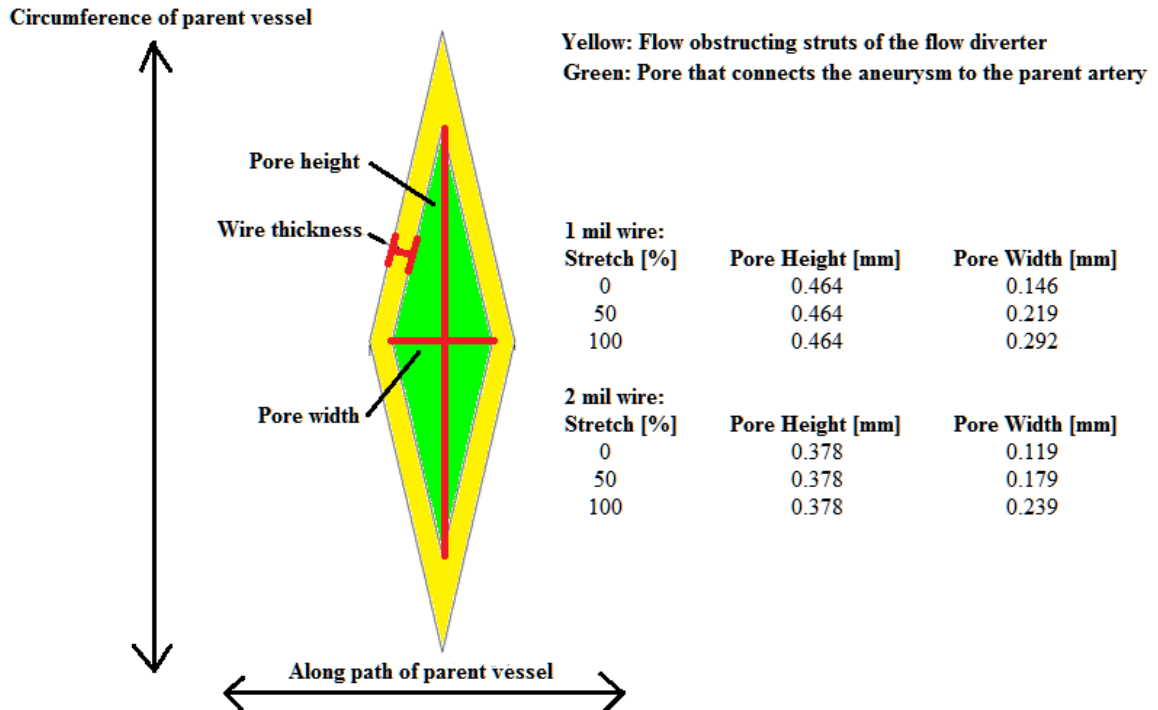


Figure 4-28. The dimensions of the pores connecting the aneurysm to the parent vessel are shown.

The effect of the wire diameter of the braid was also examined. Comparisons were made between braids woven using 1 mil, or 0.001 in. diameter, and 2 mil wires. The characteristics of the pores connecting the parent artery to the aneurysm for the braid modeled with 1mil wires can be found in Table 4-4 and Figure 4-29. The characteristics for the braid modeled with 2 mil wires can be found in Table 4-5 and Figure 4-30.

Table 4-4. The characteristics of the pores connecting the parent artery to the aneurysm for the flow diverter modeled with a 1 mil wire are listed.

1 mil Wires	RC-SOD147-6			RC-SOD147-12(F/R)		
	Porosity [%]	Pores	Pores/mm ²	Porosity [%]	Pores	Pores/mm ²
0% Stretch	60.1	357	18.4	48.8	409	14.7
50% Stretch	63.6	244	12.6	57.4	314	11.3
100% Stretch	62.9	181	9.31	52.1	214	7.7

Table 4-5. The characteristics of the pores connecting the parent artery to the aneurysm for the flow diverter modeled with a 2 mil wire are listed.

2 mil Wires	RC-SOD147-6			RC-SOD147-12(F/R)		
	Porosity [%]	Pores	Pores/mm ²	Porosity [%]	Pores	Pores/mm ²
0% Stretch	43.8	383	19.7	35.8	447	16.1
50% Stretch	43.1	248	12.8	41.1	338	12.2
100% Stretch	43.0	186	9.6	43.6	269	9.69

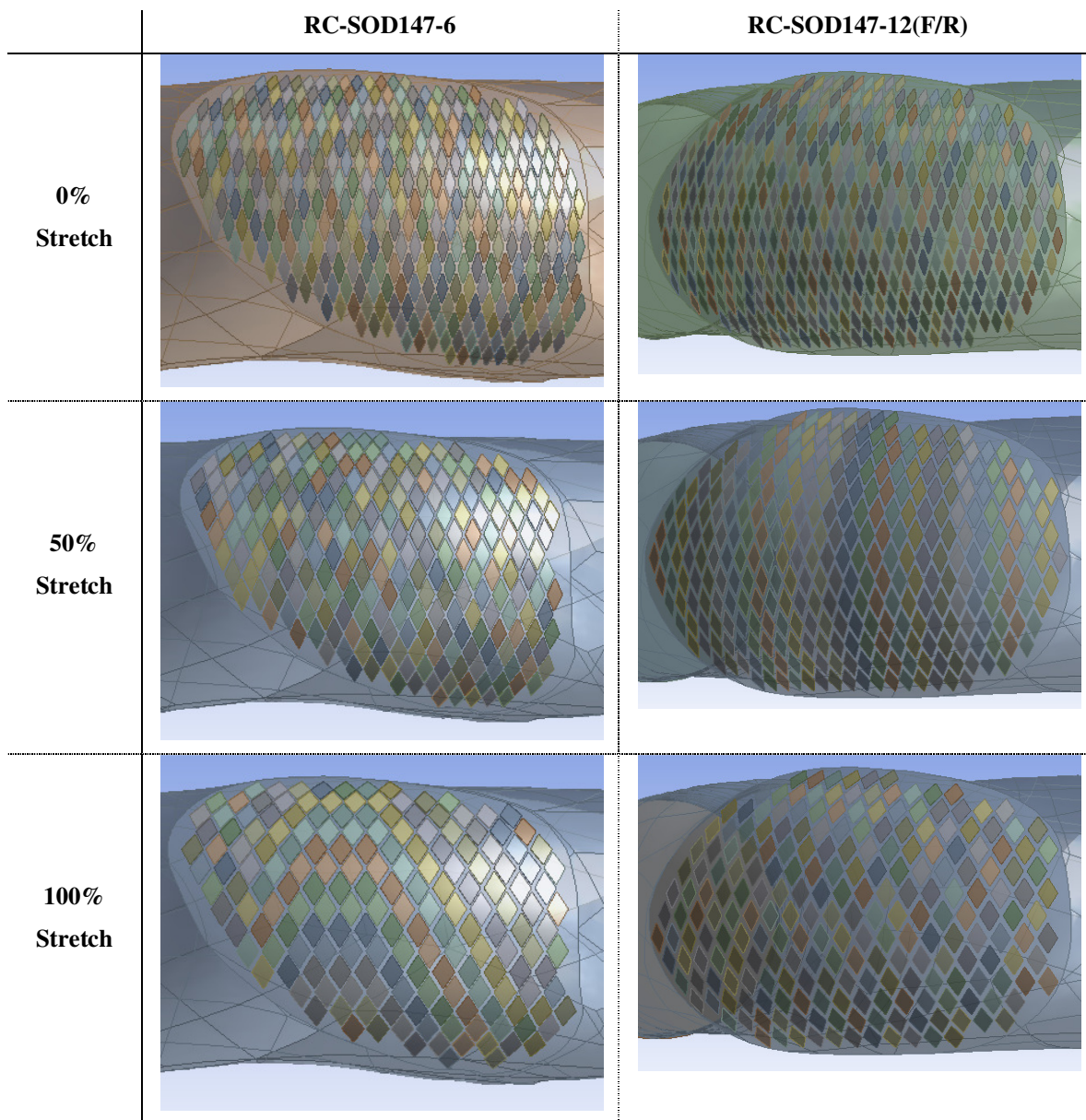


Figure 4-29. The colored diamonds are the pores connecting the aneurysm to the parent artery when the flow diverter was modeled with 1 mil diameter wires. Note that the pores are absent near the edges of the neck due to the state of the modeling method available when the simulations in this chapter were conducted. The regions of solid blockage likely explain why the porosity dropped when the pore size increased from the 50% stretch to the 100% scenario.

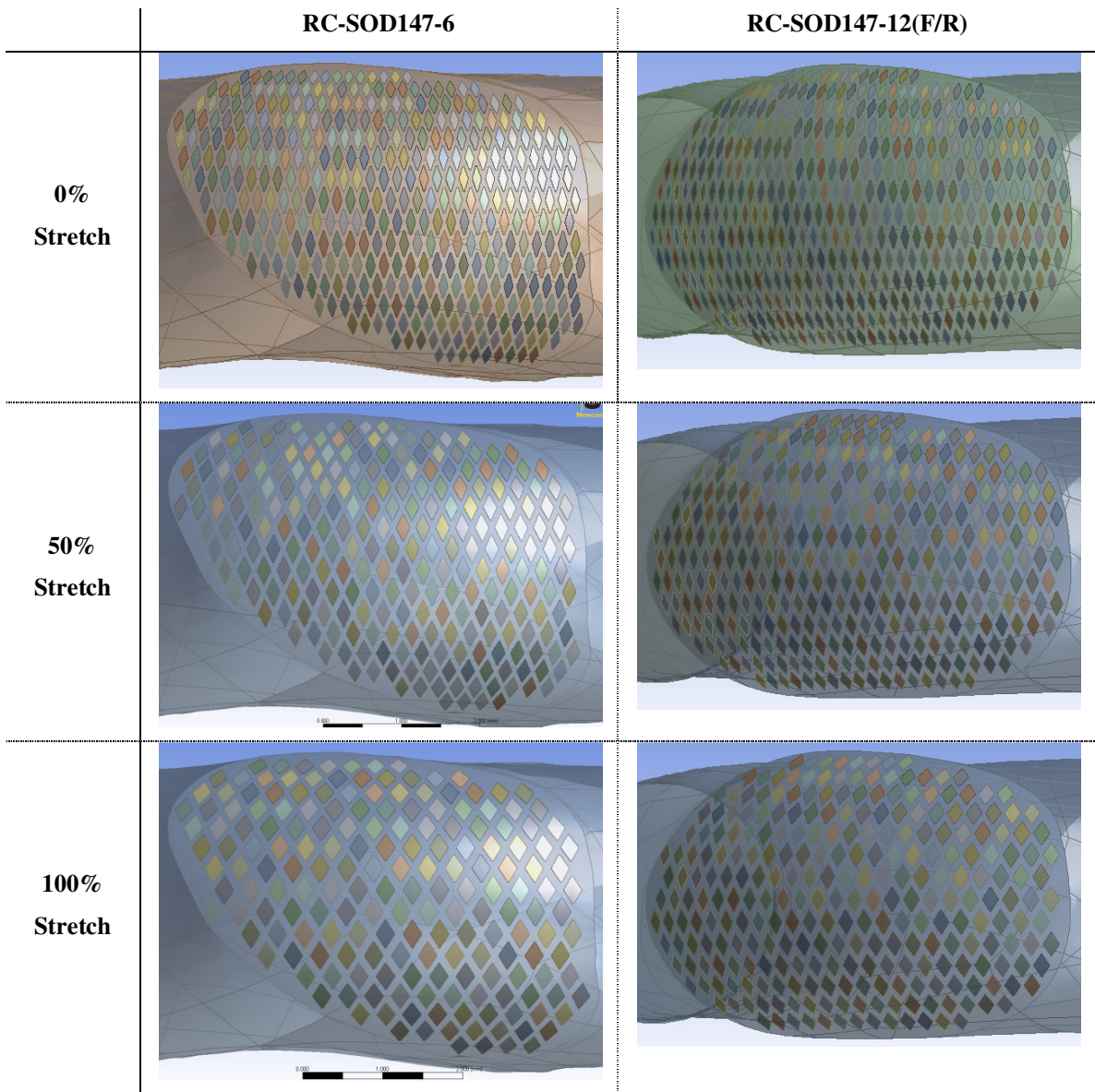


Figure 4-30. The colored diamonds are the pores connecting the aneurysm to the parent artery when the flow diverter was modeled with 2 mil diameter wires. Note that the pores are absent near the edges of the neck due to the state of the modeling method available when the simulations in this chapter were conducted. The regions of solid blockage likely explain why the porosity dropped when the pore size increased from the 50% stretch to the 100% scenario.

The flow rate of fluid entering the aneurysms under the different combinations of pore stretching, flow domain, and Reynolds numbers are summarized in Figure 4-31. In the simulations where the flow diverter was modeled with 1 mil diameter wires, the flow rate increased with Reynolds number as expected. The effect of the pore stretching was somewhat clouded. Pores with 0% stretch exhibited the lowest flow rate into the aneurysm as expected. However, the flow rates for 50% and 100% stretch were in close proximity to each other. In some cases, such as for the Reynolds number = 773 in the RC-SOD147-12(F) flow domain, the flow rate through pores at 50% stretch was actually slightly higher than that through cells with 100% stretch. This was likely due to the porosities of the two perforation patterns. With reference to Table 4-4, the porosity actually dropped from 57.4% to 52.1% when the stretch was 50% and 100% respectively. Despite larger pores, the modeling method employed at this stage of the research left large blockages at the edges of the neck between the aneurysm and the parent artery.

In the simulations where the flow diverter was modeled with 2 mil diameter wires, the flow rates into the aneurysm trended as expected for the RC-SOD147-12(F) and RC-SOD147-12(R) domains. Flow rates increased as the cells enlarged and as the Reynolds numbers increased. Table 4-5 shows that porosity increased as the degree of stretching increased, as it would be expected. However, in the RC-SOD147-6 domain, porosity did not increase with stretching. This was an artifact of the pore modeling method used at this stage of the research. The flow rates of fluid entering the aneurysm were very similar, as were the porosities of the perforated membranes modeled with 2 mil diameter wires.

For the purposes of verification of CFD simulations by means of PIV experimental data, the flow rate of fluid entering the aneurysms after the placement of the flow diverter with 1 mil diameter wires will be used. With reference to Figures 4-31, for a Reynolds number of 580, it is predicted that after the flow diverters are placed across the aneurysm necks, about 45 – 52%, 23 – 33%, and 28 – 42% of the flow in the untreated cases will enter the aneurysms of the domains RC-SOD147-6, RC-SOD147-12(F), and RC-SOD147-12(R) respectively.

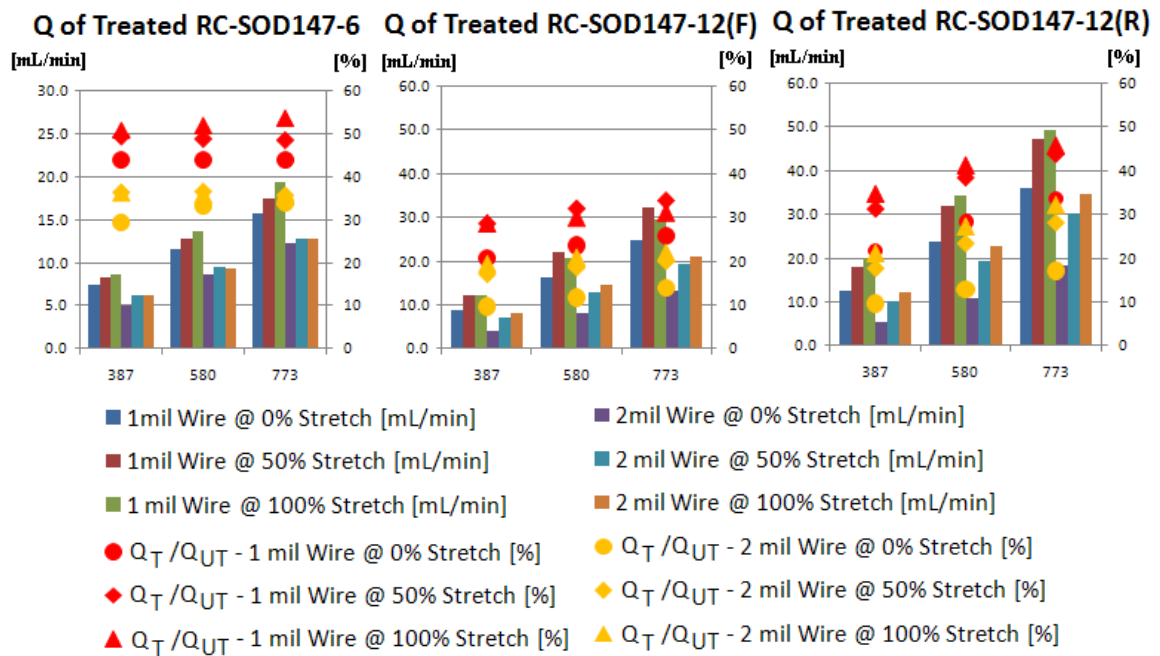


Figure 4-31. The flow rates of blood entering the aneurysm in the different domains are shown for different combinations of Reynolds number, degree of pore stretching, and wire diameter that forms the perforated mesh connecting the aneurysm to the parent artery.

4.3.5: Effect of Offset Cells for 2 mil Wires

A physician has no control over the rotational positioning of the Pipeline Embolization Device flow diverter when it is placed across an aneurysm inside a patient. Therefore, a small study was conducted to examine the effect of rotationally offsetting the pores that connect the aneurysm to the parent artery. The pores were offset rotationally by about half the height of the cell, which is defined as the open pore (green diamond on Figure 4-28) plus the flow obstructing border (yellow border on Figure 4-28). The pore patterns examined are shown in Figure 4-32 and Figure 4-33 and their characteristics are summarized in Table 4-6 and Table 4-7. Due to the modeling technique used at this stage of research, the pores at the edges of the flow diverter were once again absent, therefore contributing to the slight differences in porosity after the pores were offset.

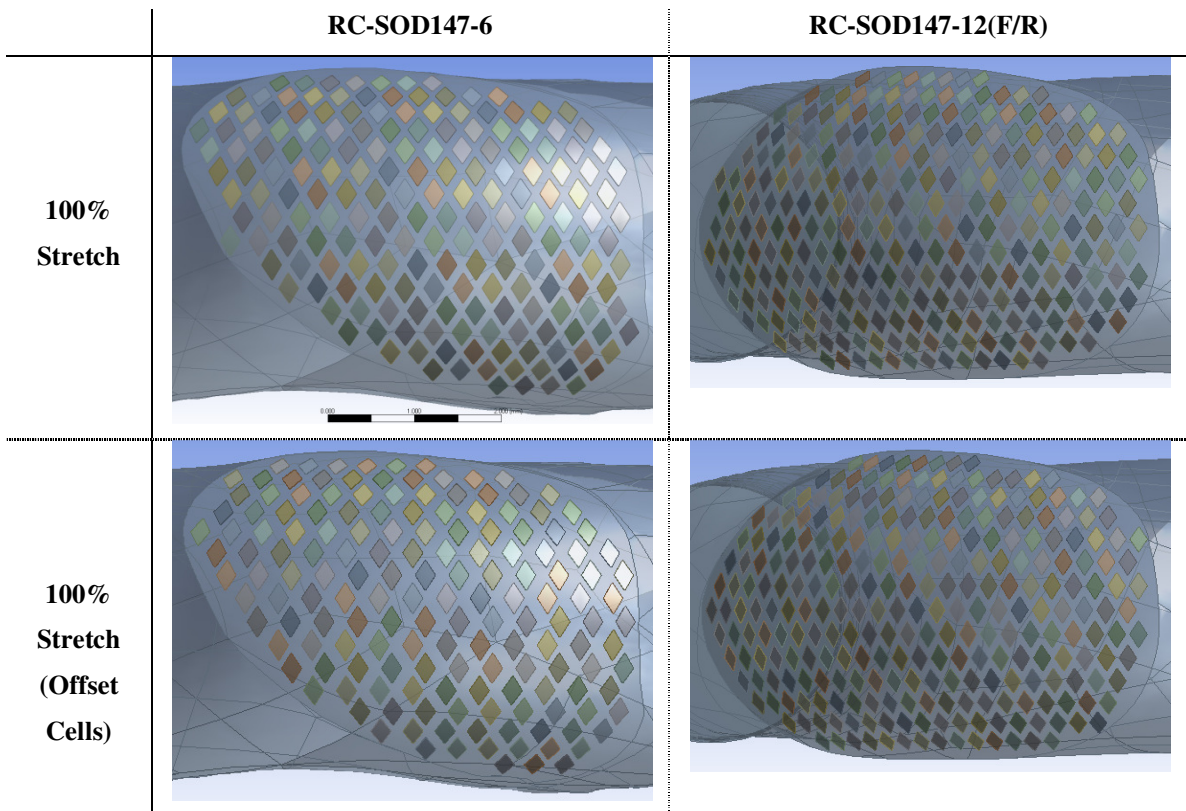


Figure 4-32. The colored diamonds are the pores connecting the aneurysm to the parent artery when the flow diverter was modeled with 2 mil diameter wires. Note that the pores are absent near the edges of the neck due to the state of the modeling method available when the simulations in this chapter were conducted.

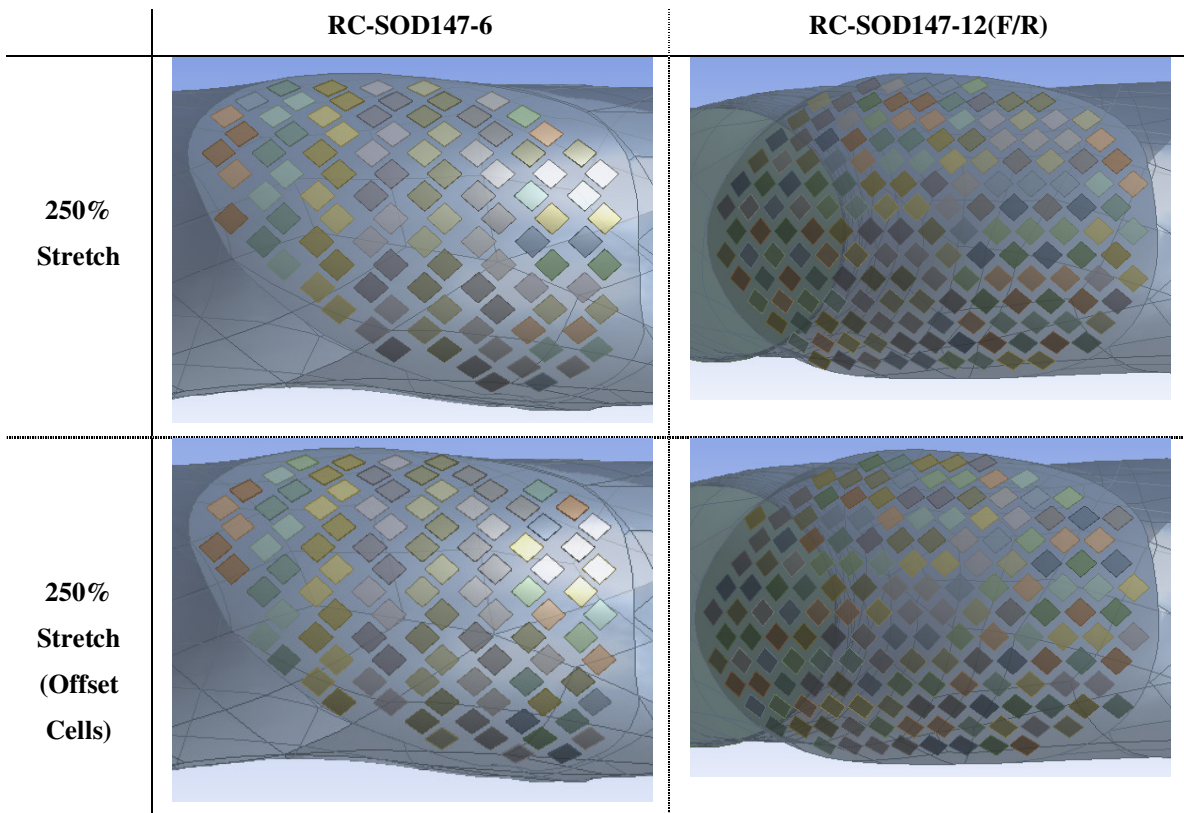


Figure 4-33. The colored diamonds are the pores connecting the aneurysm to the parent artery when the flow diverter was modeled with 2 mil diameter wires. Note that the pores are absent near the edges of the neck due to the state of the modeling method available when the simulations in this chapter were conducted.

Table 4-6. The characteristics of the pores connecting the parent artery to the aneurysm for the flow diverter modeled with a 2 mil wire are listed.

2 mil Wires	RC-SOD147-6			RC-SOD147-6 (Cells offset by ½ cell height)		
	Porosity [%]	Pores	Pores/mm ²	Porosity [%]	Pores	Pores/mm ²
100% Stretch	38.2	165	8.5	37.1	160	8.2
250% Stretch	39.0	96	4.9	39.8	98	5.0

Table 4-7. The characteristics of the pores connecting the parent artery to the aneurysm for the flow diverter modeled with a 2 mil wire are listed.

2 mil Wires	RC-SOD147-12 (F/R)			RC-SOD147-12 (F/R) (Offset Cells)		
	Porosity [%]	Pores	Pores/mm ²	Porosity [%]	Pores	Pores/mm ²
100% Stretch	43.6	269	9.7	43.5	268	9.7
250% Stretch	47.0	165	5.9	46.1	162	5.8

The flow rates of blood entering the aneurysms are summarized in Figure 4-34. Velocity contours of at the plane approximately bisecting the aneurysm are presented in Appendix B. No significant differences in flow rate of fluid entering the aneurysms were observed. This suggests that while there may be minuscule differences in the flow field near the perforated membrane, the metric of flow rate into the aneurysm is minimally affected by the rotational position of the diamond shaped pores. It is also interesting to note that despite increasing the pore size in the RC-SOD147-6 domain, there was little increase in the flow rate of fluid entering the aneurysm. This was likely due to very similar porosity levels, at 38.2 and 39% for 100 and 250% stretch respectively.

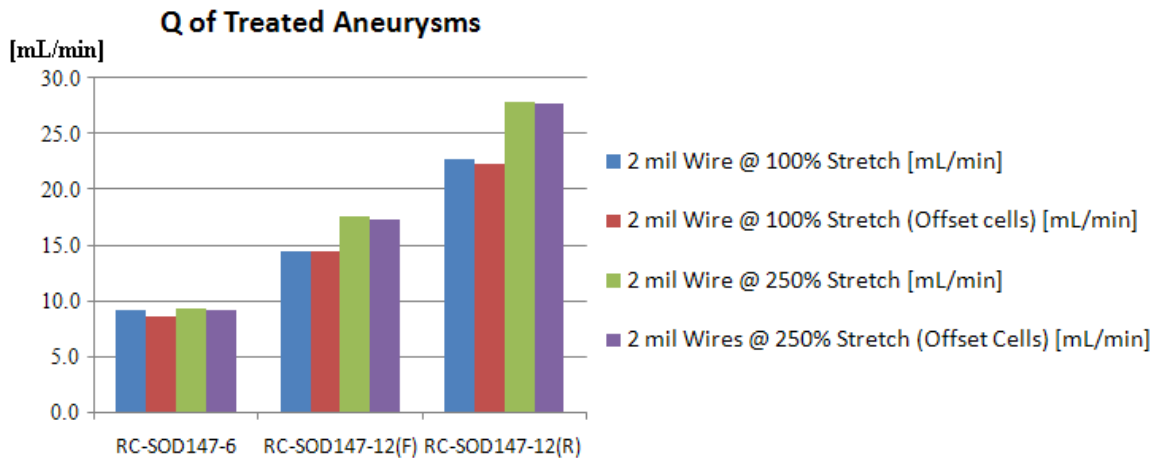


Figure 4-34. The flow rates of blood entering the aneurysm when the pores were offset circumferentially by half the cell height were compared. No significant difference was observed, meaning that the physician placing the flow diverter inside the patient does not need to be concerned about the rotational orientation of the device.

4.3.6: Comparison of CFD Simulation and PIV Experimental Results

Highly detailed PIV experimental data were acquired for the flow domains RC-SOD147-6, RC-SOD147-12(F), and RC-SOD147-12(R). The distance between planes was 0.4mm. The flow rate of blood entering the aneurysms were quantitatively compared between PIV and CFD results. Velocity contour plots on planes at approximately matching locations were qualitatively compared side by side to visualize differences in the flow patterns. The Reynolds numbers were approximately 580. Examination of the Pipeline Embolization Device flow diverter under a microscope revealed that the individual wires are approximately 1 mil in diameter.

Figures 4-35 and 4-36 visualize the locations of the planes on which the velocity contours were mapped from the PIV data set. Figure 4-37 visualizes the approximately locations of the sampling line on the PIV results on which the absolute normal velocities were calculated and integrated to yield the flow rate of fluid entering and exiting the aneurysm. Figure 4-38 visualizes the location of the plane on which the normal velocity vectors were integrated to yield the flow rate of fluid entering and exiting the aneurysm from the CFD simulations.

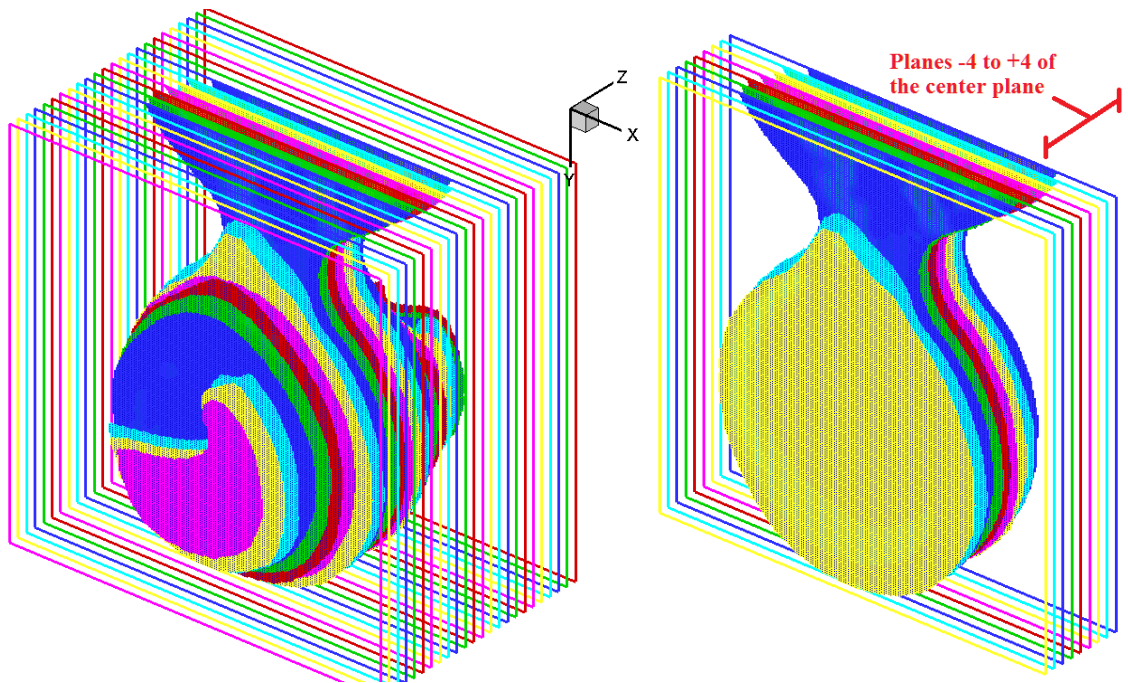


Figure 4-35. Left: The high resolution data set for RC-SOD147-6 is comprised of 24 planes in the axial view. **Right:** Only nine planes are needed to span the neck that connects the aneurysm to the parent artery. Therefore, the normal velocity is integrated along the necks in the nine planes to yield the volumetric flow of fluid entering and exiting the aneurysm.

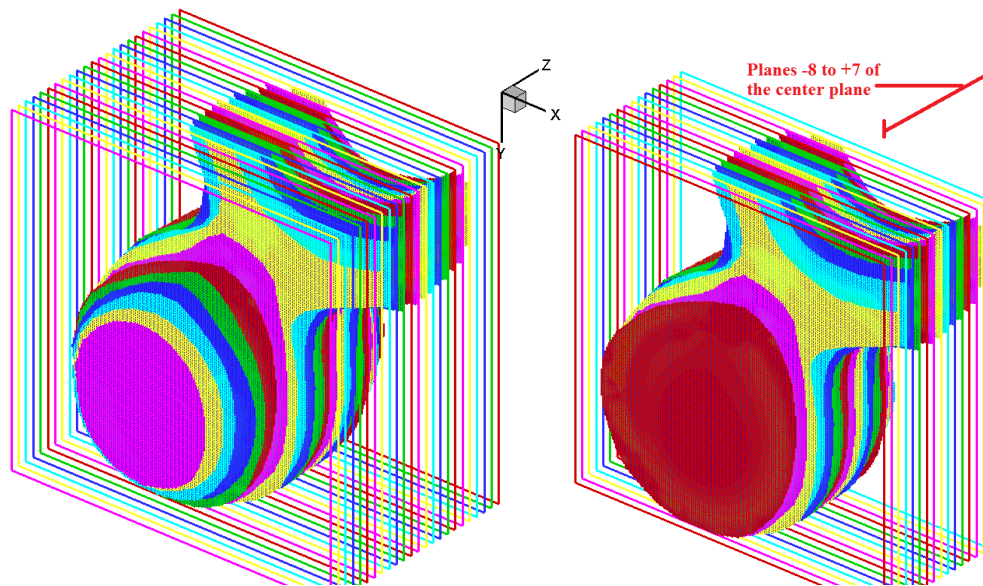


Figure 4-36. Left: The high resolution data sets for RC-SOD147-12(F) and RC-SOD147-12(R) are comprised of 24 planes in the axial view. **Right:** Only 16 planes are needed to span the neck that connects the aneurysm to the parent artery. Therefore, the normal velocity is integrated along the necks in the 16 planes to yield the volumetric flow of fluid entering and exiting the aneurysm.

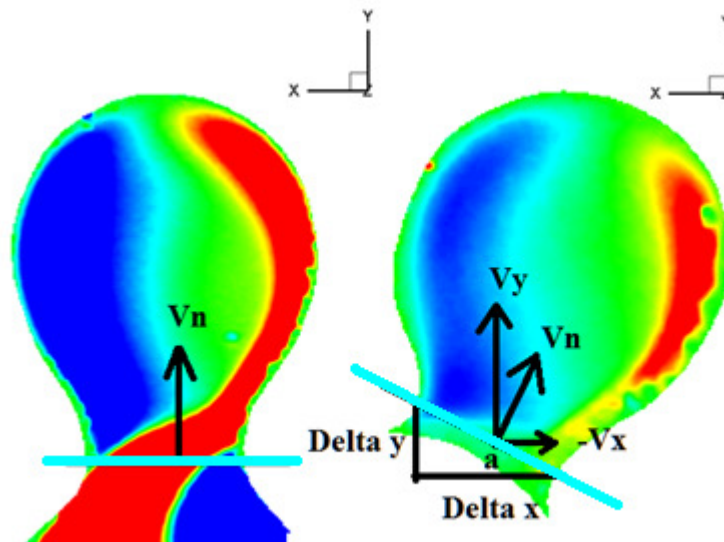


Figure 4-37. For the PIV data set, the absolute normal velocity vectors were calculated (Eq. 4-8) at the necks (thick light blue line) of the aneurysms for the RC-SOD147-6 (**left**) and RC-SOD147-12 (**right**) flow domains. The **absolute** normal velocity vectors were then integrated along the sampling line to yield the flow rate of fluid entering and exiting the aneurysm for a particular plane (Eq. 4-9). The sum of the flow rates from nine planes in the case of RC-SOD147-6, and 16 planes in the case of RC-SOD147-12(F/R) was the flow rate of fluid entering and exiting the aneurysm.

$$a = \tan^{-1}\left(\frac{\text{delta } y}{\text{delta } x}\right) \quad (\text{Eq. 4 - 7})$$

$$V_N = V \cdot n = -V_x * \sin(a) + V_y * \cos(a) \quad (\text{Eq. 4 - 8})$$

$$Q_{\text{PLANE,IN AND OUT}} = \int_{\text{NECK}} |V_N| * ds * \text{Thickness between planes} \quad (\text{Eq. 4 - 9})$$

$$Q_{\text{IN}} = Q_{\text{OUT}} = 0.5 * \sum_{\text{PLANES}} Q_{\text{PLANE,IN AND OUT}} \quad (\text{Eq. 4 - 10})$$

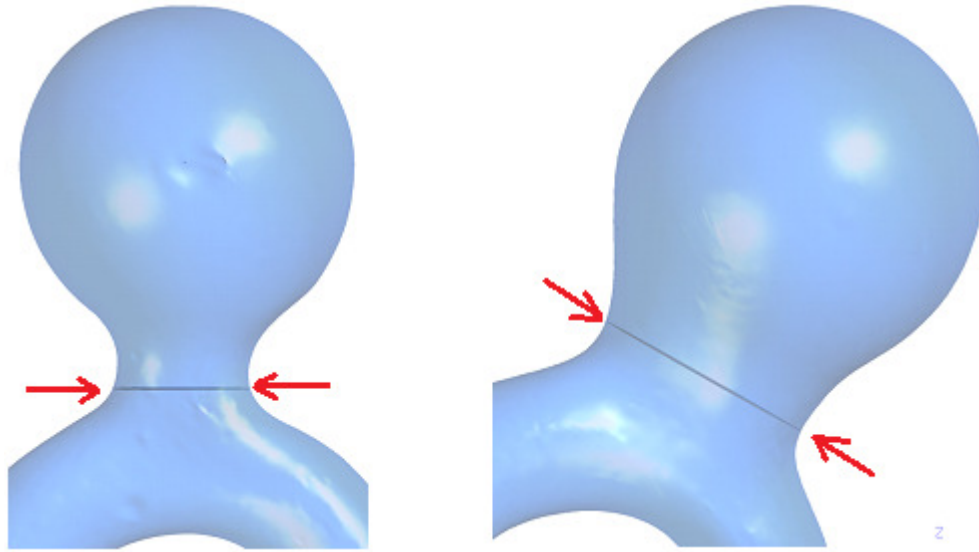


Figure 4-38. For the CFD data set, the normal velocity vectors were calculated at the necks (gray planes, pointed to by red arrows) for RC-SOD147-6 (**left**) and RC-SOD147-12 (F/R) (**right**) flow domains. The normal velocity vectors were then integrated along the neck area to yield the flow rate of fluid entering and leaving the aneurysms.

The shapes of the fluid jets entering the RC-SOD147-6 and RC-SOD147-12 aneurysms are compared between what was observed experimentally and simulated computationally in Figures 4-39, 4-40, and 4-41. The velocity contour plots qualitatively look similar in the untreated RC-SOD147-6 aneurysm. Experimentally, the jet penetrated a little less into the aneurysm after placement of the flow diverter.

The flow structures in the untreated RC-SOD147-12(F) aneurysm looked similar between CFD and PIV, but more flow was observed experimentally in the center plane. This may be due to capture of particle movement throughout the thickness of the laser sheet, which is about 0.5mm thick. The flow structure after placement of the flow diverter looked fairly different between CFD and PIV. This may have been due to

the actual shape of the flow diverter in the glass model, as shown in Figures 4-44 and 4-46, which was different than the shape modeled computationally.

The flow structures in the untreated and treated RC-SOD147-12(R) aneurysm looked similar between CFD and PIV, but more flow was observed experimentally in the center plane. This may be due to capture of particle movement throughout the thickness of the laser sheet, which is about 0.5mm thick.

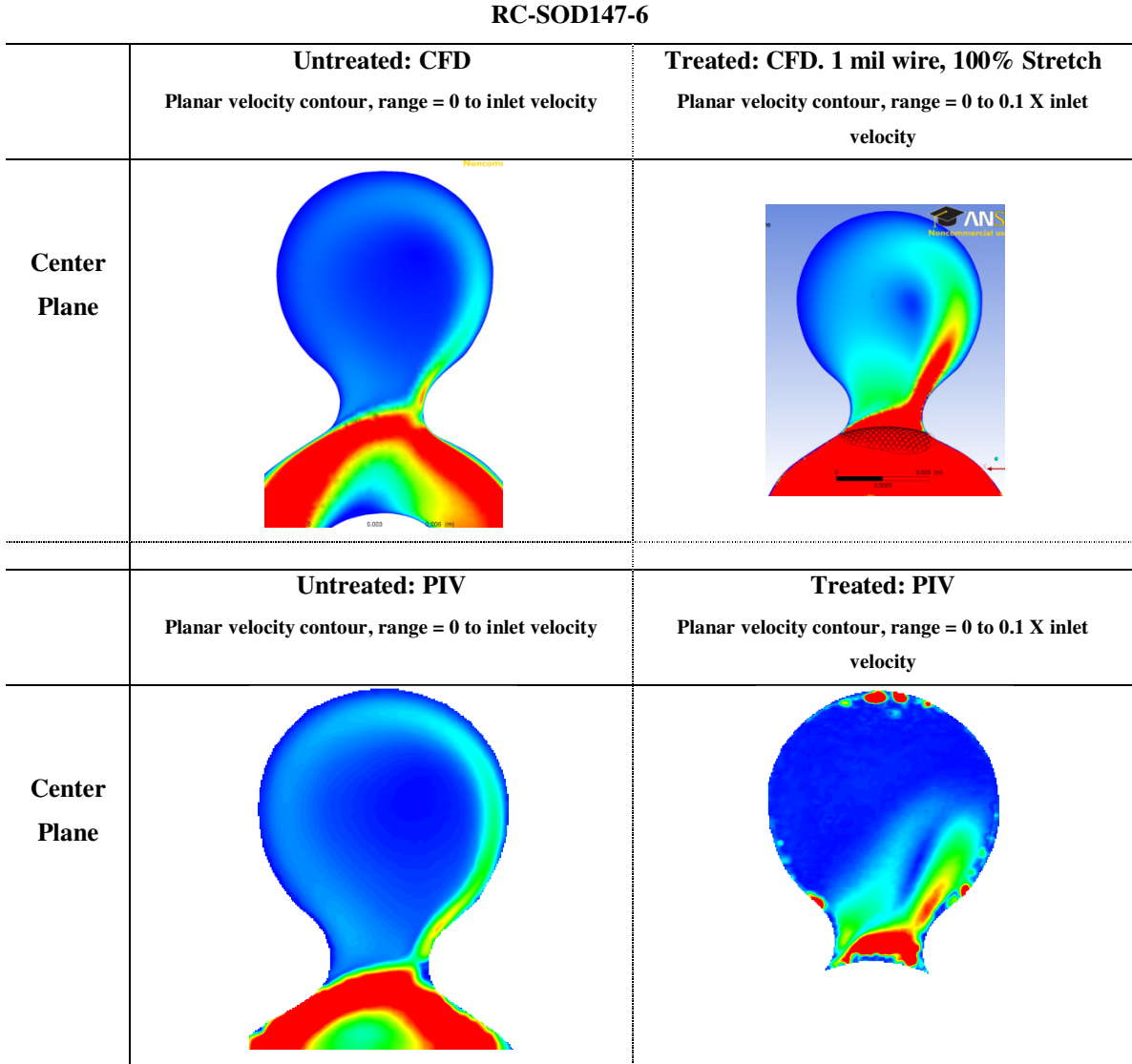


Figure 4-39. The velocity contours at approximately the midplane bisecting the aneurysm was compared between the CFD simulation and the PIV experiment. The general flow structure and flow magnitude was qualitatively similar.

RC-SOD147-12(F)

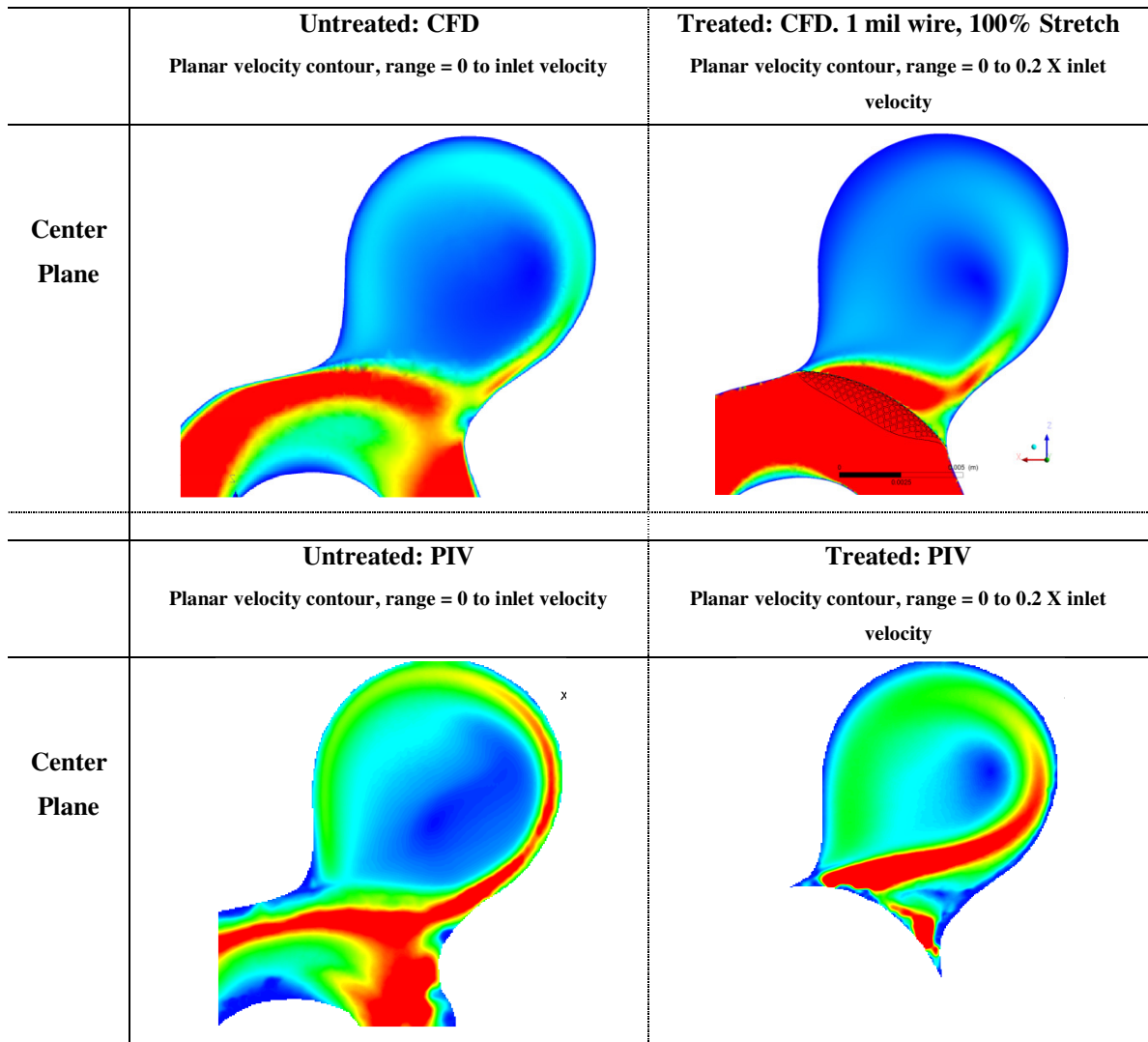


Figure 4-40. The velocity contours at approximately the midplane bisecting the aneurysm was compared between the CFD simulation and the PIV experiment. The general flow structure was qualitatively similar in the untreated aneurysm, but increased flow entering the aneurysm was observed experimentally. The flow structure of the treated aneurysm was fairly different computationally and experimentally. This may have been due to the shape of the deployed flow diverter, which is shown in Figure 4-46 and discussed later in this chapter.

Summation of the flow rates in the treated and untreated cases from the individual planes described in Figures 4-35, 4-36 and 4-37 allowed for the calculation of the ratio of flow rates entering the aneurysm after and before the placement of the flow diverter. These Q_T/Q_{UT} ratios are summarized in Figure 4-42. In the flow domains of RC-SOD147-12(F) and RC-SOD147-12(R), the ratio was within the range predicted

by 0 – 100% stretching of the pores. In RC-SOD147-6, the Q_T/Q_{UT} ratio was about 8% higher than that predicted from simulations where the diamond shaped pores were stretched to 100% of their original width.

RC-SOD147-12(R)

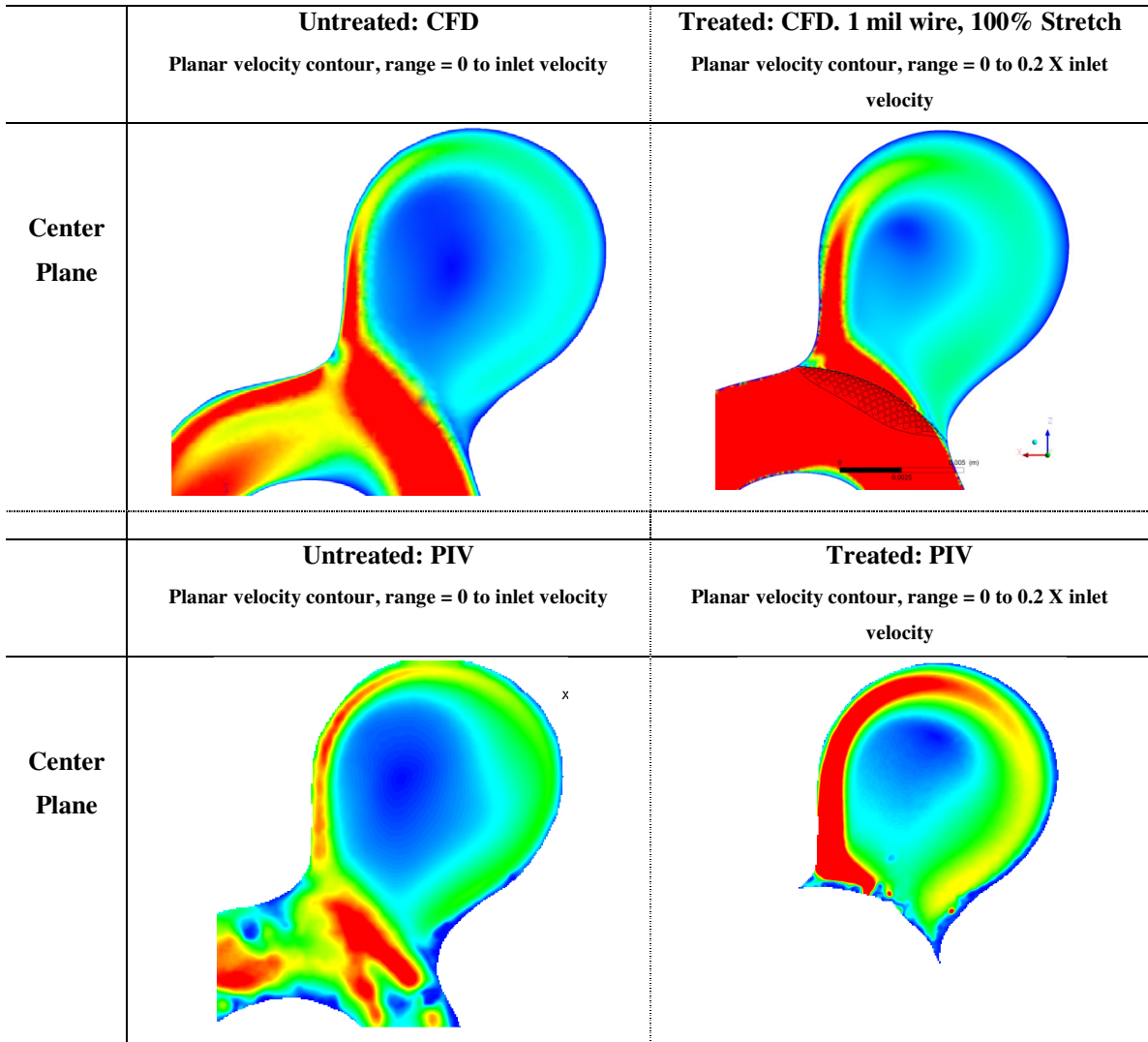


Figure 4-41. The velocity contours at approximately the midplane bisecting the aneurysm was compared between the CFD simulation and the PIV experiment. The general flow structure was qualitatively similar, but increased flow entering the aneurysm was observed in the treated and untreated scenarios.

Q_T/Q_{UT} - Comparison Between CFD and PIV

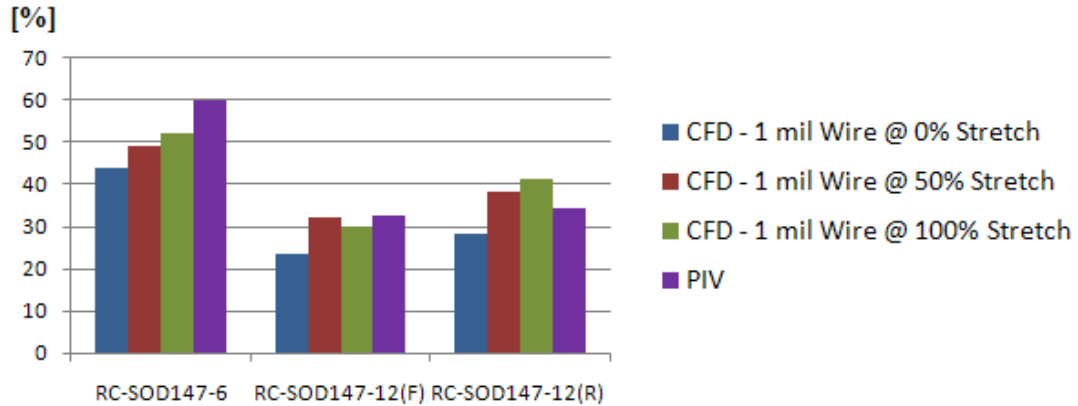


Figure 4-42. The fraction of fluid entering the aneurysm after placement of the flow diverter divided by the flow rate entering the untreated aneurysm predicted by computer simulation of cells stretched up to 100% of their original width are compared to the experimental PIV observations.

An examination of the flow rates entering the aneurysm in the treated cases, Q_T , between the CFD simulations and the PIV experiments further indicate that the majority of flow phenomena are captured. In reference to Figure 4-43, the Q_T from the CFD and the PIV data sets are in close proximity when plotted on separate axes. A factor of approximately three between the two axes was expected, as the inlet velocities were scaled by three to account for the difference in kinematic viscosity of blood in the CFD simulations and the sodium iodide in PIV experiments. A slightly higher than expected Q_T observed in RC-SOD147-12(F) from the PIV data set was balanced out by a slightly higher than expected Q_{UT} to arrive at a Q_T/Q_{UT} ratio that fell within the range predicted by CFD simulations.

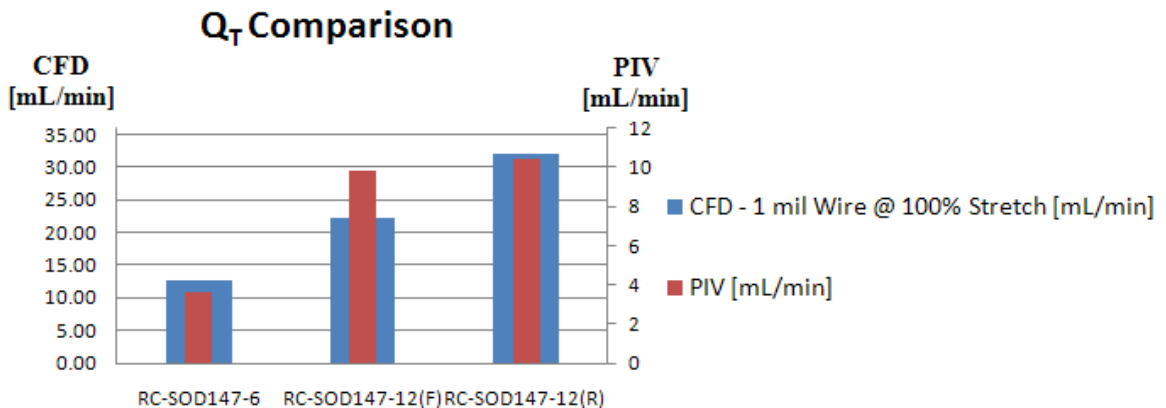


Figure 4-43. The Q_T from the CFD and PIV datasets are compared. A factor of three is applied to account for the difference in kinematic viscosity between the sodium iodide solution used in PIV and the blood used in CFD.

A number of possibilities exist for explaining the small differences in the Q_U/Q_{UT} ratio between what was predicted by CFD simulations and what was observed with PIV experiments. With reference to Figure 4-44, it is not possible to determine the exact dimensions of the diamond pores connecting the aneurysm to the parent artery based on the images taken for the PIV measurements. The microCT scanner available to capture the geometry of the glass models did not have a high enough resolution to discretize the individual wire strands that make up the braided Pipeline Embolization Device. Pores near the wall of the aneurysm neck measured around $275\mu\text{m}$ wide. Figure 4-28 shows that this width is close to the width of diamonds woven from 1 mil wires stretched to 100% of their original width. However, the heights of the pores could not be measured.

Figure 4-44 shows that the placement of the flow diverter is also susceptible to the technique of the investigator. In addition to variable pore dimensions, the curvature of the overall flow diverter is also variable. In the case of RC-SOD147-12(F) and RC-SOD147-12(R), gaps can be observed between the walls of the glass models (green arrow) and the edges of the flow diverter (blue arrow). The displacement and curvature of the gaps funnel the incoming fluid differently from what was predicted in the computer simulations, where the flow diverters were in perfect contact with the walls of the flow domain. At the outer curve of the flow diverter, there is little-to-no control over the degree that the flow diverter bulges into the aneurysm. This bulge affects the incidence angle of the incoming jet of fluid relative to the flow diverter wall, which influences the flow diverting effect of the pores. Figure 4-45 illustrates the placement and curvature of the diamond pores in the computer simulations. Figure 4-46 illustrates how the actual flow diverter was shallower than the computer model when the RC-SOD147-12(F) data were taken, whereas it protruded more into the aneurysm when the RC-SOD147-12(R) data were taken.

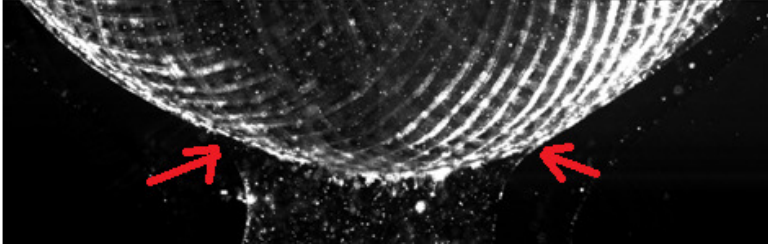
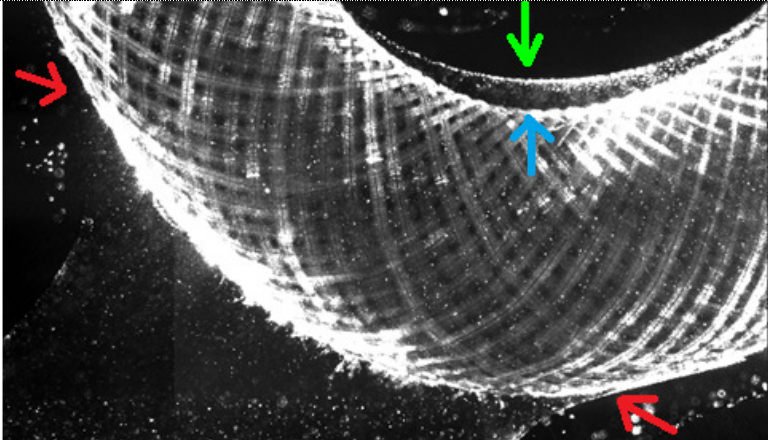
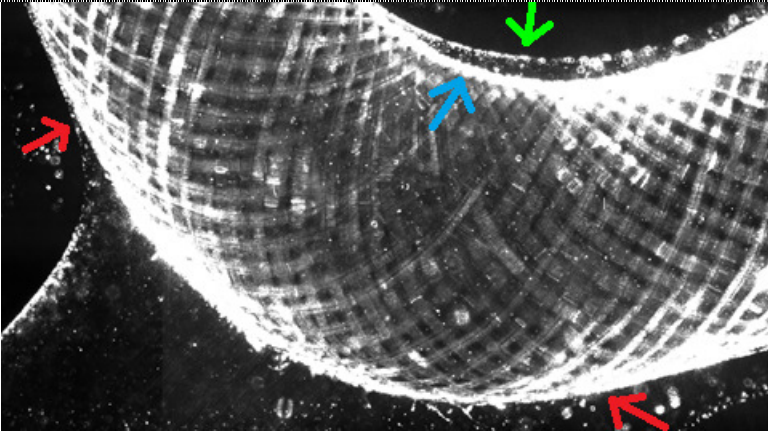
Flow Domain	Close-Up View of Deployed Flow Diverter
RC-SOD147-6	
RC-SOD147-12(F)	
RC-SOD147-12(R)	

Figure 4-44. Close up views of the flow diverters placed inside the glass models revealed that the pore dimensions were variable throughout the circumference of the flow diverter. There was also variability from run to run in the curvature of the flow diverter. While good contact was present at the upstream and downstream edges of the aneurysm neck (pointed to by red arrows), the gap between the flow diverter and the vessel wall (denoted by blue and green arrows respectively) was dependent on deployment technique of the investigator.

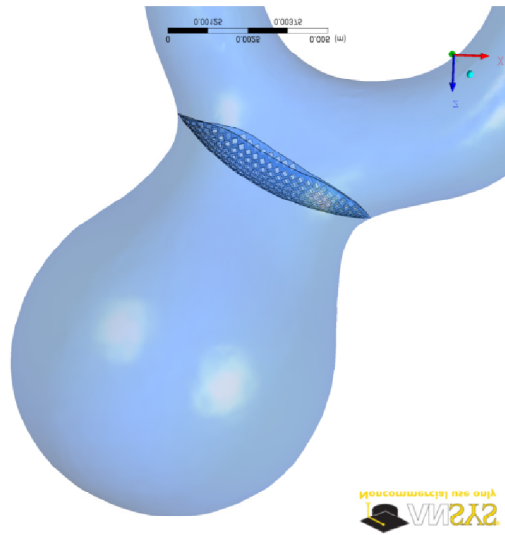


Figure 4-45. The curvature and positioning of the flow diverter in the computer model is shown.

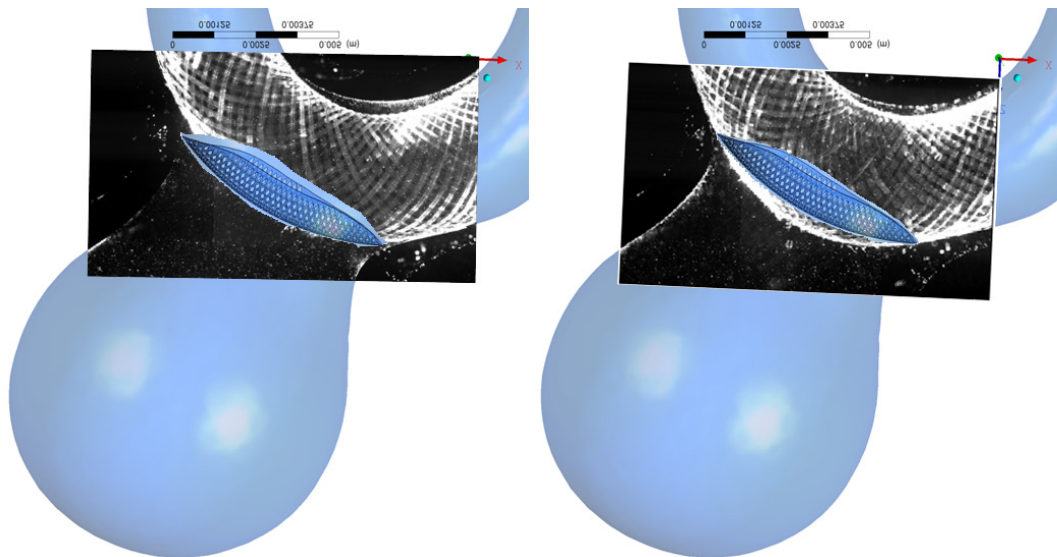


Figure 4-46 Left: The position of the flow diverter when acquiring PIV data in the RC-SOD147-12(F) domain is overlaid over the position of the flow diverter in the computer simulation. The flow diverter for the PIV data set did not protrude as much into the aneurysm compared to that in the simulation, possibly leading to diamonds thinner than the 100% stretch scenario. **Right:** The position of the flow diverter when acquiring PIV data in the RC-SOD147-12(R) domain is overlaid over the position of the flow diverter in the computer simulation. The flow diverter for the PIV data set protruded deeper into the aneurysm compared to that of the computer simulation, possibly leading to diamonds stretched out greater than the 100% stretch scenario.

Lastly, three more possibilities exist for explaining the moderate differences in the Q_T/Q_{UT} ratio between the PIV experimental observations and the CFD simulations. The first is that the fluid properties of the sodium iodide solution and the output from the peristaltic pump may have varied slightly between runs. The system is flushed with boiled water every day, requiring the addition of concentrated sodium iodide solution to maintain the correct index of refraction. This would have led to comparisons at Reynolds numbers different from 580. In regard to Figure 4-31, the Q_T/Q_{UT} ratio is affected by the Reynolds number. The second possibility is that the geometry reconstructed from the microCT scan did not fully capture the curvature of the glass model.

The third and possibly most important source of error is that the planar velocity contours of the PIV data set may have been unable to fully account for high velocity gradients on the plane and within the plane thickness. The laser sheet used to illuminate the plane has a certain thickness, essentially illuminating a 3D volume instead of a 2D plane. Illuminated particles that are used for velocity calculations are randomly distributed within this 3D volume. These averaged planar velocity contours may have led to incorrect values of V_N , which are used to calculate the Q_T and Q_{UT} from the PIV data set. Additional experimentation where different laser sheet thicknesses are used, as well as different PIV processing parameters where a denser velocity map is calculated would have shed light on the severity of this third source of error.

Despite the modest differences in the efficacy of the flow diverter observed experimentally and predicted computationally, it is fair to conclude that the simulation method was sufficiently verified to proceed with simulations in idealized geometries to predict the performance of a particular flow diverter design within a window of likely vessel geometries and flow conditions inside the human neurovasculature.

4.4 EFFECT OF FLOW DIVERTING DEVICES IN IDEALIZED GEOMETRIES

INTRODUCTION

In the foregoing section, it was concluded that the method used to represent the perforated mesh of the flow diverter was sufficient. The next step was to understand and quantify the performance of the flow diverter when placed in a range of idealized geometries, where irregularities of the aneurysm bulb shape, parent vessel diameter, curvature of the bend, and other difficult to characterize geometric features are absent. While aneurysms and vessels of the neurovasculature will deviate from these idealized models, the use of idealized flow domains allows for the identification of trends in how effective the flow diverter will be within a wide range of geometries.

METHOD

Three geometric parameters were varied. The diameter of the parent artery was kept at 3mm to mimic the upper regions of the internal carotid artery. The radius of curvature of the bend ranged from 3 to 6 mm to mimic the different tortuosities present in the human neurovasculature. The aneurysms were placed at three points along the curve of the bend, as it has been observed through prior work that it has a strong effect on the shape of the jet entering the aneurysm. Lastly, the upstream vasculature is varied between a straight inlet, a curve in the same plane as the bend in which the aneurysm lies (planar curve), and a curve perpendicular to the plane on which the aneurysm lies (perpendicular curve) to mimic the three dimensional nature of the neurovasculature.

Two different flow speeds were applied to geometries with a straight inlet to understand the effectiveness of the flow diverter when the patient has an elevated heart rate.

Flow Domain Numbers

New domain identification numbers were assigned for the idealized geometries, as shown in Table 4-8. The dimensions of interest include the parent artery diameter (PA), radius of curvature of the bend (RoC, defined as the distance from the bend center to the centerline of the vessel), the location of the aneurysm (Deg, short for degree), the diameter of the aneurysm bulb (Anu), and the length of the aneurysm neck (Neck).

The different combinations of aneurysm locations and bend radii, with their associated upstream geometries, are shown in Appendix B. For flow domains with curved upstream vessels, the radius of curvature was kept the same as the segment on which the aneurysm lies with one exception. Due to interference with the upstream vessel, the radius of curvature of the upstream segment for domain D was raised to 3.5mm. Domain D with three different upstream segments are shown in Figure 4-47. The different parameters are illustrated in Figure 4-48.

The range of vessel diameters, radii of curvature, and placement of the aneurysm were selected to roughly mimic the range of the human neurovasculature and the orientation of aneurysms around bends. The planar and perpendicular upstream curves roughly mimic the twists and turns of the internal carotid artery.

Table 4-8. The geometric parameters of the different idealized flow domains.

Domain	PA [mm]	RoC [mm]	Deg	Anu [mm]	Neck [mm]
A	3	3	90	8	4.79
B	3	4	90	8	5.07
C	3	6	90	8	5.42
D	3	3	120	8	4.75
E	3	3	60	8	4.75
F	3	4	120	8	5.06
G	3	4	60	8	5.06
H	3	6	120	8	5.45
I	3	6	60	8	5.45

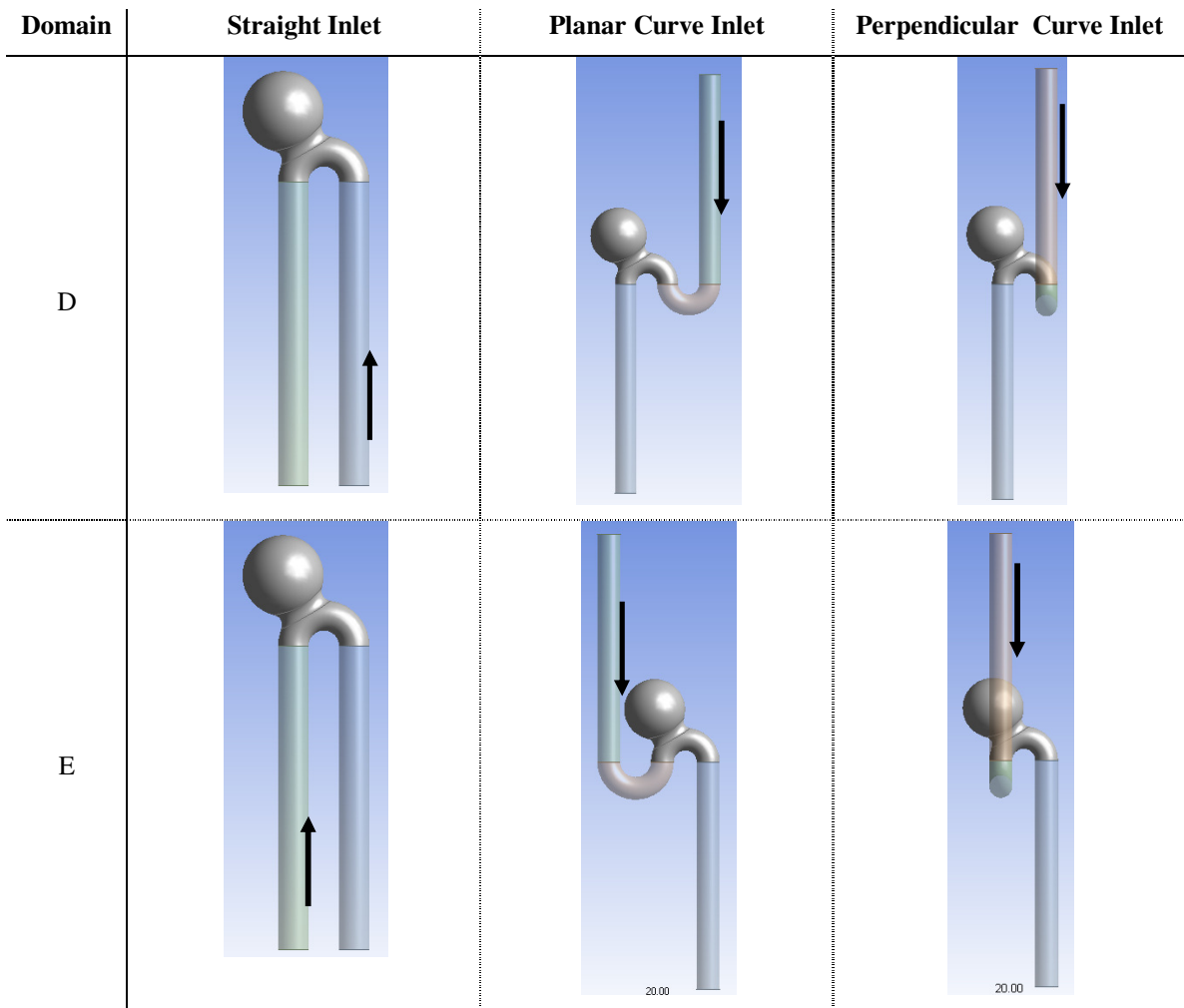


Figure 4-47. The different upstream segments for flow domains D and E are shown. The black arrow indicates the direction of flow.

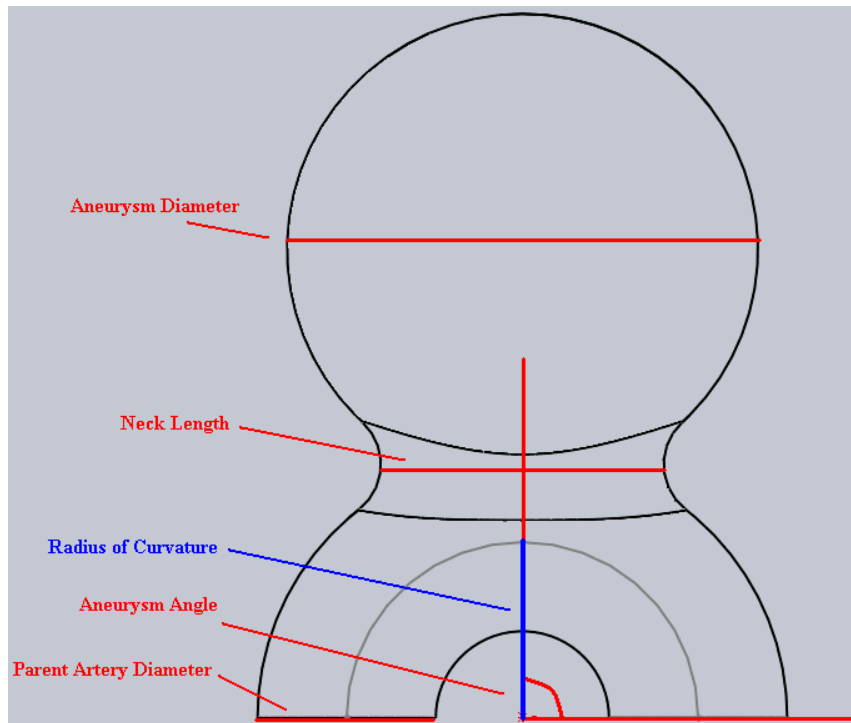


Figure 4-48. The different geometric parameters of the idealized flow domains are shown. The outline of domain A is shown.

Flow Speeds

The simulations in Chapters 4.4.1 and 4.4.2 were conducted with the flow rate profile of a resting patient at 60 beats per minute [18], or BPM. An exercise profile from [36] with the heart rate at 150BPM was used in Chapter 4.4.3 to examine the effectiveness of the flow diverter when the patient is at a moderately high activity level. The two flow profiles imposed at the inlets of the flow domains are shown in Figure 4-49. It should be noted that the two profiles were derived from different sources. Observations comparing the efficacy of the flow diverter between the two heart rates should, therefore, be cautiously applied.

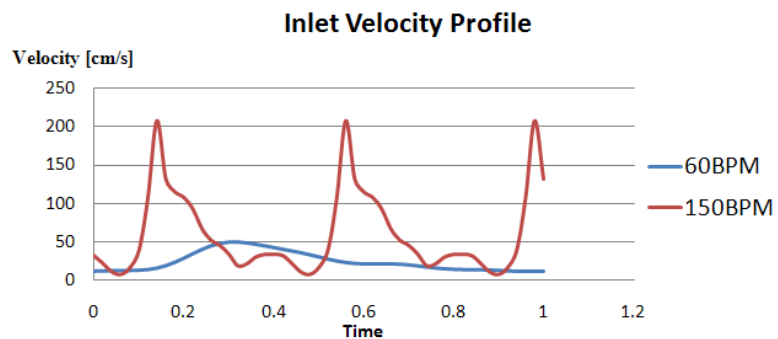


Figure 4-49. The two inlet profiles at 60 BPM [18] and 150 BPM [36] are shown.

Modeling the Flow Diverter as an Array of Diamond Shaped Pores

After examination of the Q_T/Q_{UT} ratios from Chapter 4.3, it was decided that the diamond shaped pores will be modeled with 100% stretch, as described in Figure 4-28. A minor change in the modeling method led to partial pores at the edge of the neck that more closely mimic the geometry of the flow diverter near the vessel wall. A comparison of the pore pattern used in Chapters 4.3 and 4.4 is shown in Figure 4-50.

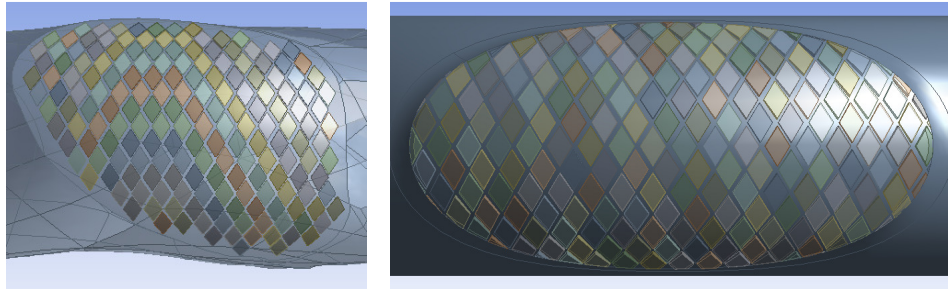


Figure 4-50. The modeling method for the pores was improved to allow for partial pores near the vessel wall. An example of the pore pattern in Chapter 4.3 is shown on the left. An example of the pore pattern in Chapter 4.4 is shown on the right. Note the presence of partial diamonds in the pore pattern of Chapter 4.4.

Simulation Plan

As illustrated in Figure 4-51, the simulations for Chapter 4.4 are grouped into answering three questions:

- 4.4.1: How well do steady simulations predict the mean behavior of the flow diverter in the presence of pulsatile flow?
- 4.4.2: What is the effect of upstream vessel geometry on the effectiveness of the flow diverter?
- 4.4.3: Is the flow diverter still effective when the patient is exercising?

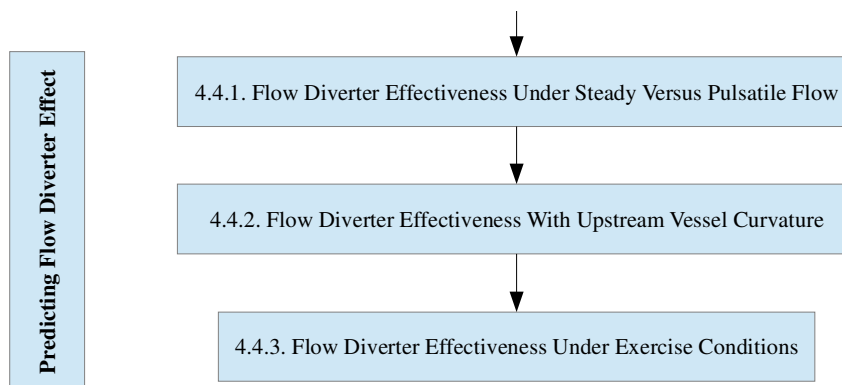


Figure 4-51. The simulations in Chapter 4.4 are grouped to facilitate the understanding of (a) how well steady flow approximates a pulsatile flow, (b) the effect of upstream curvature, and (c) the effectiveness of the flow diverter under exercise conditions.

Flow Metrics of Interest

The flow metrics of interest to be extracted from the computer simulations of idealized geometry are as follows.

The time-averaged Q , or flow rate, of blood entering the aneurysm is of interest as it is an indicator of how long blood resides inside the aneurysm before being washed out. The lower the Q , the longer blood stagnates inside the aneurysm, the more likely a clot will form to heal the aneurysm. The peak Q of blood entering the aneurysm during the cardiac cycle is of interest as it indicates the strength of the pulsed jets of blood entering the aneurysm. Dampening the peak Q reduces the oscillatory stress experienced by the aneurysm wall and also likely leads to faster clot formation. The two Q 's are measured across a plane defined at the aneurysm neck, as illustrated earlier in Figure 4-38 of Chapter 4.3.6.

The time-averaged spatial-average velocity and maximum velocity on the center plane bisecting the aneurysm is then calculated, as illustrated in Figure 4-52. The velocity is of interest because it is an indicator of how quickly blood is moving and its resistance to clumping together and forming blood clots. Due to the time-intensive nature of creating the quasi-volumetric PIV dataset as illustrated in Figures 4-35 and 4-36 of Chapter 4.3.6, it is likely that experimental and computational data presented by medical device firms, such as Covidien, to promote the effectiveness of their devices is based on the fluid behavior in the center plane of the aneurysm. Extracting simulation data from similar locations will provide insight into the validity of such claims.

The time-averaged wall shear stress (WSS) at the aneurysm neck is also calculated, as illustrated in Figure 4-52. Reduction of WSS reduces the likelihood of aneurysm rupture due to mechanical stress imposed on the tissue wall at the impact site where the jet entering the aneurysm impinges on the vessel wall.

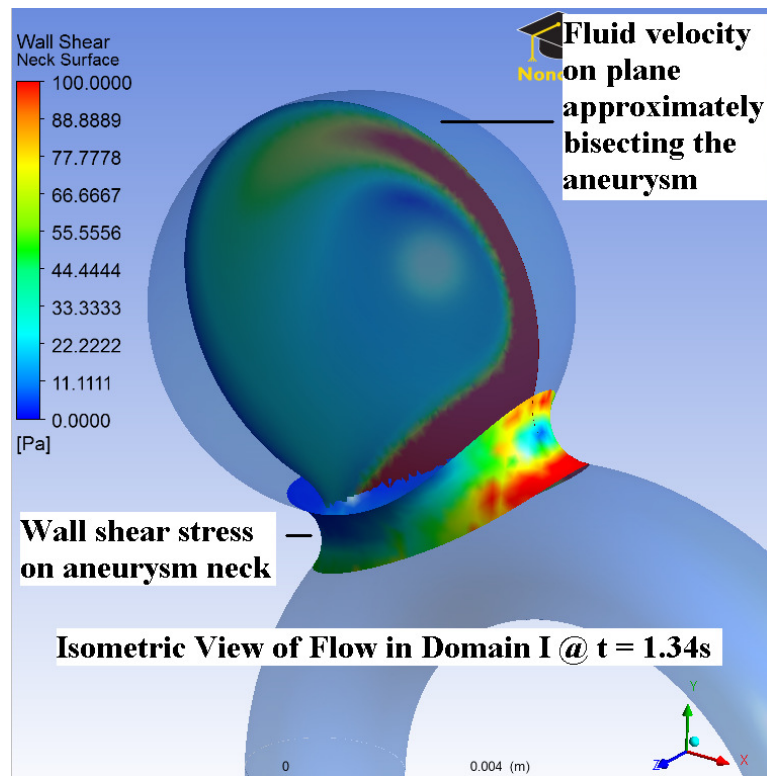


Figure 4-52. The center plane bisecting the aneurysm and the aneurysm neck are shown. The velocity of blood is calculated on the center plane. The wall shear stress is calculated at the neck. The typical convention with color contours is blue at the bottom and red at the top of the range.

OBSERVATIONS

4.4.1: Comparing Flow Diverter Effectiveness for Steady Flow and Pulsatile Flow

The time averaged flow rate of fluid entering the aneurysm is summarized in Figure 4-53. The peak flow rate entering the aneurysm throughout the cardiac cycle is summarized in Figure 4-54. The time-averaged maximum fluid velocity on the center plane of the aneurysm and the time-averaged spatial average fluid velocity on the center plane of the aneurysm are summarized in Figures 4-55 and 4-56. The time averaged WSS at the aneurysm neck for the different domains are summarized in Figure 4-57. The time-dependent flow rates in the different domains are conveyed in Appendix B.

The flow rates from simulations with a steady inlet are generally slightly greater than those with a pulsatile inlet. However, the effectiveness of the flow diverter (Q_T/Q_{UT}) is very similar between the steady flow approximation and the time-average value from the pulsatile flow simulations. The Q_T/Q_{UT} ratios were also very similar between the peak and time-averaged Q_T/Q_{UT} ratios of the pulsatile inlet.

There was little difference between the steady inlet and the pulsatile inlet for the max V, avg V, and avg WSS metrics. The largest difference was in the time-averaged max V for domains D and E, where there was a 5 – 8% difference in the Max V_T/V_{UT} ratios between the time-averaged pulsatile value and the steady state approximation. The average WSS at the neck was reduced by about 50% in nearly all geometries. The flow diverter was relatively ineffective in domain E. However, the WSS in domain E with the flow diverter presented was in close proximity to that found in the other domains.

This set of simulations suggests that the steady inlet simulations may be a reasonable approximation of time-averaged values of the pulsatile inlet condition. However, the reduction of average velocity on the center plane over-predicts reduction in flow (Q) into the aneurysm. For example, in domain A, the time-averaged spatial average velocity (Avg V) dropped by ~90%, but the flow rate (Q) only dropped by ~75%.

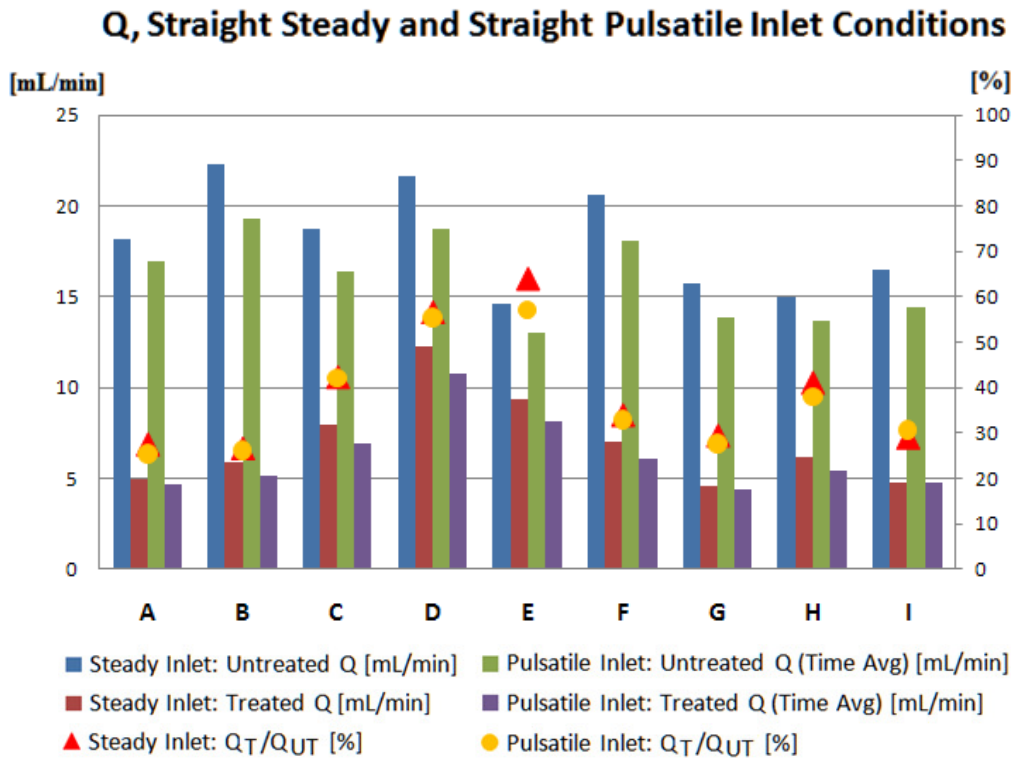


Figure 4-53. The flow rates of fluid entering the aneurysms in the simulations with steady flow are compared to the time-averaged flow rates in simulations with a pulsatile flow. In general, the steady flow slightly over-predicted the flow rates, but the Q_T/Q_{UT} ratios are very similar.

Peak Q, Straight Pulsatile Inlet Conditions

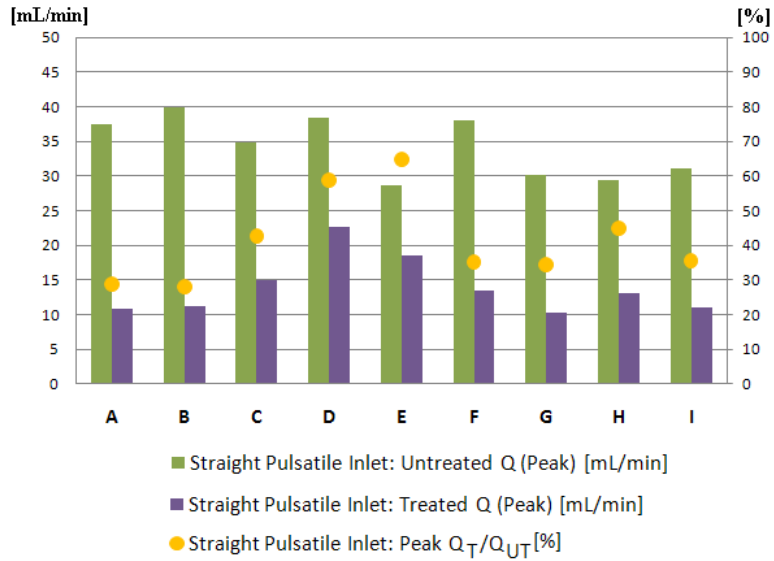


Figure 4-54. The peak flow rates of fluid entering the aneurysms during the cardiac cycle are shown. The peak Q_T/Q_{UT} ratios are very similar to the time-averaged ratios shown in Figure 4-53.

Max V in Center Plane, Straight Steady and Straight Pulsatile Inlet Conditions

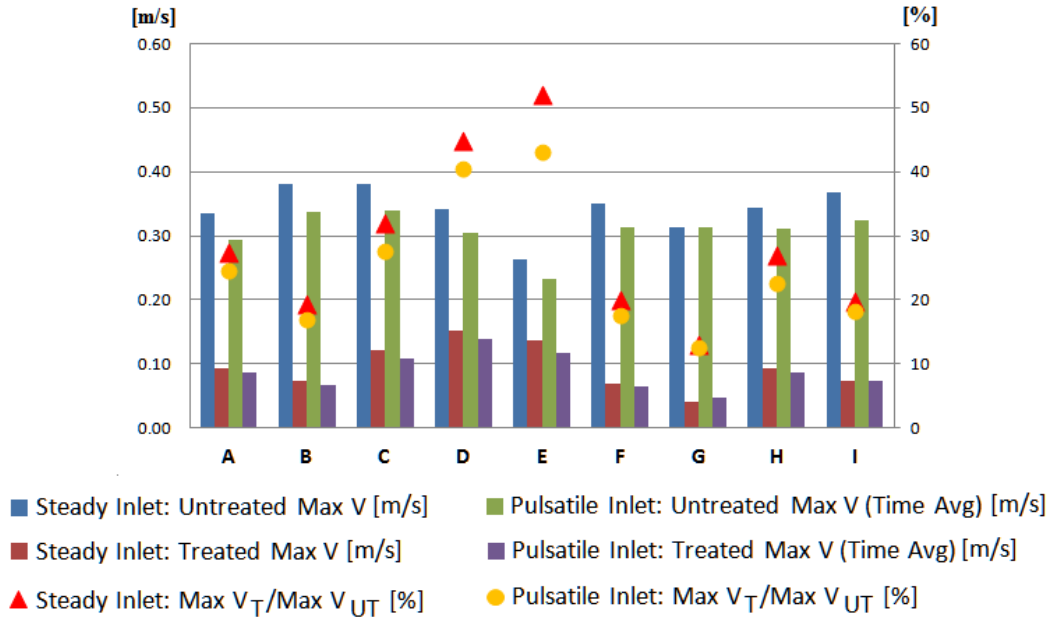


Figure 4-55. The maximum velocities of fluid in the center plane inside the aneurysms in the simulations with steady flow are compared to the time-averaged maximum velocities in simulations with a pulsatile flow. In general, the steady flow slightly over-predicted the maximum velocities, but the Max V_T/V_{UT} ratios are very similar.

Avg V in Center Plane, Straight Steady and Straight Pulsatile Inlet Condition:

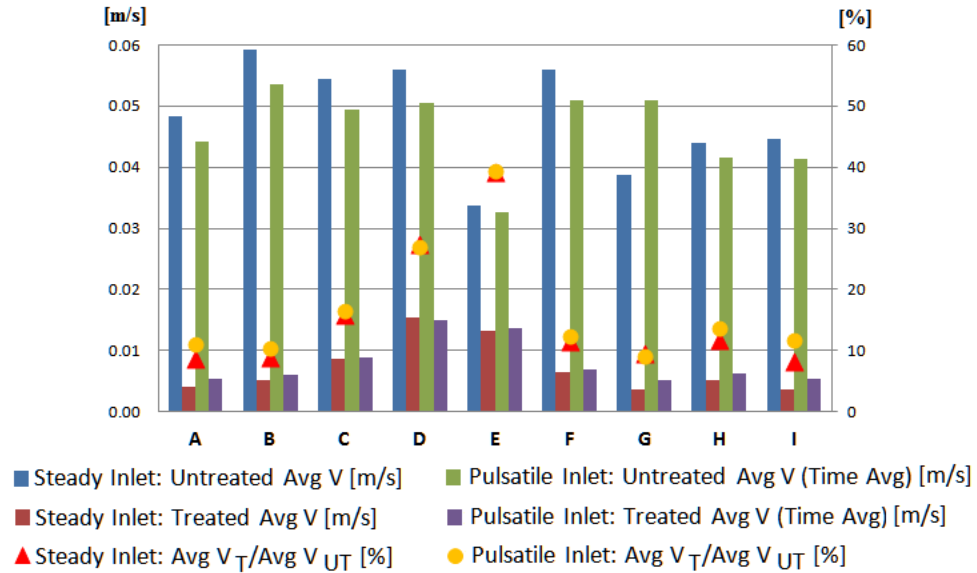


Figure 4-56. The average velocities of fluid in the center plane inside the aneurysms in the simulations with steady flow are compared to the time-averaged spatial-average velocities in simulations with a pulsatile flow. In general, the steady flow slightly over-predicted the average velocities, but the Avg V_T/V_{UT} ratios are very similar.

Avg WSS at Neck, Straight Steady and Straight Pulsatile Inlet Conditions

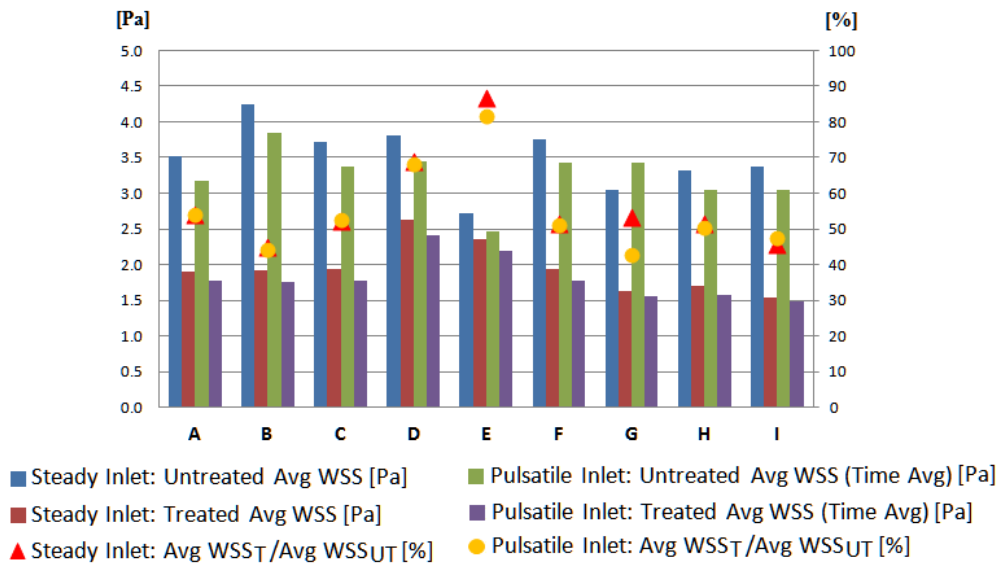


Figure 4-57. The average WSS at the aneurysm neck was examined for the different domains with a steady or a pulsatile inlet flow. The steady flow simulation slightly over-predicted the WSS in all scenarios except for domain G.

4.4.2: Effectiveness of the Flow Diverter in the Presence of Upstream Vessel Curvature

The time averaged flow rate of fluid entering the aneurysm is summarized in Figure 4-58. The time-averaged maximum fluid velocity and the time-averaged spatial-average fluid velocity on the center plane of the aneurysm are summarized in Figures 4-59 and 4-60. The time-averaged WSS at the aneurysm neck for the different domains are displayed in Figure 4-61. The time-dependent flow rates in the different domains are shown in Appendix B.

In general, the presences of an upstream planar curve segment greatly disrupted the flow entering the aneurysm. The flow entering the untreated aneurysm increased with the radius of curvature. Only one domain (H) had flows in the planar curve similar to flows found in the perpendicular curve and the straight inlet. Interestingly, the Q_T/Q_{UT} ratios in domains with a planar curve were always a few percentage points lower than those with a perpendicular curve upstream segment. Referring back to Figure 4-31, the Q_T/Q_{UT} ratios were also lower when the Reynolds numbers for the flow domains were lower.

In general, the effectiveness of the flow diverter in reducing flow into the aneurysms was similar between domains with a straight inlet (Figure 4-53) versus a perpendicular curve upstream (Figure 4-58). More noticeable differences were observed when comparing the reduction in maximum and averaged velocities inside the aneurysm.

This set of simulations suggests that the upstream geometry has negligible effect on the effectiveness of the flow diverter in reducing flow into the aneurysm. However, it must be understood that flow into aneurysms with a planar upstream segment already have low flow (Q_{UT}) before placement of the flow diverter. With clinical data in hand, this may lead to an estimation of the upper threshold of Q where clot formation inside the aneurysm can be induced.

Q, Planar Curve and Perpendicular Curve Pulsatile Inlet Conditions

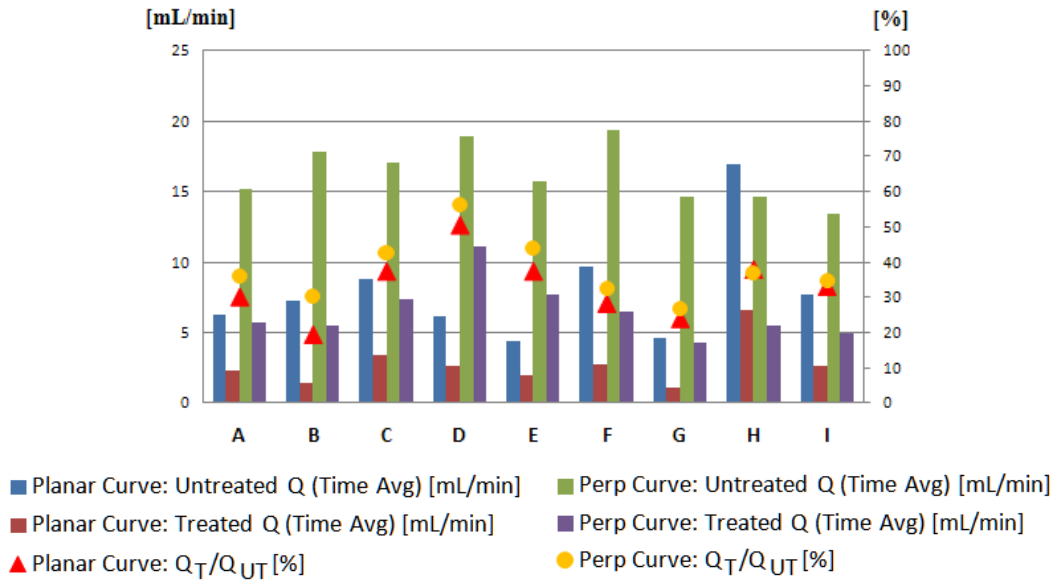


Figure 4-58. The time-averaged flow rates of fluid entering the aneurysms in the simulations with a planar curve upstream segment are compared to the time-averaged flow rates in simulations with a perpendicular curve upstream segment. In general, flow into aneurysms with a planar curve upstream segment was a portion of that into aneurysms with a straight or perpendicular curve upstream segment.

Max V in Center Plane, Planar Curve and Perpendicular Curve Pulsatile Inlet Conditions

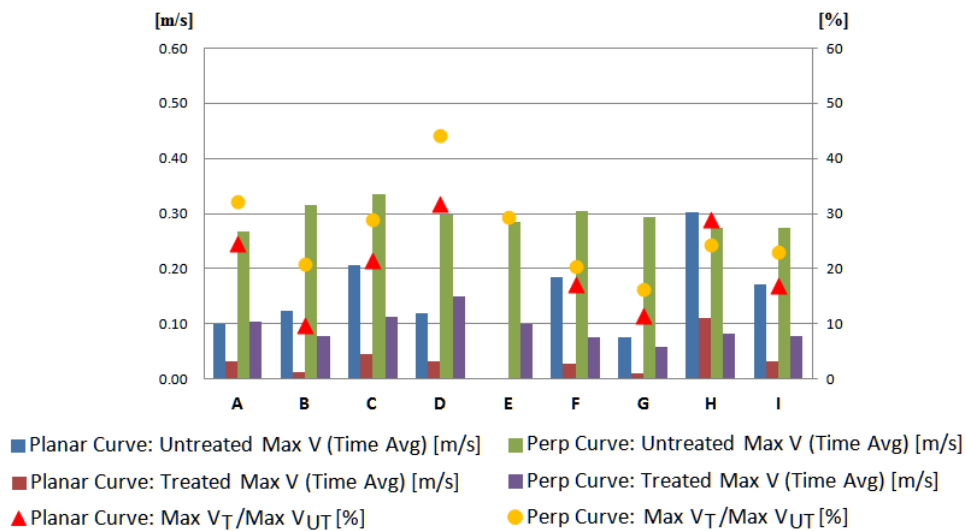


Figure 4-59. The time-averaged maximum velocities of fluid in the center plane inside the aneurysms with a planar curve upstream segment are compared to the velocities inside aneurysms with a perpendicular upstream segment. In general, the flow diverter was less effective in reducing the time averaged maximum velocity in the presence of a perpendicular upstream curve than in the presence of a planar upstream curve.

Avg V in Center Plane, Planar Curve and Perpendicular Curve Pulsatile Inlet Conditions

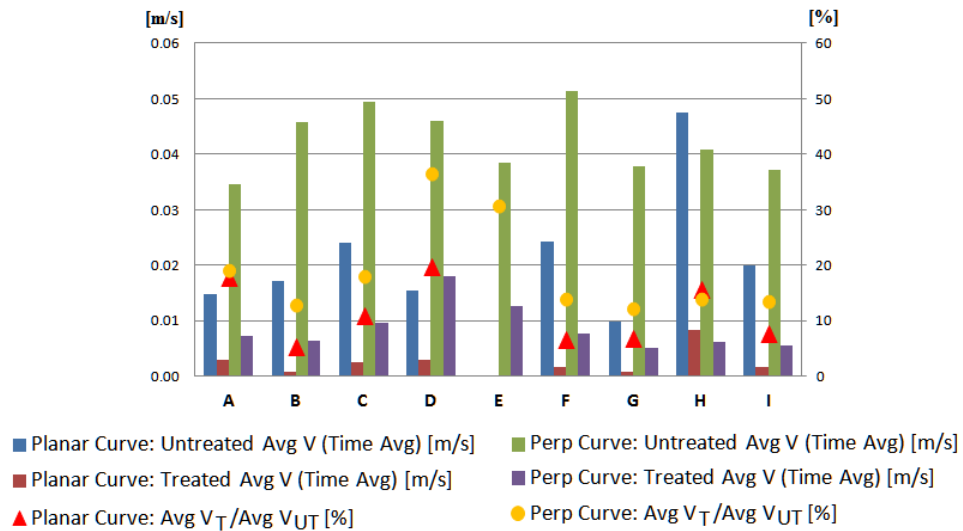


Figure 4-60. The time-averaged spatial-average velocities of fluid in the center plane inside the aneurysms with a planar curve upstream segment are compared to the velocities inside aneurysms with a perpendicular upstream segment. In the presence of a planar curve upstream segment, the average velocity in the center plane of the aneurysm increased with the radius of curvature. However, average velocity was generally lower compared to when a perpendicular vessel segment was upstream of the aneurysm.

Avg WSS at Neck, Planar Curve and Perpendicular Curve Pulsatile Inlet Conditions

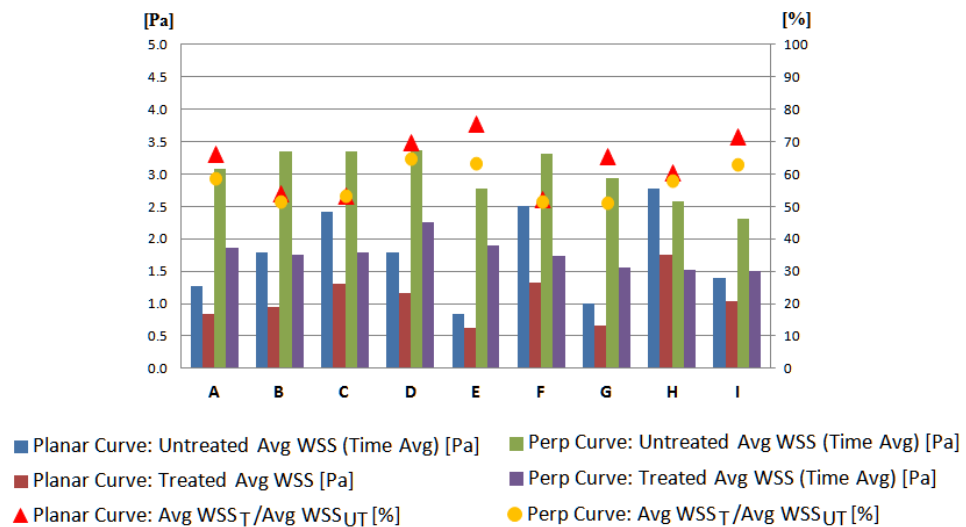


Figure 4-61. The time-averaged WSS at the aneurysm neck for domains with a planar curve upstream segment are compared to the WSS for domains with a perpendicular upstream segment. The flow diverter was roughly equally effective in reducing WSS. However, aneurysm necks with a perpendicular upstream curve generally experienced higher WSS than aneurysm necks with planar upstream curve vessels.

4.4.3. Effectiveness of Flow Diverter at Exercise Conditions

The time averaged flow rate of fluid entering the aneurysm is conveyed in Figure 4-62. The peak flow rate entering the aneurysm is presented in Figure 4-63. The time averaged maximum fluid velocities on the center plane of the aneurysms and the spatial-average fluid velocities on the center plane of the aneurysms are displayed in Figures 4-64 and 4-65. The time averaged WSS at the aneurysm neck for the different domains are summarized in Figure 4-66. The time dependent flow rates in the different domains are shown in Appendix B.

The Q_T/Q_{UT} ratios at 150BPM were several percentage points higher than those at 60BPM. Much like what was already observed in Figure 4-31, the Q_T/Q_{UT} ratios were higher when the Reynolds numbers were higher.

The difference in ratios of treated to untreated values between 60BPM and 150BPM became much more noticeable when examining the velocities in the center plane of the aneurysm. There the max and average V_T/V_{UT} ratios for the 150BPM simulations were on average about 15 and 20% higher than for the 60BPM simulations. As mentioned in the metrics of interest, the velocity is also of interest because it has a local effect on the formation of blood clots.

The effectiveness of the flow diverter in reducing the mean WSS in the aneurysm neck was similar between 60BPM and 150BPM for most domains. Two outliers were observed in domains E and G, where the flow diverter was significantly less effective in reducing the mean WSS under exercise conditions than under rest conditions. It is of concern that even with the presence of the flow diverter, the average WSS_T at exercise is still multiples of the WSS_{UT} at rest.

The outcomes of this set of simulations suggest that additional research is needed for post-operative management of patients after the treatment of aneurysms using a flow diverter. The Q_T at 150BPM was in most cases as high as the Q_{UT} at 60BPM. The average V_T at 150BPM was on par with the average V_{UT} in the center plane of the aneurysm at 60BPM. 150 BPM is well within the range of heart rate observed for moderate exercise. If the patient is up and walking within days of minimally invasive surgery before clot formation inside the aneurysm, the efficacy of the flow diverter is detrimentally affected.

Additional research is needed to better understand the velocity profiles of blood inside the neurovasculature. Jiang [36] measured blood flow in select blood vessels at different exercise levels for the same subjects and compared intraaneurysmal flow between rest and exercise conditions. In hindsight, the simulations of chapters 4.4.1 and 4.4.2 should have been conducted using pulsatile profiles from the same reference. However, it should be noted that the resting profiles from Stuhne [66] and Devault [18] are

noticeably different than the resting profile from Jiang [36]. Simulations of a wider variety of pulsatile profiles will lead to a better understanding if the post-operative management of patients is needed.

Q, Straight Pulsatile 60BPM and 150BPM Inlet Conditions

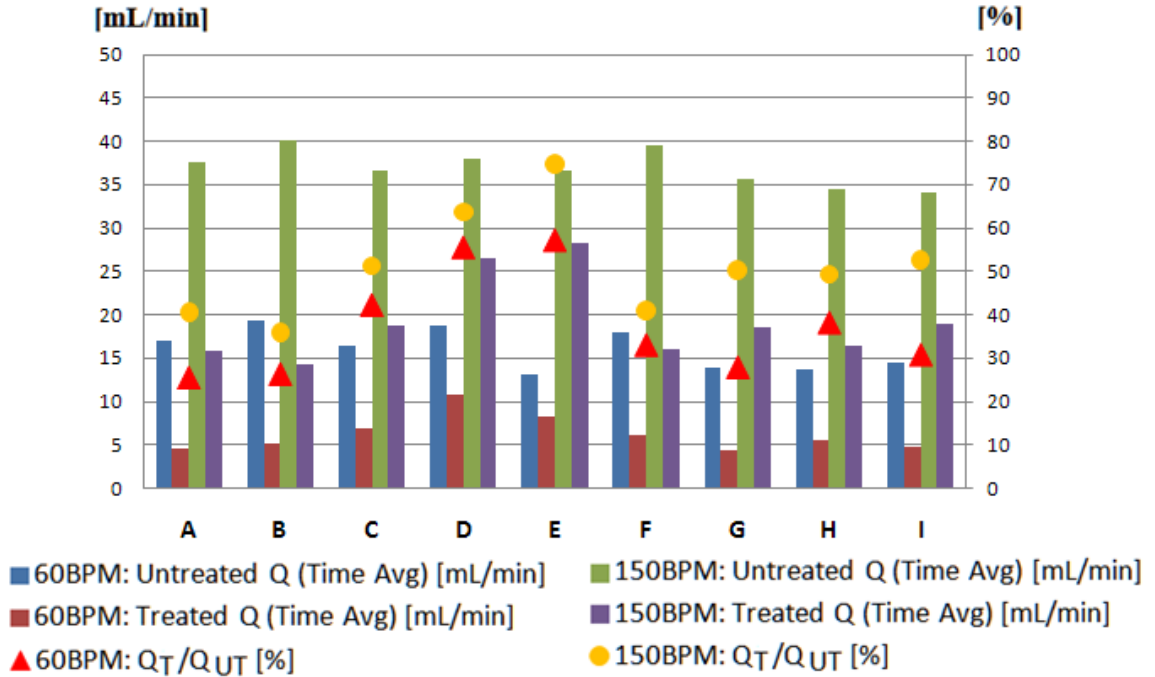


Figure 4-62. The time-averaged flow rates of fluid entering the aneurysms in the simulations with a 60BPM inlet profile are compared to the time-averaged flow rates in simulations with a 150BPM inlet profile. Intraaneurysmal flow after placement of a flow diverter was higher in exercise conditions than the untreated aneurysm at rest.

Peak Q, Straight Pulsatile 60BPM and 150BPM Inlet Conditions

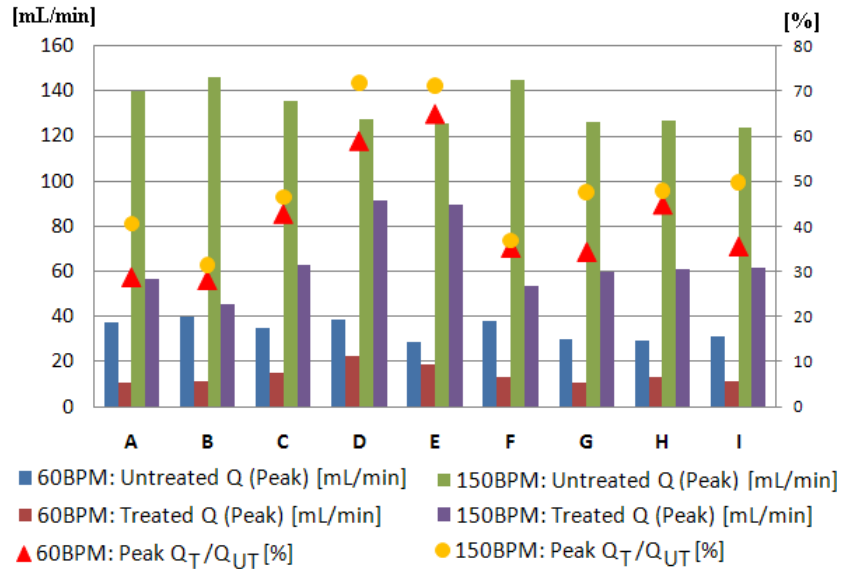


Figure 4-63. The peak flow rates of fluid entering the aneurysms in the simulations with a 60BPM inlet profile are compared to the peak flow rates in simulations with a 150BPM inlet profile. Intraaneurysmal flow after placement of a flow diverter was higher in exercise conditions than the untreated aneurysm at rest.

Max V in Center Plane, Straight Pulsatile 60BPM and 150BPM Inlet Conditions

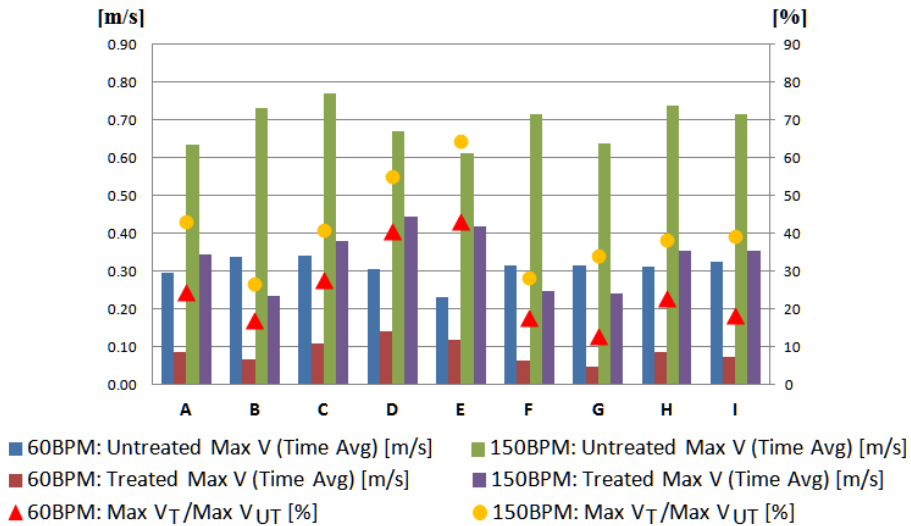


Figure 4-64. The time-averaged maximum velocities of fluid in the center plane inside the aneurysms with a 60BPM inlet profile are compared to the time-averaged maximum velocities in simulations with a 150BPM inlet profile. The flow diverter was less effective in reducing the time averaged maximum velocity in the center plane of the aneurysm in all domains.

Avg V in Center Plane, Straight Pulsatile 60BPM and 150BPM Inlet Conditions

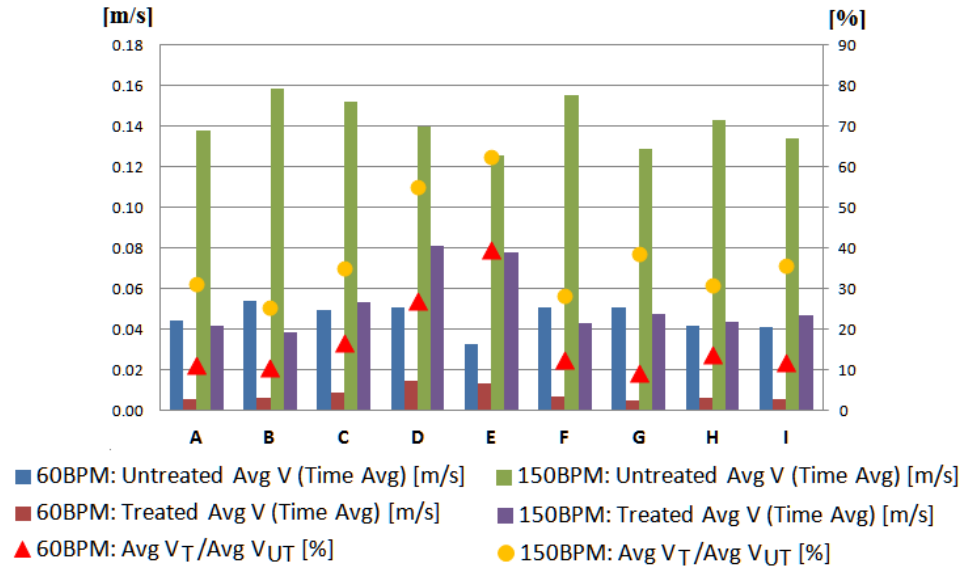


Figure 4-65. The time-averaged average velocities of fluid in the center plane inside the aneurysms with a 60BPM inlet profile are compared to the time-averaged average velocities in simulations with a 150BPM inlet profile. The flow diverter was less effective in reducing the time averaged spatial average velocity in the center plane of the aneurysm in all domains.

Avg WSS at Neck, Straight Pulsatile 60BPM and 150BPM Inlet Conditions

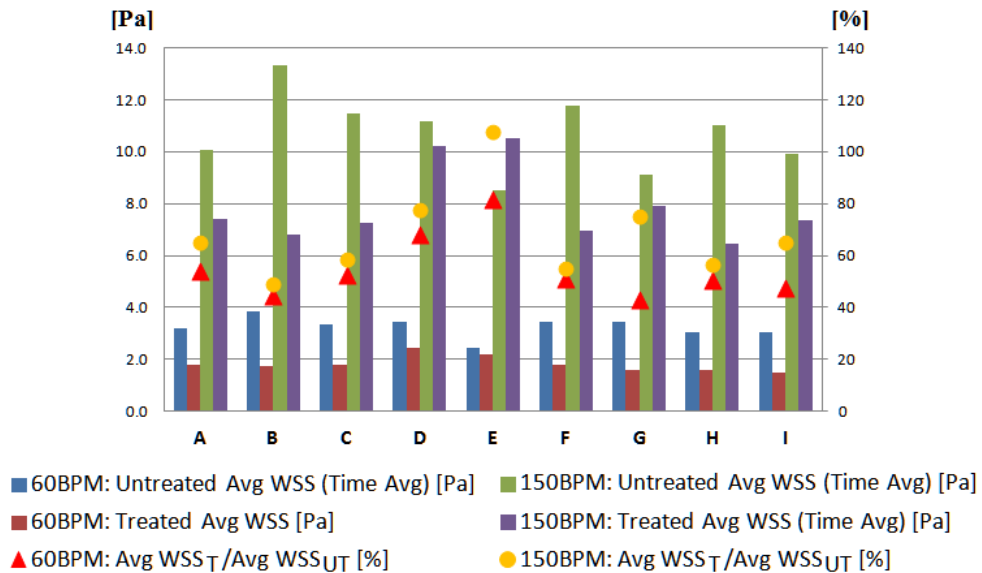


Figure 4-66. The time-averaged WSS at the aneurysm neck for domains with a 60BPM inlet profile are compared to the time-averaged WSS in simulations with a 150BPM inlet profile. Exercise greatly increases the WSS experienced at the wall of the aneurysm neck, even after placement of the flow diverter.

4.5 DISCUSSION OF COMPUTER SIMULATIONS

Verification in its strictest sense would require “point by point comparison with a number of gold standards to understand variability and accuracy. For intraaneurysmal hemodynamics, this is simply not possible because no proven in vivo method...is available. Also, because the mechanisms for the pathogenesis of aneurysms...are not well understood, it is not known which variables are important and what level of accuracy is needed for clinical purposes.” [100] Therefore, verification of CFD simulations using PIV results in this body of research was limited to a *qualitative comparison* of velocity profiles at select planes in the aneurysm and a *quantitative comparison* of the total flow rate of blood entering the aneurysm.

However, verification of the simulations using PIV data is important because, once verified, the simulations can provide certain information, such as flow rate of blood crossing the aneurysm neck or wall shear stress, that would be very difficult to obtain experimentally. Confidence in the computer simulations allows for rapid extraction of fluid flow information anywhere in the flow domain. Changes to the vessel geometry or pulsatile flow conditions are relatively simple to implement numerically. Much of the computation activity is handled by the CFX software, allowing a researcher or engineer to focus on the interpretation of results. However, special care must be taken when simulations are performed for conditions that lie beyond the range verified using experimental results. Unexpected flow phenomena may occur.

The verification comparison discussed in Chapter 4.3.6 demonstrated that the simplification of the flow diverter geometry by modeling it as an array of diamond shaped pores connecting the parent artery to the aneurysm resulted in similar flow rates of fluid entering the aneurysm compared to experimental results. With reference to Figures 4-39 and 4-41, flow entering the aneurysm in the RC-SOD147-6 and RC-SOD147-12(R) domains exhibited remarkable similarity between the PIV and CFD results. A somewhat greater difference was observed with RC-SOD147-12(F), but Figure 4-42 illustrates that the Q_T/Q_{UT} ratio was within the range predicted when the diamond shaped pores were stretched +0%, +50%, and +100% of the initial width.

The deployed shape of the Pipeline Embolization Device is highly non-uniform and can lead to discrepancies between the PIV experimental results, the CFD simulation results, and what actually happens clinically (inside a patient). The curvature of the flow diverter is assumed in the computer simulations to roughly follow the curvature of the parent vessel, as illustrated in Figures 4-21 and 4-45. However, Figure 4-46 quite clearly illustrates that the deployed shape of the PED deviates from this assumed shape. Figure 4-44 also illustrates that the shape of the pores vary along the circumference of the

device. All of these geometric deviations contribute to differences between what is observed experimentally and what is predicted computationally.

As illustrated by Figure 4-31, the effectiveness of the flow diverter in reducing the flow rate of blood entering the aneurysm is dependent on the final shape of the diamond-shaped pores. As such, the flow diverter should be designed in such a manner to sufficiently retard flow entering the aneurysm regardless of the deployment technique of the physician and the bend imposed by the surrounding vascular geometry.

Once it is accepted that modeling the flow diverter as an array of diamond shaped pores is a reasonable approach to assess the effect of geometry, simulations carried out in idealized geometry demonstrated that the effectiveness of the flow diverter varied depending on the radius of curvature of the parent artery, the location of the aneurysm along the bend, and the geometry of the upstream vasculature. Referring to Figure 4-67, reduction in flow entering the aneurysm after placement of the flow diverter varied from as high as ~80% to as low as ~40%. The geometry of the upstream vessel had a minor influence, with the largest variability observed in domain E, as described in Figure 4-47. This is a reasonable outcome, as the incoming fluid profile is largely shaped by the upstream geometry and experiences only minor alteration by the bend in the parent artery before entering the aneurysm.

Q_T and Q_T / Q_{UT} in Domains with Different Upstream Segments

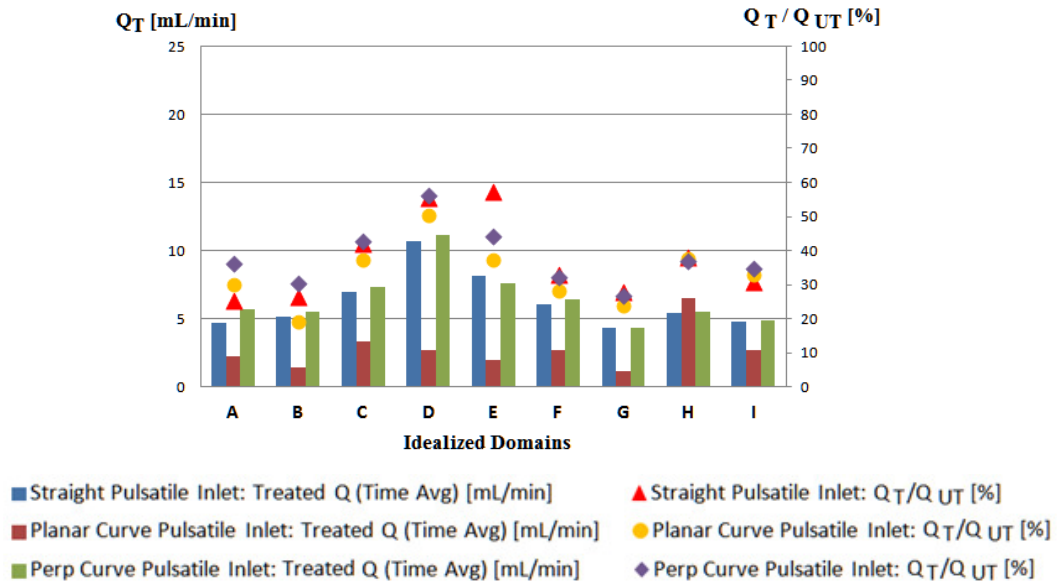


Figure 4-67. The flow rates entering treated aneurysms (Q_T) for domains with a straight, planar curve, and perpendicular curve upstream segment are compared. The effectiveness of the flow diverter (defined as the Q_T/Q_{UT} ratio) is also compared.

This outcome suggests that future studies should also vary the aneurysm neck dimension in combination with the radius of curvature of the parent artery to determine which combinations result in a greater intraaneurysmal flow. The original purpose for investigating domains RC-SOD147-6, RC-SOD147-12(F), and RC-SOD147-12(R) was to experimentally observe how the position of the aneurysm along the bend affects intraaneurysmal flow. These experimental domains were analogous to the idealized domains C, H, and I (defined in Chapter 4.4) respectively. Reconstruction of the internal geometry of the glass models highlighted the significant difference in the lengths of the aneurysm necks. If it is kept in mind that simulations in experimentally derived domains were performed with an inlet Reynolds number different from that of the idealized domains, Figure 4-68 illustrates that if the dimensions of the aneurysm neck are kept somewhat constant, the flow entering the aneurysm should be similar (Q_T of domains C, H, and I). It was predicted that when the aneurysm is biased away from the inlet (domain H), flow entering the aneurysm is less than when the aneurysm is biased towards the inlet (domain I). This is opposite of what was observed in the experimentally derived domains (-12(F) and -12(R) respectively). Figure 4-69 illustrates how it is difficult to quantify the complexities of non-idealized geometry. The bend of the parent artery is slightly irregular. The curvature of the upstream aneurysm neck is different between the forward (F) and reverse (R) orientations.

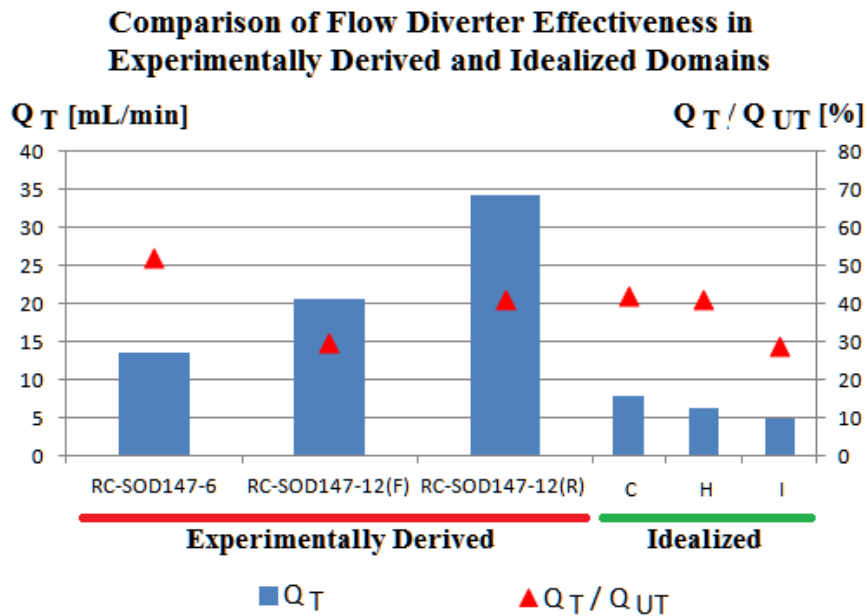


Figure 4-68. The flow rates of blood into aneurysms with the flow diverter present (Q_T) are compared between the experimentally derived flow domains and their idealized analogues. The effectiveness of the flow diverter is also compared. Please note that computer simulations in the experimentally derived domains were conducted with a $Re = 580$, whereas simulations in the idealized domains were conducted with a $Re = 270$. Therefore, the absolute flow rates between the two groups should not be compared.

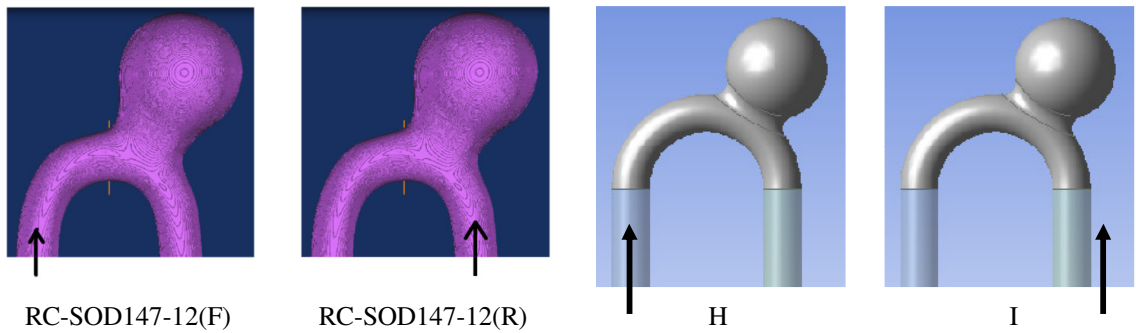


Figure 4-69. The geometry derived from the glass models are compared to their idealized analogues. The black arrow indicates the inlet flow. It is difficult to quantify the slight irregularities of the bend in the parent artery. It is also difficult to determine the effect of aneurysm angular offset when the curvature of the aneurysm neck is different between the two sides of the aneurysm.

There is ambiguity in the claim made by Covidien of the Pipeline Embolization Device, where an “85% reduction in circulation within [the] aneurysm” occurs after placement of the device [101]. Of the different metrics examined from the computer simulations, the metric that experienced a drop close to 85% is the time-averaged spatial-average velocity in the center plane inside the aneurysm. However, it should be noted that in the presence of the tightest curves (A, D, and E), the reduction was limited to around 60 - 70%, as illustrated in Figure 4-70. It is unfortunate that the testing methods used to establish this claim of “85% reduction in circulation” is not publicly available for study. Different flow domains and simulation parameters may have been used by the Chestnut Medical (or Covidien) engineering staff.

Max V_T / V_{UT} and Avg V_T / V_{UT} in Domains with Different Upstream Segments

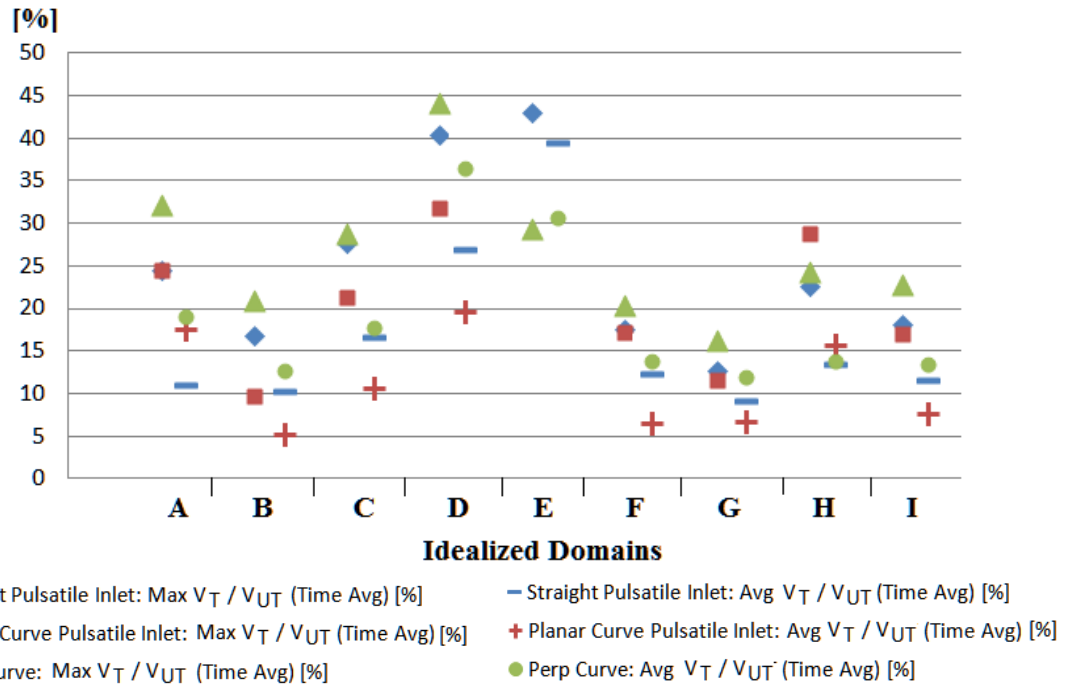


Figure 4-70. The treated to untreated ratios of time-averaged maximum ($Max V_T / V_{UT}$) and spatial-average ($Avg V_T / V_{UT}$) velocities in the center plane of the aneurysm are compared for three different upstream vessel configurations. Of the metrics compared in this body of research, the closest metric that matched PED’s marketing claim of “85% reduction in circulation” is the time-averaged spatial-average velocity.

In general, flow rates of blood entering the aneurysm in domains with an upstream planar curve were a fraction of the flow rates with a straight or perpendicular curved upstream segment. The difference was so great that in most situations (with domain H being the exception), flow entering a treated aneurysm with a straight or a perpendicular curve upstream vessel segment was similar or higher than that of the untreated aneurysm with a planar curve upstream segment. Figure 2-3 shows that an upstream planar curve is largely confined to the C1 to C3 segments of the internal carotid artery. This may partially explain the paucity of aneurysms found in this region of the neurovasculature, as blood inside any aneurysm that forms will likely stagnate and coagulate, thereby healing the aneurysm.

The remarkable increase in the flow rate of blood entering the aneurysm under exercise conditions suggests that post-operative management of the patient should include a regimen of reduced physical activity until the clot forming inside the aneurysm has reached a certain size. However, it should be noted that the pulsatile inlet flows used for the simulations came from different literature citations. The activity level of the patient, flow measurement method, and variability within the general population means that additional research using a distribution of inlet flow profiles should be pursued to understand if a rest regimen should be imposed for some time after placement of a flow diverter.

A better understanding of physiological conditions would lead to greater insight as to what flow metrics are responsible for the coagulation of blood inside the aneurysm to initiate healing. Other researchers are pursuing blood coagulation models coupled with fluid dynamic simulations [102, 103] to understand the progression of clot formation inside untreated aneurysms. Application of these techniques to aneurysms clinically treated with a flow diverter will allow for validation of these blood coagulation models. The qualitative metrics developed by Cebal [61] can also be applied to predict the likelihood of aneurysm rupture while the clot is forming inside the aneurysm.

Ultimately, animal studies are needed to validate the blood coagulation models and to establish minimum flow reduction thresholds, or some other indicator that predicts a positive outcome. This requires a better understanding of the fluid mechanics of aneurysms created in rabbits. Biochemical responses such as tissue inflammation and immune response to the flow diverter material also influence the ultimate efficacy of the device.

5.0: *IN VIVO* EXPERIMENTS

5.1. SPECIFIC AIMS OF *IN VIVO* EXPERIMENTS

Male New Zealand rabbits weighing around 3.5 to 4.5kg at time of surgery were used. Rabbits were selected because of ease of handling (compared to dogs or pigs), relatively low cost, and history of use as the animal model for evaluating flow diverters. Figure 5-1 summarizes the research plan for this portion of the dissertation.

The main objectives for the animal studies were to:

1. Develop surgical techniques for creating aneurysms in rabbits and maintaining them for survival studies.
2. Explore the limits of the elastase induced aneurysm model in terms of the size and shapes of aneurysms that can be created.
3. Obtain information on blood flow in nearby vessels to understand the remodeling response after ligation of the left common carotid artery.
4. Predict the initial flow conditions at the time of flow diverter placement across the aneurysm using CFD simulations.

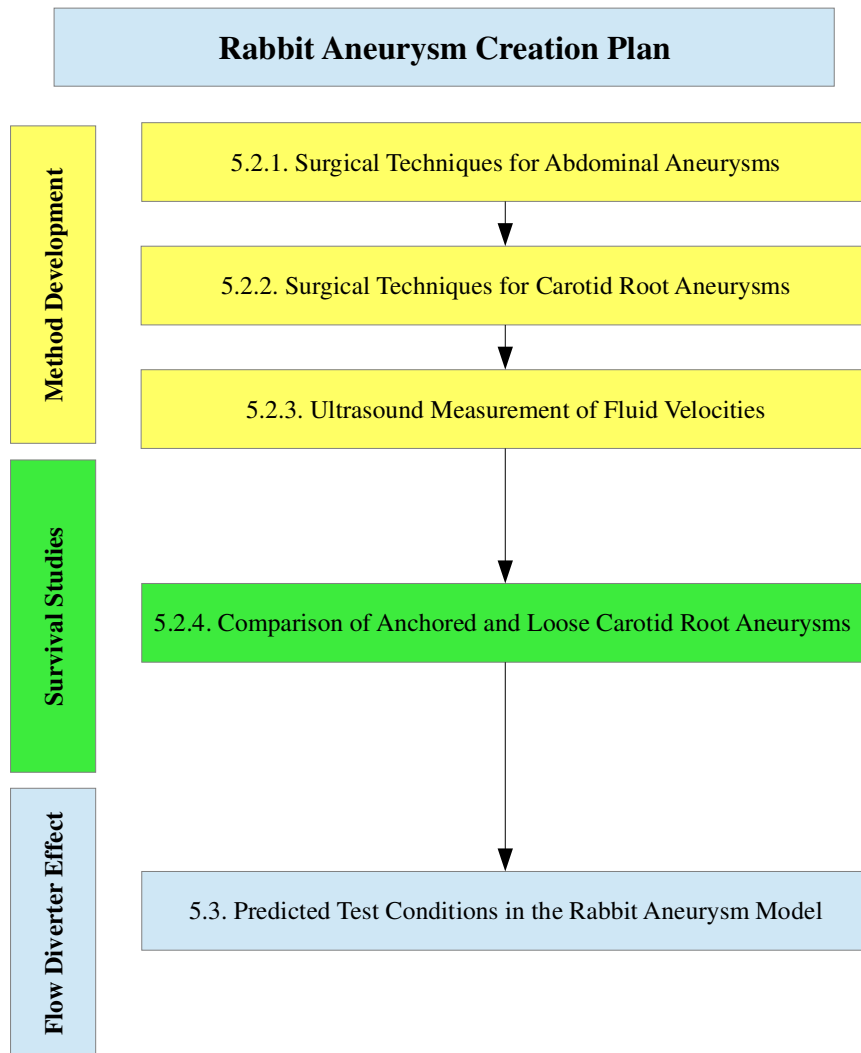


Figure 5-1. The animal research consisted of exploring the limits of the elastase induced aneurysm creation technique, refining surgical techniques for survival studies, measuring the flow of blood in vessels near the aneurysm, and predicting the flow of blood entering the aneurysm prior to placement of a flow diverter.

5.2. DEVELOPMENT OF AN IMPROVED RABBIT ANEURYSM MODEL

5.2.1. Surgical Techniques for Abdominal Aneurysms

The creation of aneurysms was first attempted on the abdominal aorta. The ease of surgical entry and a large, straight segment of vessel allowed for the experimentation with different application techniques and concentrations of porcine elastase (Worthington Biochemical Corporation, #LS006365). The elastase solution is a watery mixture that is absorbed by the blood vessel and weakens the wall by enzymatic digestion of elastin. The rabbit was induced into an anesthetized state with a mixture of 34mg ketamine and 5mg xylazine per kilogram of rabbit, then maintained with 2% isoflurane inhaled via a mask with 1L/min of O₂.

The abdominal aorta below the renal arteries was initially accessed through a midline incision of the belly. Internal organs were gently pushed aside and connective tissue dissected until the aorta was isolated (Figure 5-2). As the elastase application methods matured and survival studies were pursued, it was found that this approach was too invasive and led to poor survival rates. The intestinal track was disrupted and control of body temperature was difficult with so many organs exposed.

Starting at rabbit 011 and 012B, the incision was made from the left side and tissue dissected between the back muscles and the abdominal cavity (Figure 5-3). It was a much less traumatic surgery, reducing the incision from about eight inches down to about two inches, and led to a much more robust recovery of the animal.

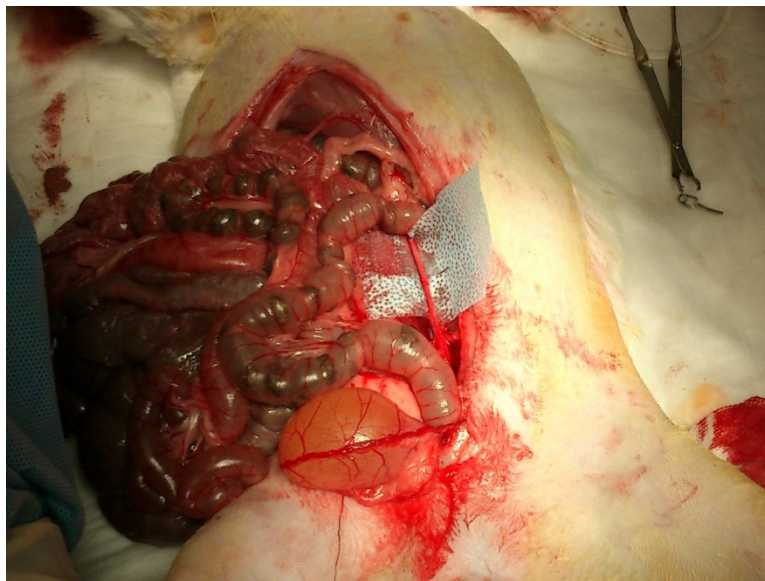


Figure 5-2. The abdominal aorta of Rabbit 002 was accessed through a midline incision at the belly. Guts were gently set aside and various methods for applying elastase were attempted.



Figure 5-3. The abdominal aorta of Rabbit 012B was accessed through an incision on the left side of the rabbit. Tissue was dissected between the back muscles and the abdominal cavity. Trauma was significantly reduced and the rabbit recovered faster than those where the aorta was accessed through a midline incision.

Various methods for applying the elastase were attempted. A mold was rapid prototyped out of TangoPlus, a soft resin, by a company called Red Eye Prototyping (Figure 5-4). Despite attempts to form a tight seal, elastase leaked all over and yielded fusiform aneurysms. A felt-tipped “marker” was then attempted (Figure 5-5, left). While elastase was confined to a small area, a large volume of elastase was needed to fully hydrate the felt tip. The amount of elastase transferred to the vessel was also unknown. A micro-needle was then used to dispense the elastase (Figure 5-5, right). With use of a surgical microscope, the needle tip could be precisely maneuvered over the abdominal aorta. However, the volume of elastase dispensed was too small and did not appear cause sufficient damage to the aorta to initiate formation of an aneurysm. Table 5-1 summarizes the observed outcomes. In short, saccular aneurysms were not observed.

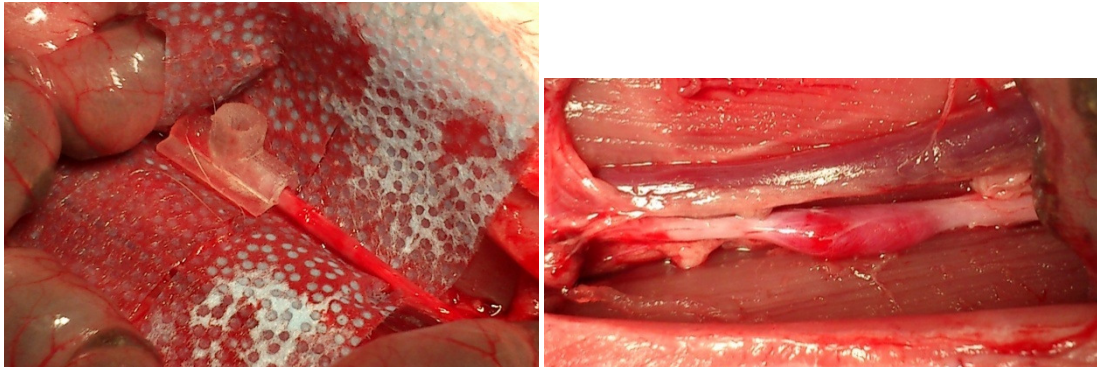


Figure 5-4. Left. A soft mold rapid prototyped out of TangoPlus by Red Eye Prototyping (Chaska, MN) was placed over the abdominal aorta. The intention was to constrain the elastase in the small cylindrical well, thereby exposing only a portion of the vessel to elastase. Different methods for forming a tight seal were attempted. Vacuum grease, glue, gels, and other fillers injected between the mold and the blood vessel failed to stop the spread of elastase. **Right.** Fusiform aneurysms were generated.

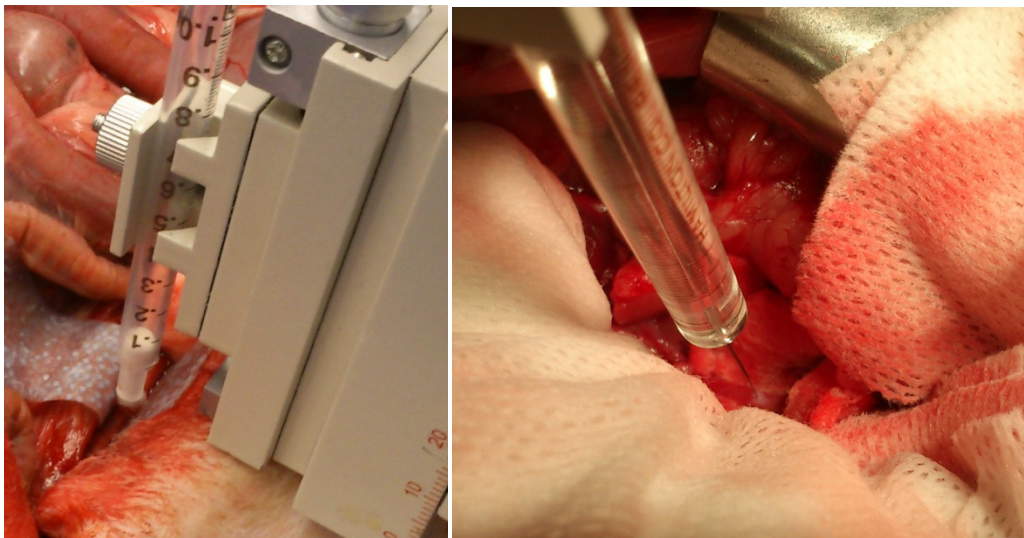


Figure 5-5. Left: The tip of a syringe was packed with a dense, felt like material to hold the elastase solution. While the contact area was constrained as desired, the felt insert absorbed much of the elastase solution and it was not possible to determine how much elastase actually transferred to the vessel wall. **Right:** A microsyringe was used to dispense elastase. While the drop location and volume was well characterized, dispensing was a slow process and ultimately didn't damage the aorta sufficiently to initiate aneurysm formation.

Table 5-1. Aneurysms created at the abdominal aorta site are summarized below. U = units of elastase.

Rabbit	Surgery	Elastase Application	Observations
001	Acute	<ul style="list-style-type: none"> Suction based mechanical trauma followed by elastase soaked Gelfoam 	<ul style="list-style-type: none"> Circular spots of tissue disruption
002	Acute	<ul style="list-style-type: none"> Tangoplus mold with 6U of elastase in well 	<ul style="list-style-type: none"> Elastase leaked and formed fusiform aneurysm
004	Acute	<ul style="list-style-type: none"> Tangoplus mold, painted elastase using brush 	<ul style="list-style-type: none"> Small bump formed on side of aorta
005	Acute	<ul style="list-style-type: none"> Elastase hydrated felt tipped syringe 	<ul style="list-style-type: none"> No significant change in aorta surface
006	Survival to 1d	<ul style="list-style-type: none"> Elastase hydrated felt tipped syringe 4 different volumes of 100U/mL elastase applied at 4 sites: 10, 30, 40, and 50 μL 	<ul style="list-style-type: none"> All four sites experience tissue damage and discoloration All sites occluded at followup, reason unknown
008	Acute	<ul style="list-style-type: none"> 0.3U @ 100U/mL dripped onto aorta using microsyringe 	<ul style="list-style-type: none"> Died from complications from renal artery rupture during access of aorta
009	Survival to 28d	<ul style="list-style-type: none"> 0.07U @ 100U/mL dripped onto aorta using microsyringe 	<ul style="list-style-type: none"> Blister formed on the aorta, but was completely gone at followup; vessel looked pristine
010	Acute	<ul style="list-style-type: none"> 0.03U and 0.06U @ 100U/mL dripped onto 2 sites of the aorta using microsyringe 	<ul style="list-style-type: none"> Rabbit died during recovery, no evidence of aneurysm rupture found
011	Survival to 2d	<ul style="list-style-type: none"> 0.03U @ 100U/mL dripped onto aorta using microsyringe 	<ul style="list-style-type: none"> Aorta started with a welt, possibly due to damage while isolating vessel Aneurysm ruptured at 2 days
012A	Acute	<ul style="list-style-type: none"> None 	<ul style="list-style-type: none"> Touched aorta with tissue coagulator while attempting to control bleeding; aorta ruptured and the rabbit died from uncontrolled bleeding
012B	Survival to 12d	<ul style="list-style-type: none"> Used a 1mL syringe with plunger in place to prevent leakage 35U @ 465U/mL dispensed 	<ul style="list-style-type: none"> Elastase sucked out of syringe tip via capillary action; plunger tip didn't contain elastase Slightly fusiform aneurysm present, ~50% increase in diameter

5.2.2. Surgical Techniques for Carotid Root Aneurysms

The target location for aneurysm creation was shifted back to the conventional site at the right common carotid artery (R CCA) root after gaining more experience with surgical management of the rabbits and application of elastase. The shift also occurred because the curvature inherent in human neurovasculature could not be replicated with the straight rabbit abdominal aorta. The aneurysms generated in the abdominal aorta were of the fusiform variety and did not meet the intended use of the animal model.

The right common carotid artery root was accessed through an incision parallel and about five mm to the right of the trachea, ending just above the sternum. Tissue was very carefully blunt dissected, first by locating the right common carotid artery, then tracking it down to the brachiocephalic trunk. The root of the R CCA where it bifurcates from the right subclavian artery (R SCA) is close to the top of the sternum. Biological variabilities were observed, with the root as far as 1.5cm caudal to the top of the sternum, making access difficult. Figure 5-6 illustrates the exposed brachiocephalic trunk.

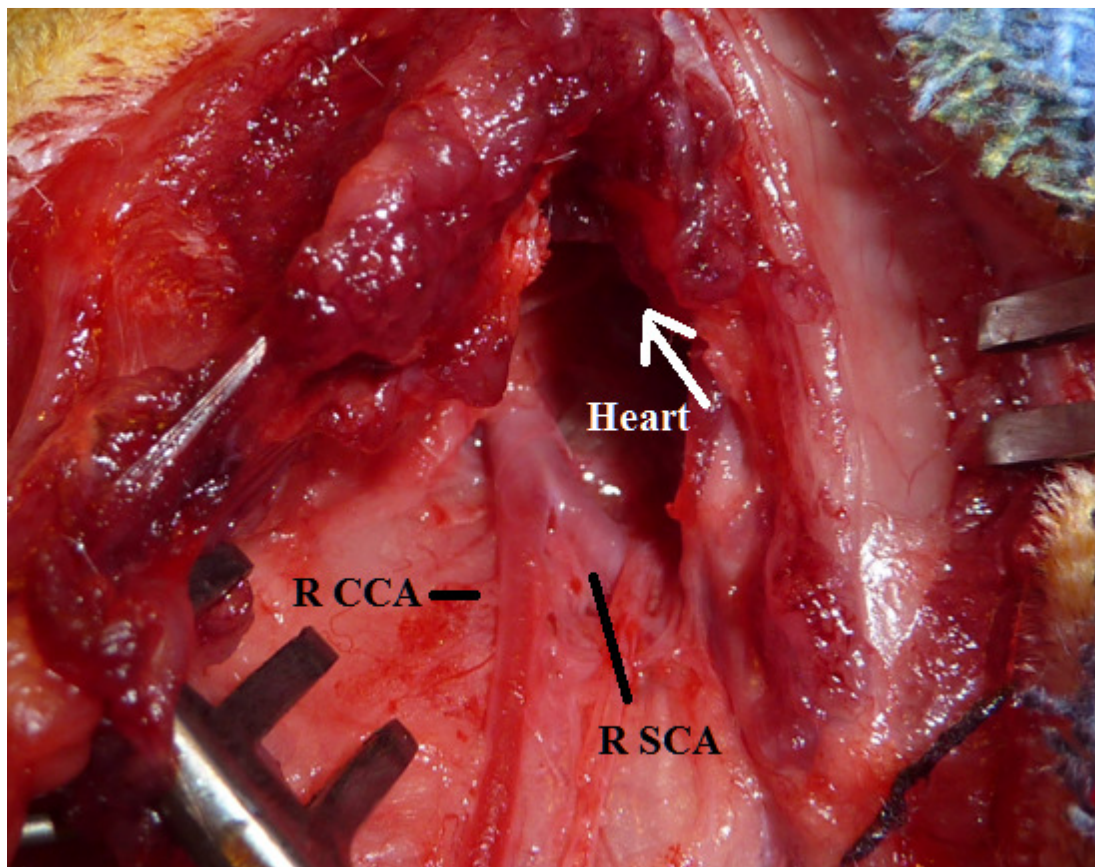


Figure 5-6. The right brachiocephalic trunk is accessed through an incision just to the right of the trachea. The right common carotid (R CCA) and subclavian (R SCA) arteries are exposed.

The conventional technique for creating aneurysms [92] involves intravascular immersion of an elastase solution to damage the R CCA root. The R CCA is then tied off to form an aneurysm sac. Since extravascular exposure to elastase had generated aneurysms in the abdominal aortic site, it was decided that the additional risk of complications from inserting catheters and balloons into the R CCA were not desirable. Aneurysms were instead induced by using a small paintbrush with a round #5/0 tip to paint elastase at selected locations. The aneurysm sac was still formed by ligating the R CCA at some distance away from the bifurcation.

Administration of 81mg/day of aspirin was started at rabbit 017 after observing significant inflammation in the RCCA vessel walls at follow-up. 2000U of heparin daily was started at rabbit 025 to further reduce inflammation and thrombus found in the aneurysms at followup. The heparin protocol was then modified to injecting 1000U after isolating the aneurysm root, waiting 20 minutes before applying elastase, then administering another 1000U about 2 hours after the first injection. This final protocol appeared to manage the thrombus and inflammation inside the aneurysm fairly well, leading to relatively patent aneurysms at followup.

Intubation with a 2.5mm diameter tube was adopted as protocol at rabbit 028. The high incidence of death from respiratory distress led to assisted breathing in hopes that the survival rate would improve. The Ohmeda 7000 ventilator was set to the lowest flow rate possible, which was 2L/min O₂. Breaths per minute varied between 20 to 25. The intubation cuff was not expanded to allow for escape of excess air. Backpressure was monitored and kept below 15mm Hg.

At the followup surgery, a 4F sheath (Avanti by Cordis) was inserted into the femoral artery. A 4F Glidecath catheter (by Terumo) was advanced up to the aneurysm along with a J-tipped 0.035" Glidewire under fluoroscopic guidance. Radiopaque dye (Optiray 320) was injected manually and angiograms taken (Ziehm Vista) to document the aneurysm size.

A summary of the observations is listed in Table 5-2. After 25 rabbits, the surgical technique was refined to the point where no acute complications were expected while accessing of the RCCA root. However, rabbits were still dying from respiratory distress, even with intubation.

It was also observed that the size of the aneurysms created using this technique was limited to diameters of around 5 mm or less, much like the conventional model as described in Figure 2-43. While the fluid mechanics of blood entering the rabbit aneurysm may still be comparable to aneurysms inside the human neurovasculature, the inability to generate larger aneurysms to evaluate the performance of a flow diverter across large and giant aneurysms was a little disappointing.

Table 5-2. A summary of selected rabbit experiments used to develop the R CCA root aneurysm technique.
U = units of elastase.

Rabbit	Surgery	Elastase Application Notes	Summarized Observations
013	Acute	<ul style="list-style-type: none"> 70U @ 465U/mL elastase squirted onto RCCA root with fine needle 	<ul style="list-style-type: none"> R CCA root was bulging after application of elastase; aneurysm ruptured while ligating RCCA to form aneurysm
014	Survival to 10d	<ul style="list-style-type: none"> Painted 12U @ 465U/mL elastase 	<ul style="list-style-type: none"> Small aneurysm with a bit of thrombus inside
015A	Acute	<ul style="list-style-type: none"> None 	<ul style="list-style-type: none"> Knicked artery while isolating R CCA root
015B	Survival to 12d	<ul style="list-style-type: none"> Painted 7U @ 465U/mL elastase 	<ul style="list-style-type: none"> R CCA root was bulging after application of elastase; small square shaped aneurysm at f/u
016	Survival to 29d	<ul style="list-style-type: none"> Painted 16U @ 465U/mL elastase 	<ul style="list-style-type: none"> Small bump at follow up, lots of inflamed tissue
017	Survival to 28d	<ul style="list-style-type: none"> Painted 15U @ 1000U/mL elastase 	<ul style="list-style-type: none"> ~6mm diameter aneurysm observed with no inflammation or thrombus inside the tissue
018	Acute	<ul style="list-style-type: none"> None 	<ul style="list-style-type: none"> Knicked artery while isolating R CCA root
019	Acute	<ul style="list-style-type: none"> None 	<ul style="list-style-type: none"> Knicked artery while isolating R CCA root
020	Survival to 22d	<ul style="list-style-type: none"> Primed vessel with 2% lidocane, painted 11U @ 750U/mL elastase 	<ul style="list-style-type: none"> Observed massive bulge (~8mmD) initially, but resulted in largely thrombosed aneurysm at 22d
021	Acute	<ul style="list-style-type: none"> None 	<ul style="list-style-type: none"> Knicked artery while isolating R CCA root
022	Acute	<ul style="list-style-type: none"> None 	<ul style="list-style-type: none"> Knicked artery while isolating R CCA root
023	Acute	<ul style="list-style-type: none"> Primed vessel with 2% lidocane, painted 10U @ 500U/mL elastase 	<ul style="list-style-type: none"> Large bulge from rabbit 020 was considered likely to be temporary; chest of rabbit 023 was kept open long enough to observe aneurysm shrink in size as lidocane wore off Rabbit died during recovery from respiratory complications; was wheezing
024	Survival to 6d	<ul style="list-style-type: none"> Primed vessel with 2% lidocane, painted 35U @ 500U/mL elastase 	<ul style="list-style-type: none"> Didn't see saccular shape form acutely Choked on aspirin at day six
025A	Acute	<ul style="list-style-type: none"> None 	<ul style="list-style-type: none"> Unable to control subcutaneous bleeding
025B	Survival to 18d	<ul style="list-style-type: none"> Painted 55U @ 1000U/mL elastase 	<ul style="list-style-type: none"> Significant thrombosis inside aneurysm at 18d occupying about 2/3rd of the volume
026A	Acute	<ul style="list-style-type: none"> None 	<ul style="list-style-type: none"> Knicked artery while isolating R CCA root
026B	Acute	<ul style="list-style-type: none"> None 	<ul style="list-style-type: none"> Respiratory failure during surgery, uncontrolled drop in core temperature
026C	Survival to 18d	<ul style="list-style-type: none"> Painted 40U @ 1000U/mL elastase 	<ul style="list-style-type: none"> Observed a bulge of ~2.5 times the diameter acutely There was a little bit of inflamed tissue at the aneurysm tip, but a ~3mm diameter x 5mm tall aneurysm remains

027	Survival to 3d	<ul style="list-style-type: none"> Painted 60U @ 1000U/mL elastase 	<ul style="list-style-type: none"> Saw a bulge of ~2.5 times the diameter acutely Died at day 3 from respiratory distress
028	Survival to 26d	<ul style="list-style-type: none"> Painted 20U @ 1000U/mL elastase 	<ul style="list-style-type: none"> Saw a bulge of ~2.5 times the diameter acutely Aneurysm ~ 4mm diameter x 8mm tall was observed at 26d
029	Survival to 2d	<ul style="list-style-type: none"> Painted 25U @ 1000U/mL elastase 	<ul style="list-style-type: none"> Saw a bulge of ~2.5 times the diameter acutely Died from respiratory distress at two days
030	Survival to 21d	<ul style="list-style-type: none"> Painted 20U @ 500U/mL elastase 	<ul style="list-style-type: none"> Aneurysm ~ 4mm diameter x 4mm tall was observed at 21d
031	Survival to 25d	<ul style="list-style-type: none"> Painted 20U @ 500U/mL elastase 	<ul style="list-style-type: none"> Narrow neck aneurysm with max diameter of ~3mm and ~6mm tall was observed at day 25 The aneurysm had no signs of thrombus or inflamed tissue
032	Acute	<ul style="list-style-type: none"> Painted 20U @ 500U/mL elastase 	<ul style="list-style-type: none"> Died from respiratory distress during recovery
033	Survival to 12d	<ul style="list-style-type: none"> Painted 17U @ 500U/mL elastase 	<ul style="list-style-type: none"> Saw a bulge of ~2.5 times the diameter acutely Found dead in cage; post-mortum indicated complications in the digestive tract

5.2.3. Measurement of Fluid Velocities using an Ultrasound Probe

Ultrasound measurements were made using the Zonare Z.One ultrasound cart and the L14-5sp probe by Dr. Islam Shehata and Dr. John Ballard. Blood velocities at the L SCA, R SCA, L CCA, and R CCA were measured for rabbits 034, 035, 038, 041, 042, and 043 before the aneurysm was induced, after the aneurysm was induced, and at followup surgery 11 – 30 days after.

The artery of interest for the velocity measurement is first located in B mode. As shown in Figure 5-7, the vessel diameter is measured. The gain and tissue depth settings of the probe are adjusted as needed to visualize the artery. Color Doppler mode is then used to visualize flow inside the blood vessel and hone in the orientation of the ultrasound probe. Once the desired imaging plane is achieved, Pulse Wave Doppler, as illustrated in Figure 5-8, is used to quantitatively measure flow. The ultrasound emission direction and window is adjusted to obtain quality measurements.

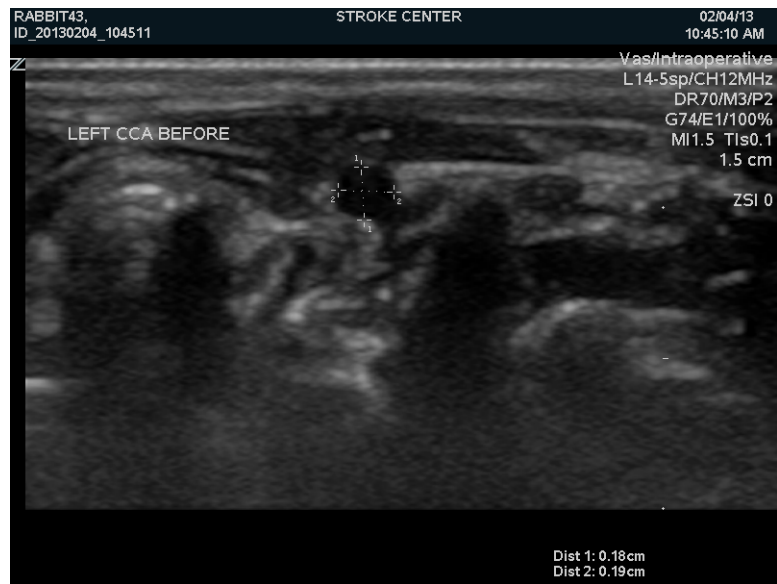


Figure 5-7. The ultrasound B mode is used to locate the vessel of interest. Vessel diameter is measured in this mode.

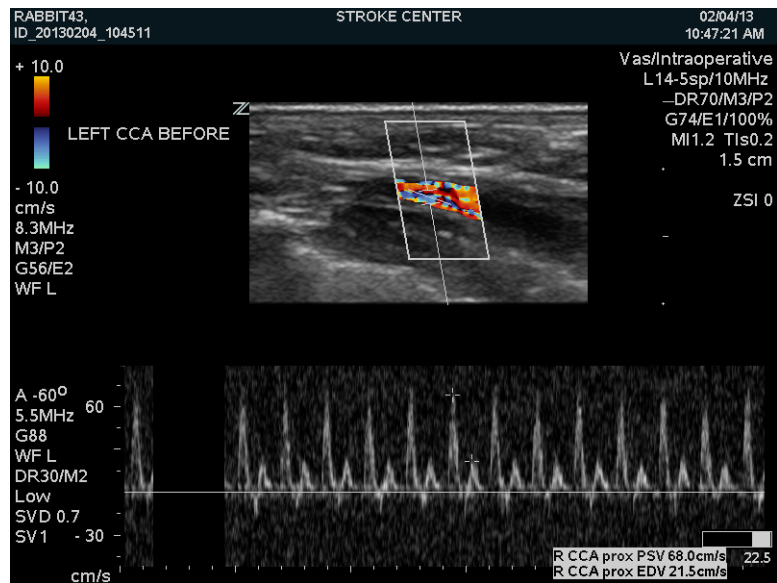


Figure 5-8. The ultrasound Pulse Wave Doppler mode is used to measure blood flow in arteries of interest.

Drs. Shehata and Ballard were also able to detect flow inside the aneurysm by placing the probe a little cranial and right of the sternum. However, the technique is highly dependent on the orientation and patency of the aneurysm. If the aneurysm is oriented in the anterior direction (Figure 5-13), the probe will not be able to detect flow. If the aneurysm size is only a fraction of the sampling window of the probe, flow will also not be detectable. However, this technique has merit as a novel and non-invasive method for

monitoring the progression of aneurysm formation as well as clot formation after placement of a flow diverter. Figure 5-9 illustrates the location of the probe. Figure 5-10 illustrates the measurement of flow inside the aneurysm using the Color Doppler (left) and Pulse Wave modes (right) of the L14-5sp probe.



Figure 5-9. The ultrasound probe was placed in the rectangle drawn on the rabbit's chest to image and measure flow inside the aneurysm. Quality of the image and measurements depend on the orientation and size of the aneurysm. Aneurysms oriented in the anterior or posterior directions were very difficult to visualize.

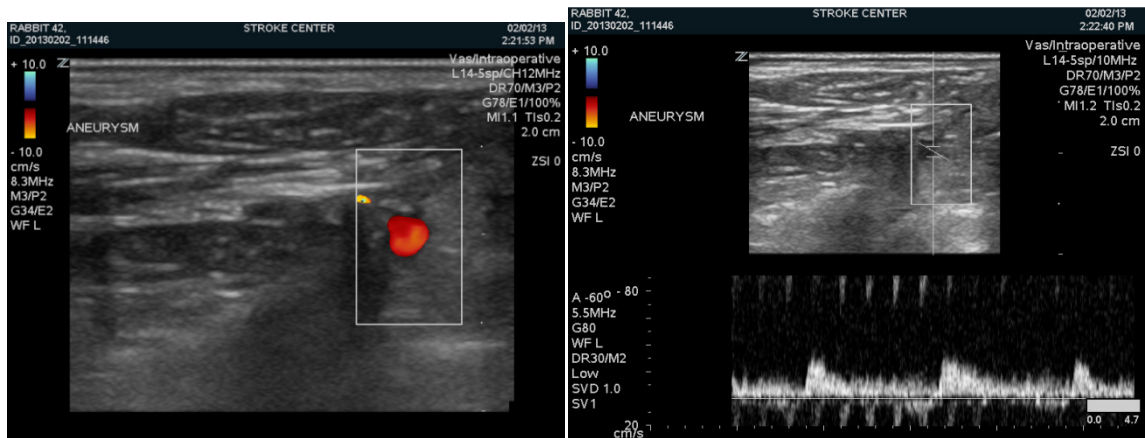


Figure 5-10. Left. The Color Doppler mode is used to visualize flow inside the aneurysm. **Right.** The Pulse Wave Doppler mode is used to measure blood flow inside the aneurysm.

5.2.4. Morphological Comparison of Anchored and Loose Carotid Root Aneurysms

It appeared that the external application of elastase was unable to generate aneurysms with diameters larger than that of the conventional method. Therefore, the focus shifted towards controlling the direction of the blood jet entering the aneurysm. As shown in Figure 5-6, Dr. Divani and the author were able to isolate the RCCA all the way down to the root with minimal vessel rupture related complications. After the RCCA was ligated and elastase applied to initiate aneurysm formation, rabbits were put into three experimental groups.

In one experimental group (rabbits 034 to 038, Figure 5-11), the RCCA was anchored to nearby tissue. By controlling the orientation of the aneurysm, different intraaneurysmal flows can be created. A flow diverter can then be evaluated for efficacy under a variety of initial inflow conditions. In the second group (rabbits 039 and 040, Figure 5-12), the RCCA was severed to allow for greater manipulation of the aneurysm orientation before anchoring. In the third group (rabbits 041 to 043, Figure 5-13), the RCCA was severed but the aneurysm was not anchored. It was instead allowed to take a natural shape based on the pressure inside the aneurysm.

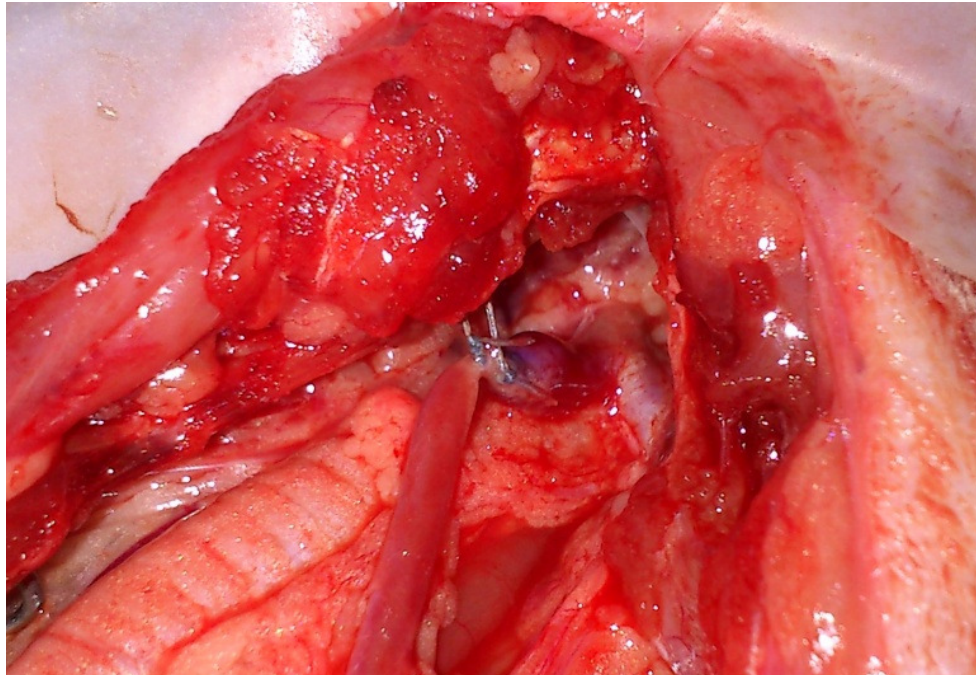


Figure 5-11. The aneurysm at time of creation in rabbit 036 is shown. The RCCA was left intact and the aneurysm anchored to nearby tissue to pull the tip towards the left side of the body.

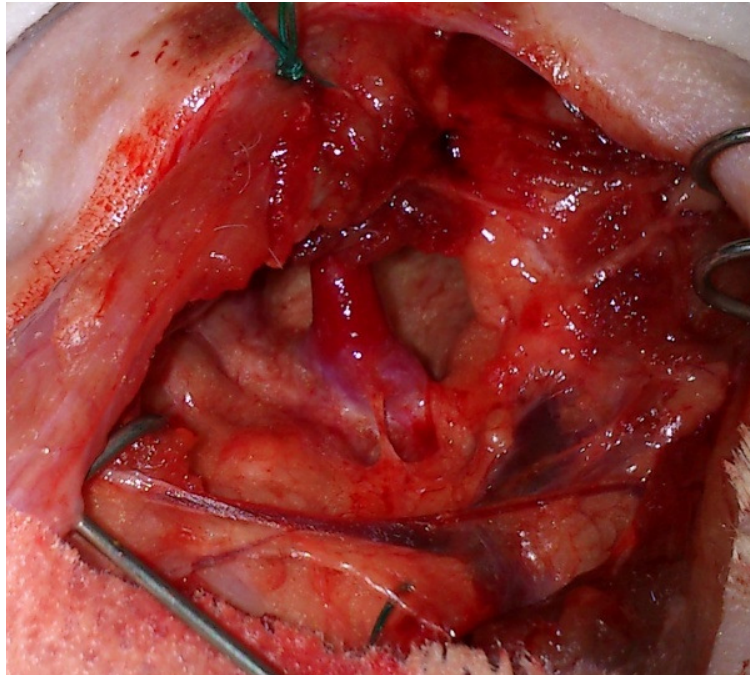


Figure 5-12. The aneurysm at time of creation in rabbit 039 is shown. The RCCA was severed and the aneurysm anchored to nearby tissue to pull the tip towards the sternum and the left side of the body. Without the constraining distal RCCA, the aneurysm was oriented in a much more drastic direction compared to the example shown in Figure 5-11.

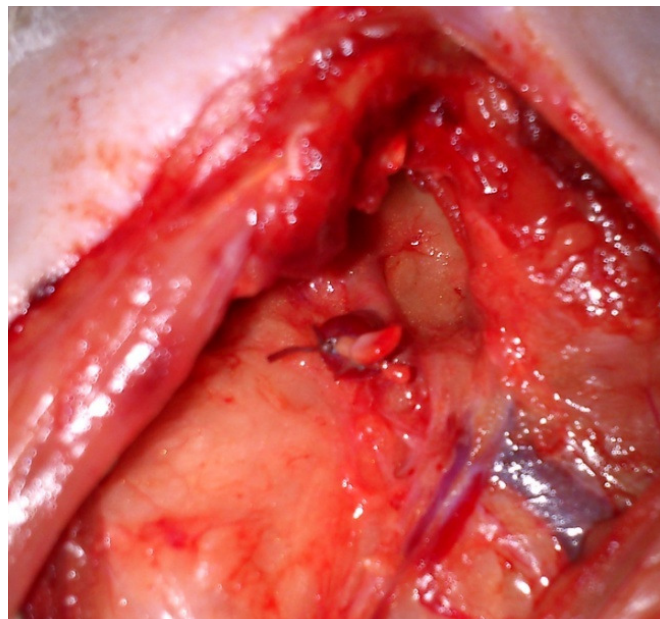


Figure 5-13. The aneurysm at time of creation in rabbit 041 is shown. The RCCA was severed and the aneurysm was not anchored.

At the follow-up surgery, the size and orientation of the aneurysms were assessed fluoroscopically. Unfortunately, none of the rabbits from group two (rabbits 039 and 040) survived to the planned sacrifice date. The angiograms from groups one and three are shown in Figures 5-14 and 5-16. Aneurysms of decent size were then taken down to Fairview Hospital for CT imaging (Siemens Somatom Flash, Syngo Acquisition Workplace). Radiopaque dye was injected through a 4F sheath inserted in the femoral vein at 5cc / second (Infusion Stellant SCT-310) for a total of 20cc. CT scans of the aorta arch area commenced after a 30 second delay to allow for the radiopaque dye to circulate into the lungs and out the heart to illuminate the arterial system.

The 3D geometries were reconstructed using Mimics and are shown in Figures 5-15 and 5-17. After sacrificing the rabbits, the aneurysms were excised and slit open to observe for thrombus and inflamed tissue. Images of excised aneurysms can be found in Appendix C.

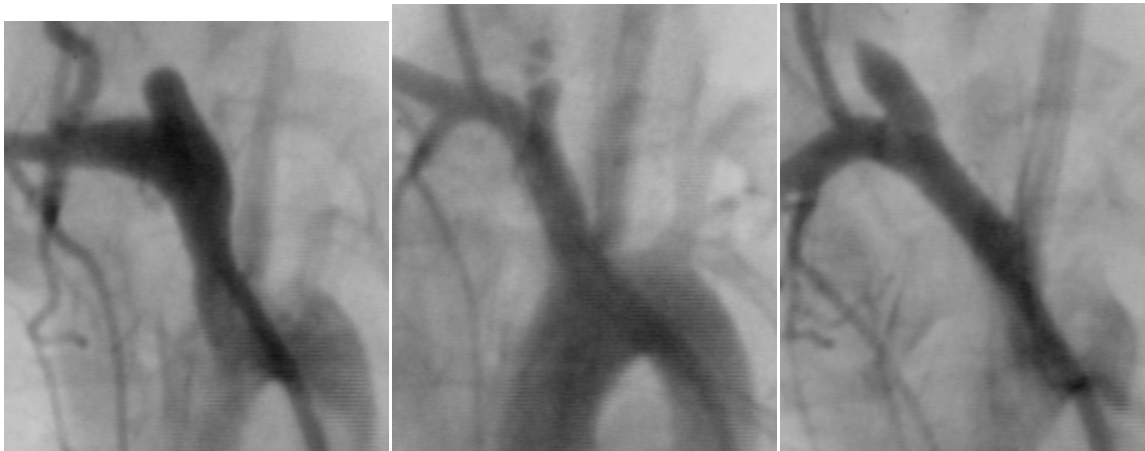


Figure 5-14. Angiograms of group one aneurysms of rabbits 034 (left), 035 (middle), and 038 (right) at follow-up.

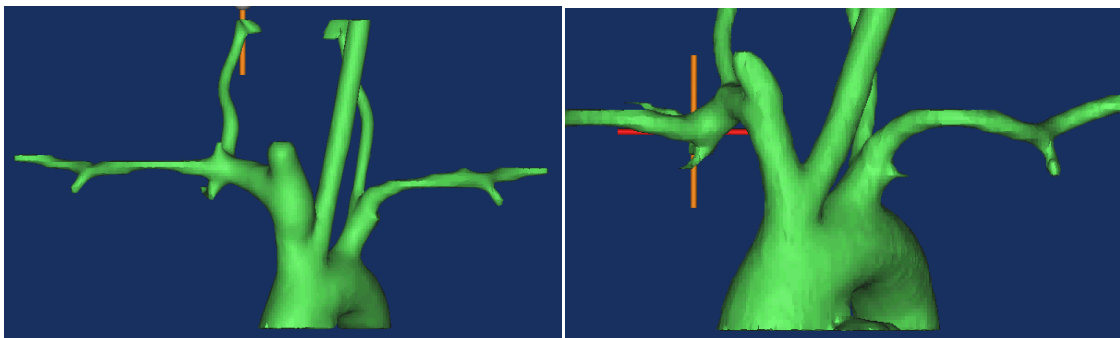


Figure 5-15. 3D reconstructions of the group one aneurysms of rabbits 034 (left) and 038 (right).

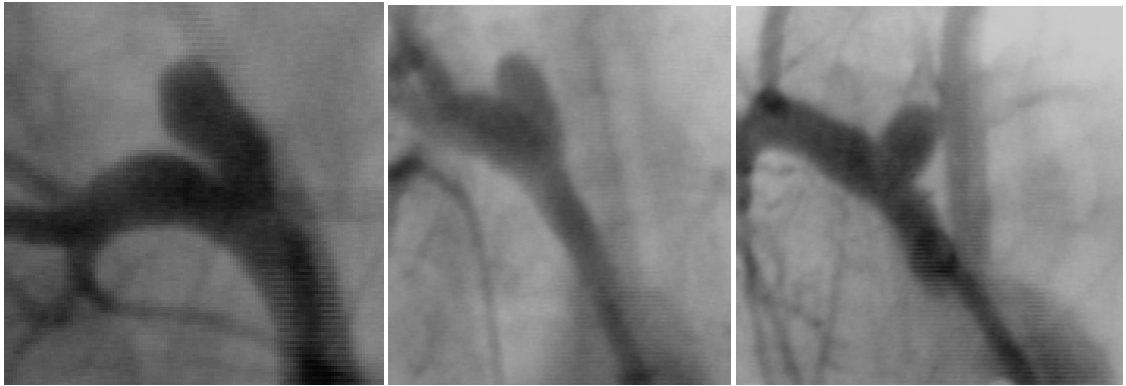


Figure 5-16. Angiograms of group three aneurysms of rabbits 041 (left), 042 (middle), and 043 (right) at follow-up.

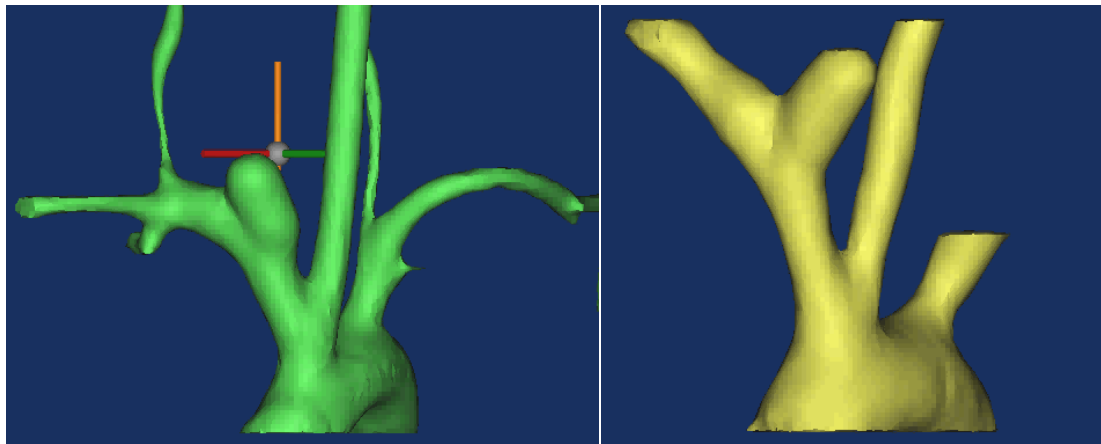


Figure 5-17. 3D reconstructions of the groups 3aneurysms of rabbits 041 (left) and 043 (right) are shown.

Given the small sample size of the different anchoring methods, it is difficult to make definitive statements. In general, the group one and three aneurysms were fairly similar at followup, with the rabbit 43 being the outlier. Aneurysms were not any more spherical with the lack of stress from anchoring. It was unfortunate that rabbits from group two did not survive, as their initial geometries were markedly different.

It was determined that significantly less elastase than previously thought was needed to initiate the aneurysms. In earlier experiments, up to 60U of elastase were applied without yielding larger aneurysms. Unlike the conventional intrasvascular application of elastase, external application of elastase greatly reduced the amount necessary and time of procedure. It appeared that one or two applications at high concentrations (~3U at ~250U/mL) were sufficient to induce aneurysm formation.

In all three experimental groups, elastase was painted at the distal tip of the aneurysm. It was observed that some elastase would migrate towards the root, damaging and enlarging the vessel wall. However, only two aneurysms (rabbit 031 and 041, see Appendix C) exhibited geometry that roughly resembled a neck. The

necks of other aneurysms nearly matched or exceeded the maximum diameter of the aneurysm. Two possible conjectures may explain this. The first is that while elastase was applied only at the distal tip, blood and saline in the area may have carried the elastase everywhere, affecting all exposed vessels and tissue. The second theory is that the increased flow of blood entering the right subclavian artery may have forced remodeling of the bifurcation in the brachiocephalic trunk. The neck enlarged in response to increased pressure and shear stress.

A summary of the observations for the three experimental groups is listed in Table 5-3.

Table 5-3. A summary of the rabbit experiments comparing different techniques for orienting the aneurysm are listed.

Rabbit	Surgery	Aneurysm Creation Notes	Summarized Observations
Group 1			
034	Survival to 20d	<ul style="list-style-type: none"> RCCA intact, aneurysm anchored towards left side Painted 3U @ 250U/mL elastase 	<ul style="list-style-type: none"> Observed a bulge of ~2 times the diameter acutely ~4mm diameter x ~4mm tall aneurysm at 20 days
035	Survival to 22d	<ul style="list-style-type: none"> RCCA intact, aneurysm anchored towards left side Painted 3U @ 250U/mL elastase 	<ul style="list-style-type: none"> Observed a bulge of ~2.5 times the diameter acutely Aneurysm largely occluded with tissue growth; had a Swiss cheese like appearance
036	Acute	<ul style="list-style-type: none"> RCCA intact, aneurysm anchored towards left side Painted 3U @ 250U/mL elastase 	<ul style="list-style-type: none"> Observed a bulge of ~2.5 times the diameter acutely Rabbit died during recovery from surgery
037	Acute	<ul style="list-style-type: none"> None 	<ul style="list-style-type: none"> RCCA ruptured during isolation
038	Survival to 24d	<ul style="list-style-type: none"> RCCA intact, aneurysm anchored towards left side Painted 3U @ 250U/mL elastase 	<ul style="list-style-type: none"> Observed a bulge of ~2.5 times the diameter acutely ~4mm diameter x ~8mm tall aneurysm at 24 days
Group 2			
039	Survival to 3d	<ul style="list-style-type: none"> RCCA severed, aneurysm anchored towards left side Painted 5U @ 250U/mL elastase 	<ul style="list-style-type: none"> Observed a bulge of ~2.5 times the diameter acutely Aneurysm orientation more difficult to measure with US Rabbit died from respiratory complications

040	Acute	<ul style="list-style-type: none"> RCCA severed, aneurysm anchored towards left side Painted 5U @ 250U/mL elastase 	<ul style="list-style-type: none"> Observed a bulge of ~2 times the diameter acutely Rabbit died from respiratory complications
Group 3			
041	Survival to 11d	<ul style="list-style-type: none"> RCCA severed, aneurysm free Painted 3U @ 250U/mL elastase 	<ul style="list-style-type: none"> Observed a bulge of ~2.5 times the diameter acutely ~4mm diameter x ~10mm tall aneurysm at 24 days
042	Survival to 26d	<ul style="list-style-type: none"> RCCA severed, aneurysm free Painted 3U @ 250U/mL elastase 	<ul style="list-style-type: none"> Observed a bulge of ~2.5 times the diameter acutely ~4mm diameter x ~6mm tall aneurysm at 24 days
043	Survival to 30d	<ul style="list-style-type: none"> RCCA severed, aneurysm free Painted 7U @ 250U/mL elastase 	<ul style="list-style-type: none"> Observed a bulge of ~2.5 times the diameter acutely ~4mm diameter x ~4mm tall aneurysm at 24 days

5.3. PREDICTED TEST CONDITIONS IN THE RABBIT ANEURYSM MODEL

The average ultrasound measurements of vessel diameters and blood flow for rabbits 034, 038, 041, and 043 are listed in Table 5-4. Measurements were taken at the left common carotid artery (LCCA), left subclavian artery (LSCA), right subclavian artery (RSCA), and right common carotid artery (RCCA). The average diameter and time-averaged velocity are combined to calculate the average volumetric flow rate in the rabbits, as listed in Table 5-5 and shown in Figure 5-18. The peak systolic (PSV) and end diastolic (EDV) velocities were measured by Dr. Islam Shehata, who is a physician trained in the ultrasonic acquisition of blood velocities in the clinical setting. Time-averaged velocities were calculated based on the pulse selected by Dr. Shehata for the PSV and EDV, as illustrated by the crosshairs in Figure 5-8. Changes were evident between the initial distribution of blood flow before creation of the aneurysm and at followup surgery.

Some measurements for rabbit 34 were missing because the measurement technique was still in development. Measurements in the RCCA are not available since it was sacrificed for the aneurysm stump.

Table 5-4. The average values of diameter (D, [mm]), peak systolic velocity (PSV, [cm/s]), end diastolic velocity (EDV, [cm/s]), and time-average velocity (AV, [cm/s]) are shown before aneurysm creation, immediately after aneurysm creation, and at the followup surgery. Missing measurements are left blank. In general, blood vessel diameters and blood velocities increased as a response to the ligated RCCA.

LCCA				LSCA				RSCA				RCCA			
D	PSV	EDV	AV	D	PSV	EDV	AV	D	PSV	EDV	AV	D	PSV	EDV	AV
Rabbit 34 , before creating the aneurysm (top row), after creating the aneurysm (middle), and at 20 days (bottom)															
1.3	71.4	-1.1	14.0	1.3	56.7	3.4	2.0								
1.4	105	9.4	32.5	1.3	92.2	4.1	12.8	1.2	59.5	5.0	7.4				
1.9	86.8	34.4	41.4	1.6	91.5	2.2	28.7	1.6	79.1	20.5	26.9				
Rabbit 38 , before creating the aneurysm (top row), after creating the aneurysm (middle), and at 24 days (bottom)															
2.3	46.1	16.9	16.3	1.4	73.3	9.6	15.5	1.5	96.6	8.5	16.3	1.9	71.7	6.7	13.8
1.5	98.6	8.1	25.6	1.4	106	13.9	23.6	0.9	89.1	6.3	18.9				
2.5	80.2	28.7	27.6	1.8	87.0	21.8	22.7	1.8	96.9	20.2	18.0				
Rabbit 41 , before creating the aneurysm (top row), after creating the aneurysm (middle), and at 11 days (bottom)															
1.8	71.5	5.4	8.6	1.3	154	4.9	16.8	1.5	81.1	6.9	9.0	1.8	81.1	6.3	12.9
1.6	94.4	3.9	10.4	1.3	162	8.1	23.8	1.5	116	8.7	11.7				
2.4	118	26.4	29.6	1.8	162	13.9	18.5	1.7	134	10.3	10.8				
Rabbit 43 , before creating the aneurysm (top row), after creating the aneurysm (middle), and at 30 days (bottom)															
1.9	65.1	21.3	19.5	1.8	59.9	15.3	9.6	1.7	133	23.8	19.5	1.7	63.7	22.4	17.6
1.6	76.0	10.3	20.5	1.3	61.9	7.8	9.5	1.2	63.5	7.2	9.1				
2.2	137	37.7	47.5	1.7	79.5	18.9	23.5	1.6	65.9	16.3	21.6				

Table 5-5. The time averaged flow rates (Q, [mL/min]) in different arteries are shown before aneurysm creation, immediately after aneurysm creation, and at the followup (F/U) surgery. Missing measurements are left blank.

Rabbit	LCCA			LSCA			RSCA			RCCA		
	Before	After	F/U	Before	After	F/U	Before	After	F/U	Before	After	F/U
34	11.1	30.0	70.4	1.6	9.7	36.1		5.0	32.4			
38	41.7	27.2	79.1	13.7	22.8	34.7	18.1	7.2	26.4	24.2		
41	13.2	13.0	78.0	13.4	19.9	27.2	9.5	13.0	14.8	19.7		
43	32.0	24.7	105	14.1	7.6	32.0	25.6	6.5	24.9	24.9		

Blood Flow in Arteries Before Aneurysm Creation, After, and at Followup

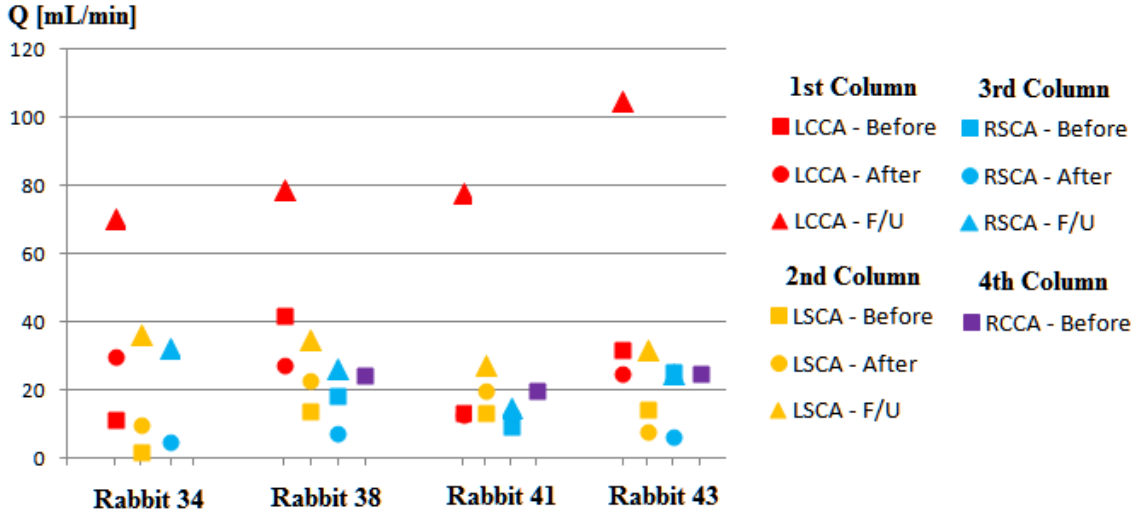


Figure 5-18. The flow rates of blood in various vessels were found to have increased by the follow up (F/U) surgery. Remodeling likely occurred to maintain a sufficient blood supply to the brain.

CT scans of the aneurysms in rabbits 034, 038, 041, and 043 were manipulated in Mimics and imported into ANSYS for computer simulations of blood flow past and into the aneurysm. Several boundary conditions were missing, of which the most important were the cardiac output and fraction of blood traveling in the descending aorta. Therefore, the following assumptions were made.

1. Based on the distribution of flow rates presented by Alneas et al. [104], the flow rate in the LVA was set to 1/3rd of the LCCA before the creation of the aneurysm.

2. Since the LCCA at followup had such a high flow rate, exceeding that of the LCCA and the RCCA combined before creation of the aneurysm, the flow rate in the RVA was set to be equal to that of the LVA.
3. The flow rate exiting the domain at the descending aorta was set to 70% of the cardiac output. As a point of reference, about 20% of the cardiac output enters the human brain. For these simulations, 30% was allocated for the brain and the arms.

The combination of measured flow rates and the assumptions listed above generated the boundary conditions listed in Table 5-6 for the simulations in rabbits 34, 38, 41, and 43. The flow rate of blood entering the domain at the ascending aorta, or the cardiac output, is within the 300 – 800 mL/min range reported in literature [105, 106]. Flow into the coronary arteries was omitted. Steady simulations with rigid walls and Newtonian human blood ($\rho = 1050 \text{ kg/m}^3$, $\mu = 0.0035 \text{ Pa}\cdot\text{s}$) were performed.

Table 5-6. Rabbit-based simulations in flow domains reconstructed from CT scans at follow-up surgery were performed with the listed boundary conditions. Steady flow conditions with rigid walls and Newtonian human blood were imposed.

Rabbit	34	38	41	43
Measured Q's [mL/min]				
LCCA	70	79	78	105
LSCA	36	34	27	32
RSCA	32	26	15	25
Assumed Q's [mL/min]				
LVA and RVA	3.7	14	4.4	11
Descending aorta	341	392	300	428
Ascending aorta	488	560	430	611

By use of the same method presented in Figures 4-37 and 4-38, the predicted flow rates of blood entering aneurysms of rabbits 34, 38, 41, and 43 were calculated as shown in Figure 5-19 and summarized in Table 5-7. The residence time was defined as the volume of the aneurysm divided by the volumetric flow rate of blood entering the aneurysm. The streamlines entering the aneurysm for the four rabbits are shown in Figures 5-20 to 5-23. The profiles of the velocities normal to the aneurysm neck (red = into the aneurysm, blue = exiting the aneurysm) for the rabbits are also shown. In rabbits 34 and 41, blood enters from one side of the aneurysm and exits from the other. In rabbits 38 and 43, blood enters mostly in the center of the aneurysm and leaves at the edges. No obvious stagnant or recirculating regions were observed.

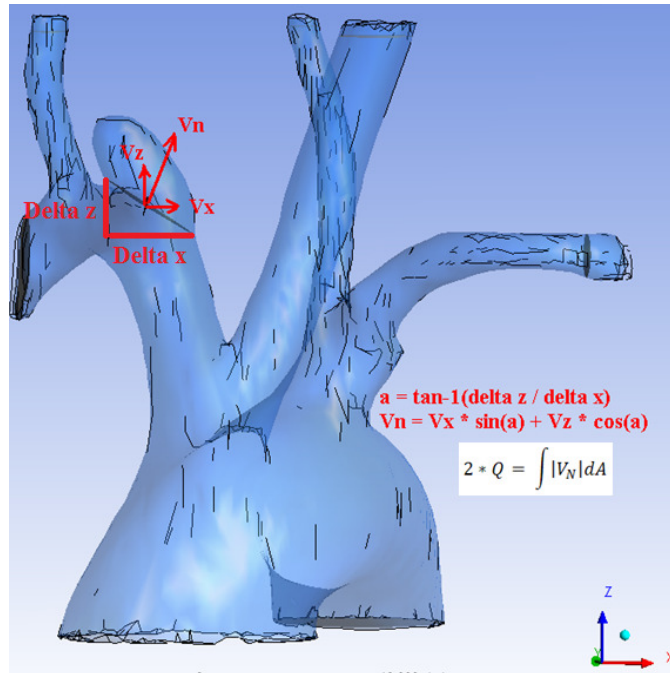


Figure 5-19. The flow rate of blood entering the aneurysm was calculated in a manner similar to earlier PIV and CFD studies.

Table 5-7. The predicted flow rates of blood entering the aneurysms and residence times.

Rabbit	34	38	41	43
Q [mL/min]	21	2.3	4.7	6.1
Volume of aneurysm [mL]	0.082	0.034	0.080	0.025
Residence time [s]	0.23	0.90	1.0	0.25

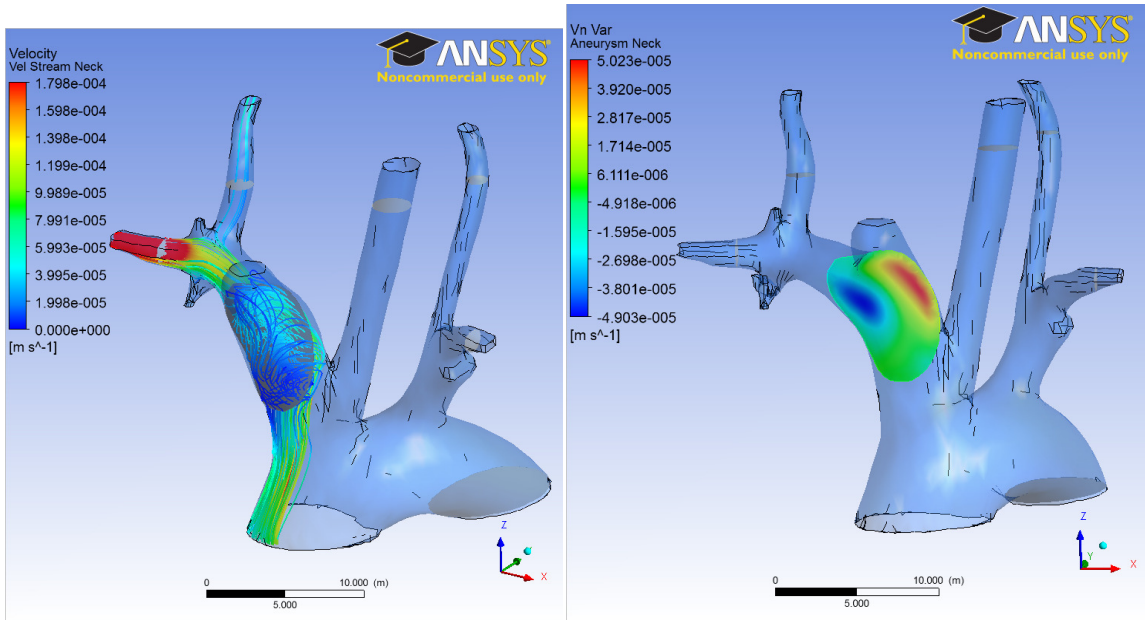


Figure 5-20. Streamlines generated from the aneurysm neck plane are shown for rabbit 34 (**left**). The profile of the velocity vector normal to the aneurysm plane (V_N) is also shown (**right**) (red = entering the aneurysm, blue = exiting the aneurysm).

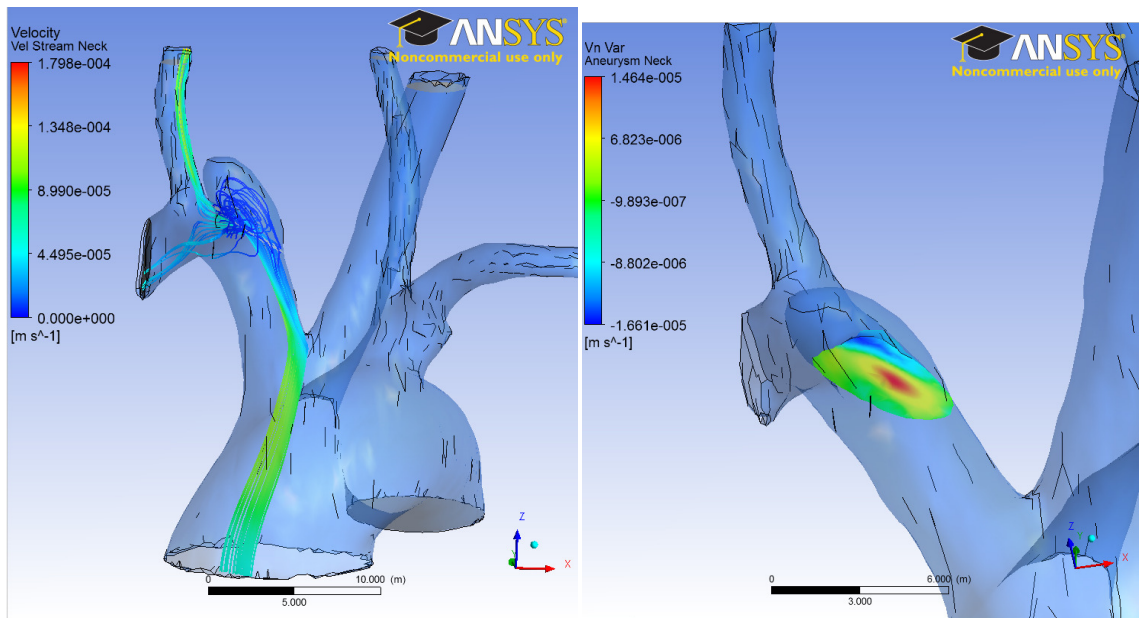


Figure 5-21. Streamlines generated from the aneurysm neck plane are shown for rabbit 38 (**left**). The profile of the velocity vector normal to the aneurysm plane (V_N) is also shown (**right**) (red = entering the aneurysm, blue = exiting the aneurysm).

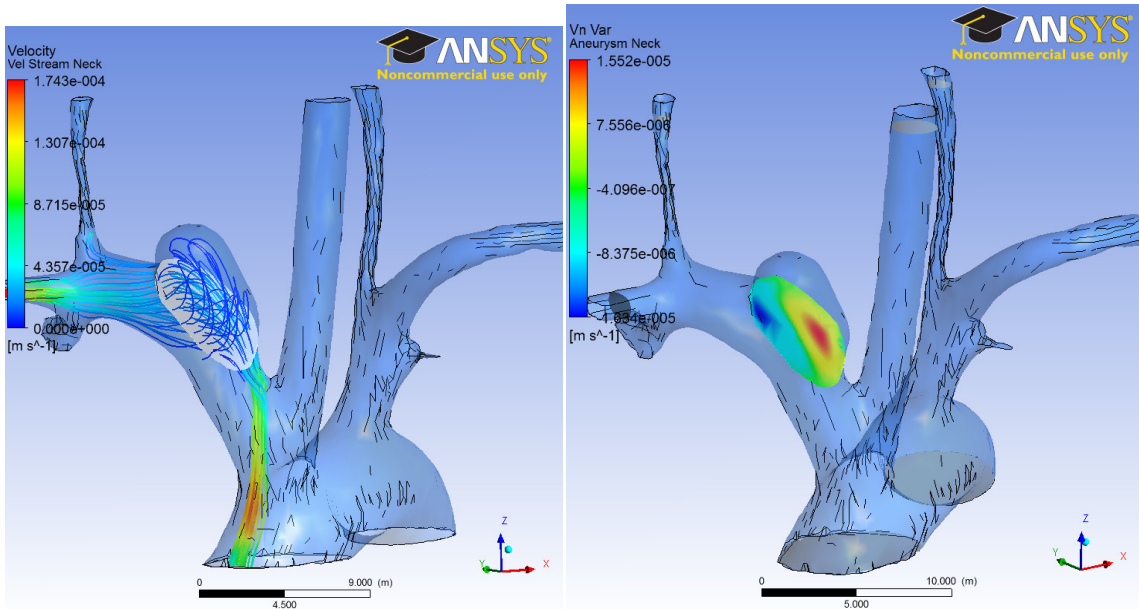


Figure 5-22. Streamlines generated from the aneurysm neck plane are shown for rabbit 41 (**left**). The profile of the velocity vector normal to the aneurysm plane (V_N) is also shown (**right**) (red = entering the aneurysm, blue = exiting the aneurysm).

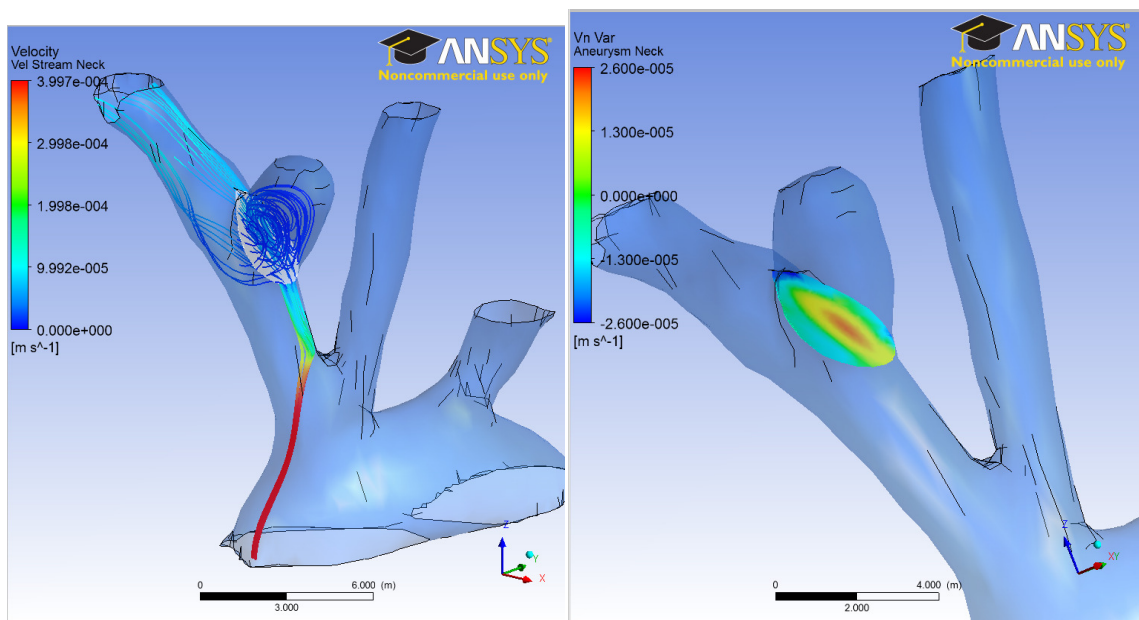


Figure 5-23. Streamlines generated from the aneurysm neck plane are shown for rabbit 43 (**left**). The profile of the velocity vector normal to the aneurysm plane (V_N) is also shown (**right**) (red = entering the aneurysm, blue = exiting the aneurysm).

5.4. DISCUSSION OF ANIMAL STUDIES

An extravascular approach for creation of elastase induced RCCA stump aneurysms was investigated. This technique saves time, allows for targeted application of the elastase onto the vessel wall, eliminates the need for angiography time and catheters while inducing the aneurysm, and grant greater flexibility in orientation of the aneurysm relative to the parent vessel.

The surgical techniques developed allow for aneurysm creation at the LCCA root. While it was not presented in this body of research, Dr. Divani is also pursuing creation of aneurysms at the root of the LCCA. The upstream geometry is different from that of aneurysms created at the root of the RCCA and allows for evaluation of devices with different initial intraaneurysmal flow conditions.

The diameters of the aneurysms created were limited to ranges similar to that reported in literature. Since the elastase is applied topically on the vessel wall and requires a tiny amount, experimentation using highly concentrated (500 – 1000U/mL) elastase was pursued. While the sample size was limited and the anti-thrombogenic regimen was evolving until rabbit 025, the use of more concentrated elastase did not appear to yield aneurysms with larger diameters. The aneurysms described in Chapter 5.2.4 averaged around 4 mm in diameter.

An interesting outlier, rabbit 020, indicates that the RCCA stump may be capable of stretching to larger diameters. Early in the development of the surgical technique, the RCCA was typically irritated while isolating it from surrounding tissues, inducing vasospasm. Lidocane was applied to relax the vessel tissue prior to application of elastase. In rabbit 020, elastase was applied shortly after lidocane and the aneurysm sac swelled to around 8mm in diameter, as illustrated in Figure 5-24. However, it was determined in rabbit 023 that the unexpected increase in aneurysm diameter was temporary and likely due to the lidocane. Finding a mechanical or chemical mechanism to make this swelling permanent will greatly increase the flexibility of the elastase induced aneurysm model in providing different initial intraaneurysmal flow patterns for evaluating different flow diverter designs.

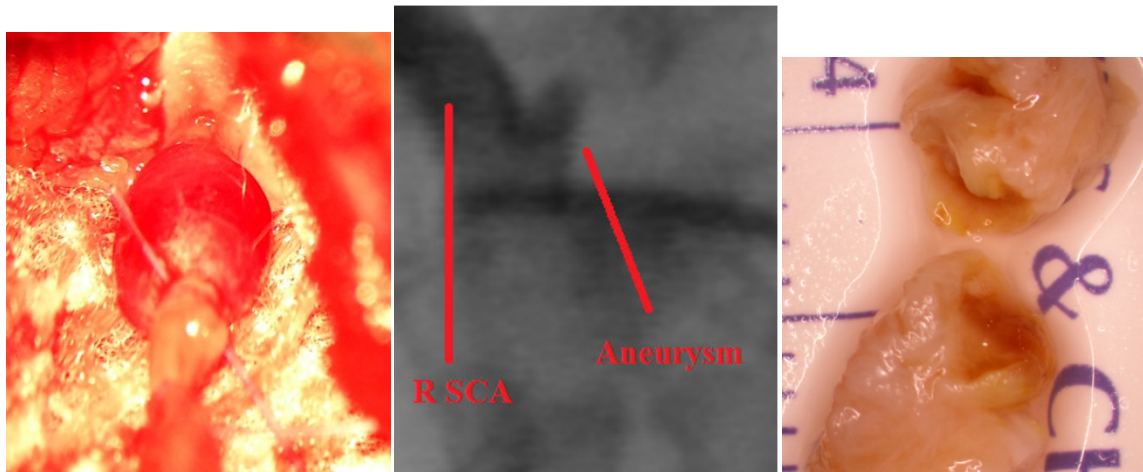


Figure 5-24. The aneurysm induced in rabbit 020 actually swelled to around 8 mm in diameter (**left**). However, the chest cavity of rabbit 23 was kept open for some time after application of the elastase and it was observed that the aneurysm shrank as the effect of the lidocaine wore off. The daily heparin and aspirin regimen was not yet instituted when the aneurysm was induced in rabbit 20. At followup surgery, thrombus and inflamed tissue had reduced the aneurysm to a tiny and unusable stump (**middle, right**).

Inflammation and thrombus formation inside the aneurysms were rare for the final set of rabbits.

Administration of 81mg/kg of aspirin starting two days before surgery, 1000U of heparin about 30 minutes before elastase application, 1000U of heparin about three hours after elastase application, and 2000U of heparin daily for about a week after creation of the aneurysm significantly reduced the incidence of thrombus and inflamed tissue.

However, rabbits were still dying to complications from surgery. Most of the rabbits that died early in the development of the surgical technique expired because of uncontrolled bleeding from a nicked or ruptured artery. In the final set of rabbits, only one rabbit (037) died from a ruptured vessel. However, three died from respiratory complications during recovery. Rabbits that survived to the desired endpoint were alert and mobile an hour or two after cessation of isoflurane. Rabbits that died would develop wheezing when taken off of oxygen and eventually expire. At the conclusion of this body of work, the source of these complications was still undetermined.

Acquisition of aneurysm geometry and flow in nearby vessels allowed for a better understanding of the intraaneurysmal flow before placement of a flow diverter. Correlating the fluid mechanics of blood entering the aneurysm with the functional endpoint (i.e. did the aneurysm clot or not?) allows for the evaluation of different flow diverter designs before moving on to a clinical study where human subjects are used. An understanding of which flow metrics matter and if there is a certain threshold to meet for healing,

allows for greater flexibility in accommodating other design requirements of the flow diverter. For example, a tighter braid will reduce flow more aggressively, but the increased metallic surface area poses additional risks of intraluminal thrombus formation or blockage of perforating vessels in the parent artery.

However, acquisition of velocity profiles when the rabbit is conscious and/or under exercise conditions is difficult, if not unethical, to acquire. As discussed at the end of the CFD chapter (Chapter 4), when a human patient is at moderate to high activity levels, the flow rate of blood entering the aneurysm greatly increases. Intraaneurysmal flow of a treated aneurysm during exercise conditions can exceed that of an untreated aneurysm during rest conditions. While a rest regimen can be imposed on a human patient, it is not possible to similarly control a rabbit while evaluating the flow diverter. Acquisition of velocity profiles in a rabbit under exercise-like conditions may be possible with the use of adrenaline while under anesthesia. However, this possibility has not yet been explored.

Ultrasound has been demonstrated to be a viable tool for non-invasive monitoring of intraaneurysmal flow. Previously published research monitored [6, 94, 95, 107, 108] the growth and treatment of the aneurysms using angiographic techniques. This involved sacrificing the femoral artery and injecting radiopaque dye into the rabbit. Discovering the appropriate orientation for the ultrasound probe has demonstrated that a non-invasive technique can be used instead. This greatly reduces the number of animals required when performing a time-course study, unless histology of the aneurysm is desired at every time point.

Analysis of intraaneurysmal flow suggests that the aneurysm in each rabbit should be characterized prior to use in evaluating device performance. Figure 5-25 summarizes the residence time of blood inside idealized aneurysms simulated in Chapter 4.4 and the untreated rabbit aneurysms simulated in Chapter 5.3. The flow diverter was modeled as 1mil diameter wires with +100% pore stretching in the idealized aneurysms. The residence time was defined as the aneurysm volume divided by the volumetric flow rate of blood entering the aneurysm (Q). It is an approximate metric that does not take into account the distribution of fluid velocities within the aneurysm, but serves as an initial point of comparison. Figure 5-25 illustrates that residence time in the untreated rabbit aneurysms varied greatly. Two untreated aneurysms, in rabbits 38 and 41, had residence times that mimicked those of the untreated idealized aneurysms with a straight or perpendicular curve upstream segment. This suggests that flow diverters placed in these two rabbits will be tested in conditions that are physiologically relevant both from the geometrical and the fluid mechanical perspectives.

Residence Time of Blood Inside Idealized Aneurysms from Chpt. 4.4 and Rabbit Aneurysms from Chpt. 5.3

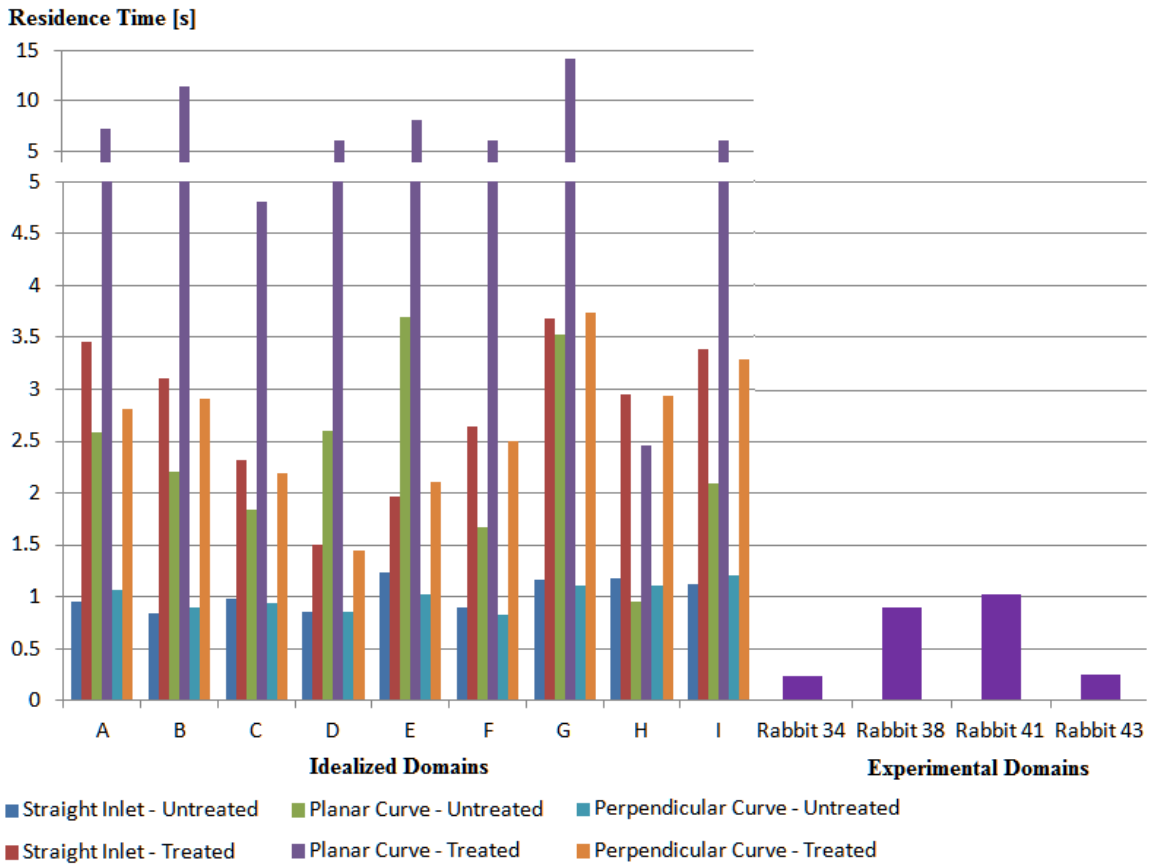


Figure 5-25. The residence time of blood in the aneurysm is compared between the idealized computational aneurysms with human physiological flow conditions, and rabbit aneurysms with rabbit flow conditions. It appears that the untreated flow conditions mimic those of untreated aneurysms with a straight or a perpendicular curve inlet. This suggests that flow diverters placed in the rabbit will be tested in conditions that are physiologically relevant both from the geometrical and the fluid mechanical perspectives.

Fluid dynamics analysis of animal and clinical results must be combined with functional outcomes (i.e. did the aneurysm occlude?) to tune blood coagulation models and determine which flow metrics and under what thresholds will aneurysms occlude. Figure 5-25 illustrates that untreated aneurysms simulated with straight (dark blue bar, 1st bar from the left) or perpendicular curve (light blue bar, 5th bar from the left) inlets were found to have residence times less than 1.25s. Since the Pipeline Embolization Device has successfully treated similar aneurysms most of the time [109], Figure 5-25 suggests that a residence time somewhere above 1.5 seconds will lead to occlusion of the aneurysm. However, residence times in untreated aneurysms with planar curve upstream segments (green bar, 3rd bar from the left) are in some cases (D and E) higher than residence times in treated aneurysms with straight (red bar, 2nd bar from the left) or perpendicular curve (orange bar, 6th bar from the left) upstream segments. More clinical research is needed to confirm if these types of aneurysms are rare or typically much smaller than aneurysms with perpendicular curve upstream segments.

Finally, the biological response needs to be taken into account as well. Positive feedback loops may accelerate healing. As mentioned before, residence time as defined in this discussion is a very approximate metric of intraaneurysmal flow. A metric that better accounts for the distribution of intraaneurysmal fluid velocity will reflect how blood in stagnant portions of the aneurysm will coagulate and effectively alter the geometry of the flow domain. Research is also needed to determine if the metallic wires of the flow diverter, which triggers the foreign body response, also exerts a time dependent effect. If the pores shrink due to accumulation of tissue or thrombus on the individual wires, the effective porosity decreases. This may form a positive feedback loop where decreased intraaneurysmal flow leads to a decreased pore size, which in turn leads to an even lower intraaneurysmal flow.

6.0: CONCLUDING REMARKS AND NEXT STEPS

CONCLUDING REMARKS AND NEXT STEPS

The combination of benchtop experiments, computational simulations, and animal model evaluations has led to a better understanding of the performance of the current generation of flow diverters for aneurysm management. Each piece of the mosaic offers unique perspectives into how the device performs. Benchtop PIV experiments fully captured the fluid mechanics and structural nuances of the flow diverter, particularly its actual deployed shape. The CFD simulations offered an efficient method for predicting device performance for a greater range of aneurysm and parent vessel geometries. The animal studies demonstrated that aneurysms with residence times less than 1.5s remained open. Implantation of flow diverters in rabbit aneurysms in the future can be used to validate coagulation models presented by researchers such as Rayz et al. [110] and Sequeira et al. [102]. Pursuing knowledge in all three synergistic modalities paints a much more comprehensive picture for predicting how the next generation of flow diverters will perform inside human patients.

Observations generated in this body of research indicate that the flow diversion effect may not be as high as believed in the past. Figure 6-1 summarizes the effect of the diverter in reducing the flow entering the aneurysms and the reduction in time-averaged spatial average velocity in the midplane of the aneurysms from Chapter 4.4. The time-averaged spatial-average V_T/V_{UT} metric consistently underestimates how much blood was still entering the aneurysm after placement of the flow diverter.

The “85% reduction in recirculation” claimed by the designers of the PED was likely based on a decrease in vorticity. The work presented by Seong et al. [111] derived their “hydrodynamic circulation” metric based on integration of instantaneous vorticity on velocity fields measured at the plane of symmetry of the model. Figure 6-2 illustrates two such measurements, as well as a summary of the hydrodynamic circulation values measured for various flow diverter designs. This may be the basis for the claim of “85% reduction in circulation” for the PED. Figure 6-3 summarizes the velocity curl, or vorticity, calculated on the same planes as V_T and V_{UT} for the simulations of Chapter 4.4.1. An ~85% reduction in vorticity is observed in most flow domains. Aneurysms that lie on the tightest curves (D and E) are again found to be problematic for the flow diverter.

Q_T / Q_{UT} and Avg V_T / V_{UT} in Domains with Different Upstream Segments

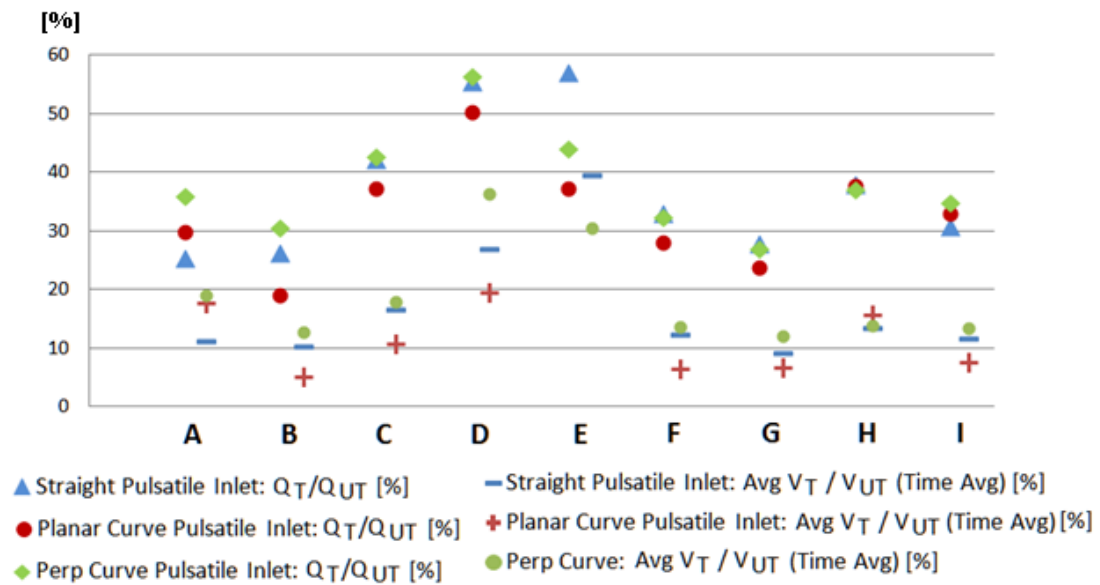


Figure 6-1. The Q_T/Q_{UT} and time averaged spatial average V_T/V_{UT} metrics are summarized for the idealized aneurysms discussed in Chapter 4.4. The flow diversion effect of the PED may not be as high as believed in the past.

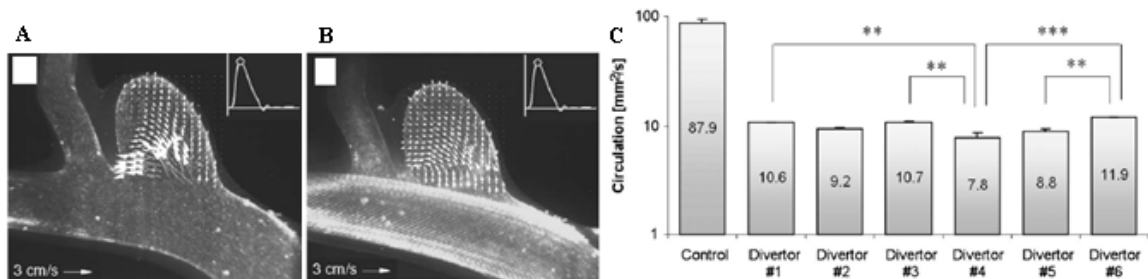


Figure 6-2. The hydrodynamic circulation metric used by Seong et al. [111] is based on fluid vorticity in PIV measurements taken at the plane of symmetry. It is similar to the location where the V_T and V_{UT} metrics were calculated by simulations in Chapter 4.4. The arrows in Figure 6-2A represent velocity vectors and illustrate flow in an untreated aneurysm. The arrows in Figure 6-2B illustrate velocity of fluid in a treated aneurysm after placement of a flow diverter. The plot on Figure 6-2C summarizes the hydrodynamic circulation values observed by Seong for different flow diverter designs. An approximately 85% reduction in circulation was observed.

Velocity Curl in Aneurysm Midplane, Straight Pulsatile Inlet

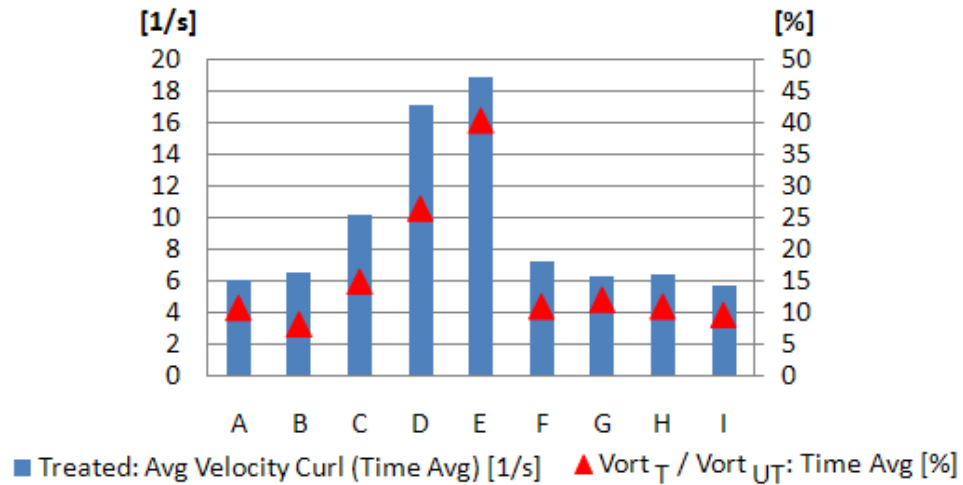


Figure 6-3. The velocity curl, or vorticity, is calculated on the midplane of the aneurysms in the idealized flow domains of Chapter 4.4.

However, the exact morphology of the flow diverter after implantation is of great importance.

Referring back to Figure 4-31, the effectiveness of the flow diverter in reducing inflow to the aneurysm varies by as much as 20% depending on the size of the diamond pores. It has already been illustrated in Figure 4-44 that the PED changes shape when placed in tight bends. Wang et al. [112] performed μ CT scans with a resolution of $17\mu\text{m}$ to capture the final shapes of the flow diverters after deployment in 22 rabbit aneurysms. Figure 6-4 illustrates one such reconstruction. Based on the percentage of the neck covered by the metal wires and the state of the aneurysm at follow-up surgery, Wang concluded that 35% of actual coverage predicted occlusion with a specificity and sensitivity of 100% and 53.8% respectively. 27% of actual coverage predicted occlusion with a specificity and sensitivity of 76.9% and 62.5%.

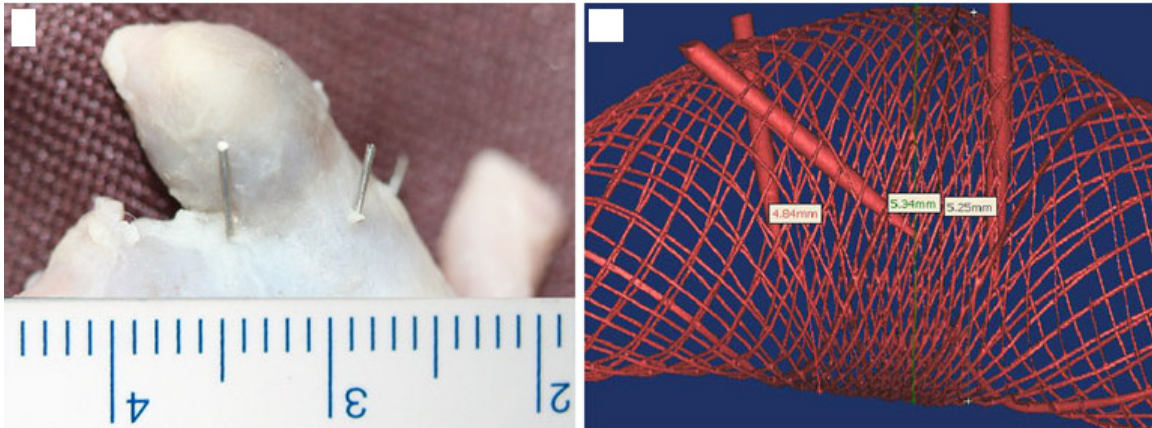


Figure 6-4. One of the rabbit aneurysms treated by Wang et al. [112] that was excised at the conclusion of the study is shown. A microCT scan with a 17 μ m resolution was used to characterize the shape of the flow diverter. Wang et al. correlated the degree of aneurysm neck coverage by the metal wires of the diverter with the occlusion observed at followup and found that a 35% metal coverage predicted occlusion with a specificity and sensitivity of 100% and 53.8% respectively.

Flow diverter performance in aneurysms of different bulb diameters and neck sizes should also be evaluated. Examination of flow entering RC-SOD147-6, RC-SOD147-12(F/R), and domains C, H, and I illustrates that neck geometry has a particularly large influence on the flow of blood entering the aneurysm.

Correlation of dye uptake angiographically to the intraaneurysmal flow should be pursued in the glass models described in Chapter 3.3. Dye injection should be simulated and verified in the idealized models described in Chapter 4.4. This will bridge the knowledge gap between underlying the fluid mechanics and the clinical effects observed by physicians after placement of the flow diverter. Simulation of dye uptake in the range of idealized models can be used to train physicians as to what to expect in the clinical setting after placement of a flow diverter. Sadasivan et al. [113], Cebal et al. [100], and Ford et al. [114] have already started down this path, but none have incorporated all four elements of experimental, computational, animal, and clinical studies before and after placement of a flow diverter. Figure 6-5 illustrates the comparison between dye uptake observed angiographically and simulated computationally by Cebal.

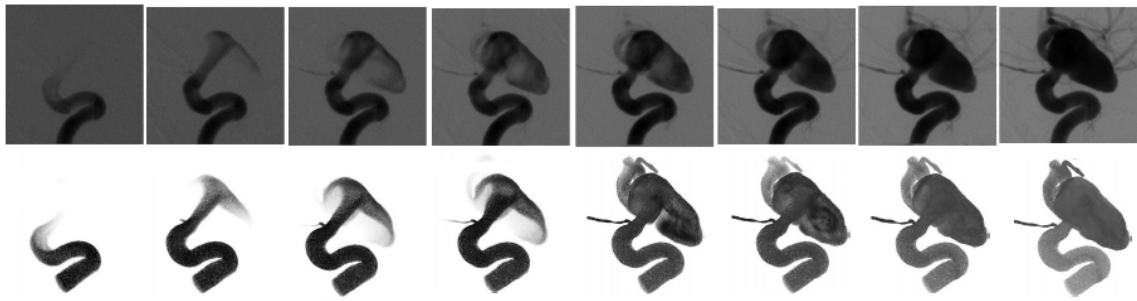


Figure 6-5. The uptake of dye observed angiographically (top) was compared to what was predicted from CFD (bottom) under pulsatile flow (time progresses from left to right). The geometry was reconstructed from a CT scan of the patient. [100]

An alternative method for constructing flow diverters can serve as a much more flexible platform for evaluating different pore designs. The braided wire tube forms the backbone of all 1st generation devices (PED, Silk, FRED, Neuroendograph). Its mechanical properties (flexibility, radial force, radiopacity), fluid diversion properties (pore shape, susceptibility to compression or stretching of pores), and foreign body response are intertwined. A perforated stent graft platform, presented by Nakayama et al. [115] and illustrated in Figure 6-6, decouples the flow diversion properties from the mechanical properties of the device. This allows for evaluation of a large number of pore shape, size, and distribution combinations. An optimal configuration may be achieved with this platform.

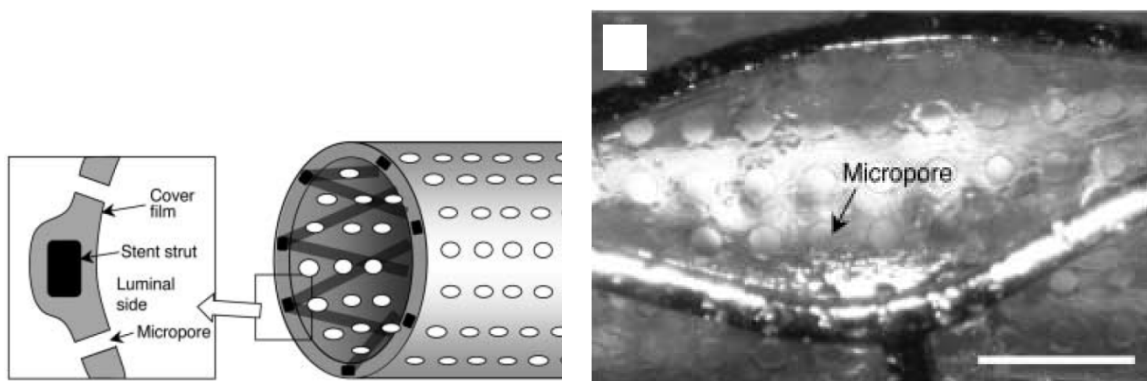


Figure 6-6. A cartoon of the stent graft platform presented by Nakayama et al. [115] is shown on the **left**. A close up view of the device while mounted on the coating pin is shown on the **right**.

A heightened level of understanding of intraaneurysmal clotting kinetics and foreign body response is important for designing the second generation of flow diverters. Already, flow diverters are being considered for use by physicians as a first line treatment for all aneurysms, as opposed to just large and wide necked aneurysms. Complications, particularly post-procedural subarachnoid hemorrhage,

will occur more frequently with expanded use and need to be resolved for continued adoption by the neurovascular community [116]. Tse et al. [109] reported that the PED was susceptible to deployment failure when implanted in highly tortuous vessels due to increased friction of the device with the catheter wall. Furthermore, the pores of the braided structure are susceptible to opening up in highly tortuous vessels, thereby reducing its flow diverting properties. Placement of overlapping PEDs presents its own technical challenges, as well as an increased risk for occlusion of perforator vessels.

Three theories exist for explaining SAH. The “hemodynamic theory” by Cebal [117] suggests that exclusion of the aneurysm in some cases raises the pressure exerted on nearby tissue, leading to hemorrhaging. This theory is somewhat at odds with the clinical history of endovascular coiling, where the aneurysm is similarly excluded. Differences in administration of anti-thrombotic medications may be responsible.

The “inflammation theory” by Turowski [118] suggests that a delayed formation of organized thrombus may result in an inflammatory reaction where the aneurysm wall and nearby vessels are further weakened and at increased risk of rupture. Quicker formation of organized thrombus using a more aggressive flow diverter may address this SAH risk factor.

The “foreign emboli” theory by Deshmukh [119] suggests that the deployment mechanism of the PED is susceptible to generating emboli. The coarse nature of the wire braid may be too abrasive against the PTFE liner found in most microcatheters, and eject tiny strands of emboli during device deployment. A smoother device, such as the polymeric stent graft, may produce less emboli and address this SAH risk factor.

Overall, a comprehensive method has been presented for evaluating the next generation of flow diverting devices. Evaluation of the PED indicates that flow diverters that exclude blood from the aneurysm more severely should be examined. The polymeric stent graft offers greater possibilities in optimizing the pore pattern than the braided metal wire tube. It is hoped that a combination of engineering fundamentals and elucidating animal studies will provide the basis for on-label (approved by the Food and Drug Administration and the European Commission) use of an optimized second generation device(s) for treatment of all intracranial aneurysms.

7.0: REFERENCES AND BIBLIOGRAPHY

REFERENCE LIST

- [1] Neurology Channel. *Stroke*. <http://www.neurologychannel.com/stroke/index.shtml>. Accessed November 2009
- [2] Vega et al. *Intracranial Aneurysms: Current Evidence and Clinical Practice*. **Am Family Physician**. (2002). 64: 601 – 608.
- [3] Toronto Brain Vascular Malformation Study Group. *Endovascular Embolization Treatment of Aneurysms*. http://brainavm.oci.utoronto.ca/malformations/content/treat_embo_aneurysm.htm. Accessed November 2009.
- [4] Spectrum Health (A). http://applications.spectrum-health.org/media/coe_heart/images/GS_clipping%20treatment%20for%20cerebral%20aneurysm_lg.gif. Accessed November 2009
- [5] Spectrum Health (B). http://applications.spectrum-health.org/media/coe_heart/images/GS_coil%20procedure%20cerebral%20aneurysm_lg.gif. Accessed November 2009.
- [6] Kallmes et al. *A New Endoluminal Flow Disrupting Device for Treatment of Saccular Aneurysms*. **Stroke**.(2007). 38: 2346 – 2352.
- [7] http://openi.nlm.nih.gov/detailedresult.php?img=3216267_IJVM2012-654627.001&req=4 Accessed March 2013
- [8] http://www.print2webcorp.com/news/Vineland/HealthConnection/20110818/p06_07_a2.htm Accessed March 2013
- [9] <http://www.microvention.com/index.php?id=33> Accessed March 2013
- [10] D’Urso et al. *Flow Diversion for Intracranial Aneurysms*. **Stroke**. (2011) 42: 2363 – 2368.
- [11] Lylyk et al. *Curative Endovascular Reconstruction of Cerebral Aneurysms with the Pipeline Embolization Device: The Buenos Aires Experience*. **Neurosurgery**. (2009). 64: 632 – 643.
- [12] Cebal et al. *Efficient Simulation of Blood Flow Past Complex Endovascular Devices using an Adaptive Embedding Technique*. **IEEE Transactions on Medical Imaging**. (2005). 24: 468 – 476.
- [13] Malek et al. *Hemodynamic Shear Stress and Its Role in Atherosclerosis*. **JAMA**.(1992). 282: 2035 – 2042.
- [14] Meddean. <http://www.meddean.luc.edu/lumen/MedEd/neuro/neurovasc/navigation/ica.htm>. Accessed August 2010.
- [15] http://en.wikipedia.org/wiki/File:Circle_of_Willis_en.svg. Accessed August 2010.
- [16] <http://upload.wikimedia.org/wikipedia/commons/3/33/ICAs.jpg> Accessed August 2010
- [17] Alastruey et al. *Modeling the Circle of Willis to Assess the Effects of Anatomical Variations and Occlusions on Cerebral Flows*. **J Biomechanics**. (2007). 40: 1794 – 1805.
- [18] Devault et al. *Blood Flow in the Circle of Willis: Modeling and Calibration*. **Multiscale Model Simul**.(2008). 7: 888 – 909.
- [19] Dhar et al. *Morphology Parameters for Intracranial Aneurysm Rupture Risk Assessment*. **Neurosurgery**. (2008). 63: 185 – 197.
- [20] Moore et al. *3D Models of Blood Flow in the Cerebral Vasculature*. **J Biomech**. (2006). 39: 1454 – 1463.
- [21] Hartkamp et al. *Circle of Willis Collateral Flow Investigated by Magnetic Resonance Angiography*. **Stroke**. (1999). 30: 2671 – 2678.
- [22] Krabbe-Hartkamp et al. *Circle of Willis: Morphologic Variation on Three-dimensional Time of Flight MR Angiograms*. **Radiology**. (1998) 207: 103-111.
- [23] Huang et al. *Stent Assisted Embolization of Wide Neck Anterior Communicating Artery Aneurysms: Review of 21 Consecutive Cases*. **Am J Neuroradiol**. (2009).
- [24] Fisher et al. *Regulation of Middle Cerebral Artery Blood Velocity During Dynamic Exercise in Humans: Influence of Aging*. **J Appl Physiol**. (2008). 105: 266 – 273.
- [25] Tsutsumi et al. *Endovascular Treatment of Tiny Ruptured Anterior Communicating Artery Aneurysms*. **Neuroradiology**. (2008). 50: 509 – 515.
- [26] Krejza et al. *Carotid Artery Diameter in Men and Women and the Relation to Body and Neck Size*. **Stroke**. (2006). 37: 1103 – 1105.

- [27] Turk et al. *Use of Self Expanding Stents in Distal Small Cerebral Vessels*. **Am J Neuroradiol.** (2007). 28: 533 – 536.
- [28] Khader et al. *A Comparative Study of Transient Flow Through Cerebral Aneurysms Using CFD*. **Engineering and Technology.** (2009). 60: 606 – 610.
- [29] Sorteberg et al. *Effect of Acetazolamide on Cerebral Artery Blood Velocity and Regional Cerebral Blood Flow in Normal Subjects*. **Acta Neurochir.**(1989). 97: 139 – 145.
- [30] Wetzel et al. *In Vivo Assessment and Visualization of Intracranial Arterial Hemodynamics with Flow Sensitized 4D MR Imaging at 3T*. **Am J Neuroradiol.**(2007). 28: 433 – 438.
- [31] Brys. *Dynamic Cerebral Autoregulation Remains Stable During Physical Challenge in Healthy Persons*. **Am J Physiol Heart Circ Physiol.** (2003). 285: 1048 – 1054.
- [32] Chan et al. *Intracranial Blood Flow Velocity After Head Injury: Relationship to Severity of Injury, Time, Neurological Status and Outcome*. **J Neurology.**(1992). 55: 787 – 791.
- [33] Kawai et al. *Cerebral Blood Flow Velocity in Humans Exposed to 24 Hour of Head Down Tilt*. **J Appl Physio.** (1993)
- [34] Low et al. *Dynamic Cerebral Autoregulation During Passive Heat Stress in Humans*. **Am J Physiol Regul Integr Comp Physiol.** (2009). 296.
- [35] Ogoh et al. *MCA Flow Velocity and Pulse Pressure During Dynamic Exercise in Humans*. **Am J Physiol Heart Circ Physiol.** (2005). 288: 1526 – 1531.
- [36] Jiang and Strother. *Computational Fluid Dynamics Simulations of Intracranial Aneurysms at Varying Heart Rates: A “Patient Specific” Study*. **J Biomech Eng.** (2009). 131.
- [37] Alhothi et al. *Neuroform Stent Assisted Coil Embolization: New Treatment Strategy for Complex Intracranial Aneurysms with Midterm Results*. **Romanian Neurosurgery.** (2010). 17-2: 147 – 157.
- [38] Akpek et al. *Self Expandable Stent Assisted Coiling of Wide Necked Intracranial Aneurysms: A Single Center Experience*. **Am J Neuroradiol.** (2005). 26: 1223 – 1231.
- [39] Li et al. *The Feasibility and Efficacy of Treatment with a Willis Covered Stent in Recurrent Intracranial Aneurysms After Coiling*. **Am J Neuroradiol.** (2008).
- [40] Szikora et al. *Impact of Aneurysmal Geometry on Intraaneurysmal Flow: A Computerized Flow Simulation Study*. **Neuroradiology.** (2008). 50: 411 – 421.
- [41] Weber et al. *Treatment and Followup of 22 Unruptured Wide Necked Intracranial Aneurysms of the Internal Carotid Artery with Onyx HD 500*. **Am J Neuroradiol.** (2005). 26: 1909 – 1915.
- [42] Wiebers et al. *Unruptured Intracranial Aneurysms: Natural History and Clinical Management. Update on the International Study of Unruptured Intracranial Aneurysms*. **Neuroimaging Clin NA.** (2006). 16: 383 – 390.
- [43] Lang et al. *Use of Covered Stent Grafts in the Extracranial Carotid Artery: Report of Three Patients with Followup Between 8 and 42 Months*. **Am J Neuroradiol.** 25: 1760 – 1763.
- [44] Lang, Johannes. *Skull Base and Related Structures*. 1995.
- [45] Almandoz et al. *Size and Location of Ruptured Intracranial Aneurysms in a Consecutive Series of 588 Patients with First-Time Acute Subarachnoid Hemorrhage Treated Endovascularly at a Tertiary Referral Medical Center over a 16 Year Time Period*. **J NeuroIntervent Surg.** (2012). 4: A4 – A5.
- [46] Carter et al. *Epidemiology of the Size Distribution of Intracranial Bifurcating Aneurysms: Smaller Size of Distal Aneurysms and Increasing Size of Unruptured Aneurysms with Age*. **Neurosurgery.** (2006). 58: 217 – 223.
- [47] Ujiie et al. *Is the Aspect Ratio a Reliable Index for Predicting the Rupture of a Saccular Aneurysm*. **Neurosurgery.**(2001). 48: 495 – 503.
- [48] Weir et al. *The Aspect Ratio (Dome/Neck) of Ruptured and Unruptured Aneurysms*. **J Neurosurg.** (2003). 99: 447 – 451.
- [49] Raghavan et al. *Quantified Aneurysm Shape and Rupture Risk*. **J Neurosurg.**(2005). 102: 355 – 362.
- [50] Johnston et al. *Non-Newtonian Blood Flow in Human Right Coronary Arteries – Steady State Simulations*. **J Biomech.** (2004). 37: 709 – 720.

- [51] Johnston et al. *Non-Newtonian Blood Flow in Human Right Coronary Arteries – Transient Simulations*. **J Biomech.** (2006). 39: 1116 – 1128.
- [52] Burlison et al. *Computer Modeling of Intracranial Saccular and Lateral Aneurysms for the Study of Their Hemodynamics*. **Neurosurgery.** (1995). 37: 774 – 784.
- [53] Steinman. *Image Based Computational Simulation of Flow Dynamics in a Giant Intracranial Aneurysm*. **Am J Neuroradiol.**(2003). 24: 559 – 566.
- [54] Hoi et al. *Validation of CFD Simulations of Cerebral Aneurysms With Implication of Geometric Variations*.**J Biomech Eng.**(2006). 128: 844 – 851.
- [55] Cebal et al. *Blood Flow Models of the Circle of Willis from Magnetic Resonance Data*. **J Eng Math.** (2003). 47: 369 – 386.
- [56] Hoi et al. *Effects of Arterial Geometry on Aneurysm Growth: Three Dimensional Computational Fluid Dynamics Study*. **J Neurosurg.** (2004). 101: 676 – 681.
- [57] Liou et al. *Numerical and Experimental Studies on Pulsatile Flow in Aneurysms Arising Laterally From a Curved Parent Vessel at Various Angles*. **J Biomech.** (2007). 40: 1268 – 1275.
- [58] Sato et al. *The Importance of Parent Artery Geometry in Intra-Aneurysmal Hemodynamics*.**Med Eng Phys.** (2008). 30: 774 - 782.
- [59] Castro et al. *Computational Fluid Dynamics Modeling of Intracranial Aneurysms: Effects of Parent Artery Segmentation on Intra-Aneurysmal Hemodynamics*. **Am J Neuroradiol.**(2006). 27: 1703 – 1709.
- [60] Fisher et al. *Effect of Non-Newtonian Behavior on Hemodynamics of Cerebral Aneurysms*.**J Biomech Eng.** (2009). 131.
- [61] Cebal et al. *Association of Hemodynamic Characteristics and Cerebral Aneurysm Rupture*. **Am J Neuroradiol.** (2011)
- [62] Benndorf et al. *Treatment of a Ruptured Dissecting Vertebral Artery Aneurysm with Double Stent Placement: Case Report*.**Am J Neuroradiol.**(2001). 22: 1844 – 1848.
- [63] Sadasivan et al. *An Original Flow Diversion Device for the Treatment of Intracranial Aneurysms: Evaluation in the Rabbit Elastase Induced Model*. **Stroke.**(2009). 40: 952 – 958.
- [64] Szikora et al. *Treatment of Intracranial Aneurysms by Functional Reconstruction of the Parent Artery: The Budapest Experience with the Pipeline Embolization Device*. **Am J Neuroradiol.**(2010). 31: 1139 – 1147.
- [65] Vanninen et al. *Broad Based Intracranial Aneurysms: Thrombosis Induced by Stent Placement*. **Am J Neuroradiol.** (2003). 24: 263 – 266.
- [66] Stuhne et al. *Finite Element Modeling of the Hemodynamics of Stented Aneurysms*.**J Biomech Eng.** (2004). 126.
- [67] Kim et al. *Comparison of Two Stents in Modifying Cerebral Aneurysm Hemodynamics*. **Annals Biomed Eng.** (2008). 36: 726 – 741.
- [68] Seshadhri et al. *Impact of Stents and Flow Diverters on Hemodynamics in Idealized Aneurysm Models*. **J Biomech Eng.** (2011). 133.
- [69] Appanaboyina et al. *Computational Modeling of Blood Flow in Side Arterial Branches after Stenting of Cerebral Aneurysms*. **Int J Comp Fluid Dynamics.** (2008). 22: 669 – 676.
- [70] Hoi et al. *Validation of CFD Simulations of Cerebral Aneurysms with Implication of Geometric Variations*. **J Biomech Eng.** (2006). 128: 844 – 851.
- [71] Doyle et al. *3D Reconstruction and Manufacture of Real Abdominal Aortic Aneurysms: From CT Scan to Silicone Model*. **J Biomech Eng.** (2008) 130.
- [72] Ku et al. *Comparison of CFD and MRI Flow and Velocity in an In Vitro Large Artery Bypass Graft Model*. **Annals Biomed Eng.** (2005). 33: 257 – 269.
- [73] Arcaute et al. *Complex Silicone Aorta Models Manufactured Using a Dip-Spin Coating Technique and Water Soluble Molds*. **2003 Summer Bioengineering Conference.** (2003). 1093 – 1094.
- [74] Chueh et al. *Neurovascular Modeling: Small Batch Manufacturing of Silicone Vascular Replicas*. **Am J Neuroradiol.**(2009).

- [75] Barath et al. *Anatomically Shaped Internal Carotid Artery Aneurysm in Vitro Model for Flow Analysis to Evaluate Stent Effect*. **Am J Neuroradiol.** (2004). 25: 1750 – 1759.
- [76] Boutsianis et al. *CFD and PTV Steady Flow Investigation in an Anatomically Accurate Abdominal Aortic Aneurysm*. **J Biomed Eng.** (2009) 131.
- [77] Canton et al. *Hemodynamic Changes Due to Stent Placement in Bifurcation Intracranial Aneurysms*. **J Neurosurg.** (2005). 103: 146 – 155.
- [78] Chong et al. *Computer Aided Design and Fabrication of Models for In Vitro Studies of Vascular Fluid Dynamics*. **Proc Instn Mech Engrs.** (1999). 213 Part H.
- [79] Ford et al. *PIV Measured Versus CFD Predicted Flow Dynamics in Anatomically Realistic Cerebral Aneurysm Models*. **J Biomech Eng.** (2008). 130.
- [80] Friedman et al. *Effects of Arterial Compliance and Non-Newtonian Rheology on Correlations Between Intimal Thickness and Wall Shear*. **J Biomech Eng.** (1992) 114.
- [81] Ionita et al. *Particle Image Velocimetry Evaluation of Flow Modification in Aneurysm Phantoms Using Asymmetric Stents*. **Medical Imaging.** (2004).
- [82] Lieber et al. *Particle Image Velocimetry Assessment of Stent Design Influence on Intra-Aneurysmal Flow*. **Annals Biomed Eng.** (2002). 30: 768 – 777.
- [83] Meng et al. *Saccular Aneurysms on Straight and Curved Vessels are Subject to Different Hemodynamics: Implications of Intravascular Stenting*. **Am J Neuroradiol.**(2006). 27: 1861 – 1865.
- [84] Rangwala et al. *Partially Polyurethane Covered Stent for Cerebral Aneurysm Treatment*. **J Biomed Mat Res.** (2008).
- [85] Sadasivan et al. *Angiographic Quantification of Contrast Medium Washout from Cerebral Aneurysms After Stent Placement*. **Am J Neuroradiol.**(2002). 23: 1214 – 1221.
- [86] Steiger et al. *Hemodynamic Stress in Lateral Saccular Aneurysms*. **Acta Neurochir.**(1987) 86: 98 – 105.
- [87] Yu et al. *A Steady Flow Analysis on the Stented and Non-Stented Sidewall Aneurysm Models*. **Med Eng Phys.** (1999). 21: 133 – 141.
- [88] Benndorf et al. *Intraaneurysmal Flow: Evaluation with Doppler Guidewires*. **Am Soc Neuroradiol.** (1996). 17: 1333 – 1337).
- [89] Liou et al. *Hemodynamics Altered by Placing Helix Stents in an Aneurysm at a 45 Angle to the Curved Vessel*. **Phys Med Biol** (2008).53: 3763 – 3776.
- [90] Wetzel et al. *In Vivo Assessment and Visualization of Intracranial Arterial Hemodynamics with Flow-Sensitized 4D MR Imaging at 3T*. **Am J Neuroradiol.** (2007). 28: 433 – 438.
- [91] Sherif et al. *Improved Microsurgical Creation of Venous Pouch Arterial Bifurcation Aneurysms in Rabbits*. **Am J Neuroradiol.** (2011). 32: 165 – 169.
- [92] Cesar et al. *Neurological Deficits Associated with the Elastase Induced Aneurysm Model in Rabbits*. **Neurological Research.** (2009). 31: 414 – 419.
- [93] Altes et al. *Creation of Saccular Aneurysms in the Rabbit*. **AJR.** (2000). 174: 349 – 354.
- [94] Ding et al. *Can Neck Size in Elastase Induced Aneurysms be Controlled? A Prospective Study*. **Am J Neuroradiol.** (2005). 26: 2364 – 2367.
- [95] Kallmes et al. *A Second Generation, Endoluminal, Flow-Disrupting Device for Treatment of Saccular Aneurysms*. **Am J Neuroradiol.** (2009). 30: 1153 – 1158.
- [96] Tan et al. *Flow Visualization using Cavitation within Blade Passage of an Axial Waterjet Pump Rotor*. **Proceedings of the ASME 2012 Fluids Engineering Summer Meeting**. FEDSM2012-72108.
- [97] http://www.accessdata.fda.gov/cdrh_docs/pdf10/P100018c.pdf Accessed March 2013
- [98] <http://bardmedical.com/DIMENSIONArticulatingStoneBasket/Grasper> Accessed March 2013
- [99] http://en.wikipedia.org/wiki/Histogram_equalization Accessed March 2013

- [100] Cebal et al. *Computational Fluid Dynamics Modeling of Intracranial Aneurysms: Qualitative Comparison with Cerebral Angiography*. **Acad Radiol.** (2007). 14: 804 – 813.
- [101] <http://www.ev3.net/neuro/intl/flow-diversion/> Accessed March 2013
- [102] Sequeira et al. *Blood Coagulation Dynamics: Mathematical Modeling and Stability Results*. **Mathematical Biosciences and Engineering.** (2011). 8: 425 – 443.
- [103] Fogelson et al. *Coagulation under Flow: The Influence of Flow-Mediated Transport on the Initiation and Inhibition of Coagulation*. **Pathophysiology of Haemostasis and Thrombosis.** (2005). 34: 91 – 108.
- [104] Alnaes et al. *Computation of Hemodynamics in the Circle of Willis*. **Stroke.** (2007). 38: 2500 – 2505.
- [105] Edwards et al. *The Cardiac Output of the Unanesthetized Rabbit, and the Effects of Preliminary Anesthesia, Environmental Temperature, and Carotid Occlusion*. **Experimental Physiology.** (1959) 44: 309 - 321.
- [106] Fletcher et al. *Changes in Cardiac Output and Total Peripheral Resistance during Development of Renal Hypertension in the Rabbit: Lack of conformity with the Autoregulation Theory*. **Circulation Research.** (1976) 39: 633 – 639.
- [107] Ding et al. *Control of Aneurysm Volume by Adjusting the Position of Ligation During Creation of Elastase Induced Aneurysms: A Prospective Study*. **Am J Neuroradiol.** (2007). 28: 857 – 859.
- [108] Ding et al. *Long Term Patency of Elastase Induced Aneurysm Model in Rabbits*. **Am J Neuroradiol.** (2006). 27: 139 – 141.
- [109] Tse et al. *Current Status of Pipeline Embolization Device in the Treatment of Intracranial Aneurysms: A Review*. **World Neurosurgery.** In review as of April 2013.
- [110] Rayz et al. *Numerical Simulations of Flow in Cerebral Aneurysms: Comparison of CFD Results and In Vivo MRI Measurements*. **J Biomech Eng.** (2008). 130.
- [111] Seong et al. *In Vitro Evaluation of Flow Divertors in an Elastase Induced Saccular Aneurysm Model in Rabbit*. **J Biomech Eng.** (2007). 129: 863 – 872.
- [112] Wang et al. *Correlation of Aneurysm Occlusion with Actual Metal Coverage at Neck after Implantation of Flow Diverting Stent in Rabbit Models*. **Neuroradiology.** (2012). 54: 607 – 613.
- [113] Sadasivan et al. *Treatment of Rabbit Elastase Induced Aneurysm Models by Flow Diverter: Development of Quantifiable Indexes of Device Performance Using Digital Subtraction Angiography*. **IEEE Transactions on Medical Imaging.** (2009). 28: 1117 – 1125
- [114] Ford et al. *Virtual Angiography for Visualization and Validation of Computational Models of Aneurysm Hemodynamics*. (2005) **IEEE Transactions on Medical Imaging.** (2005) 24: 1586 – 1592.
- [115] Nakayama et al. *Development of Microporous Covered Stents: Geometrical Design of the Luminal Surface*. **J Artif Organs.** (2005). 28: 600 – 608.
- [116] Jabbour et al. *The Pipeline Embolization Device: What Have We Learned?* **World Neurosurgery.** In review as of April 2013.
- [117] Cebal et al. *Aneurysm Rupture Following Treatment with Flow Diverting Stents: Computational Hemodynamics Analysis of Treatment*. **Am J Neuroradiol.** (2011). 32: 27 – 33.
- [118] Turowski et al. *Early Fatal Hemorrhage after Endovascular Cerebral Aneurysm Treatment with a Flow Diverter*. **Neuroradiology.** (2011). 53: 37 – 41.
- [119] Deshmukh et al. *Histopathological Assessment of Delayed Ipsilateral Parenchymal Hemorrhages after the Treatment of Paraclinoid Aneurysms with the Pipeline Embolization Device*. **2012 Annual Meeting of the Congress of Neurological Surgeons.**

BIBLIOGRAPHY OF UNREFERENCED BACKGROUND MATERIAL

Books

Welty, Wicks, Wilson, and Rorrer. *Fundamentals of Momentum, Heat, and Mass Transfer 4th Edition*. 2001.

Vermette et al. *Biomedical Applications of Polyurethanes*. 2001.

Manuscripts

Abruzzo et al. *Histologic and Morphologic Comparison of Experimental Aneurysms with Human Intracranial Aneurysms*. **Am J Neuroradiol.**(1998). 19: 1309 – 1314.

Adler et al. *The Role of Alkaline Cleaning Solutions and Cl Containing Lubricants on Pitting Corrosion in NiTi Alloys*. **Internal publication by Memry Corporation**. 1 – 7.

Alfke et al. *Treatment of Intracranial Broad-Neck Aneurysms with a New Self Expanding Stent and Coil Embolization*. **Am J Neuroradiol.**(2004). 25: 584 – 591.

Augsburger et al. *Methodologies to Assess Blood Flow in Cerebral Aneurysms: Current State of Research and Perspectives*. **Neuroradiol.**(2009). In press.

Avellanet et al. *Aneurysm Neck Cover for Sealing an Aneurysm*. **USPTO: 7 195 636**. (2007). 1 – 11.

Bell et al. *Neurovascular Anatomy: A Practical Guide*. **Neurosurg Clin N Am.** (2009). 20: 265 – 278.

Bernacca et al. *Hydrodynamic Function of Polyurethane Prosthetic Heart Valves: Influences of Young's Modulus and Leaflet Thickness*. **Biomaterials.**(2002). 23: 45 – 50.

Bernacca et al. *Mechanical and Morphological Study of Biostable Polyurethane Heart Valve Leaflets Explanted from Sheep*. **J Biomed Mater Res.** (2002). 61: 138 – 145.

Berry et al. *Hemodynamics and Wall Mechanics of a Compliance Matching Stent: In Vitro and In Vivo Analysis*. **J Vas Interv Radiol.**(2002). 13: 97 – 105.

Biondi et al. *Neuroform Stent Assisted Coil Embolization of Wide Neck Intracranial Aneurysms: Strategies in Stent Deployment and Midterm Follow-Up*. **Neurosurgery.**(2007) 61: 460 – 469.

Bjorkesten and Troupp. *Changes in the Size of Intracranial Arterial Aneurysms*. **J Neurosurg.**(1962). 19: 583 – 588.

Black and German. *Observations on the Relationship Between the Volume and the Size of the Orifice of Experimental Aneurysms*. **J Neurosug.**(1960). 17: 984 – 990.

Bonneville et al. *Intracranial Aneurysms: an Overview*. **Neuroimng Clin NA.** (2006). 371 – 382.

- Bose and Nelson. *Endovascular Thin Film Devices and Methods for Treating and Preventing Stroke*. **USPTO: 6 605 111**. (2003). 1 – 31.
- Brash. *Exploiting the Current Paradigm of Blood Material Interactions for the Rational Design of Blood Compatible Materials*. **J Biomat Sci Polymer End.** (2000) 11: 1135 – 1146.
- Broadbent et al. *Management of Neuroform Stent Dislodgement and Misplacement*. **Am J Neuroradiol.**(2003). 24: 1819 – 1822.
- Burkelko et al. *Stent-graft Placement for Wide-Neck Aneurysm of the Vertebrobasilar Junction*. **Am J Neuroradiol.**(2004) 25: 608 – 610.
- Burns et al. *Intracranial Aneurysm Enlargement on Serial Magnetic Resonance Angiography: Frequency and Risk Factors*. **Stroke.**(2009). 40: 406 – 411.
- Burns et al. *Treatment of Unruptured Intracranial Aneurysms: Surgery, Coiling, or Nothing*. **Cur Neurology and Neuroscience Reports.** (2009). 9: 6 – 12.
- Bryne and Hubbard. *A Novel Two-Stage Technique for Construction of Experimental Aneurysms*. **Am J Neuroradiol.**(2004). 25: 319 – 321.
- Chen et al. *Phosphorylcholine Coating of ePTFE Grafts Reduces Neointimal Hyperplasia in Canine Model*. **Ann Vasc Surg.** (1997). 11: 74 – 79.
- Cho et al. *The Behavior of Vascular Smooth Muscle Cells and Platelets Onto Epigallocatechin Gallate-Releasing Poly(L-Lactide-Co-E-Caprolacton) As Stent-Coating Materials*. **Biomaterials.**(2008). 29: 884 – 893.
- Chopard et al. *A Lattice Boltzmann Simulation of Clotting in Stented Aneurysms and Comparison With Velocity or Shear Rate Reductions*. **Mathematics and Computers in Simulation.**(2006). 2: 108 – 112.
- Cross et al. *Neuroform Stent Deployment for Treatment of a Basilar Tip Aneurysm Via a Posterior Communicating Artery Route*. **Am J Neuro Radiol.**(2005). 26: 2578 – 2581.
- Crowell et al. *The Anterior Communicating Artery Has Significant Branches*. **Stroke.**(1977). 8: 272 – 273.
- Dempere et al. *CFD Analysis Incorporating the Influence of Wall Motion: Application to Intracranial Aneurysms*. **Lecture Notes in Comp Sci.** (2006). 438 – 445.
- Denton and Earthman. *Corrosion Evaluation of Wear Tested Nitinol Wire*. **Materials Science and Engineering.**(2005). 25: 276 – 281.
- Deplano et al. *Three Dimensional Numerical Simulations of Physiological Flows in a Stented Coronary Bifurcation*. **Med Biol Eng Comput.** (2004). 42: 650 – 659.
- Doerfler et al. *A Novel Flexible, Retrievable Endovascular Stent System for Small Vessel Anatomy: Preliminary In Vivo Data*. **Am J Neuro Radiol.**(2005). 26: 862 – 868.

- Ebrahimi et al. *Stent Conformity ion Curved Vascular Models with Simulated Aneurysm Neck Using Flat Panel CT: An In Vitro Study.* **Am J Neuroradiol.**(2007). 28: 823 – 829.
- Fan et al. *Numerical Simulation of Pulsatile Non-Newtonian Flow in the Carotid Artery Bifurcation.***Acta Mechanica Sinica.**(2009). 249 – 255.
- Feng et al.*The Application of Computer Simulation in the Genesis and Development of Intracranial Aneurysms.* **Technology and Health Care.**(2005). 13: 281 – 291.
- Ferguson. *Physical Factors in the Initiation, Growth, and Rupture of Human Intracranial Saccular Aneurysms.* **J Neurosurg.**(1972) 37: 666 – 677)
- Ferguson. *Turbulence in Human Intracranial Saccular Aneurysms.***J Neurosurg.**(1970) 33: 485 – 497.
- Fiorella et al.*In Stent Stenosis as a Delayed Complication of Neuroform Stent Supported Coil Embolization of an Incidental Carotid Terminus Aneurysm.* **Am J Neuroradiol.**(2004). 25: 1764 – 1767.
- Geremia et al. *Occlusion of Experimentally Created Fusiform Aneurysms with Porous Metallic Stents.***Am J Neuroradiol.**(2000). 21: 739 – 745.
- Giller et al. *Cerebral Arterial Diameters During Changes in Blood Pressure and Carbon Dioxide During Craniotomy.* **Neurosurgery.**(1993) 32: 737 – 742.
- Gonzalez et al. *Impact of Anatomic Features in the Endovascular Embolization of 181 Anterior Communicating Artery Aneurysms.* **Stroke.**(2008). 39: 2776 – 2782.
- Goodwin et al. *Covered Stent and Method of Covering a Stent.* **USPTO: 6 808 533.** (2004). 1 – 12.
- Goodwin et al. *Covered Stent and Method of Covering a Stent.* **USPTO: 7 354 449.** (2008). 1 – 12.
- Gorbet and Sefton.*Biomaterial Associated Thrombosis: Roles of Coagulation Factors, Complement, Platelets, and Leukocytes.***Biomaterials.**(2004). 25: 5681 – 5703.
- Groden et al.*Three Dimensional Pulsatile Flow Simulation Before and After Endovascular Coil Embolization of a Terminal Cerebral Aneurysm.* **J Cerebral Blood Flow and Metabolism.**(2001). 21: 1464 – 1471.
- Gunatillake et al. *Designing Biostable Polyurethane Elastomers for Biomedical Implants.***Aust. J Chem.** (2003). 56: 545 – 557.
- Gunatillake et al. *Poly(dimethylsiloxane)/Poly(hexamethylene oxide) Mixed Macrodiol Based Polyurethane Elastomers. I. Synthesis and Properties.* **J Appl Poly Sci.** (2000). 76: 2026 – 2040.
- Hahnel et al. *Small Vessel Stents for Intracranial Angioplasty: In Vitro Comparison of Different Stent Designs and Sizes by Using CT Angiography.* **Am J Neuroradiol.**(2003). 24: 1512 – 1516.
- Hashimoto et al. *Intracranial Aneurysms: Links Among Inflammation, Hemodynamics, and Vascular Remodeling.* **Neurol Res.** (2006). 28: 372 – 380.

- Higashida et al. *Initial Clinical Experience with a New Self Expanding Nitinol Stent for the Treatment of Intracranial Cerebral Aneurysms: The Cordis Enterprise Stent.* **Am J Neuroradiol.**(2005). 26: 1751 – 1756.
- Hines. *Micro-pleated Stent Assembly.***USPTO: 2006/0155367.** (2006). 1 – 23.
- Hirabayashi et al. *A Lattice Boltzmann Study of Blood Flow in Stented Aneurysm.* **Future Generation Computer Systems.** (2004). 20: 925 – 934.
- Hirabayashi et al. *Numerical Analysis of the Flow Pattern in Stented Aneurysms and Its Relation to Velocity Reduction and Stent Efficiency.***Math and Comp in Simul.** (2006). 72: 128 – 133.
- Hoffmann et al. *Determination of Instantaneous and Average Blood Flow Rates from Digital Angiograms of Vessel Phantoms Using Distance Density Curves.* **Invest Radiol.** (1991). 26: 207 – 212.
- Holloway and Christoforou. *Flexible Stent and Method of Making the Same.* **USPTO: 7 288 111.** (2007). 1 – 13.
- Hong et al. *Contact Between a Polymer and Whole Blood: Sequence of Events Leading to Thrombin Generation.* **J Lab Clin Med.** (2001). 138: 139 – 145.
- Hope et al. *Factors Influencing Successful Angiographic Occlusion of Aneurysms Treated by Coil Embolization.* **Am J Neuroradiol.**(1999). 20: 391 – 399.
- Hsu et al. *In Vitro Studies of the Neuroform Microstent Using Transparent Human Intracranial Arteries.* **Am J Neuroradiol.**(2006). 27: 1135 – 1139.
- Ionita et al. *The Asymmetric Vascular Stent: Efficacy in a Rabbit Aneurysm Model.* **Stroke.**(2009). 40: 959 – 965.
- Ionita et al. *Asymmetric Vascular Stent: Feasibility Study of a New Low Porosity Patch Containing Stent.* **Stroke.**(2008). 39: 2105 – 2113.
- Ionita et al. *Implementation of a High Sensitivity Micro Angiographic Fluoroscope for In-Vivo Endovascular Image Guided Interventions and Region of Interest Computed Tomography.* **Proc Soc Photo Opt Instrum Eng.** (2008).
- Islake et al. *Bare Stent-Graft Technique: A New Method of Endoluminal Vascular Reconstruction for the Treatment of Giant and Fusiform Aneurysms.* **Am J Neuroradiol.** (2002). 23: 1589 – 1595.
- Karmonik et al. *Comparison of Velocity Patterns in an ACoM Aneurysm Measured with 2D Phase Contrast MRI and Simulated with CFD.* **Technology and Health Care.**(2008). 16: 119 – 128.
- Khaled et al. *The Role of Porous Media in Modeling Flow and Heat Transfer in Biological Tissues.* **Int J Heat Mass Transfer.**(2003). 46: 4989 – 5003.
- Khanafer et al. *Modeling Pulsatile Flow in Aortic Aneurysms: Effect of Non-Newtonian Properties of Blood.* **Biorheology.**(2006). 43: 661 – 679.

- Kim et al. *Biostability and Biocompatibility of a Surface Grafted Phospholipid Monolayer on a Solid Substrate*. **Biomaterials**.(2004). 25: 33 – 41.
- Kim et al. *Evaluation of Effect of Partial Asymmetrical Stent Coverage*. **Medical Imaging**.(2007).
- Kontos et al. *Validity of Cerebral Arterial Blood Flow Calculations from Velocity Measurements*.**Stroke**.(1989). 20: 1 – 3.
- Krapf et al. *Complete Asymptomatic Thrombosis and Resorption of a Congenital Giant Intracranial Aneurysm*. **J Neurosurg**.(2002). 97: 184 – 189.
- Kroon et al. *Modeling of Saccular Aneurysm Growth in a Human Middle Cerebral Artery*.**J Biomech Eng**. (2008). 130.
- Lee et al. *Thrombus Organization and Healing in the Swine Experimental Aneurysm Model Part I. A Histological And Molecular Analysis*. **J Neurosurg**.(2007). 107: 94 – 108.
- Les et al. *Quantification of Hemodynamics in Abdominal Aortic Aneurysms During Rest and Exercise Using Magnetic Resonance Imaging and Computational Fluid Dynamics*. **Annals Biomed Eng**. (2010). 38: 1288 – 1313.
- Lewis et al. *Analysis of a Phosphorylcholine Based Polymer Coating on a Coronary Stent Pre and Post Implantation*. **Biomaterials**.(2002). 23: 1697 – 1706.
- Lewis. *Materials, Fluid Dynamics, and Solid Mechanics Aspects of Coronary Artery Stents: A State of the Art Review*. **J Biomed Mater Res**. (2008). 86B: 569 – 590.
- Li et al. *A New Covered Stent Designed for Intracranial Vasculature. Application in the Management of Pseudoaneurysms of the Cranial Internal Carotid Artery*. **Am J Neuroradiol**. (2007). 28: 1579 – 1585.
- Li et al. *A Structural Multi-Mechanism Damage Model for Cerebral Arterial Tissue*.**J Biomech Eng**.(2009). 131.
- Lubicz et al. *Endovascular Treatment of Intracranial Aneurysms with a Branch Arising from the Sac*.**Am J Neuroradiol**.(2006). 27: 142 – 147.
- Ma et al. *Three Dimensional Geometrical Characterization of Cerebral Aneurysms*. **Annals Biomed Eng**. (2004). 32: 264 – 273.
- Ma et al. *Nonlinear Anisotropic Stress Analysis of Anatomically Realistic Cerebral Aneurysms*.**J Biomech Eng**. (2007). 129: 88 – 96.
- Malek et al. *Hemodynamic Shear Stress and Its Role in Atherosclerosis*.**JAMA**.(1992). 282: 2035 – 2042.
- Mani et al. *Coronary Stents: A Materials Perspective*. **Biomaterials**.(2007). 28: 1689 – 1710.
- Martin et al. *Polydimethylsiloxane/Polyether-Mixed Macrodiol-Based Polyurethane Elastomers: Biostability*. **Biomaterials**.(2000). 21: 1021 – 1029.
- Masuo et al. *Study of the Patency of Small Arterial Branches After Stent Placement with an Experimental in Vivo Model*. **Am J Neuroradiol**. (2002). 23: 706 – 710.

- McClung et al. *Adsorption of Plasminogen From Human Plasma to Lysine-Containing Surfaces*. **J Biomed Mater Res.** (2000). 49: 409 – 414.
- Moore and Berry. *Fluid and Solid Mechanical Implications of Vascular Stenting*. **Annals Biomed Eng.** (2002). 30: 498 – 508.
- Narayanaswamy et al. *Animal Models for Atherosclerosis, Restenosis, and Endovascular Graft Research*. **JVIR.**(2000). 11: 5 – 17.
- Nicholson et al. *Case Report: Treatment of a Carotid Artery Pseudoaneurysm with a Polyester Covered Nitinol Stent*. **Clin Radiol.** (1995). 50: 872 – 873.
- O'Brien et al. *Passivation of Nitinol Wire for Vascular Implants – A Demonstration of the Benefits*. **Biomaterials.**(2002). 23: 1739 – 1748.
- Ogunrinade et al. *Effect of Fluid Shear Stress on the Permeability of the Arterial Endothelium*. **Annals Biomed Eng.** (2002). 30: 430 – 446.
- Ohta et al. *Poly-vinyl Alcohol Hydrogel Vascular Models for In Vitro Aneurysm Simulations: The Key to Low Friction Surfaces*. **Tech and Health Care.**(2004). 12: 225 – 233.
- Origitano. *Current Options in Clipping Versus Coiling of Intracranial Aneurysms: to Clip, to Coil, to Wait and Watch*. **Neurosurg Clin N Am.** (2008). 19: 469 – 476.
- Oshima et al. *Finite Element Simulation of Blood Flow in the Cerebral Artery*. **Comput.Methods Appl. Mech Eng.** (2001). 191: 661 – 671.
- Pai et al. *Microsurgical Anatomy of the Anterior Cerebral Artery – Anterior Communicating Artery Complex: An Indian Study*. **Neurology Asia.**(2005). 10: 21 – 28.
- Phatouros et al. *Endovascular Stenting for Carotid Artery Stenosis: Preliminary Experience Using the Shape Memory Alloy Recoverable Technology Stent*. **Am J Neuroradiol.**(2000). 21: 732 – 738.
- Plant et al. *Behavior of Human Endothelial Cells on Surface Modified NiTi Alloy*. **Biomaterials.**(2005). 26: 5359 – 5367.
- Pumar et al. *Preliminary Experience with Leo Self Expanding Stent for the Treatment of Intracranial Aneurysms*. **Am J Neuroradiol.**(2005). 26: 2573 – 2577.
- Punshon et al. *Interactions Between Endothelial Cells and a Poly(Carbonate-silsesquioxane-bridge-urea) Urethane*. **Biomaterials.**(2005). 26: 6271 – 6279.
- Radaelli et al. *Reproducibility of Haemodynamical Simulations in a Subject Specific Stented Aneurysm Model – A Report on the Virtual Intracranial Stenting Challenge 2007*. **J Biomech.**(2008). 41: 2069 – 2081.
- Radeleff et al. *Comparison of a Microporous Thermoplastic Polyurethane-Covered Stent with a Self Expanding Bare Nitinol Stent in a Porcine Iliac Artery Model*. **J Vasc Interv Radiol.** (2009). 20: 927 – 935.

- Ratner .*The Catastrophe Revisited: Blood Compatibility in the 21st Century*. **Biomaterials**.(2007). 28: 5144 – 5147.
- Rau et al. *Hemodynamic Effect of Unequal Anterior Cerebral Artery Flow Rates on the Anterior Communicating Artery Bifurcation: A Computational Fluid dynamics Study*. **Modeling and Sim in Eng**. (2008).
- Raymond et al. *Interventional Neuroradiology: The Role of Experimental Models in Scientific Progress*.**Am J Neuroradiol**.(2007). 28: 401 – 405.
- Redekop et al. *Treatment of Traumatic Aneurysms and Arteriovenous Fistulas of the Skull Base by Using Endovascular Stents*.**J Neurosurg** (2001). 95: 412 – 419.
- Resnick et al. *Fluid Shear Stress and the Vascular Endothelium: For Better and For Worse*. **Progress in Biophysics and Molec Bio**.(2003). 81: 177 – 199.
- Robertson and Ritchie. *In Vitro Fatigue Crack Growth and Fracture Toughness Behavior of Thin Walled Superelastic Nitinol Tube for Endovascular Stents: A Basis for Defining the Effect of Crack-Like Defects*.**Biomaterials**.(2007). 28: 700 – 709.
- Rolland et al. *Compliance Matching Stent Placement in the Carotid Artery of the Swine Promotes Optimal Blood Flow and Attenuates Restenosis*.**Eur J Vasc Endovas Surg**. (2004). 28: 431 – 438.
- Rudin et al. *Stent Vascular Intervention Device and Method*.**USPTO: 2003/0109917**. (2003) 1 – 8.
- Rudin.*Stent Vascular Intervention Device and Methods for Treating Aneurysms*.**USPTO: 2007/0021816**. (2007). 1 – 29.
- Saatci et al. *Treatment of Internal Carotid Artery Aneurysms with a Covered Stent: Experience in 24 Patients with Mid-Term Follow-up Results*. **Am J Neuroradiol**. (2004). 25: 1742 – 1749.
- Scheel et al. *Color Duplex Measurement of Cerebral Blood Flow Volume in Healthy Adults*.**Stroke**. (2000). 31: 147 - 150.
- Schmidt et al. *A Comparison of the Mechanical Performance Characteristics of Seven Drug Eluting Stent Systems*.**Catheterization and Cardiovascular Interventions**.(2009). 73: 350 – 360.
- Sforza et al. *Hemodynamics of Cerebral Aneurysms*.**Ann Rev Fluid Mech**. (2009). 41: 91 – 107.
- Shabalovskaya et al.*The Influence of Surface Oxides on the Distribution and Release of Nickel from Nitinol Wires*. **Biomaterials**.(2009). 30: 468 – 477.
- Shaik et al. *Numerical Simulations of Pulsatile non-Newtonian Flow in an End to Side Anastomosis Model*. **Sim Model Practice and Theory**.(2008). 16: 1123 – 1135.
- Shen et al. *Effects of Stent Design Parameters on Radial Force of Stent*. **ICBBE**.(2008)
- Shih.*The Cytotoxicity of Corrosion Products of Nitinol Stent Wire on Cultured Smooth Muscle Cells*. **J Biomed Mat Res**. (2000). 52: 395 – 403.

- Shojima et al. *Magnitude and Role of Wall Shear Stress on Cerebral Aneurysm: Computational Fluid Dynamic Study of 20 Middle Cerebral Artery Aneurysms*. **Stroke**.(2004). 35: 2500 – 2505.
- Simmons et al. *Biostability and Biological Performance of a PDMS-Based Polyurethane for Controlled Drug Release*. **Biomaterials**.(2008). 29: 2987 – 2995.
- Simmons et al. *Long Term in Vivo Stability of Poly(dimethylsiloxane)/poly(hexamethylene oxide) Mixed Macrodiol-Based Polyurethane Elastomers*. **Biomaterials**.(2004). 25: 487 - 4900.
- Singer et al. *Covered Stent Placement for Neurovascular Disease*. **Am J Neuroradiol**.(1997). 18: 507 – 509.
- Solem. *Covered Stent and Method of Making It*. **USPTO: 6 395 212**. (2002). 1 – 8.
- Spelle et al. *Saccular Intracranial Aneurysms: Endovascular Treatment – Devices, Techniques and Strategies, Management of Complications, Results*. **Neuroim Clin NA**. (2006). 16: 413 – 451.
- Starly et al. *Three Dimensional Reconstruction for Medical CAD Modeling*. **CAD Applications**.(2005). 2: 431 – 436.
- Stárosvetsky and Gotman. *Corrosion Behavior of Titanium Nitride Coated Ni-Ti Shape Memory Surgical Alloy*. **Biomaterials**.(2001). 22: 1853 – 1859.
- Steinman. *Image Based Computational Fluid Dynamics Modeling in Realistic Arterial Geometries*. **Annals Biomed Eng**. (2002). 30: 483 – 497.
- Tan et al. *Analysis of Flow Patterns in a Patient Specific Thoracic Aortic Aneurysm Model*. **Computers and Structure**.(2009). 87: 680 – 690.
- Tanaka et al. *Conformity of Carotid Stents with Vascular Anatomy: Evaluation in Carotid Models*. **Am J Neuroradiol**.(2004). 25: 604 – 607.
- Taylor et al. *Finite Element Modeling of Blood Flow in Arteries*. **Comput. Methods Appl. Mech. Eng**. (1998). 158: 155 – 196.
- Tepe et al. *Reduced Thrombogenicity of Nitinol Stents – In Vitro Evaluation of Different Surface Modifications and Coatings*. **Biomaterials**.(2006). 27: 643 – 650.
- Thierry et al. *Nitinol Versus Stainless Steel Stents: Acute Thrombogenicity Study in an Ex Vivo Porcine Model*. **Biomaterials**.(2002). 23: 2997 - 3005.
- Trager et al. *Correlation Between Angiographic and Particle Image Velocimetry Quantifications of Flow Diverters in an In Vitro Model of Elastase Induced Rabbit Aneurysms*. **J Biomech Eng**. (2009). 131.
- Tsutsumi et al. *Endovascular Treatment of Tiny Ruptured Anterior Communicating Artery Aneurysms*. **Neuroradiology**.(2008). 50: 509 – 515.
- Ujiiie et al. *Hemodynamic Study of the Anterior Communicating Artery*. **Stroke**.(1996). 27: 2086 – 2094.

- Valencia et al. *A Mechanical Study of Patient Specific Cerebral Aneurysm Models: The Correlations Between Stress and Displacement with Geometric Indices*. **Mechanics Research Communications**.(2009). 36: 642 – 651.
- Valencia et al. *Blood Flow Dynamics in Saccular Aneurysm Models of the Basilar Artery*. **J Biomech Eng**. (2006). 128: 516 – 526.
- Venkatraman et al. *Biodegradable Stents with Elastic Memory*. **Biomaterials**.(2007). 27: 1573 – 1578.
- Vidovic et al. *Carotid Artery Intima Thickness and Flow Velocity after Discontinuation of Hormone Replacement Therapy in Post menopausal Women: Followup Study*. **Clinical Sciences**. (2001). 42: 54 – 57.
- Vitek et al. *Carotid Artery Stenting: Technical Considerations*. **Am J Neuroradiol**. (2000). 21: 1736 – 1743.
- Wada et al. *Carotid Rupture During Stent Assisted Aneurysm Treatment*. **Am J Neuroradiol**.(2004). 25: 827 – 829.
- Wakhloo et al. *Self Expanding Nitinol Stents in Canine Vertebral Arteries: Hemodynamics and Tissue Response*. **Am J Neuroradiol**.(1995). 16: 1043 – 1051.
- Wanke et al. *Endovascular Treatment of Unruptured Intracranial Aneurysms*. **Am J Neuroradiol**.(2002). 23: 756 – 761.
- Wanke et al. *Stents for Intracranial Wide Necked Aneurysms: More than Mechanical Protection*. **Neuroradiology**.(2008). 50: 991 – 998.
- Wanke et al. *Treatment of Wide Necked Intracranial Aneurysm with a Self Expanding Stent System: Initial Clinical Experience*. **Am J Neuroradiol**(2003). 24: 1192 – 1199.
- Weatherford et al. *Healing Characteristics of Intraarterial Stent Grafts in an Injured Artery Model*. **Annals Vas Surg**. (1997). 11: 54 – 61.
- Weir et al. *The Aspect Ratio of Ruptured and Unruptured Aneurysms*. **J Neurosurg**.(2003). 99: 447 – 451.
- Wever et al. *Cytotoxic, Allergic, and Genotoxic Activity of a Nickel Titanium Alloy*. **Biomaterials**.(1997). 18: 1115 – 1120.
- Wheatley et al. *Heart Valve Prosthesis*. **USPTO: 6 171 335**. (2001). 1 – 13.
- Wiebers et al. *Unruptured Intracranial Aneurysms: Natural History, Clinical Outcome, and Risks of Surgical and Endovascular Treatment*. **Lancet**.(2003). 362: 103 – 110.
- Wiebers et al. *Unruptured Intracranial Aneurysms: Natural History and Clinical Management. Update on the International Study of Unruptured Intracranial Aneurysms*. **Neuroimaging Clin NA**. (2006). 16: 383 – 390.
- Williams. *On the Mechanisms of Biocompatibility*. **Biomaterials**.(2008). 29: 2941 – 2953.
- Yazdani et al. *Development of an In Vitro System to Assess Stent Induced Smooth Muscle Cell Proliferation: A Feasibility Study*. **J Vasc Interv Radiol**.(2009). 20: 101 – 106.

Ye et al. *Covalent Surface Modification of a Titanium Alloy with a Phosphorylcholine Containing Copolymer for Reduced Thrombogenicity in Cardiovascular Devices.* **J Biomed Mat Res.** (2008). 91A: 18 – 28.

Zeng and Kallmes. *Sensitivity of CFD Based Hemodynamic Results in Rabbit Aneurysm Models to Idealizations in Surrounding Vasculature.* **J Biomech Eng.** (2010)

Zhuo et al. *Procoagulant Stimulus Processing by the Intrinsic Pathway of Blood Plasma Coagulation.* **Biomaterials.**(2005). 26: 2965 – 2973.

Websites

Massachusetts General Hospital. *Diagnostic Procedures.*

<http://www.mgh-interventional-neurorad.org/rabinov2/DiagnosticImaging2/perfusionMRIandMRA/MRA1.jpg>. Accessed November 2009

APPENDIX A: SUPPLEMENTAL FIGURES AND TABLES FROM PIV

CHAPTER 3.3.1

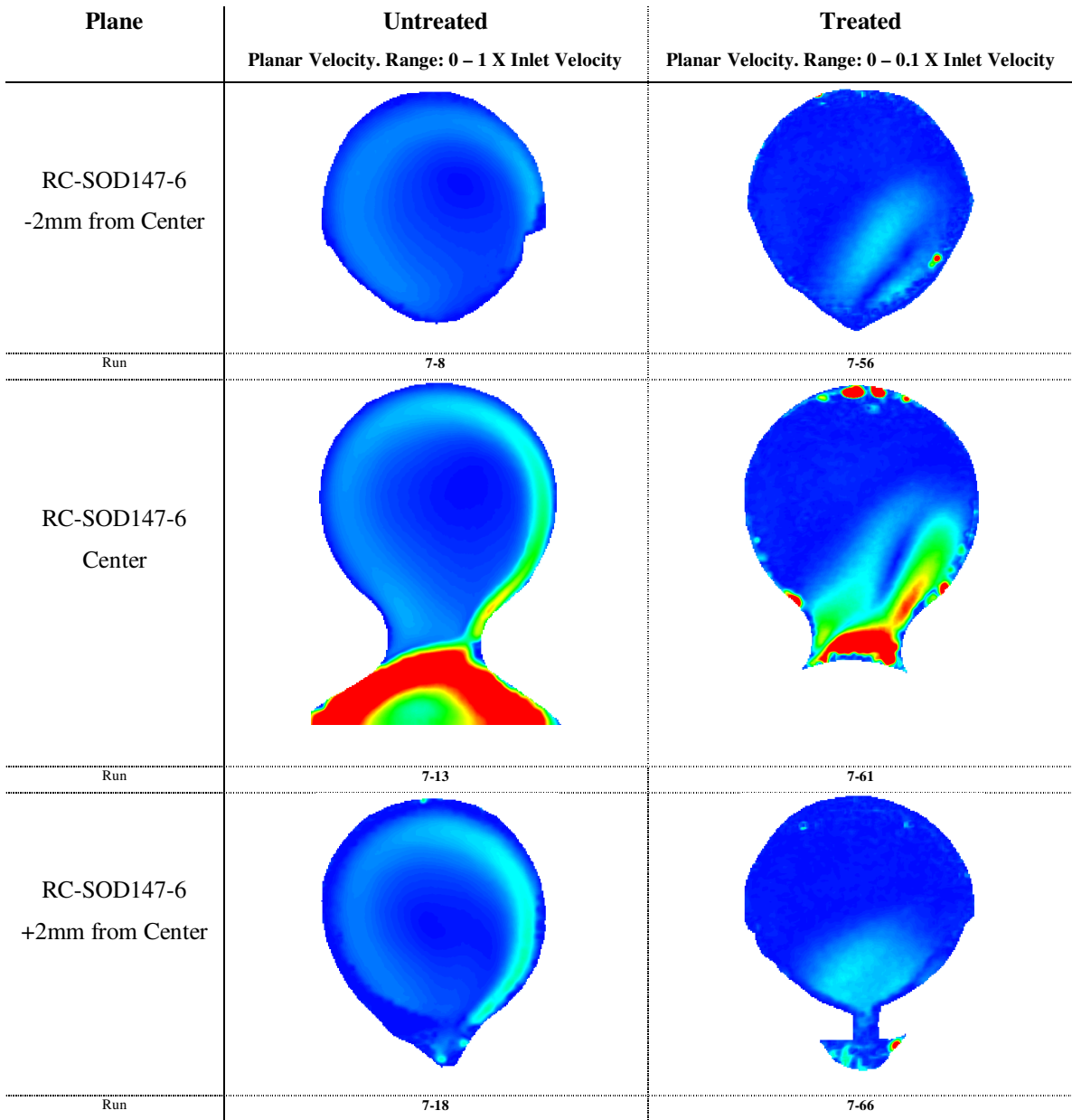


Figure A-1. The planar velocity contours are shown at the center plane and planes 2mm on either side. The color contours for the treated aneurysms ranged from 0 m/s to 1/10th of the inlet velocity to better visualize the structure of the jet entering the aneurysm.

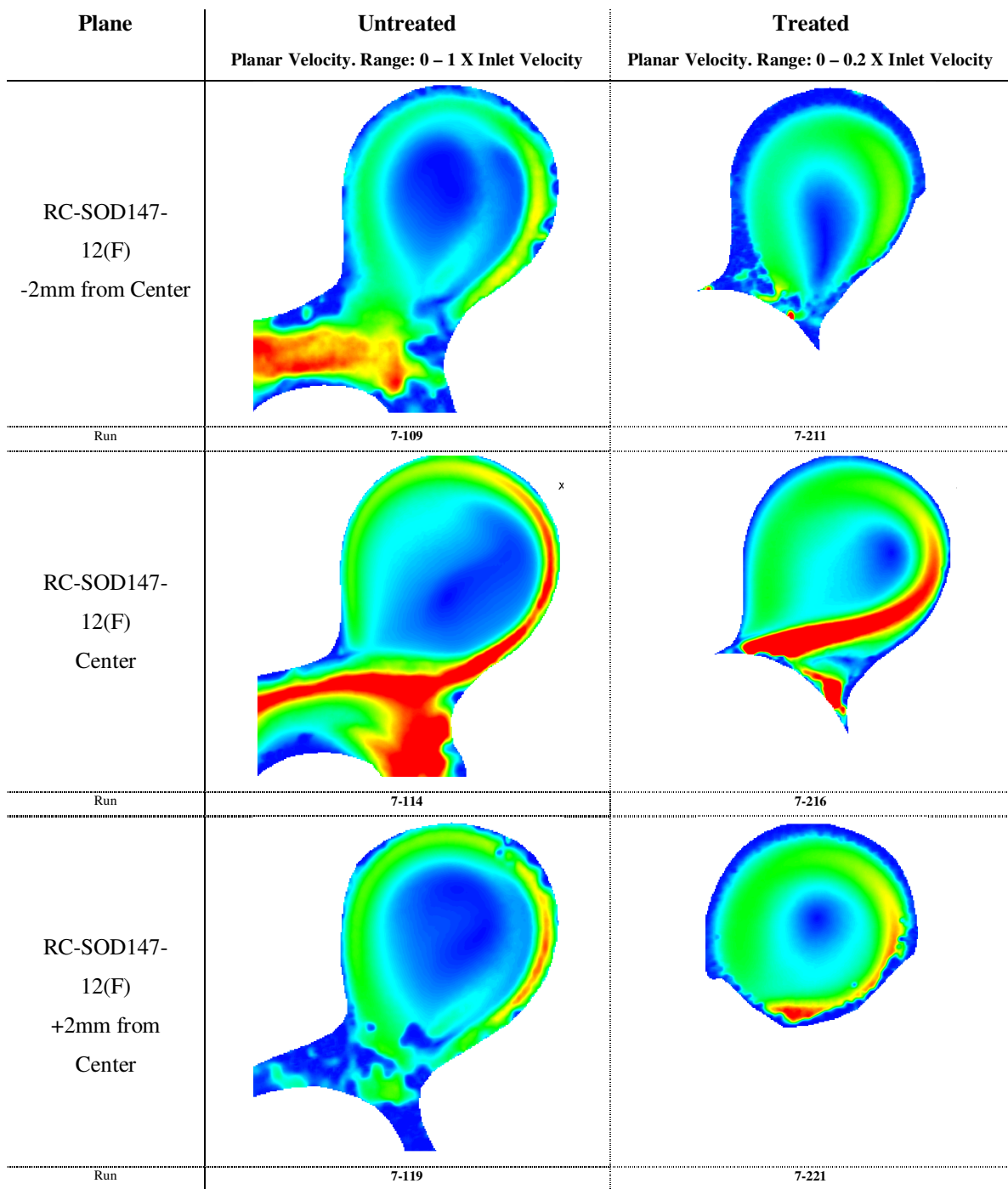


Figure A-2. The planar velocity contours are shown at the center plane and planes 2mm on either side. The color contours for the treated aneurysms ranged from 0 m/s to $2/10^{\text{th}}$ of the inlet velocity to better visualize the structure of the jet entering the aneurysm.

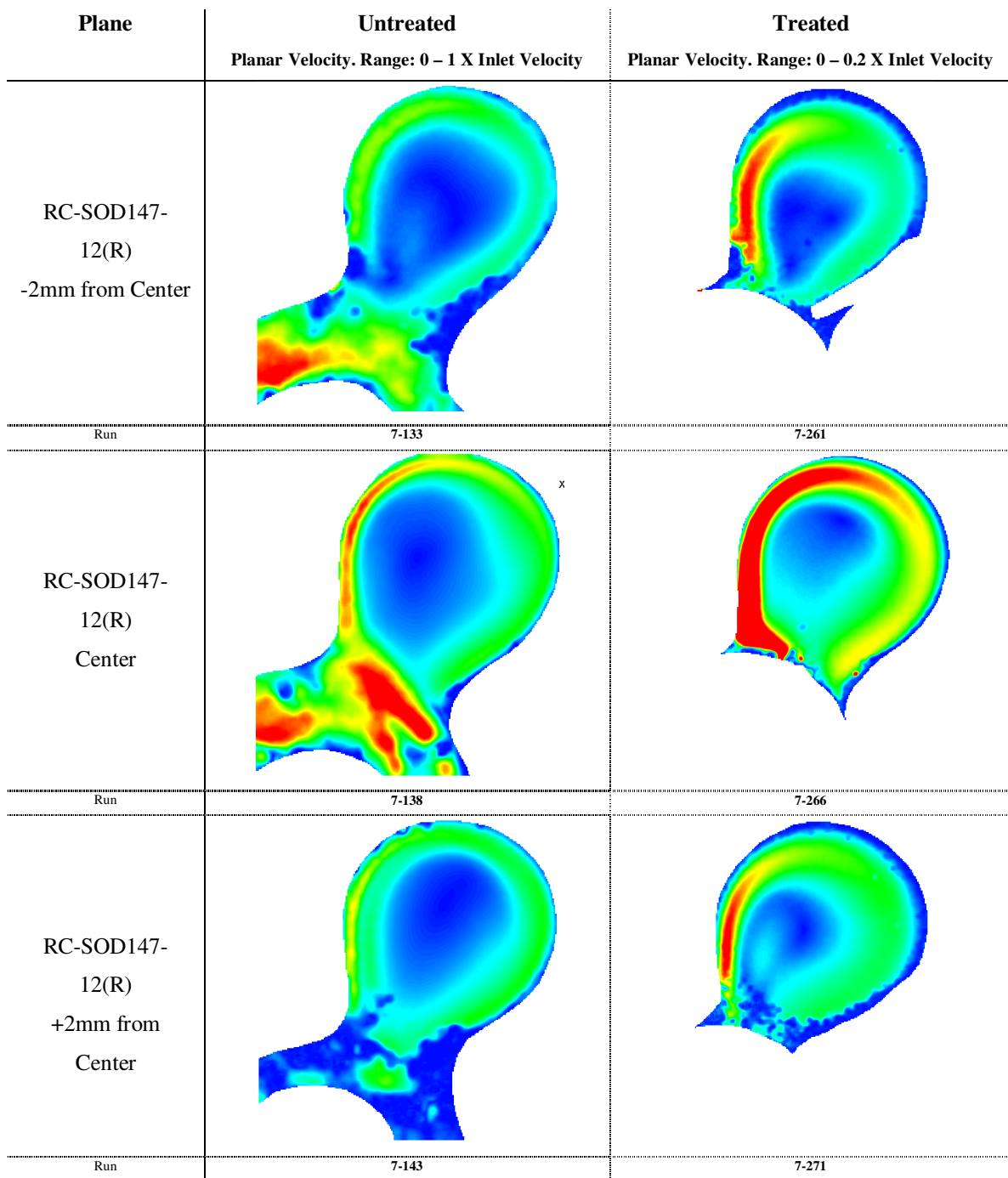


Figure A-3. The planar velocity contours are shown at the center plane and planes 2mm on either side. The color contours for the treated aneurysms ranged from 0 m/s to $2/10^{\text{th}}$ of the inlet velocity to better visualize the structure of the jet entering the aneurysm.

CHAPTER 3.3.2

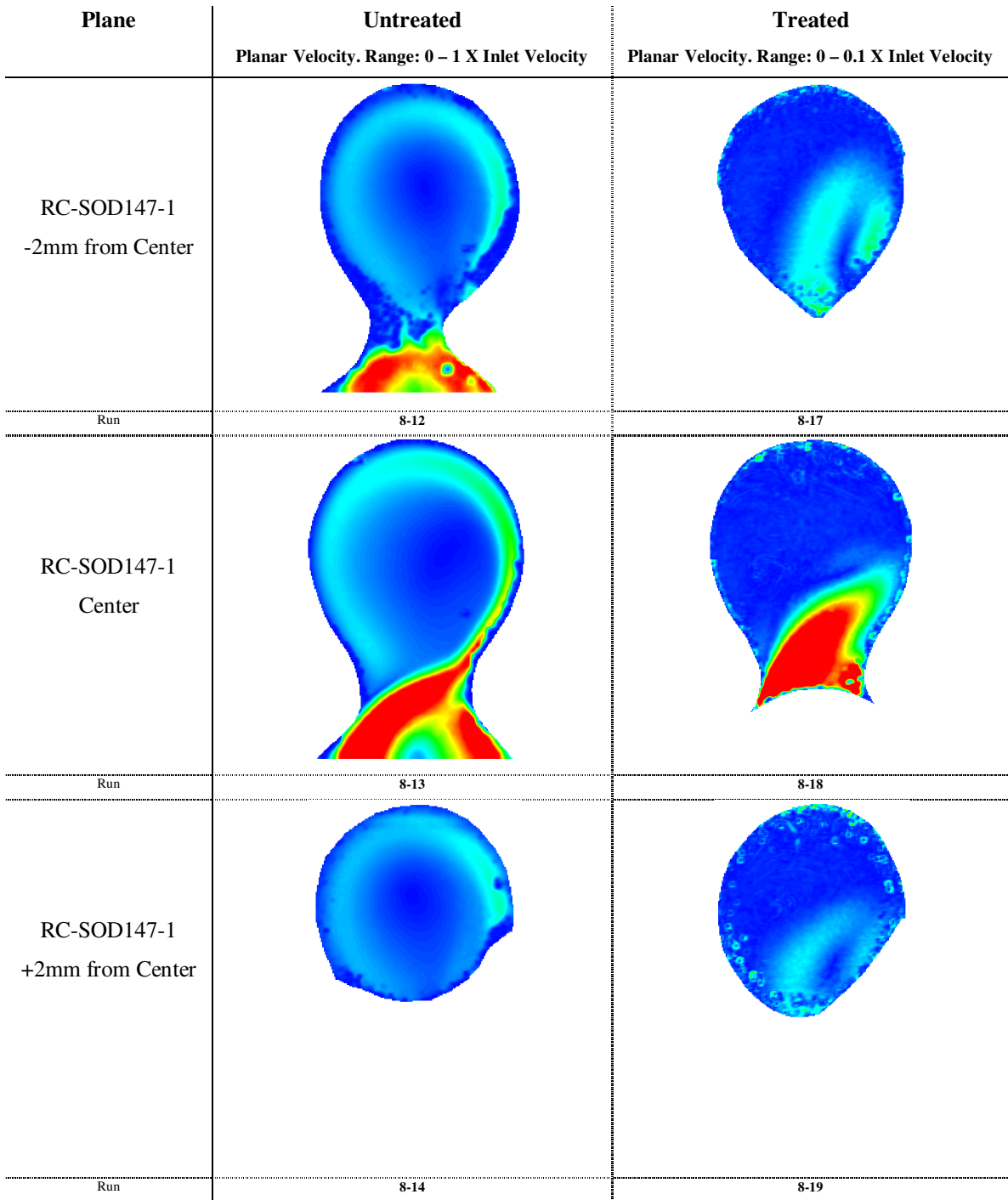


Figure A-4. The planar velocity contours are shown at the center plane and planes 2mm on either side. The color contours for the treated aneurysms ranged from 0 m/s to 1/10th of the inlet velocity to better visualize the structure of the jet entering the aneurysm.

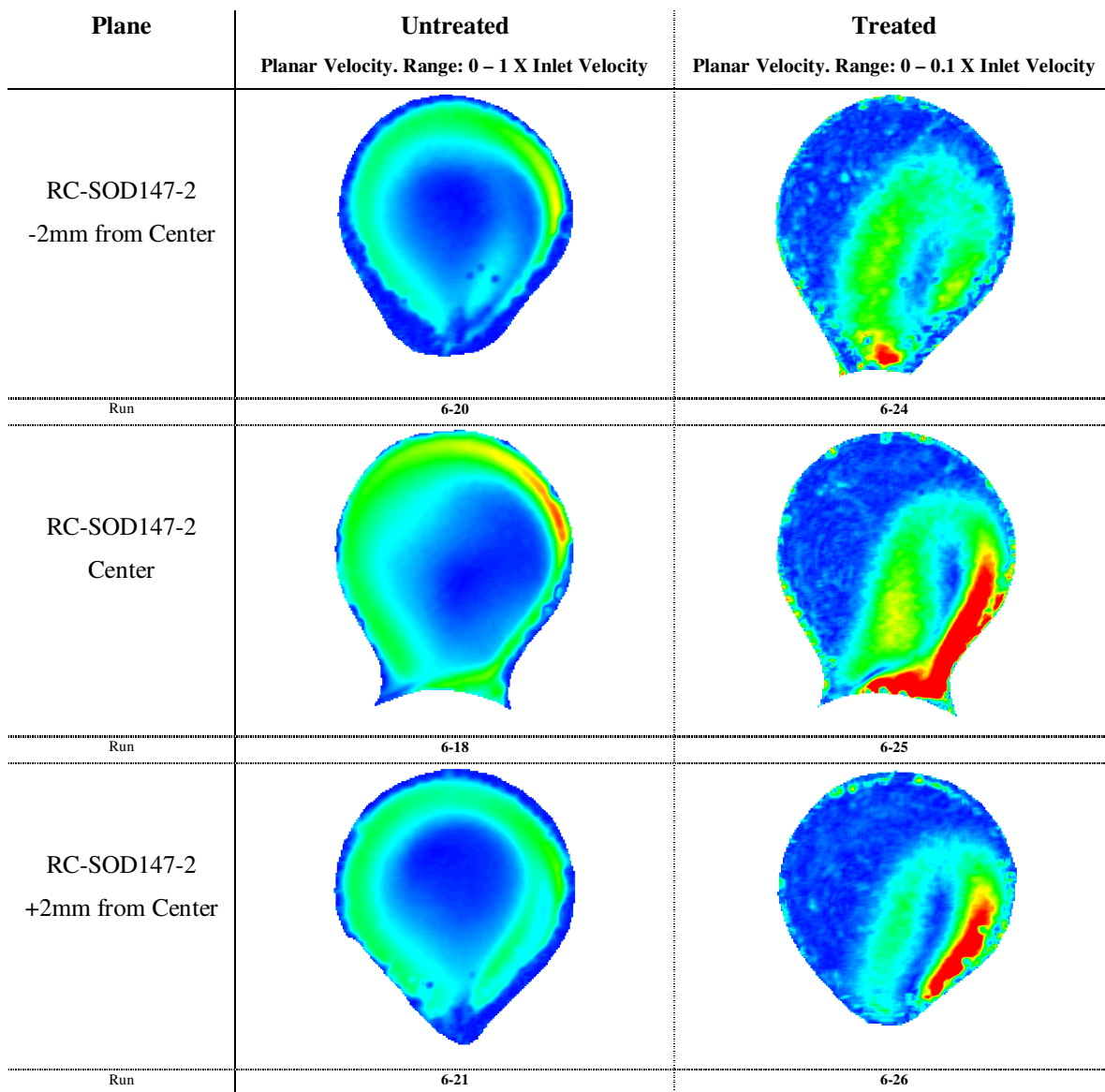


Figure A-5. The planar velocity contours are shown at the center plane and planes 2mm on either side. The color contours for the treated aneurysms ranged from 0 m/s to 1/10th of the inlet velocity to better visualize the structure of the jet entering the aneurysm.

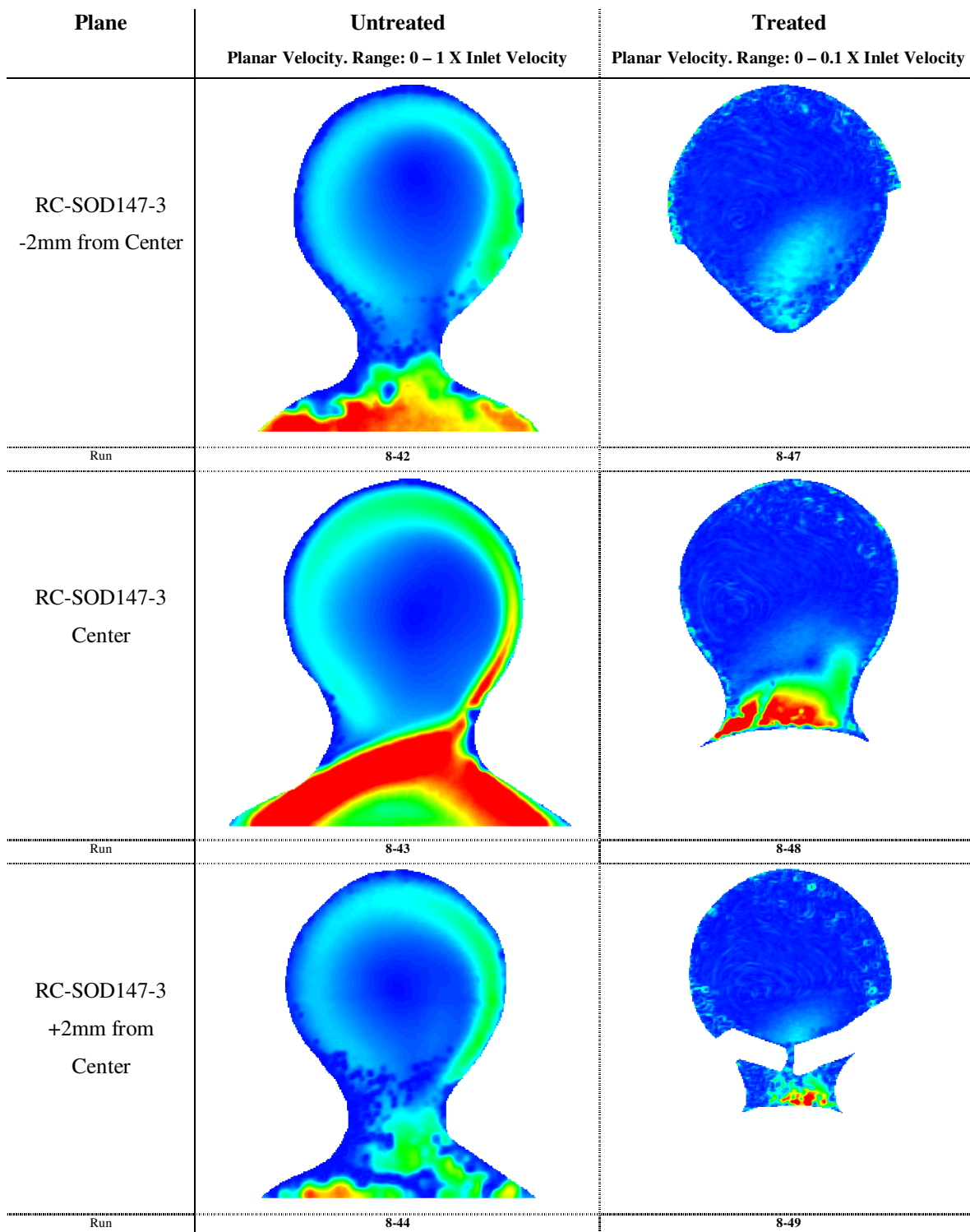


Figure A-6. The planar velocity contours are shown at the center plane and planes 2mm on either side. The color contours for the treated aneurysms ranged from 0 m/s to 1/10th of the inlet velocity to better visualize the structure of the jet entering the aneurysm.

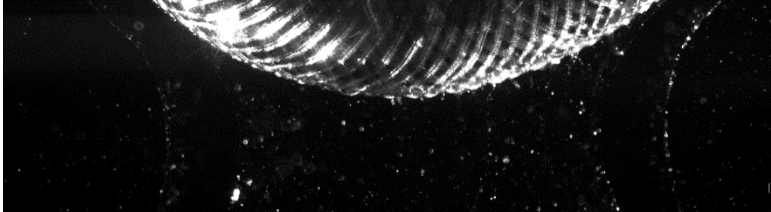
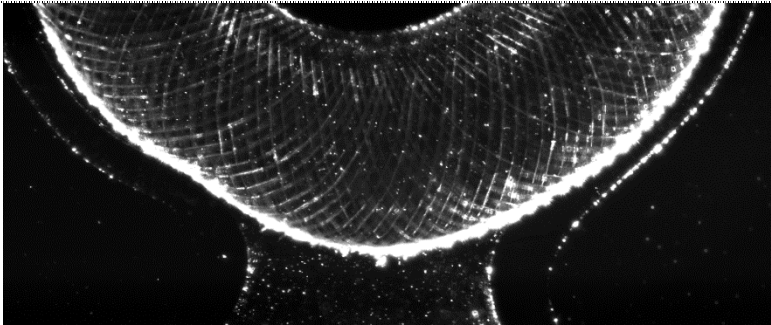
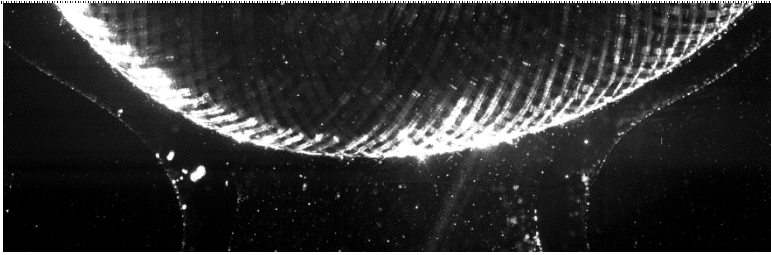
Flow Domain	Close-up View of PED
RC-SOD147-1	
RC-SOD147-2	
RC-SOD147-3	

Figure A-7. The shapes of the flow diverter inside various flow domains are shown.

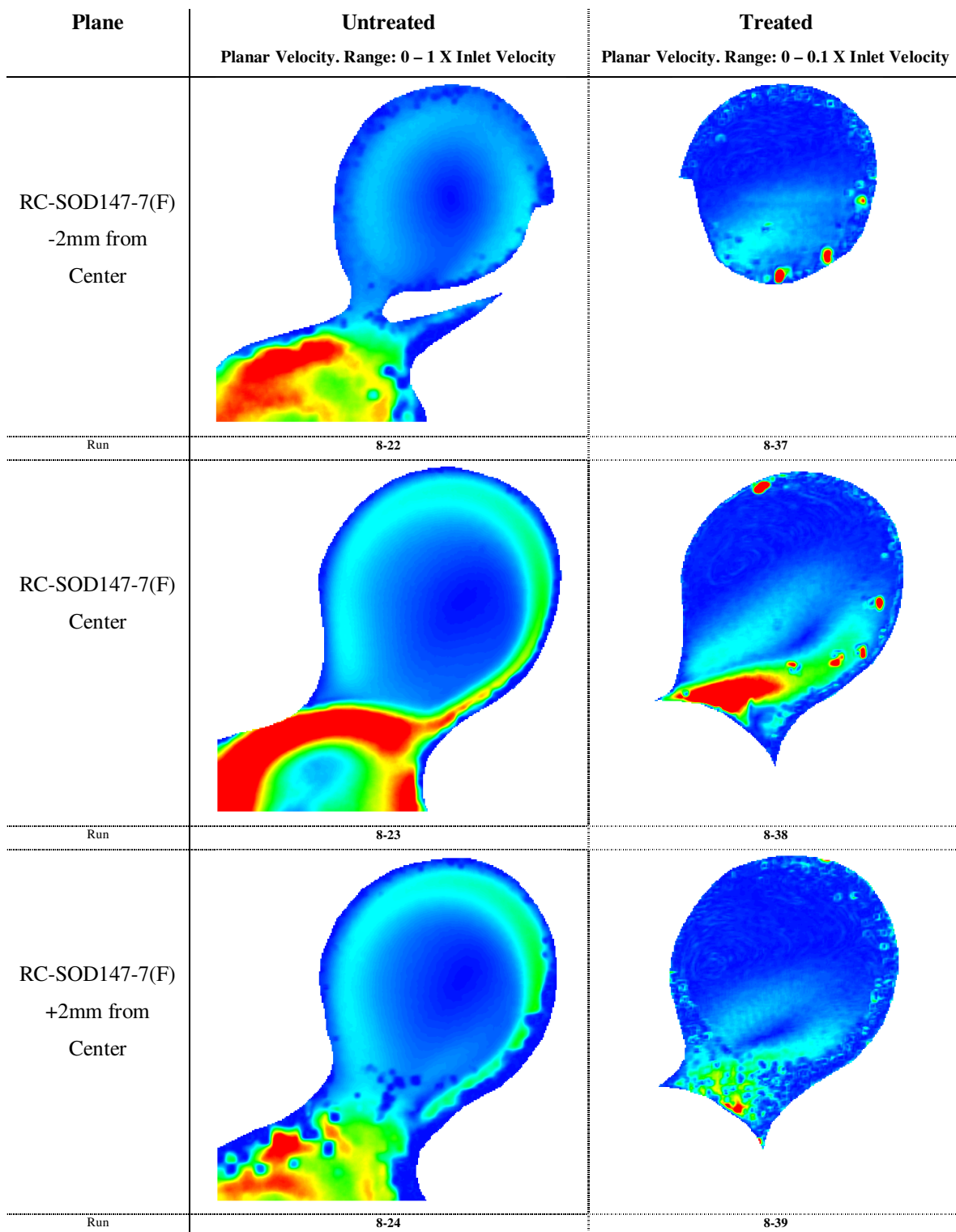


Figure A-8. The planar velocity contours are shown at the center plane and planes 2mm on either side. The color contours for the treated aneurysms ranged from 0 m/s to 1/10th of the inlet velocity to better visualize the structure of the jet entering the aneurysm.

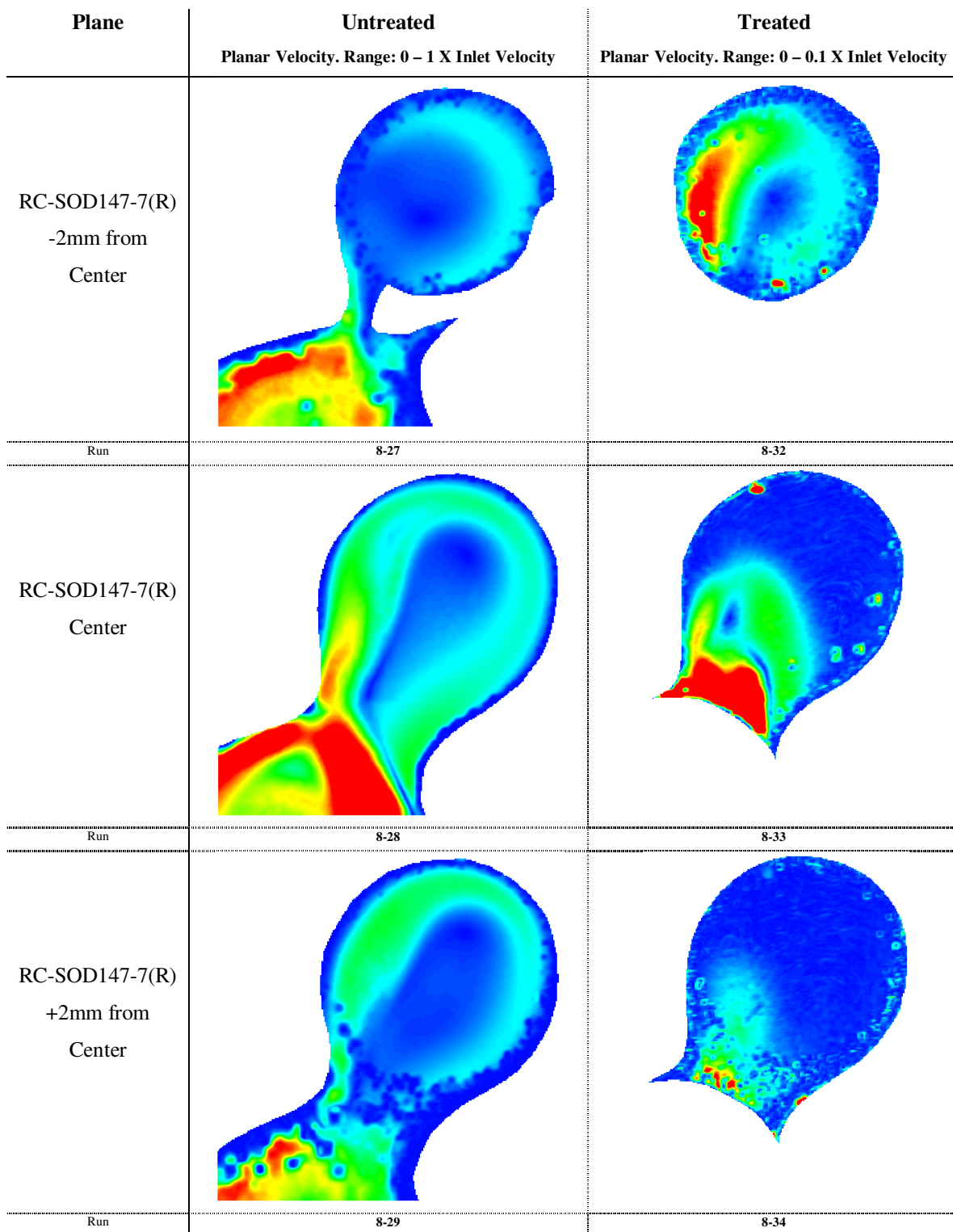


Figure A-9. The planar velocity contours are shown at the center plane and planes 2mm on either side. The color contours for the treated aneurysms ranged from 0 m/s to 1/10th of the inlet velocity to better visualize the structure of the jet entering the aneurysm.

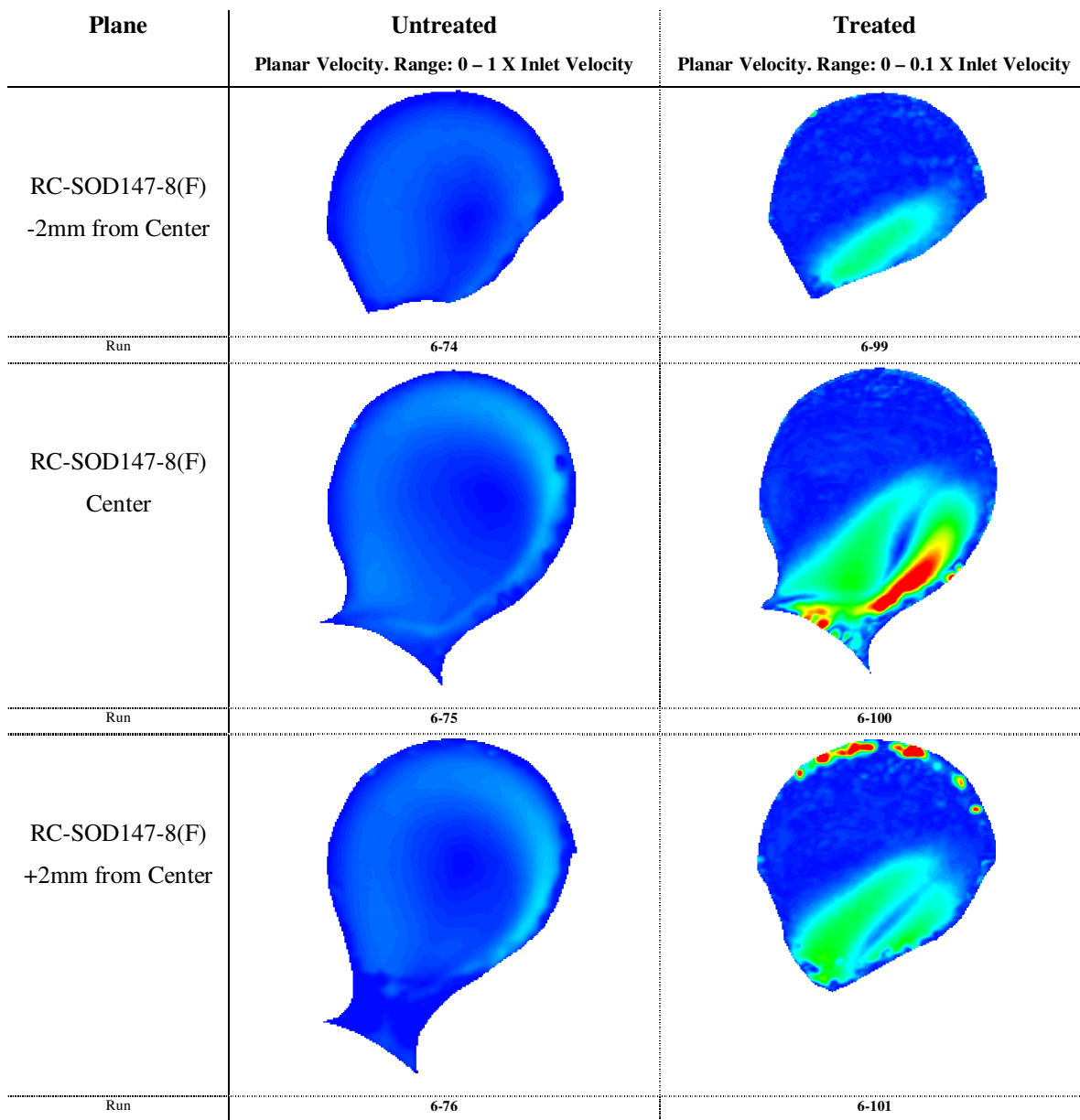


Figure A-10. The planar velocity contours are shown at the center plane and planes 2mm on either side. The color contours for the treated aneurysms ranged from 0 m/s to 1/10th of the inlet velocity to better visualize the structure of the jet entering the aneurysm.

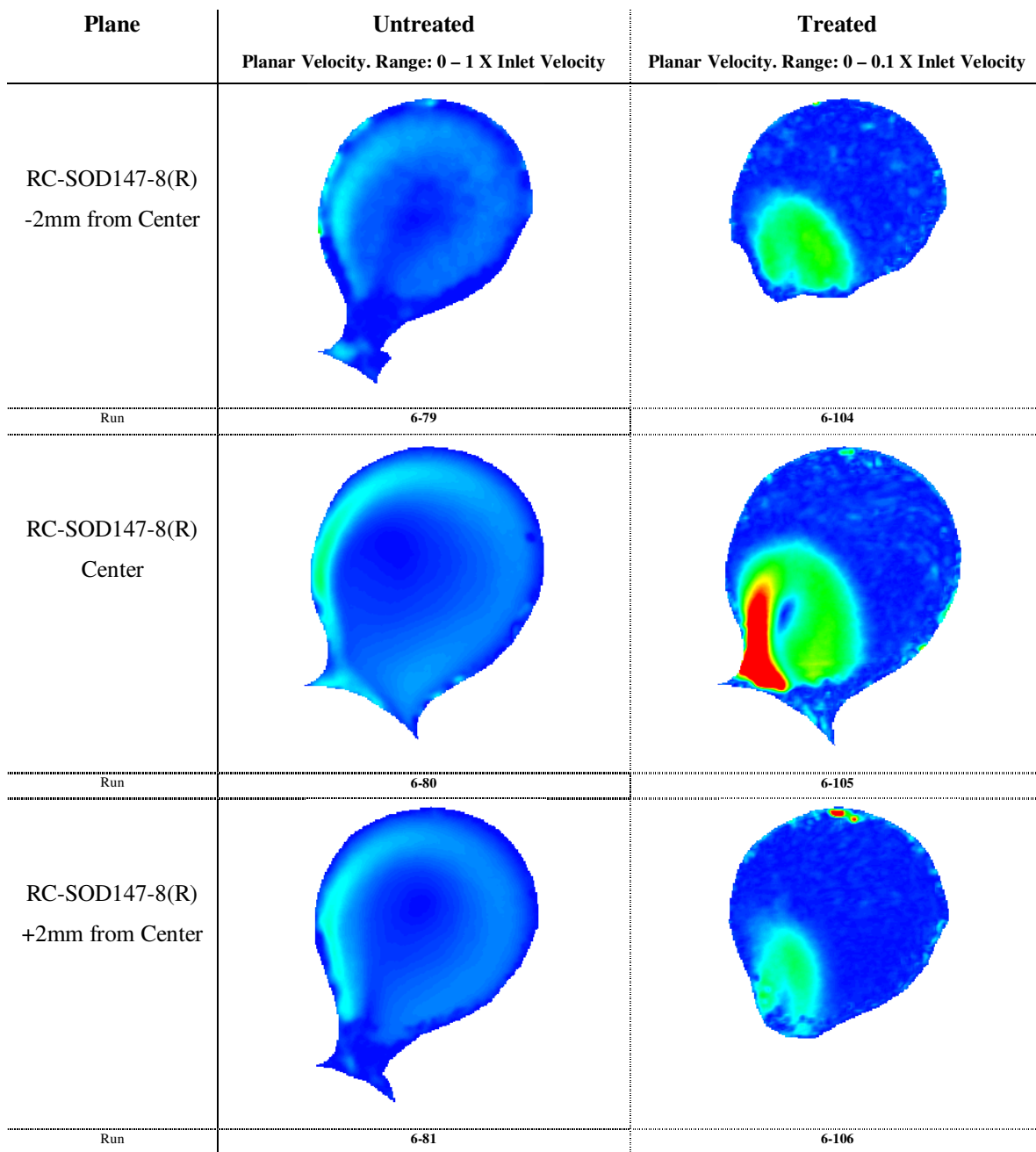


Figure A-11. The planar velocity contours are shown at the center plane and planes 2mm on either side. The color contours for the treated aneurysms ranged from 0 m/s to 1/10th of the inlet velocity to better visualize the structure of the jet entering the aneurysm.

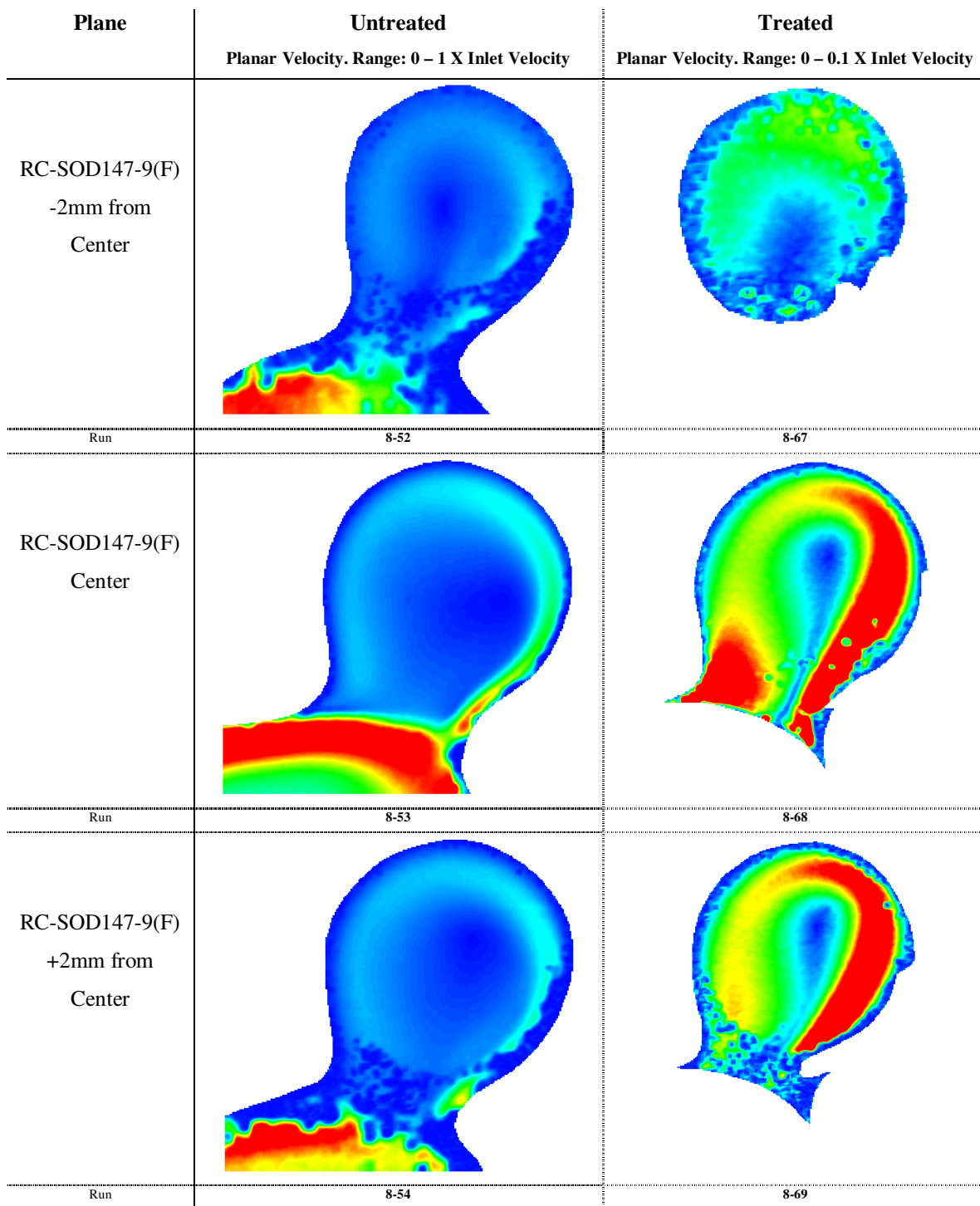


Figure A-12. The planar velocity contours are shown at the center plane and planes 2mm on either side. The color contours for the treated aneurysms ranged from 0 m/s to 1/10th of the inlet velocity to better visualize the structure of the jet entering the aneurysm.

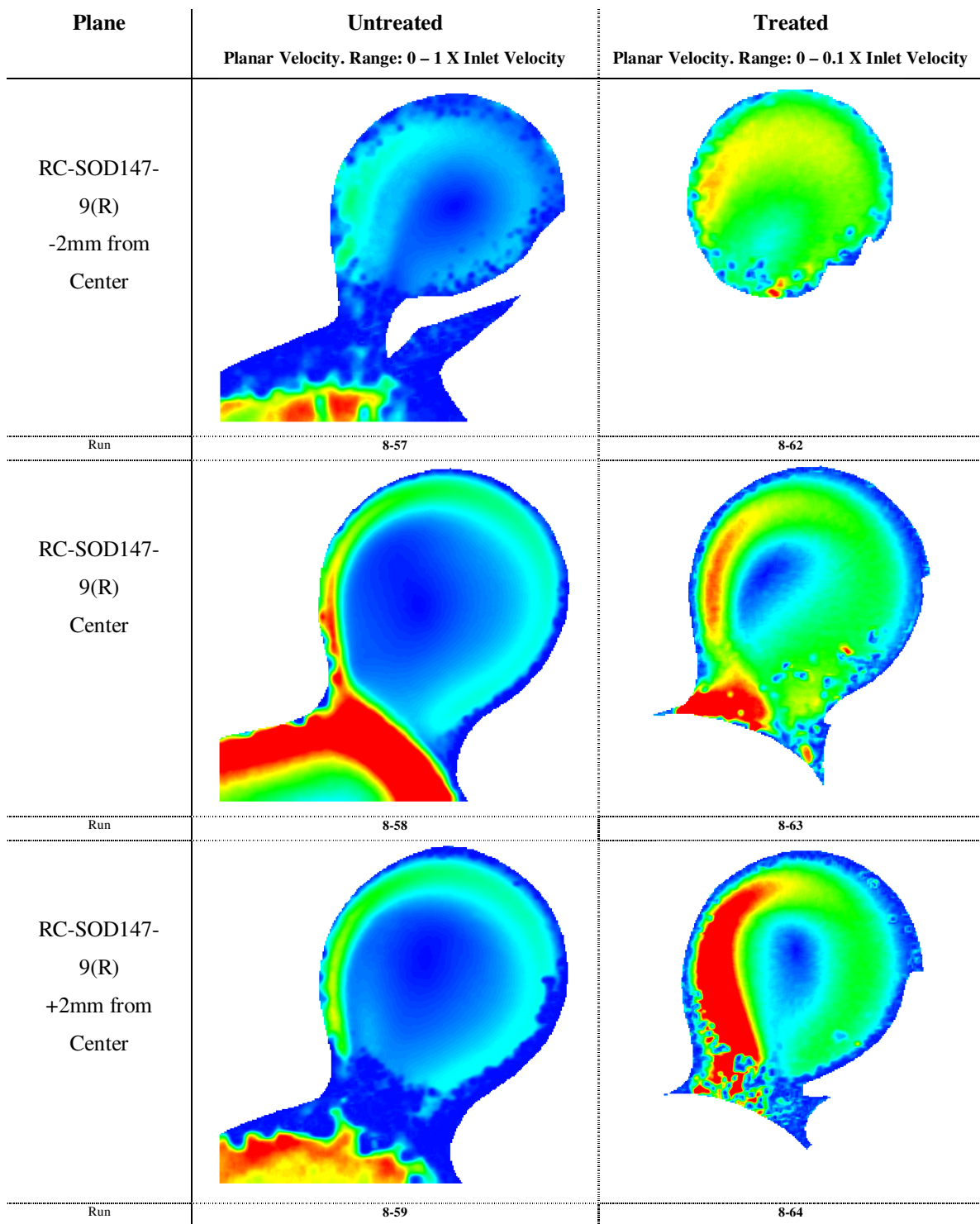


Figure A-13. The planar velocity contours are shown at the center plane and planes 2mm on either side. The color contours for the treated aneurysms ranged from 0 m/s to 1/10th of the inlet velocity to better visualize the structure of the jet entering the aneurysm.

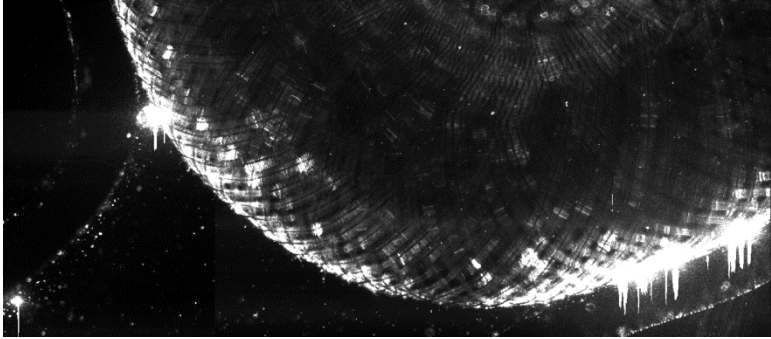
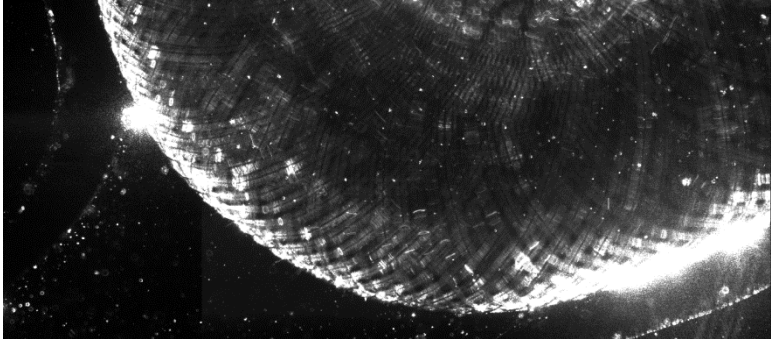
Flow Domain	Close-up View of PED
RC-SOD147-7(F)	
RC-SOD147-7(R)	

Figure A-14. The shapes of the flow diverter inside the RC-SOD147-7 flow domains are shown.

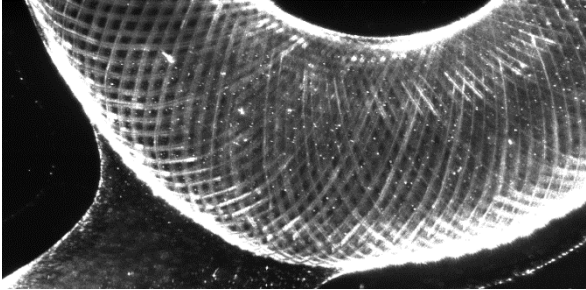
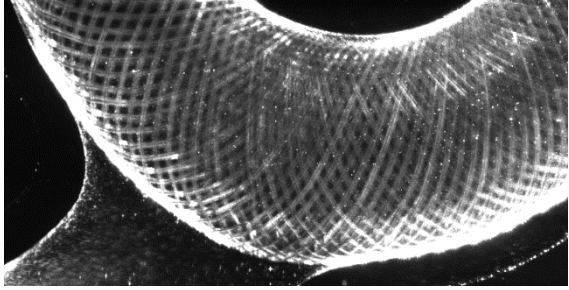
Flow Domain	Close-up View of PED
RC-SOD147-8(F)	
RC-SOD147-8(R)	

Figure A-15. The shapes of the flow diverter inside the RC-SOD147-8 flow domains are shown.

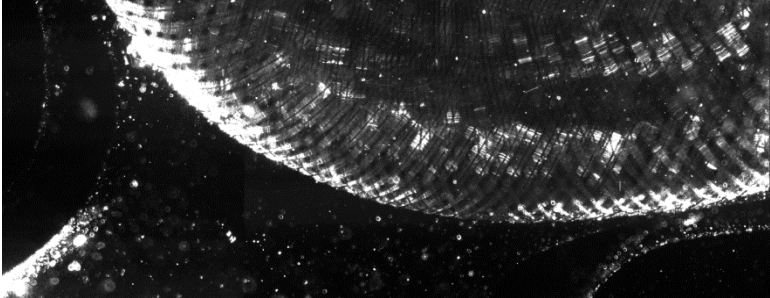
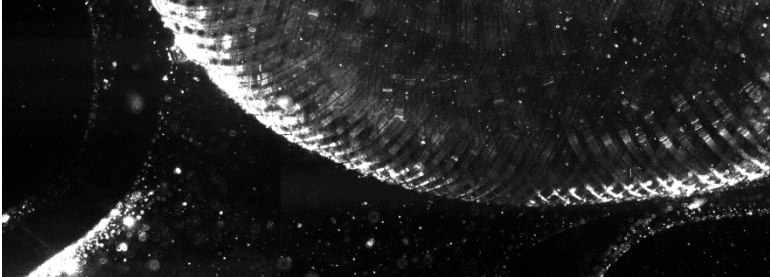
Flow Domain	Close-up View of PED
RC-SOD147-9(F)	
RC-SOD147-9(R)	

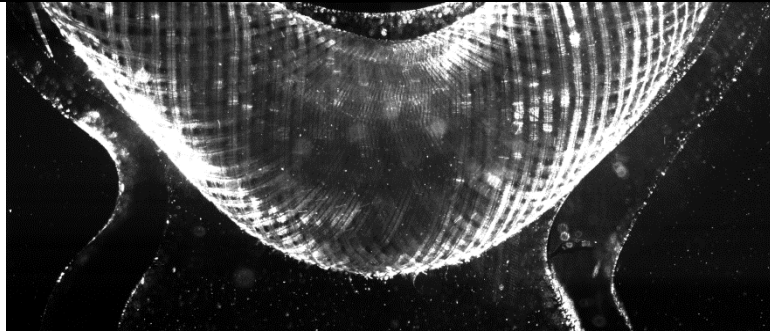
Figure A-16. The shapes of the flow diverter inside the RC-SOD147-9 flow domains are shown.

CHAPTER 3.3.3

Flow Domain

Close-up View of PED

RC-SOD68-1



RC-SOD68-3

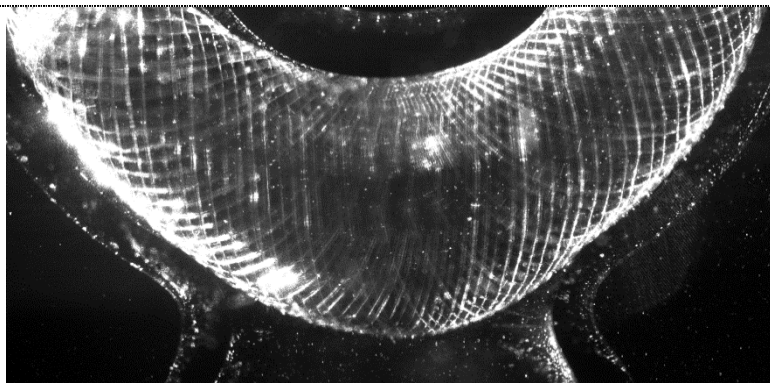


Figure A-17. The shapes of the flow diverter inside RC-SOD68-1 and -3 flow domains are shown.

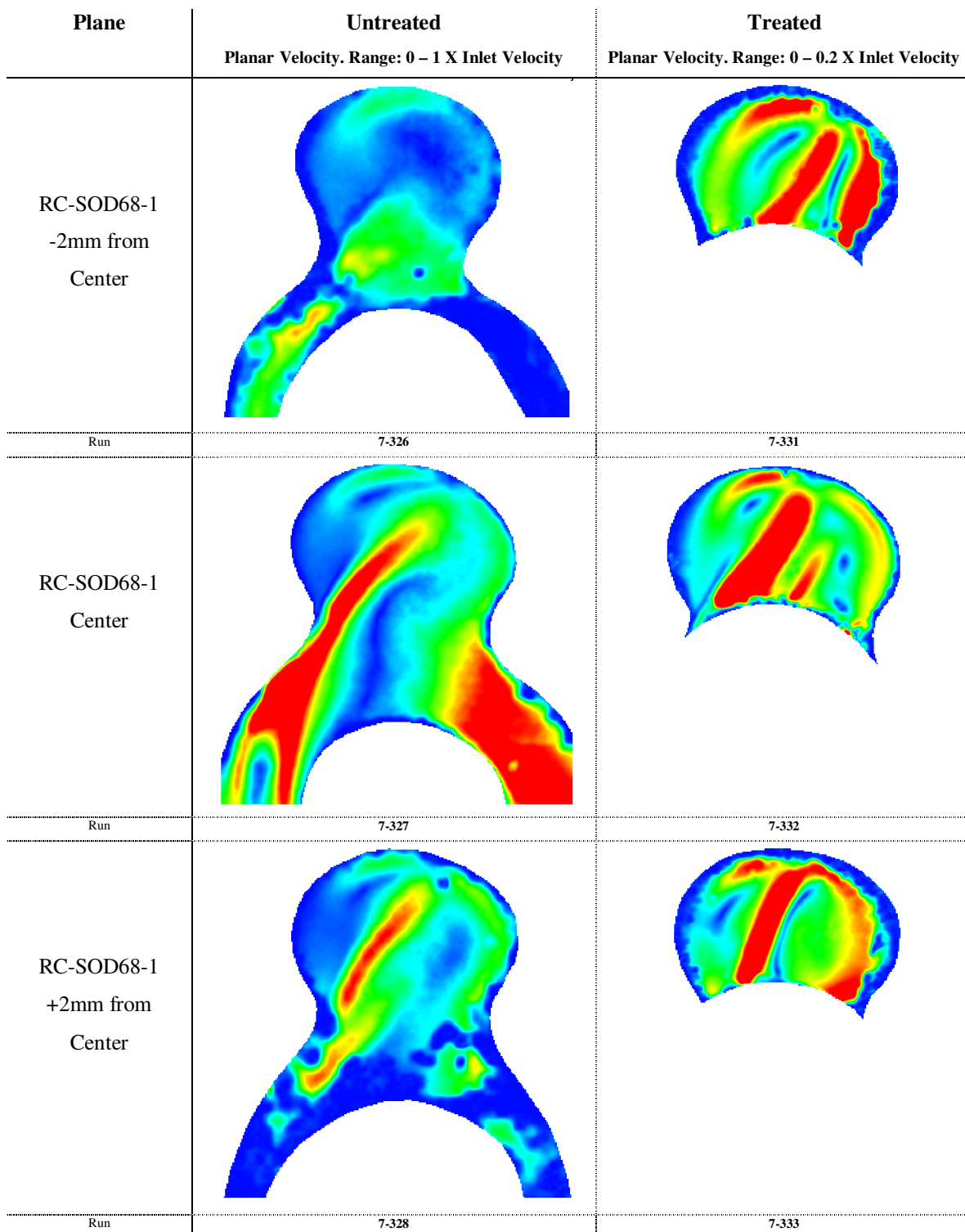


Figure A-18. The planar velocity contours are shown at the center plane and planes 2mm on either side. The color contours for the treated aneurysms ranged from 0 m/s to $2/10^{\text{th}}$ of the inlet velocity to better visualize the structure of the jet entering the aneurysm.

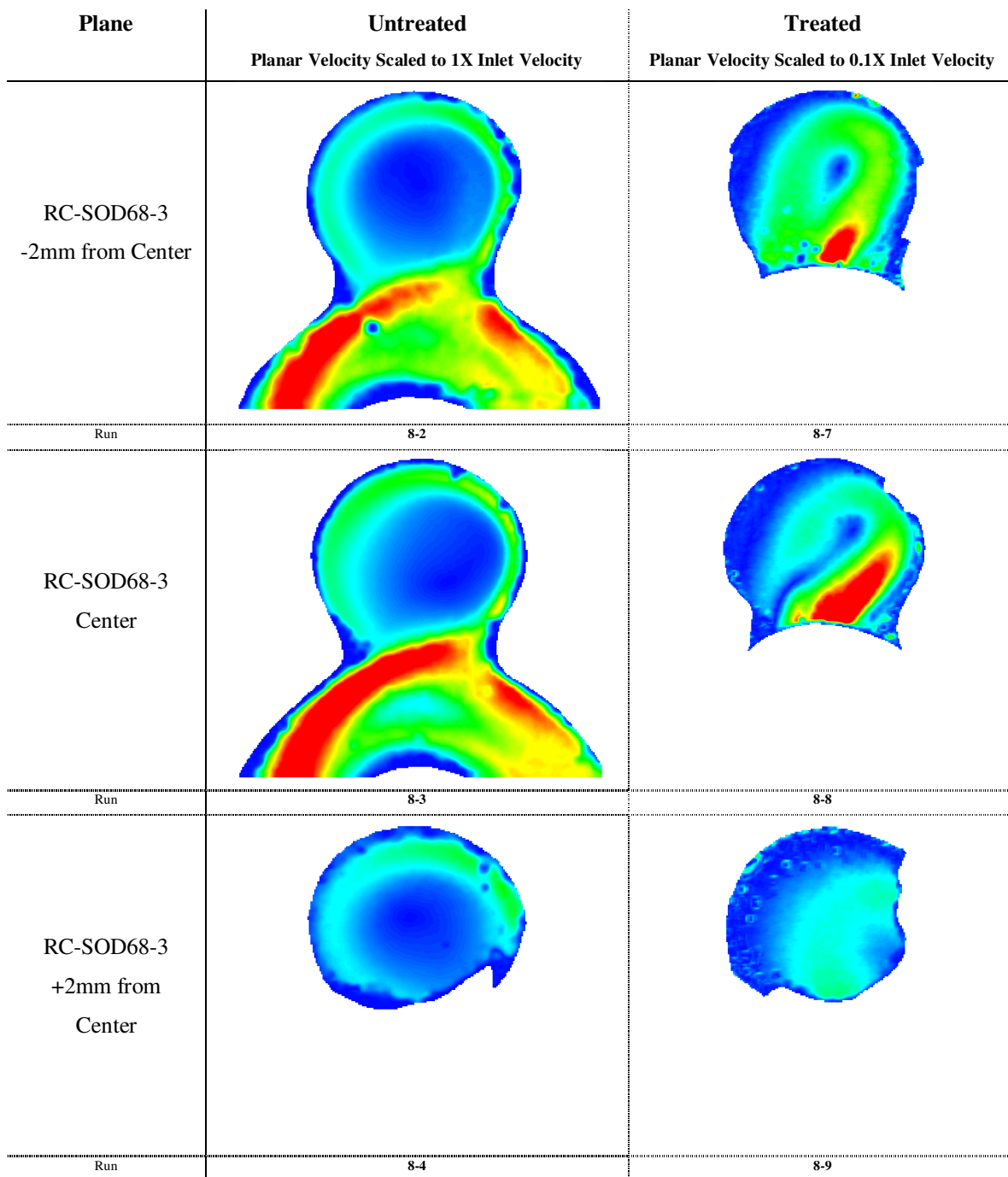


Figure A-19. The planar velocity contours are shown at the center plane and planes 2mm on either side. The color contours for the treated aneurysms are scaled to $1/10^{\text{th}}$ of the inlet velocity to better visualize the structure of the jet entering the aneurysm.

APPENDIX B: SUPPLEMENTAL FIGURES AND TABLES FROM CFD

CHAPTER 4.3.2

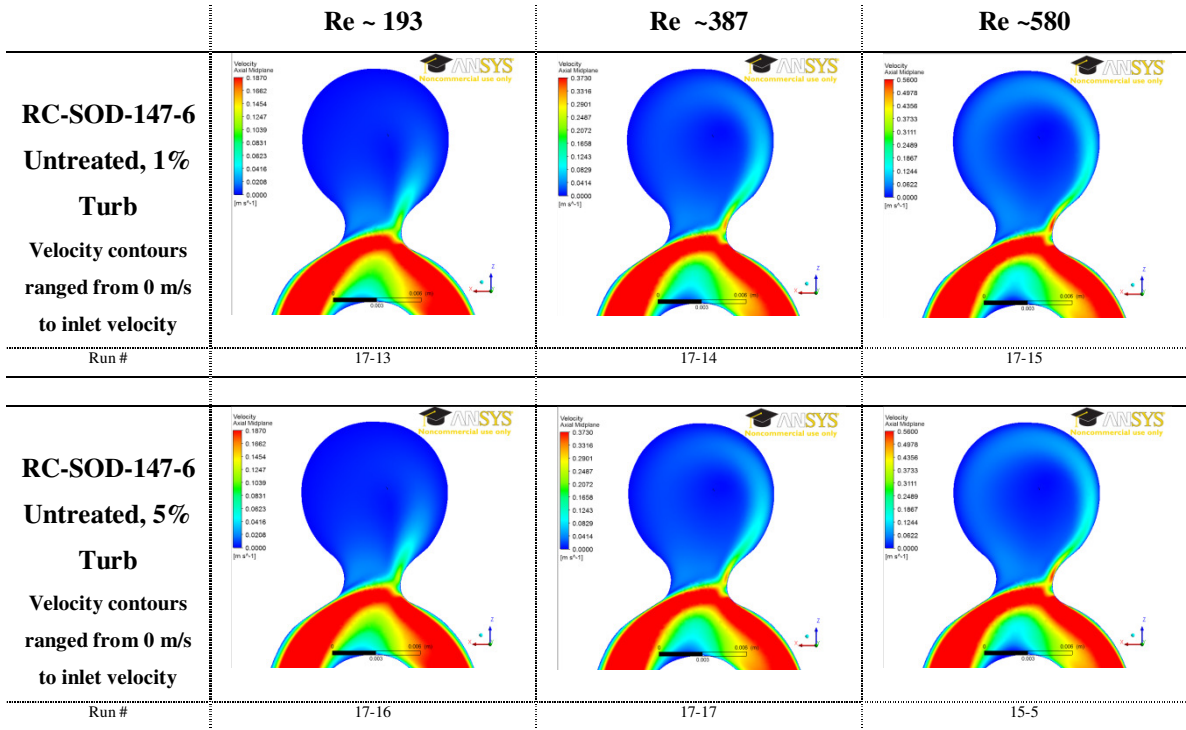


Figure B-1. The velocity contours of fluid entering the aneurysm in RC-SOD147-6 for different inlet velocities are compared.

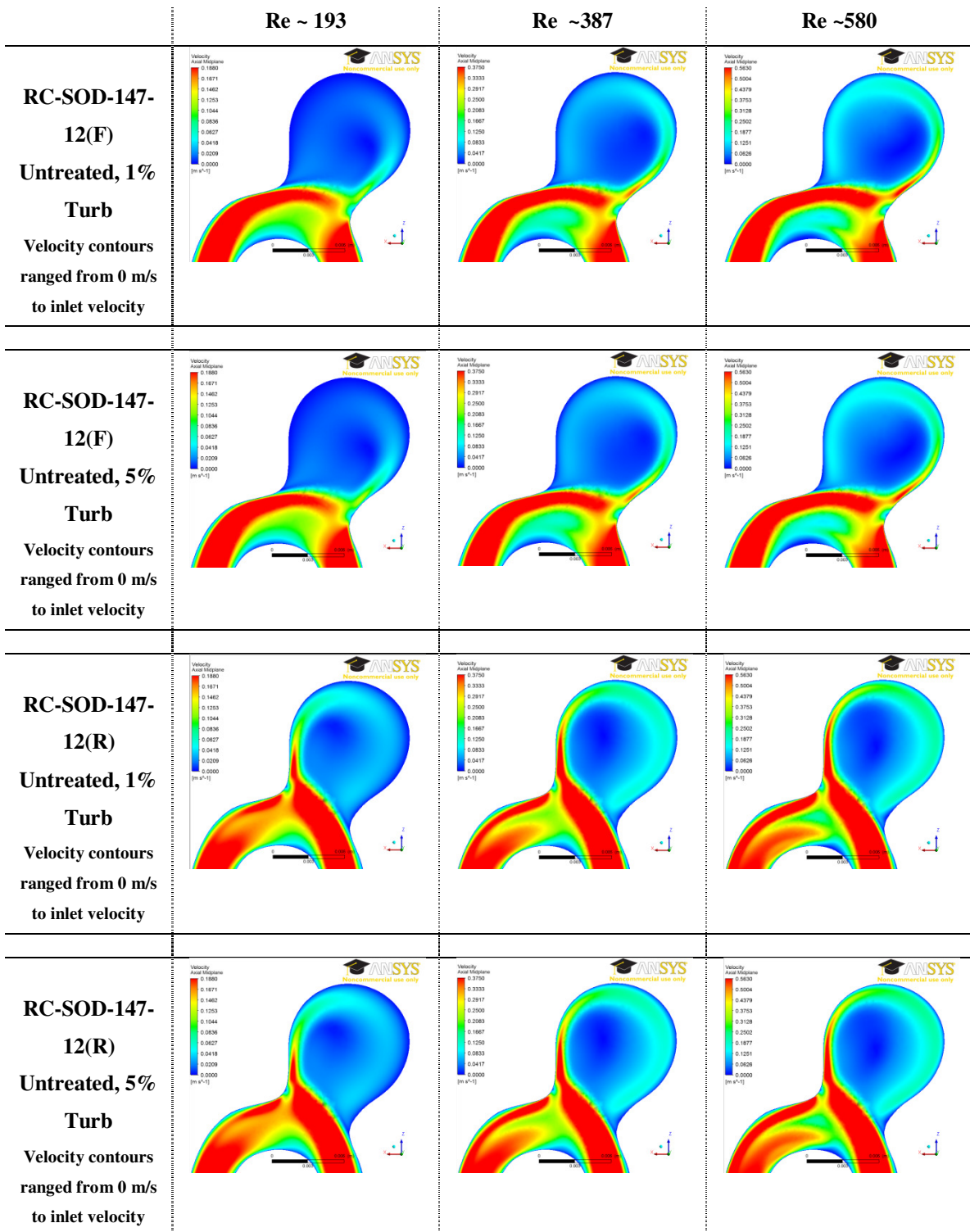


Figure B-2. The velocity contours of fluid entering the aneurysm in RC-SOD147-12(F/R) for different inlet velocities are compared.

CHAPTER 4.3.3

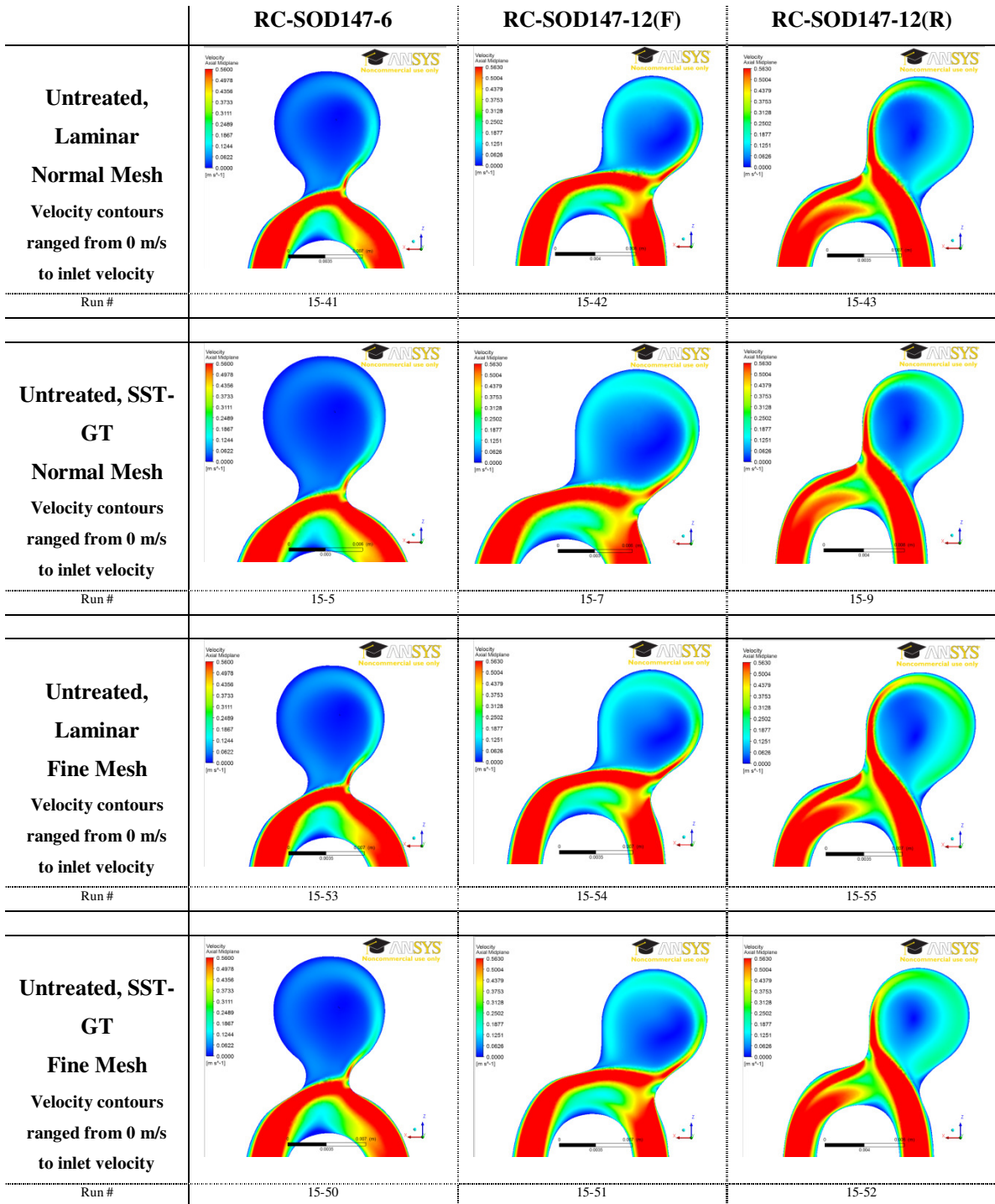


Figure B-3. The velocity contours approximately bisecting the aneurysms are shown above. Note that mesh density and flow regime has negligible effect on the flow rate of blood entering the aneurysm.

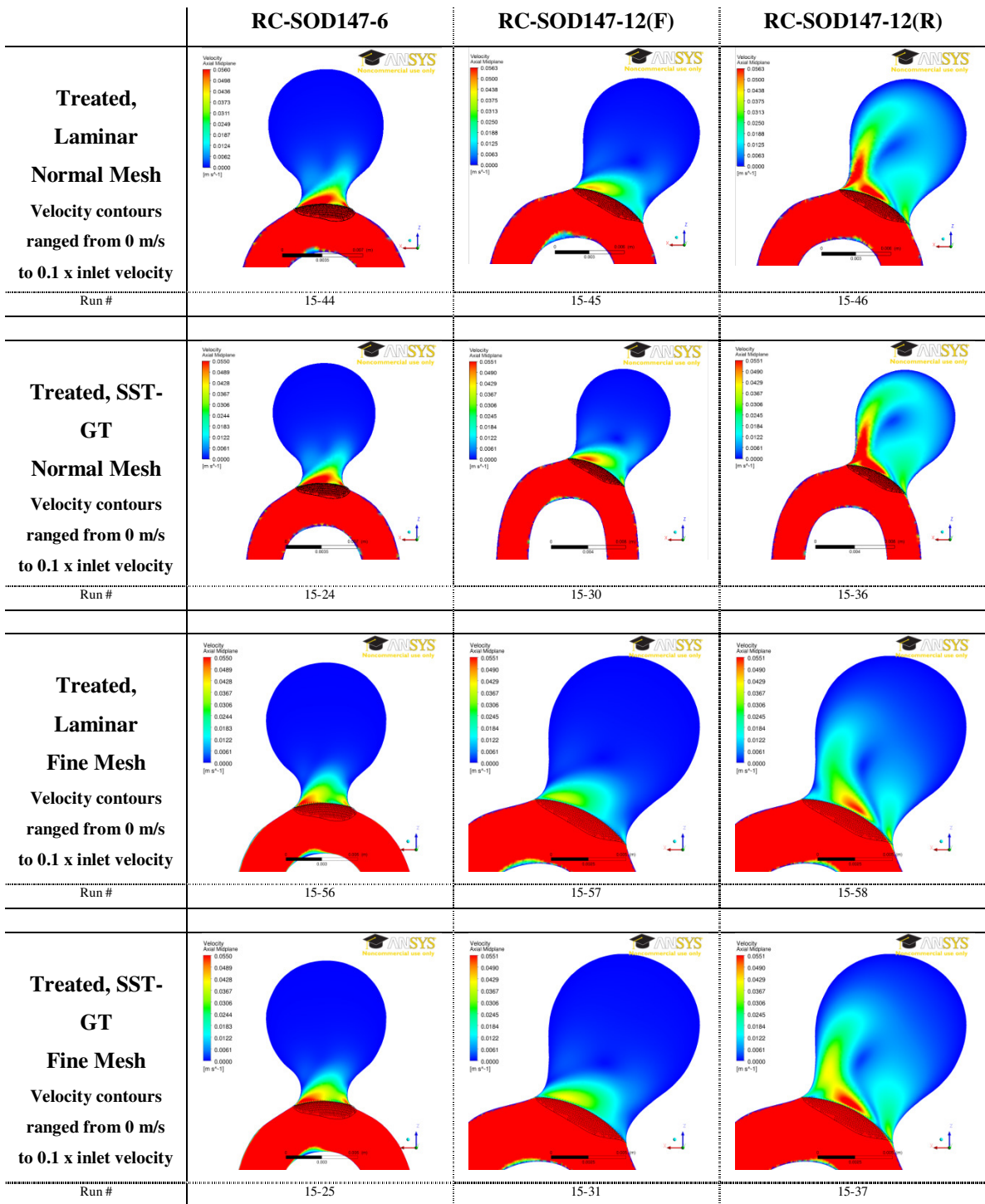


Figure B-4. The velocity contours approximately bisecting the aneurysms are shown above. Note that mesh density and flow regime has noticeable effect on the flow rate of blood entering the aneurysm as well as the contour of the fluid past the perforated membrane.

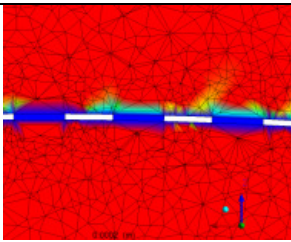
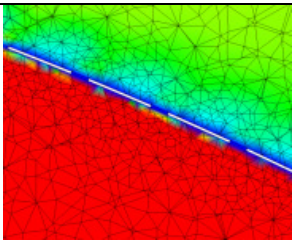
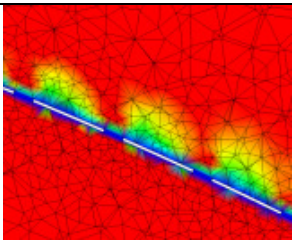
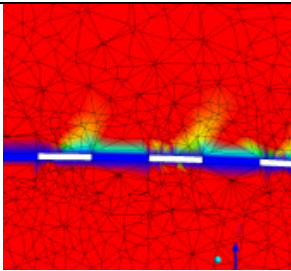
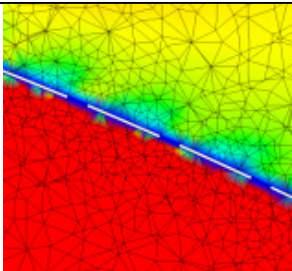
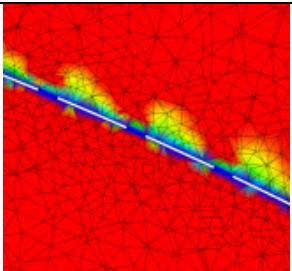
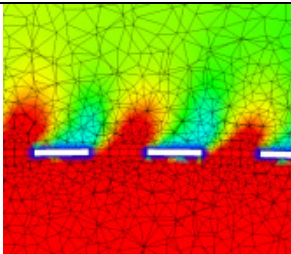
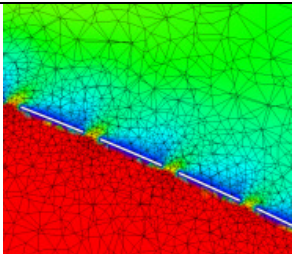
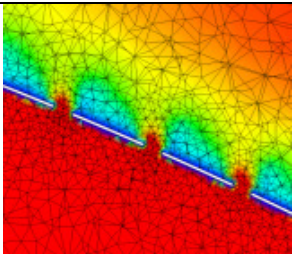
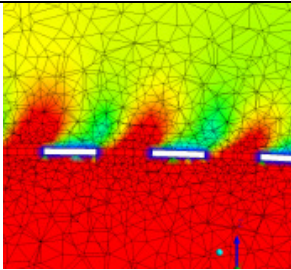
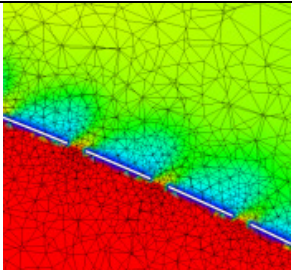
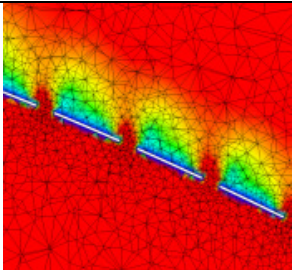
	RC-SOD147-6	RC-SOD147-12(F)	RC-SOD147-12(R)
Laminar Normal Mesh Velocity contours ranged from 0 m/s to 0.1 x inlet velocity			
Q_T/Q_{UT} [%]	31.5	9.8	18.6
SST-GT Normal Mesh Velocity contours ranged from 0 m/s to 0.1 x inlet velocity			
Q_T/Q_{UT} [%]	34.4	10.8	22.5
Laminar Fine Mesh Velocity contours ranged from 0 m/s to 0.1 x inlet velocity			
Q_T/Q_{UT} [%]	29.6	9.4	10.0
SST-GT Fine Mesh Velocity contours ranged from 0 m/s to 0.1 x inlet velocity			
Q_T/Q_{UT} [%]	29.3	9.0	13.8

Figure B-5. The velocity contours approximately bisecting the aneurysms near the pores are shown. With a fine mesh, jets of fast moving fluid rush through the pores. The struts of the membrane exhibit a shielding effect, creating a region of slow moving fluid behind it. Q_T = flow rate of fluid entering the treated aneurysm. Q_{UT} = flow rate of fluid entering the untreated aneurysm.

CHAPTER 4.3.4

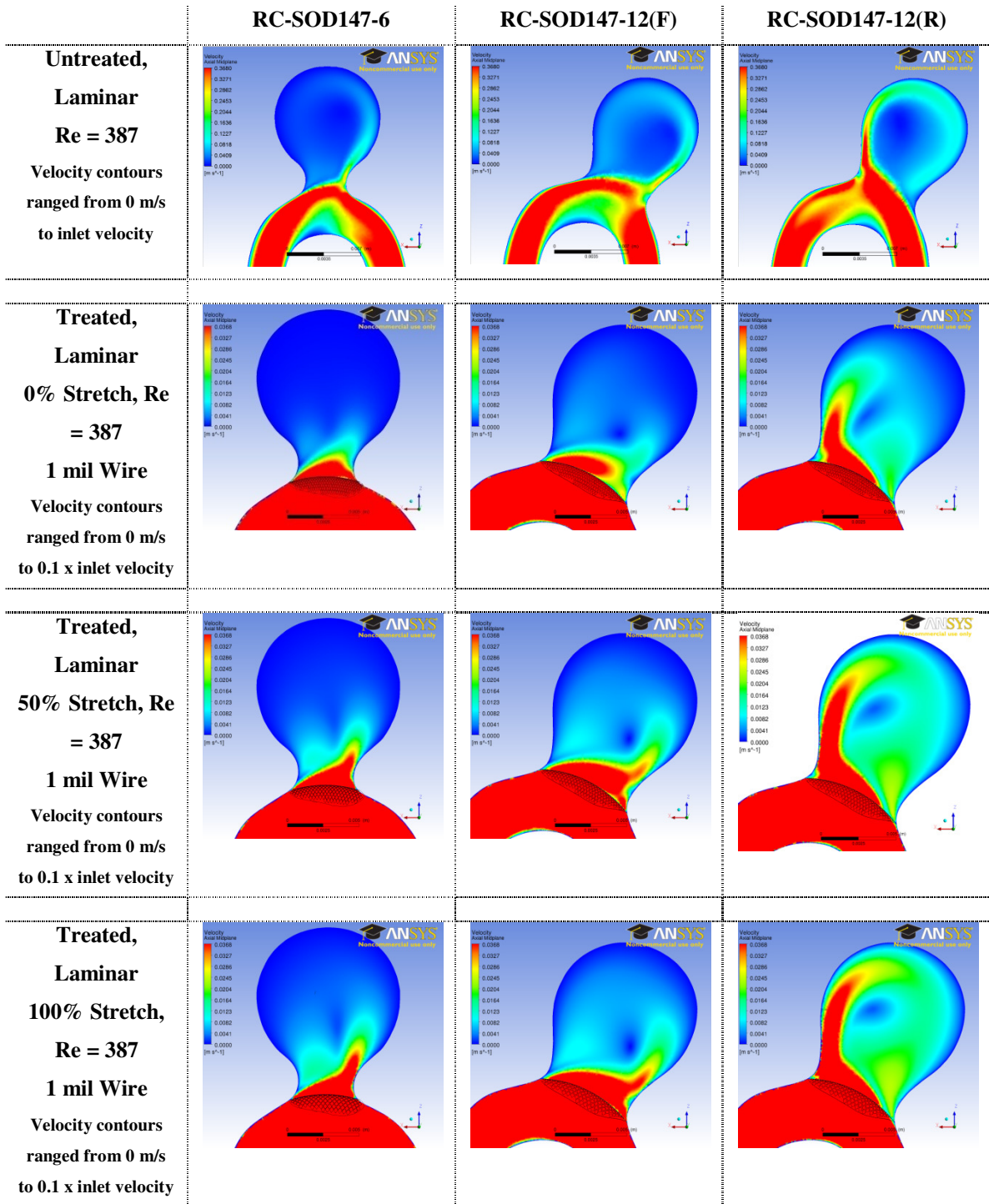


Figure B-6. The velocity contours, at Re = 387, approximately bisecting the aneurysms are shown. As the pores of the flow diverter modeled as 1 mil wires become larger, the flow of blood entering the aneurysm increases.

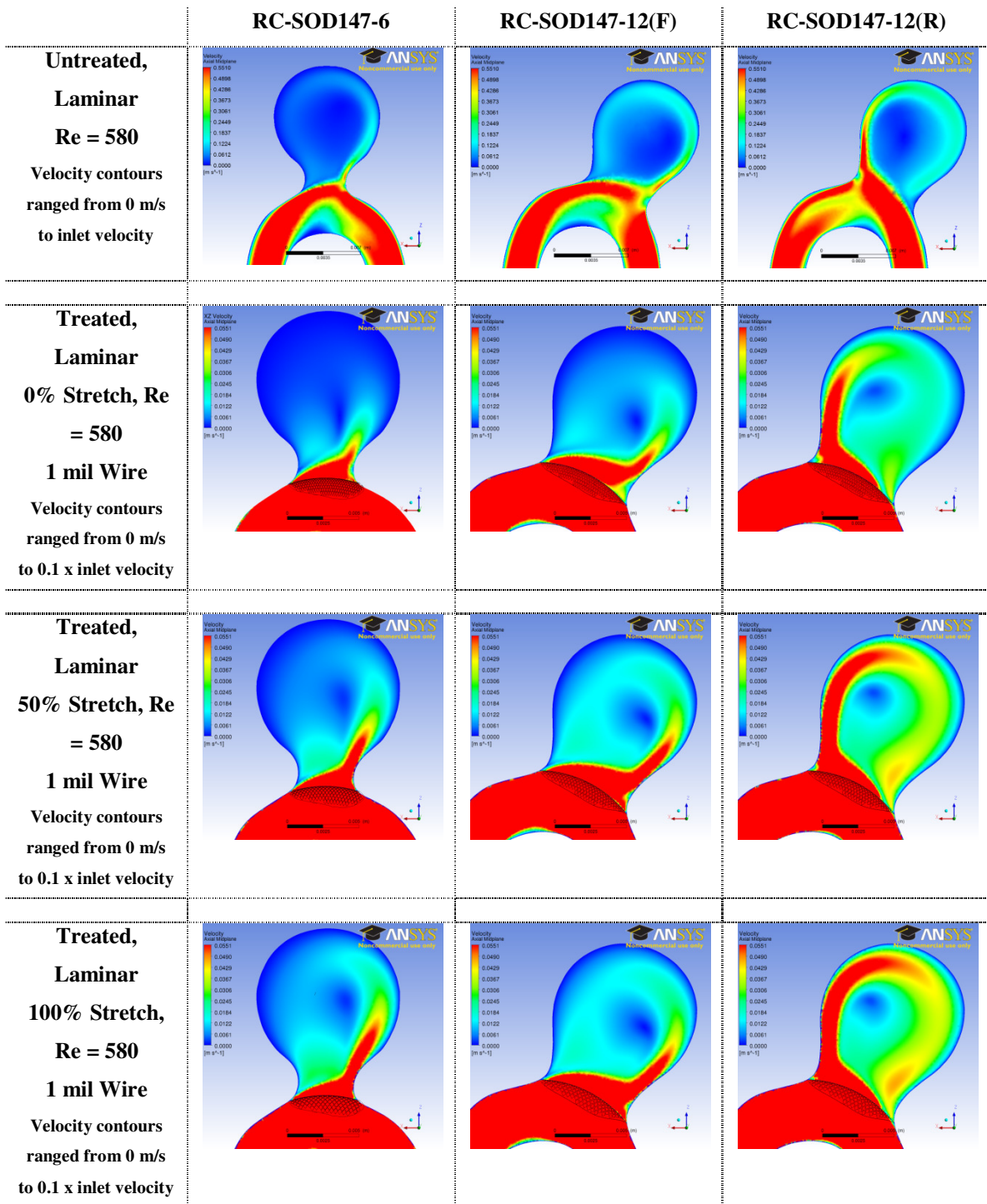


Figure B-7. The velocity contours, at Re = 580, approximately bisecting the aneurysms are shown. As the pores of the flow diverter modeled as 1 mil wires become larger, the flow of blood entering the aneurysm increases.

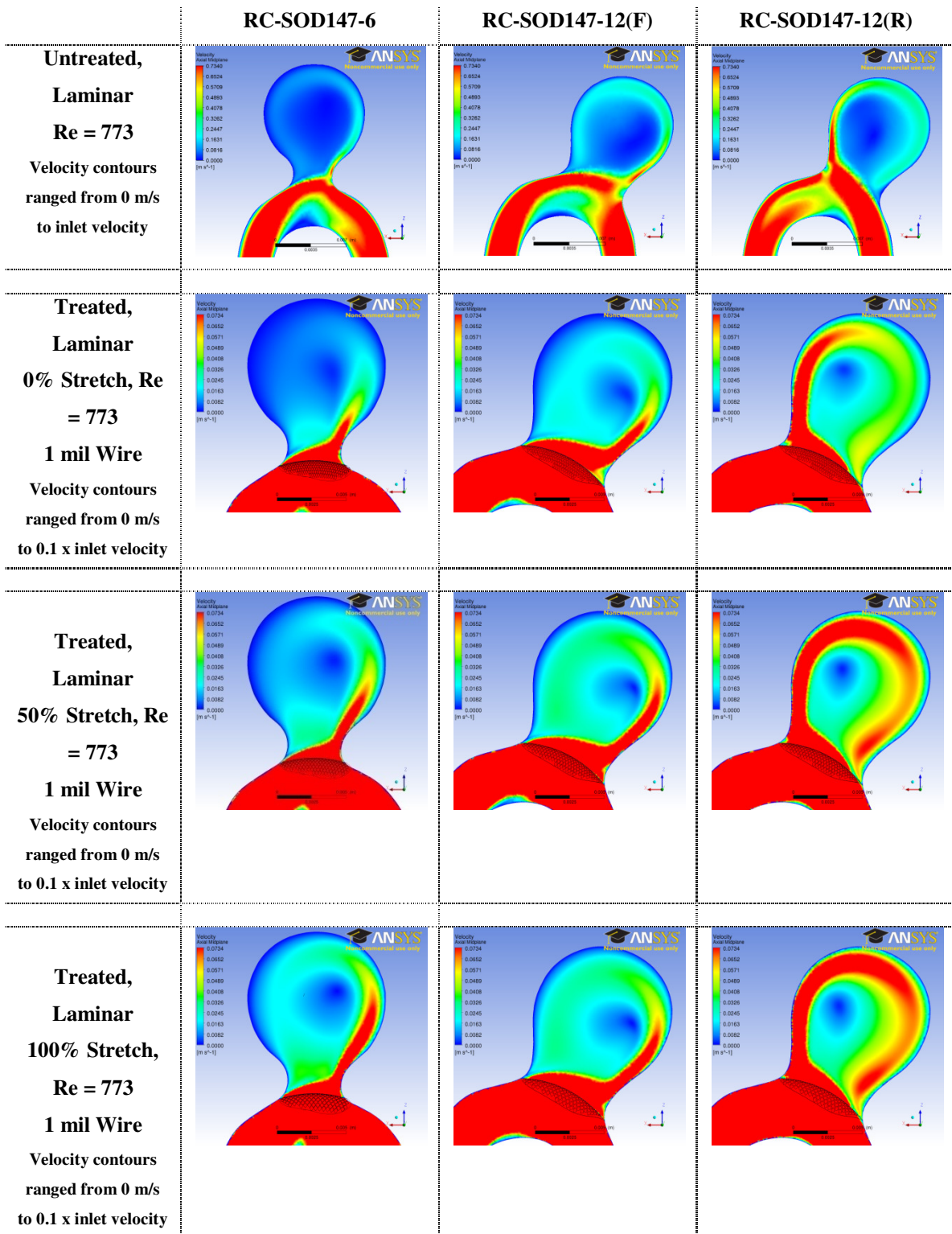


Figure B-8. The velocity contours, at Re = 773, approximately bisecting the aneurysms are shown. As the pores of the flow diverter modeled as 1 mil wires become larger, the flow of blood entering the aneurysm increases.

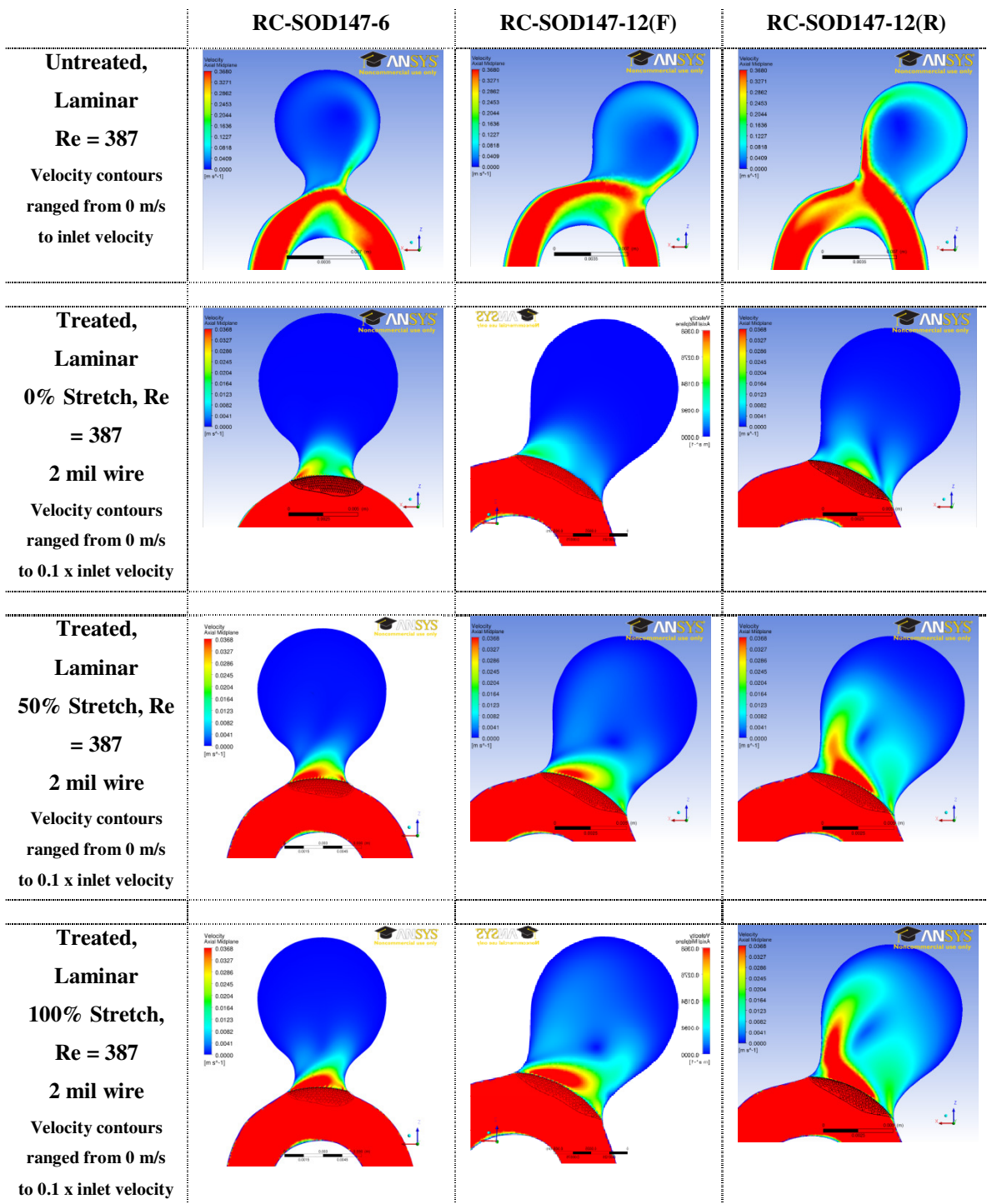


Figure B-9. The velocity contours, at $Re = 387$, approximately bisecting the aneurysms are shown. As the pores of the flow diverter modeled as 2 mil wires become larger, the flow of blood entering the aneurysm increases.

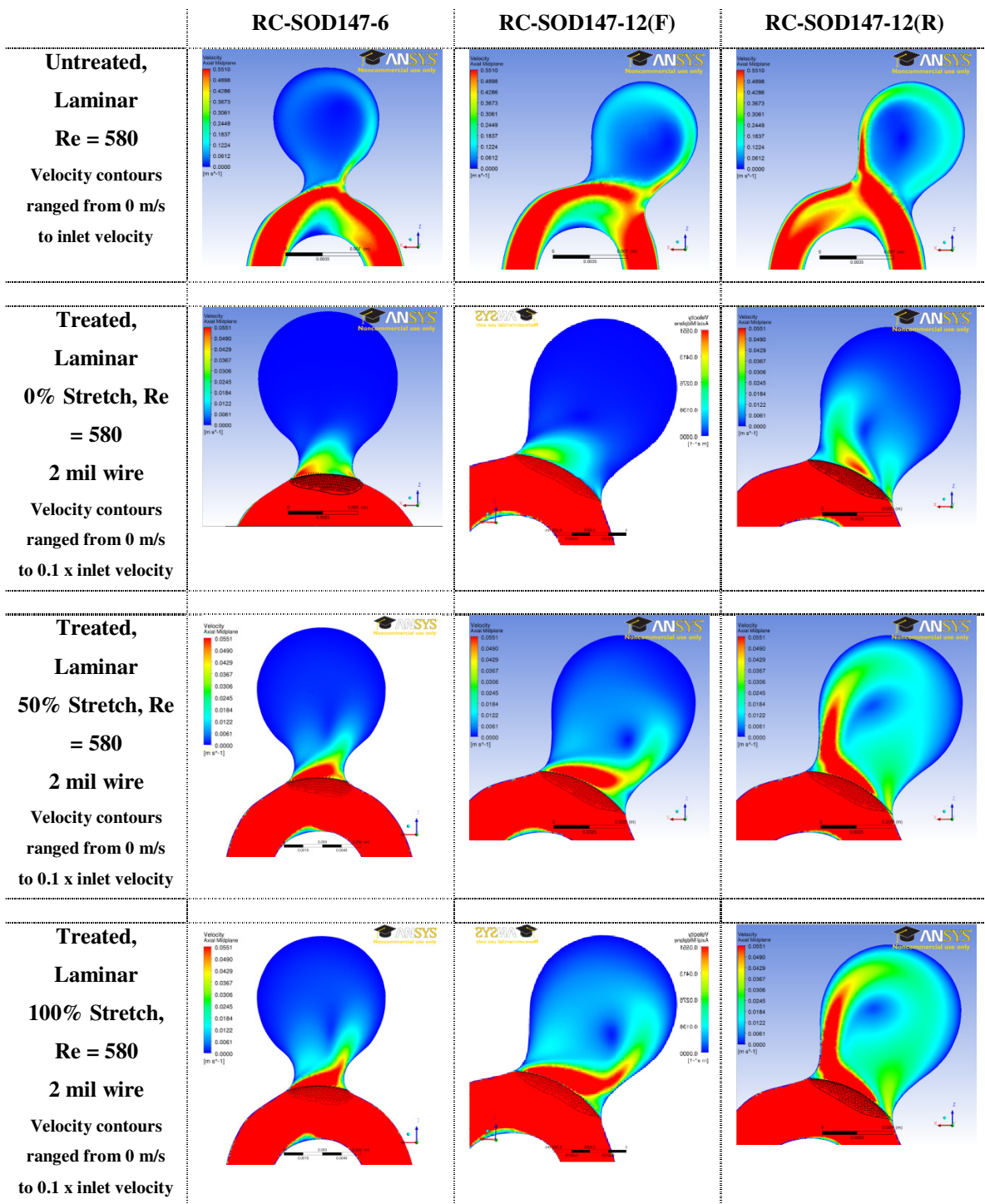


Figure B-10. The velocity contours, at Re = 580, approximately bisecting the aneurysms are shown. As the pores of the flow diverter modeled as 2 mil wires become larger, the flow of blood entering the aneurysm increases.

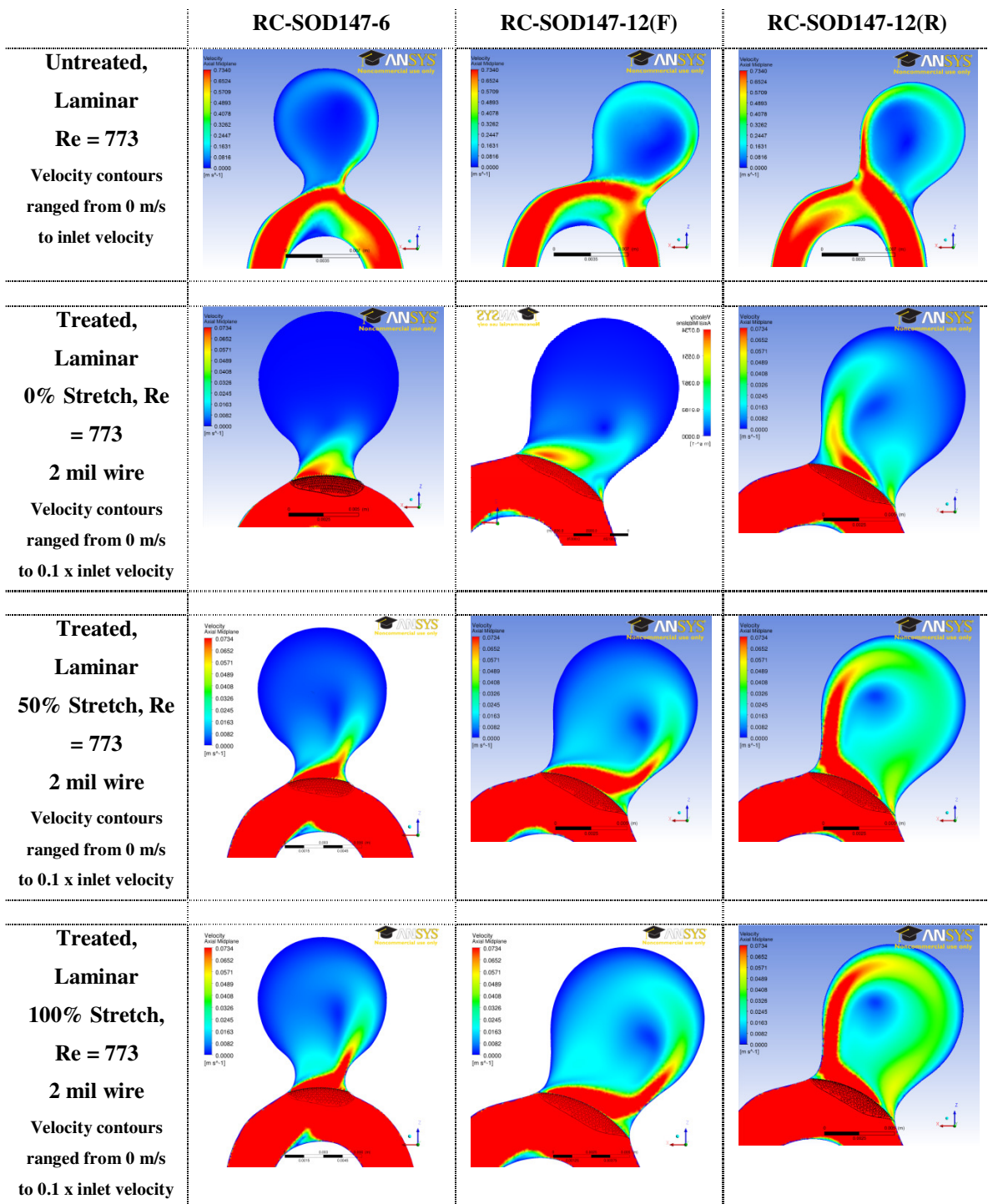


Figure B-11. The velocity contours, at $Re = 773$, approximately bisecting the aneurysms are shown. As the pores of the flow diverter modeled as 2 mil wires become larger, the flow of blood entering the aneurysm increases.

CHAPTER 4.3.5

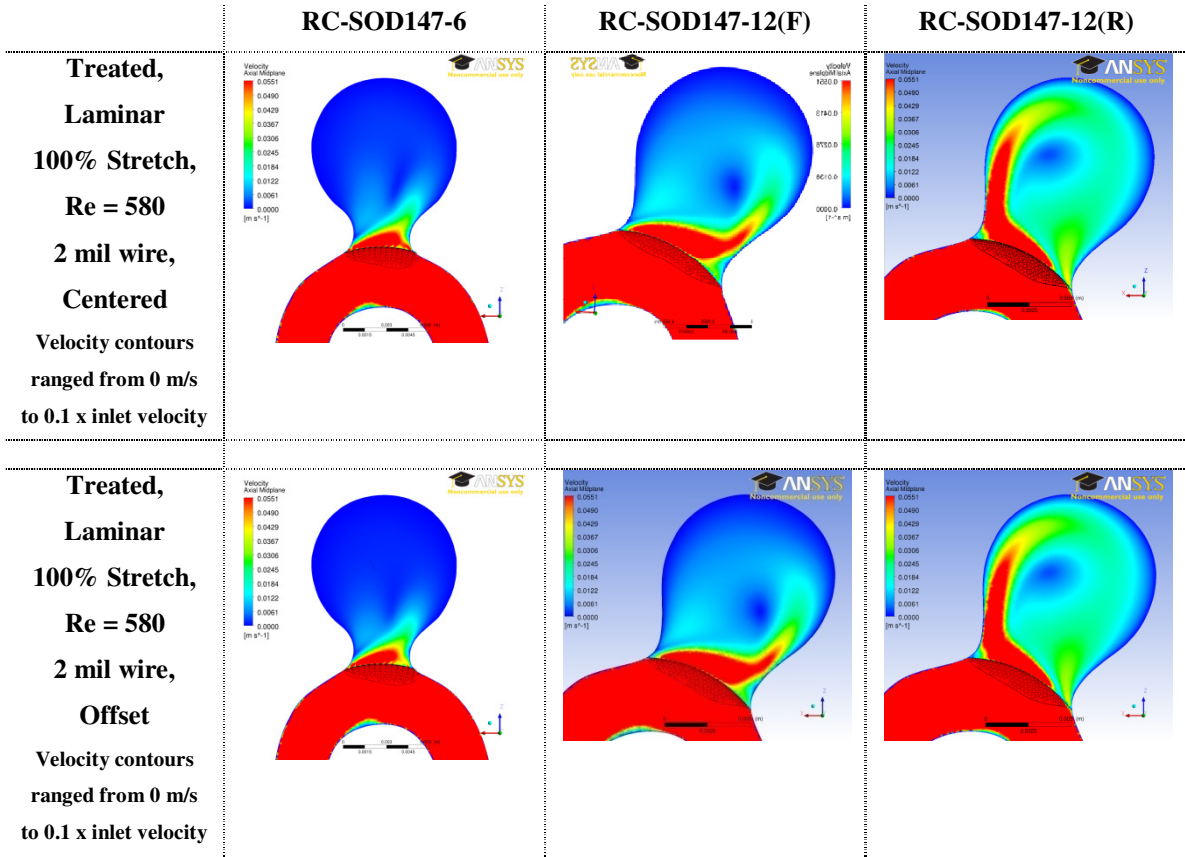


Figure B-12. The velocity contours approximately bisecting the aneurysm treated with flow diverters with pores stretched about 100% of its original width are compared. Circumferentially offsetting the pores, analogous to rotating the flow diverter inside the parent vessel, exhibited little difference in the flow rate of blood entering the aneurysm.

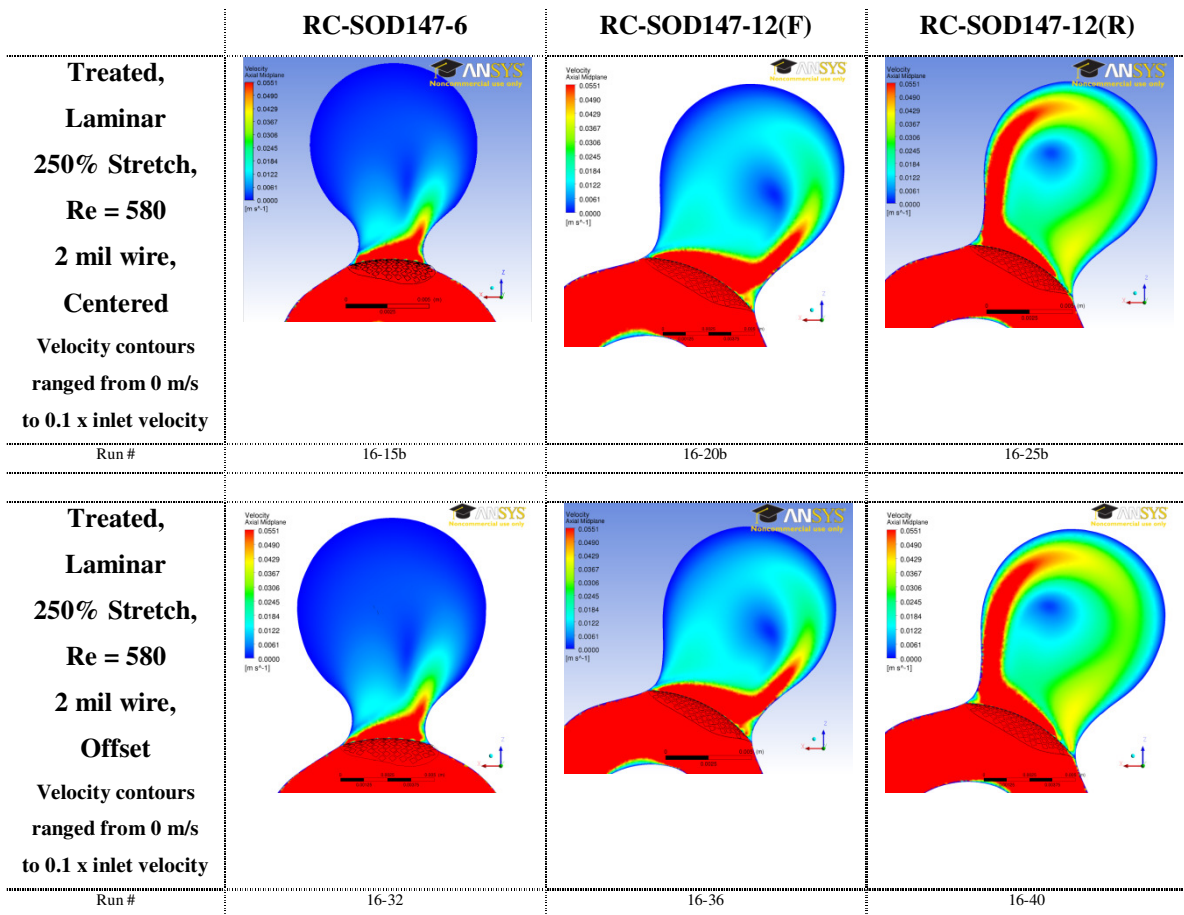
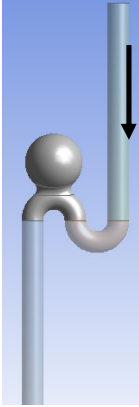
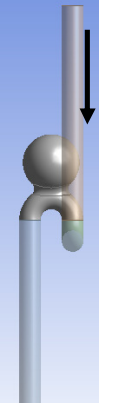
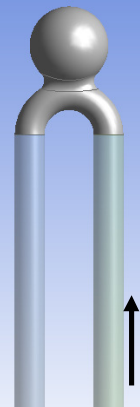
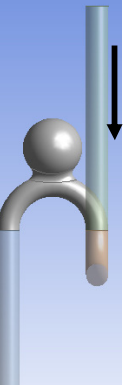


Figure B-13. The velocity contours approximately bisecting the aneurysm treated with flow diverters with pores stretched about 250% of its original width are compared. Circumferentially offsetting the pores, analogous to rotating the flow diverter inside the parent vessel, exhibited little difference in the flow rate of blood entering the aneurysm.

CHAPTER 4.4

Domain	Straight Inlet	Planar Curve Inlet	Perpendicular Curve Inlet
A			
B			
C			

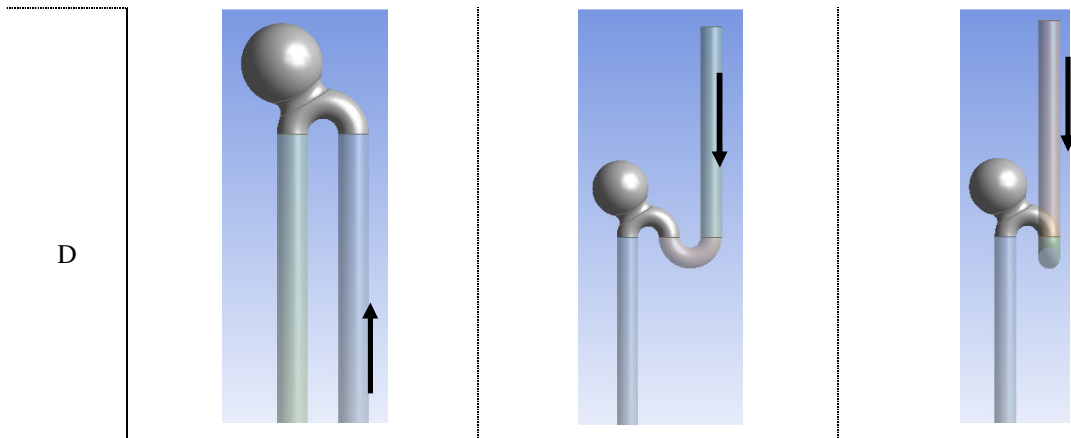


Figure B-14. Idealized flow domains A to D are shown with different upstream vessel segments. In order to maximize detail while minimizing the size of images, please note that **the domains are not to scale**. The black arrow indicates the direction of flow.

Domain	Straight Inlet	Planar Curve Inlet	Perpendicular Curve Inlet
E			
F			

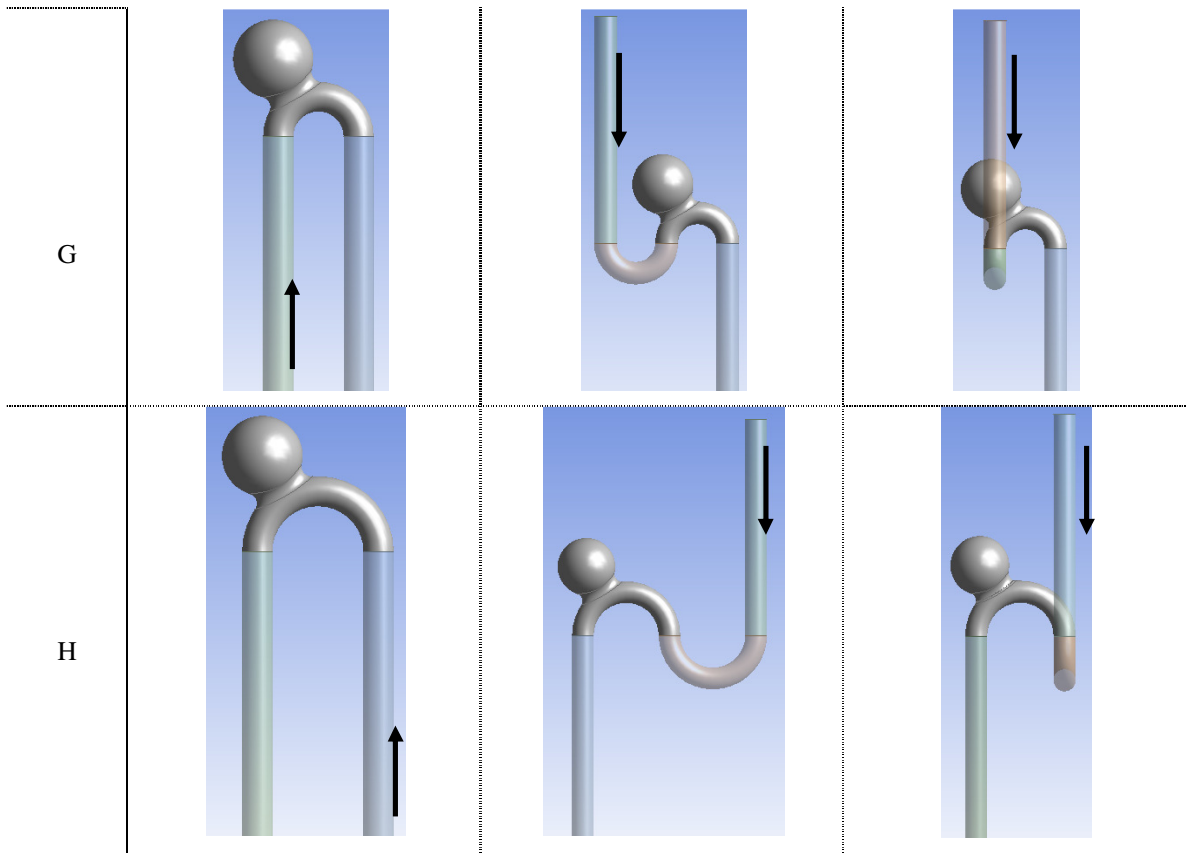


Figure B-15. Idealized flow domains E to H are shown with different upstream vessel segments. In order to maximize detail while minimizing the size of images, please note that **the domains are not to scale**. The black arrow indicates the direction of flow.

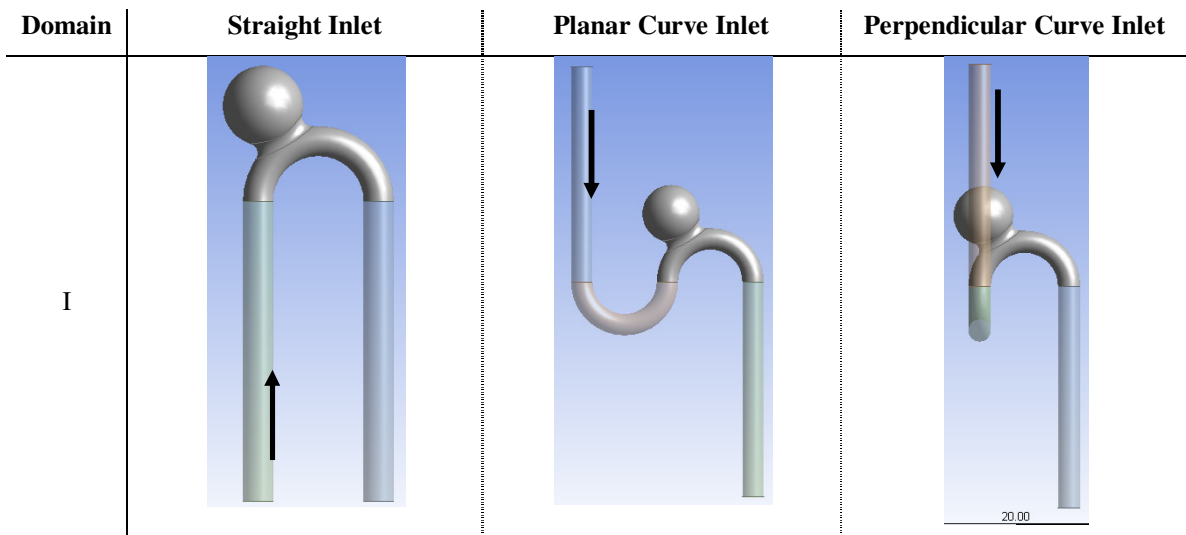


Figure B-16. Idealized flow domains I are shown with different upstream vessel segments. In order to maximize detail while minimizing the size of images, please note that **the domains are not to scale**. The black arrow indicates the direction of flow.

CHAPTER 4.4.1

Q, Straight Pulsatile Inlet: 3mm RoC Domains

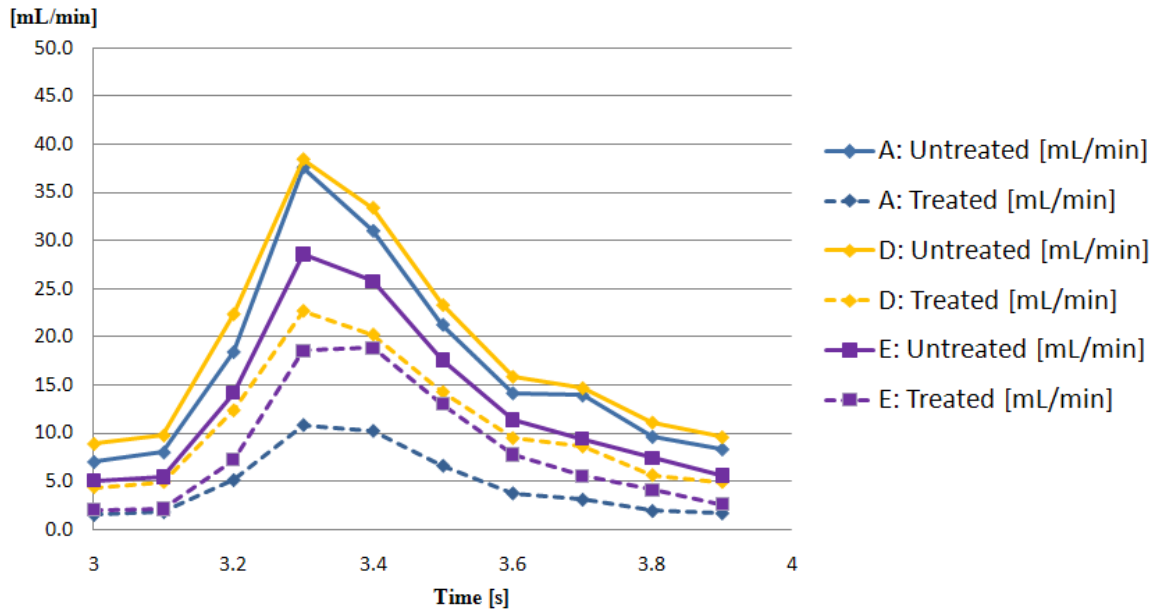


Figure B-17. The time-dependent flow rates of fluid entering the aneurysms on domains with 3mm radii of curvature are shown.

Q, Straight Pulsatile Inlet: 4mm RoC Domains

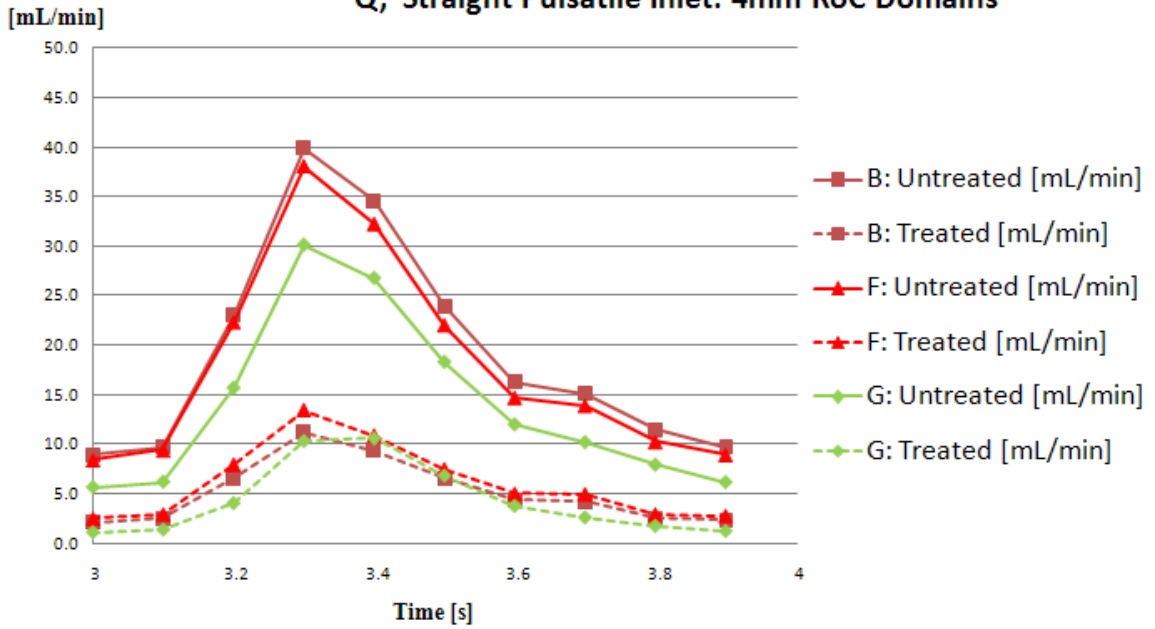


Figure B-18. The time-dependent flow rates of fluid entering the aneurysms on domains with 4mm radii of curvature are shown.

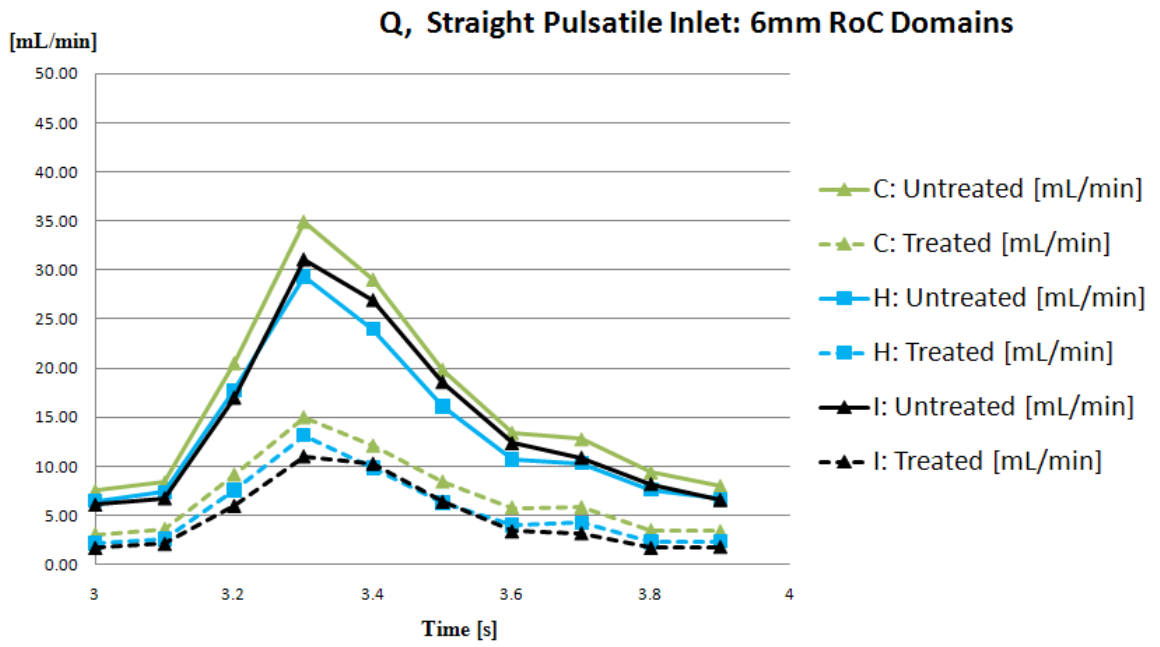


Figure B-19. The time-dependent flow rates of fluid entering the aneurysms on domains with 6mm radii of curvature are shown.

CHAPTER 4.4.2

Q, Planar Curve Pulsatile Inlet: 3mm RoC Domains

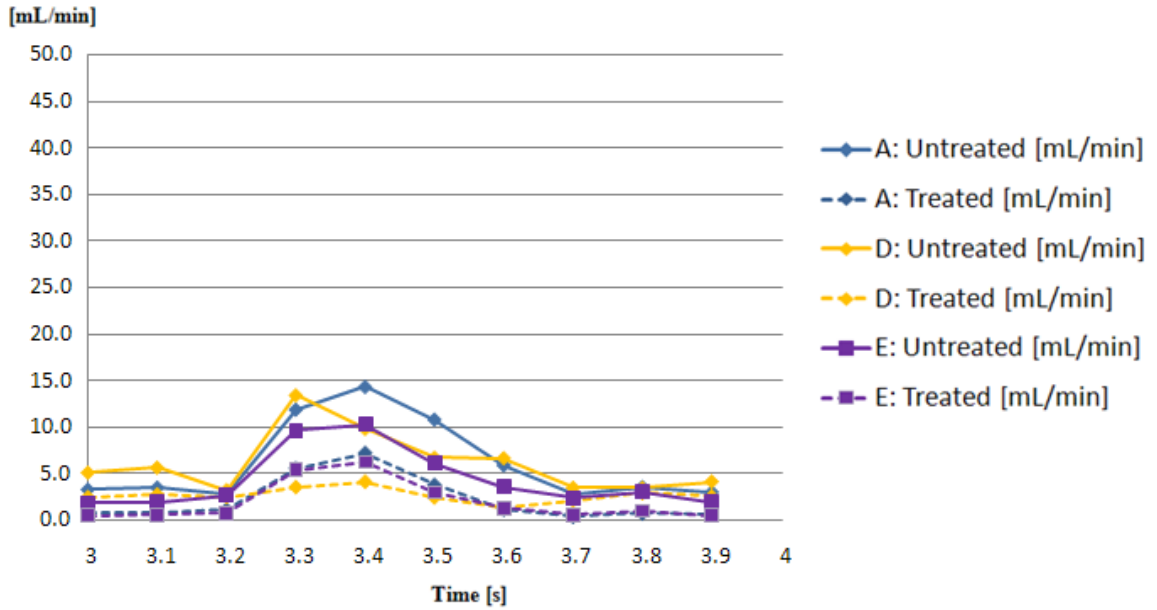


Figure B-20. The time-dependent flow rates of fluid entering the aneurysms on domains with 3mm radii of curvature are shown.

Q, Planar Curve Pulsatile Inlet: 4mm RoC Domains

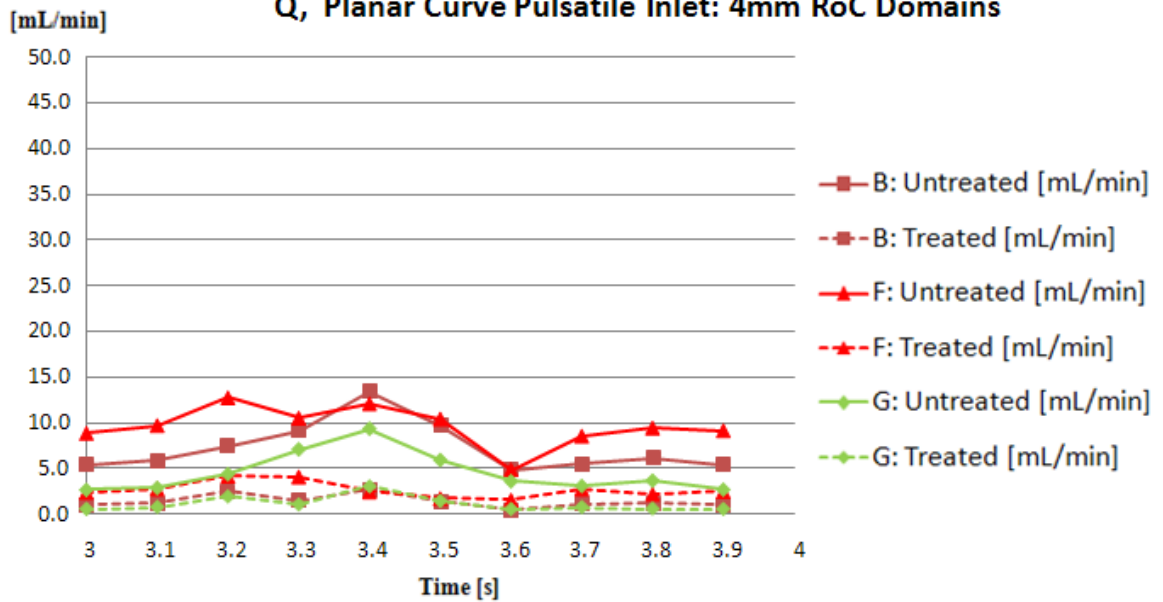


Figure B-21. The time-dependent flow rates of fluid entering the aneurysms on domains with 4mm radii of curvature are shown.

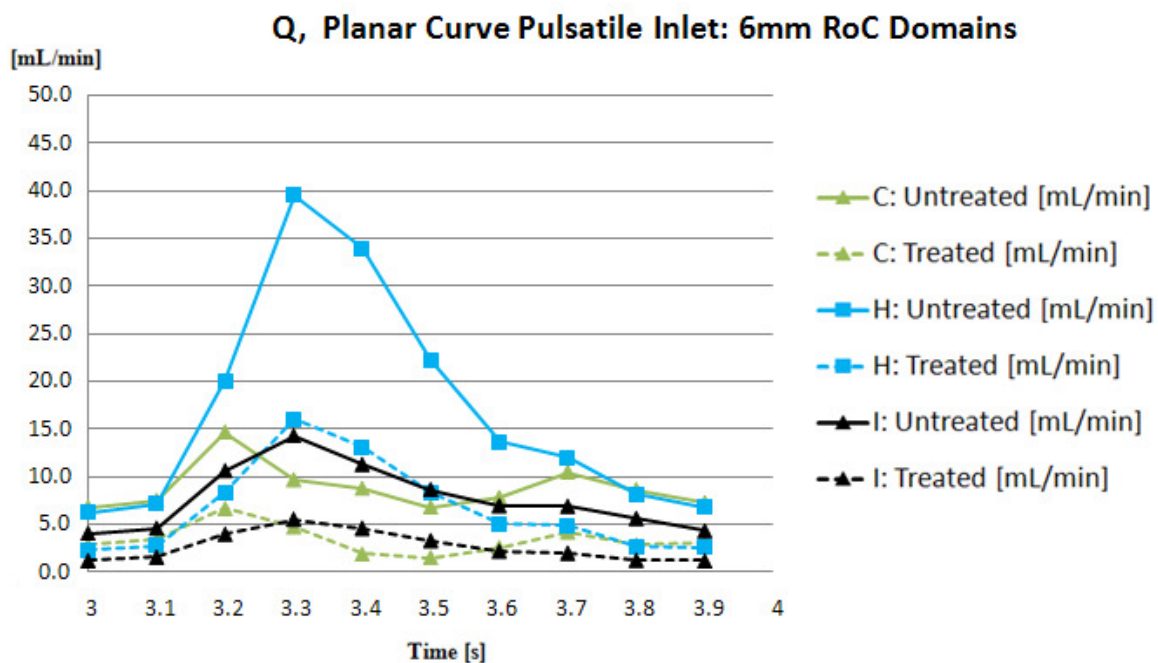


Figure B-22. The time-dependent flow rates of fluid entering the aneurysms on domains with 6mm radii of curvature are shown.

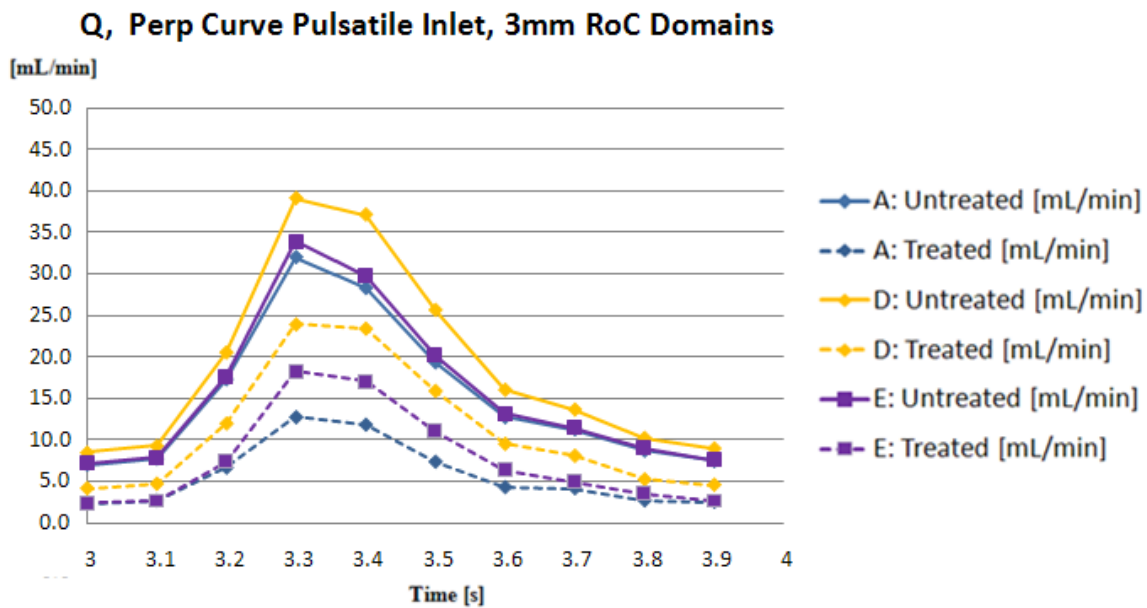


Figure B-23. The time-dependent flow rates of fluid entering the aneurysms on domains with 3mm radii of curvature are shown.

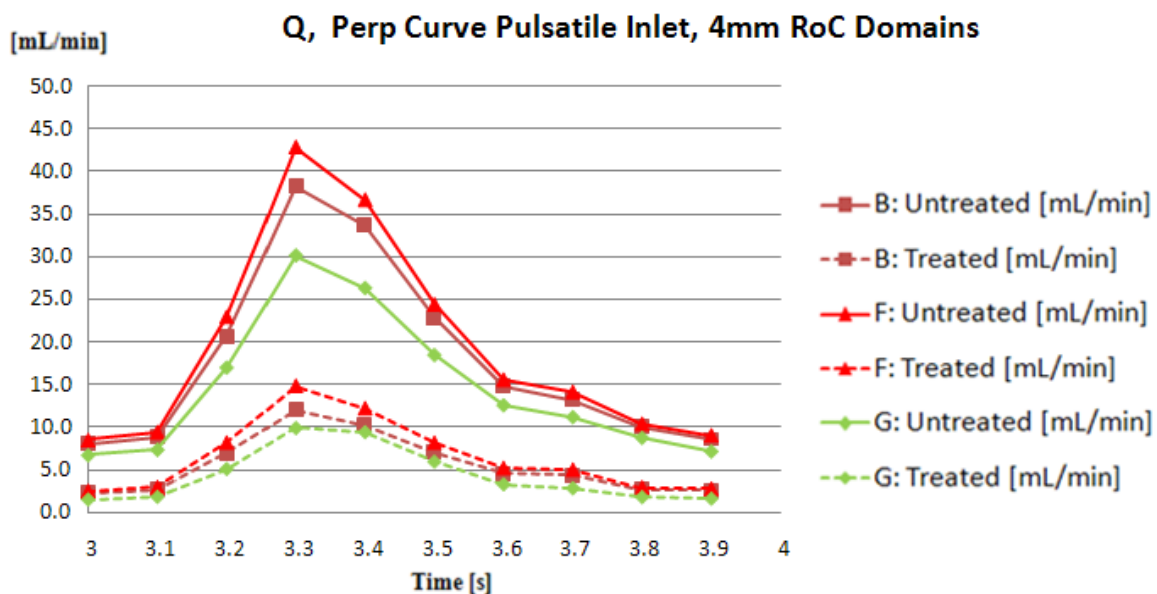


Figure B-24. The time-dependent flow rates of fluid entering the aneurysms on domains with 4mm radii of curvature are shown.

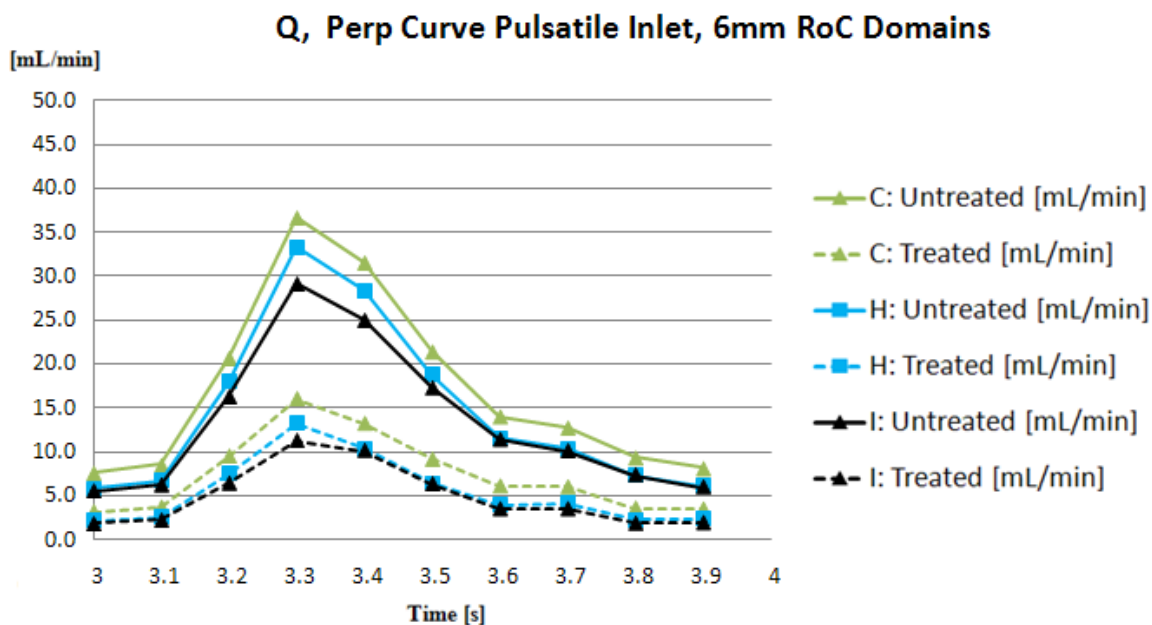


Figure B-25. The time-dependent flow rates of fluid entering the aneurysms on domains with 6mm radii of curvature are shown.

CHAPTER 4.4.3

Q, Straight Pulsatile Inlet, 150BPM, 3mm RoC Domains

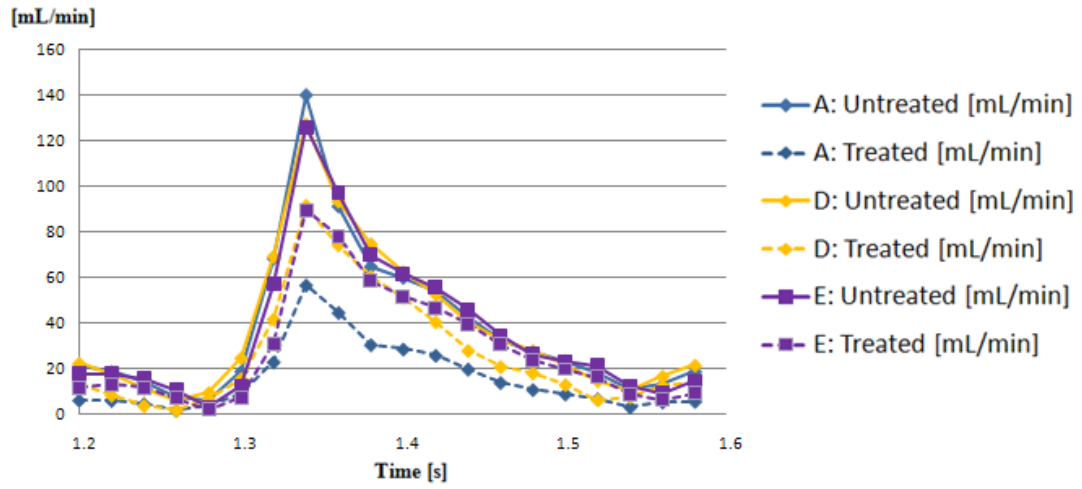


Figure B-26. The time-dependent flow rates of fluid entering the aneurysms on domains with 3mm radii of curvature are shown.

Q, Straight Pulsatile Inlet, 150BPM, 4mm RoC Domains

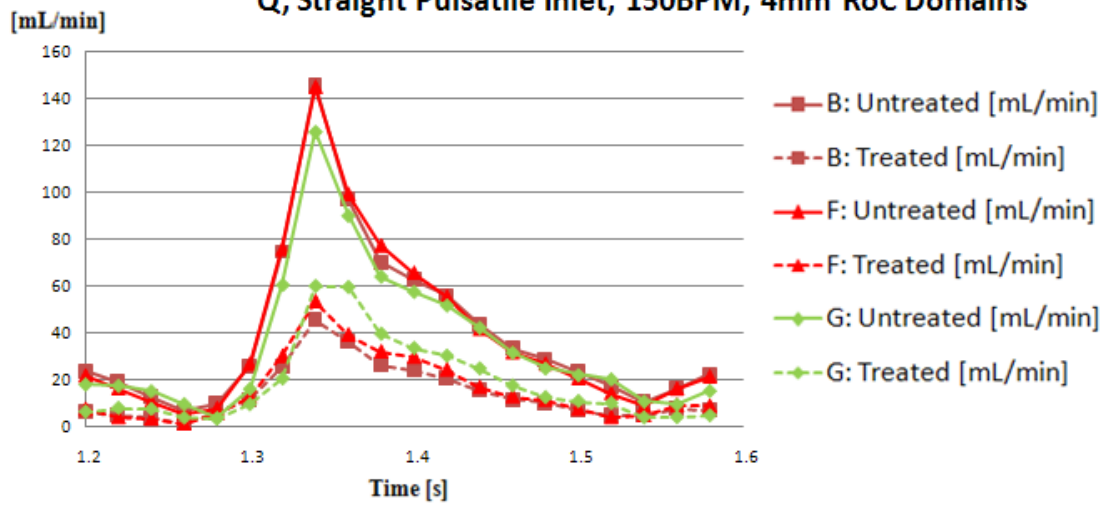


Figure B-27. The time-dependent flow rates of fluid entering the aneurysms on domains with 3mm radii of curvature are shown.

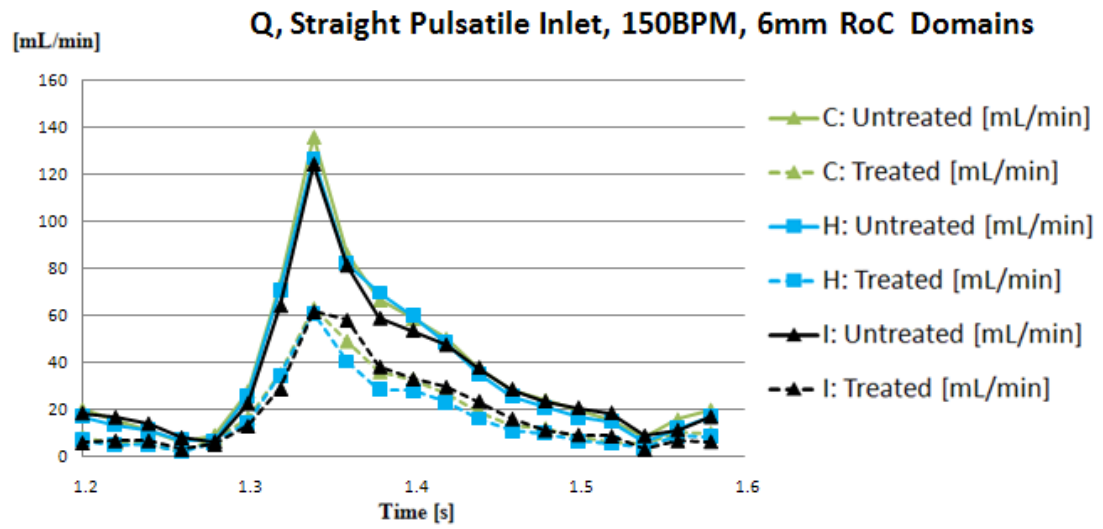


Figure B-28. The time-dependent flow rates of fluid entering the aneurysms on domains with 3mm radii of curvature are shown.

APPENDIX C: SUPPLEMENTAL FIGURES FROM ANIMAL STUDIES

CHAPTER 5.2.1



Figure C-1. Rabbit 012. At 12 days after surgery, a fusiform aneurysm about 1.5 times the original diameter was found.

CHAPTER 5.2.2

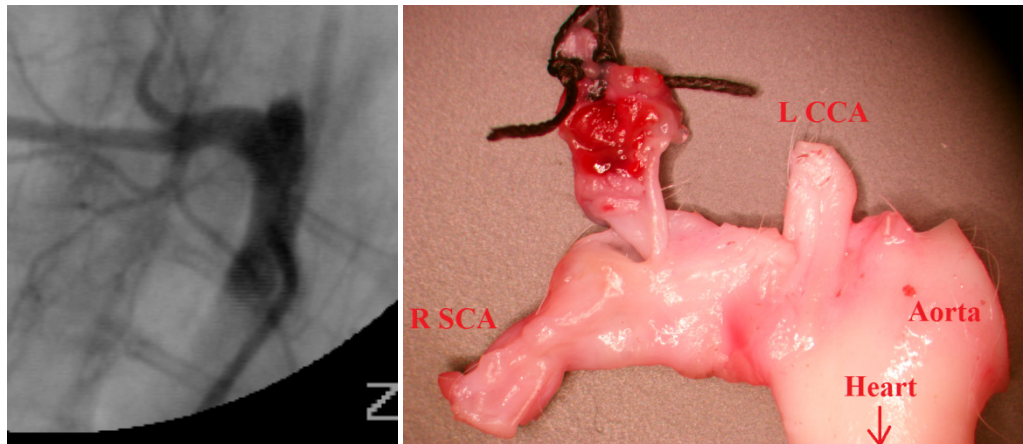


Figure C-2. Rabbit 014. At 10 days after surgery, a small sacular aneurysm could be observed.

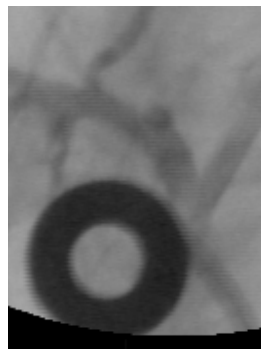


Figure C-3. Rabbit 015. At 12 days, a very small aneurysm was observed. A ¼-20 washer was placed in the field of view as a size reference.

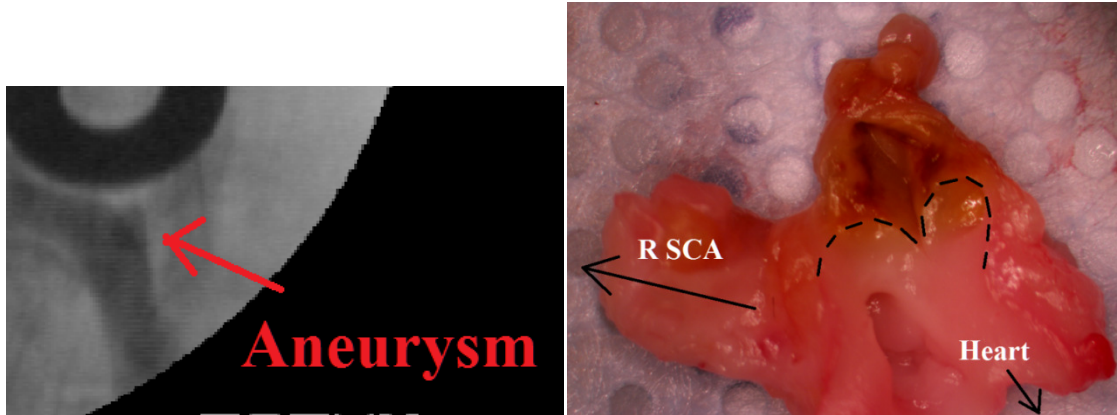


Figure C-4. Rabbit 016. While about 9mm of the RCCA was ligated to form the aneurysm, it appears most of it had inflamed and closed off, leaving behind a very small aneurysm after 29 days. The outline of the aneurysm is shown with the dashed black line.

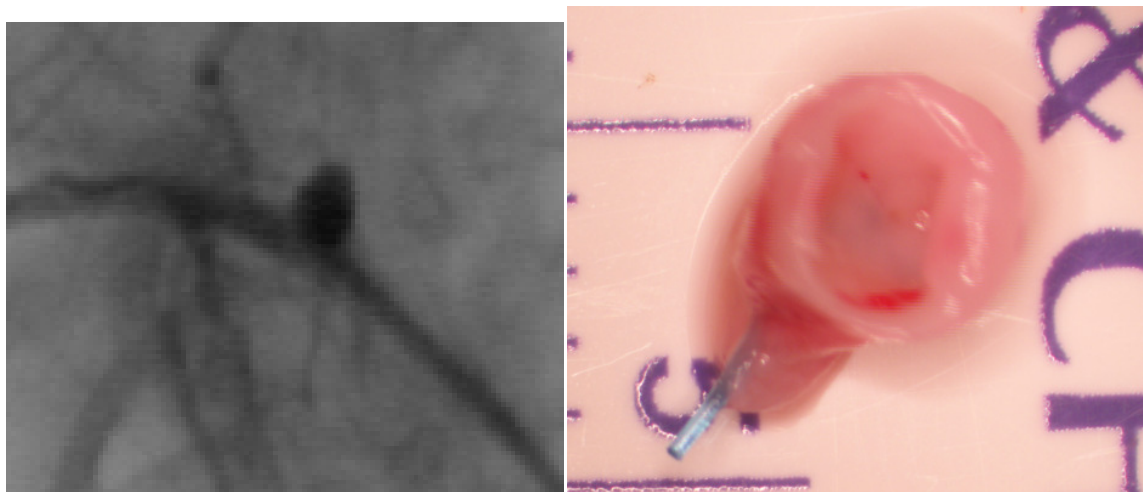


Figure C-5. Rabbit 017. Administration of aspirin led to an open and decently sized aneurysm after 28 days. The aneurysm was accidentally torn open while harvesting for histology. However, no evidence of inflamed tissue or thrombus was observed.

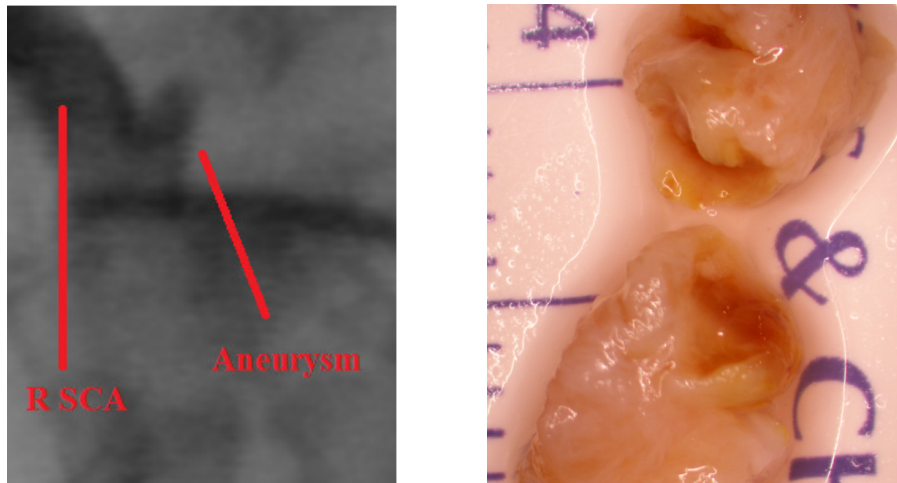


Figure C-6. Rabbit 020. The vessel wall was first primed with 2% lidocaine, which led to a significant enlargement of the vessel to about 3 times its original diameter. However, at 22 days, it was found that the stress may have been too much, as a good portion of the aneurysm was severely thrombosed.

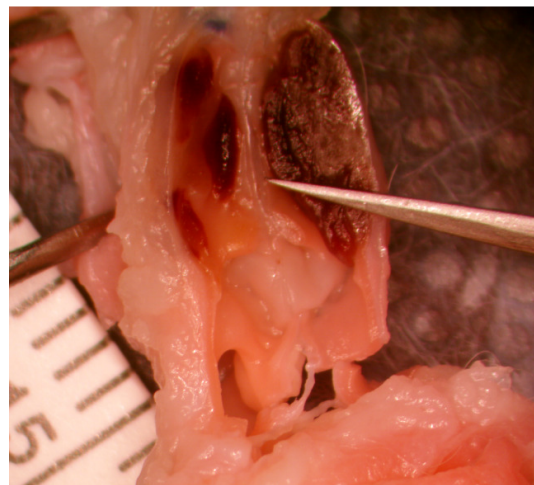


Figure C-7. Rabbit 025. Significant thrombus was observed in the aneurysm after 18 days.

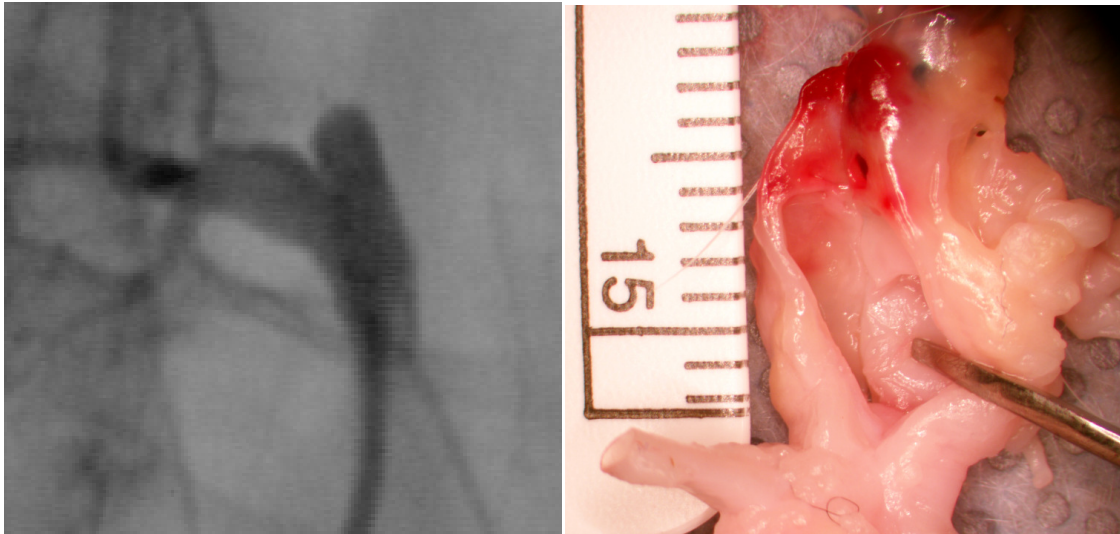


Figure C-8. Rabbit 026. A little bit of inflamed tissue at the tip of the aneurysm may have quiesced after 18 days. An aneurysm approximately 3mm in diameter and 5mm tall was left behind. Enlargement of the brachiocephalic trunk may have been due to leaked elastase.

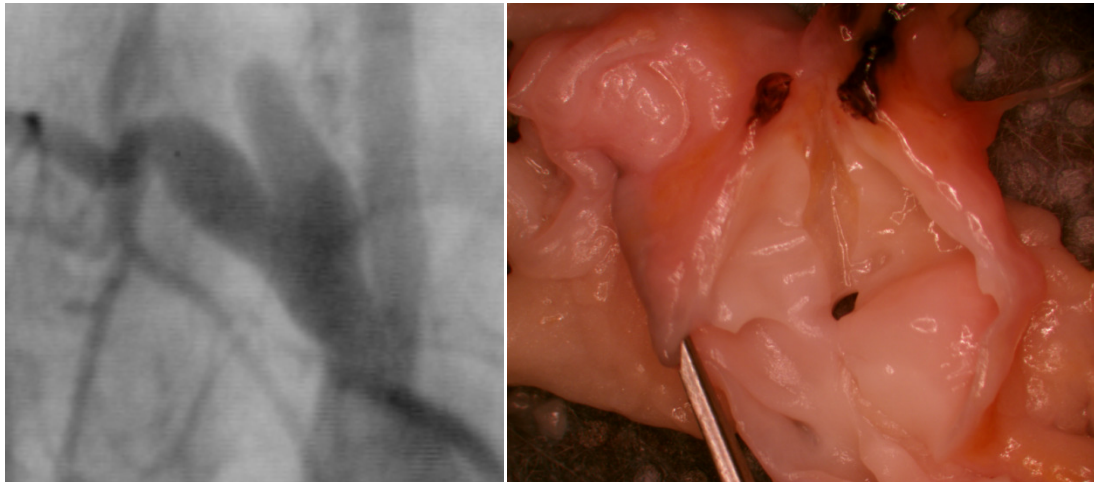


Figure C-9. Rabbit 028. The aneurysms walls were a little thicker than what the author had observed in other aneurysms. However, a sizable aneurysm was still observed at 26 days after surgery.



Figure C-10. Rabbit 030. The tip of the aneurysm appeared a little inflamed. However, the vessel wall didn't appear to thicken and no evidence of thrombus was observed.

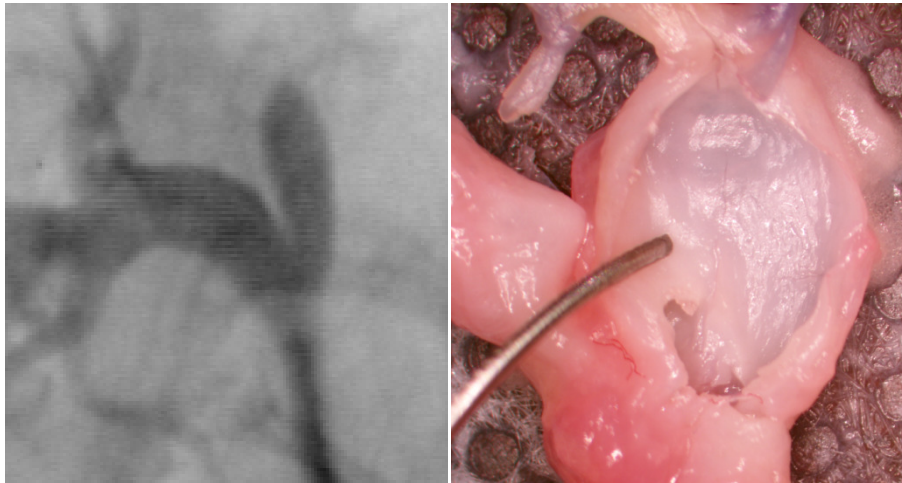


Figure C-11. Rabbit 031. The aneurysm exhibited no signs of inflamed tissue or thrombus. Careful application of elastase at the tip of the aneurysm led to almost no widening of the neck.

CHAPTER 5.2.4.

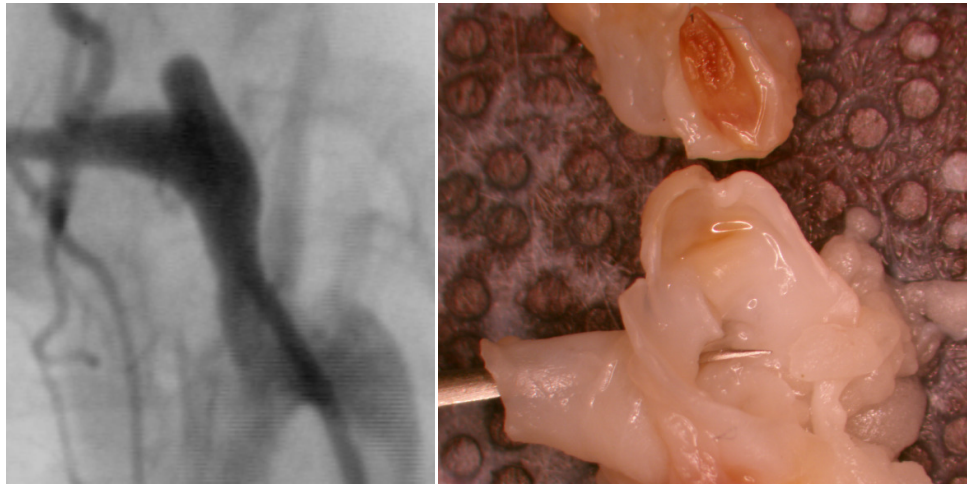


Figure C-12. Rabbit 034. A small clot was observed at the distal tip of the aneurysm. However, a ~4mm diameter x ~4mm tall aneurysm was observed after 20 days.

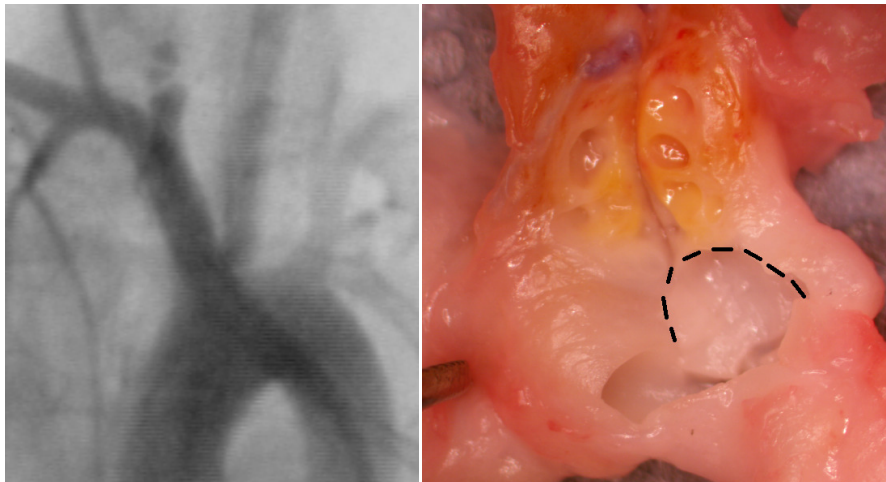


Figure C-13. Rabbit 035. The aneurysm was largely occluded by neointimal growth at day 22. The dashed black line outlines the aneurysm.

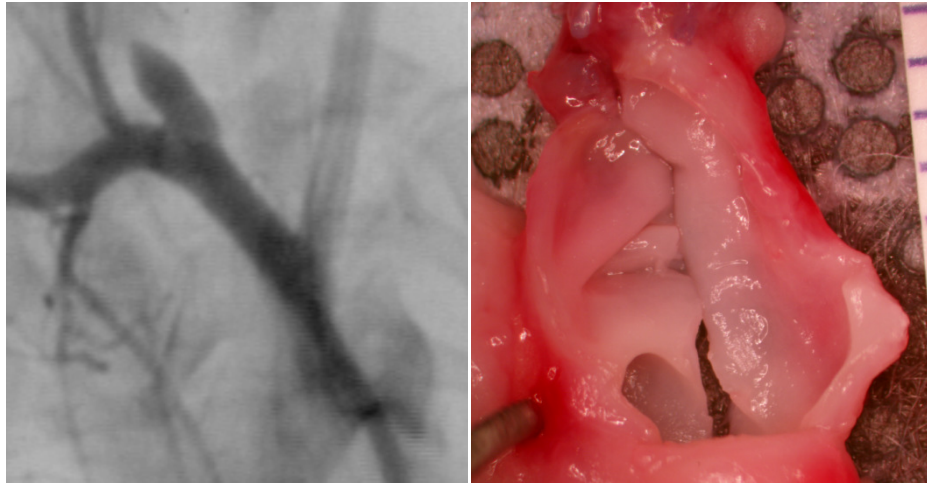


Figure C-14. Rabbit 038. The aneurysm was devoid of thrombus or inflamed tissue at 24 days.

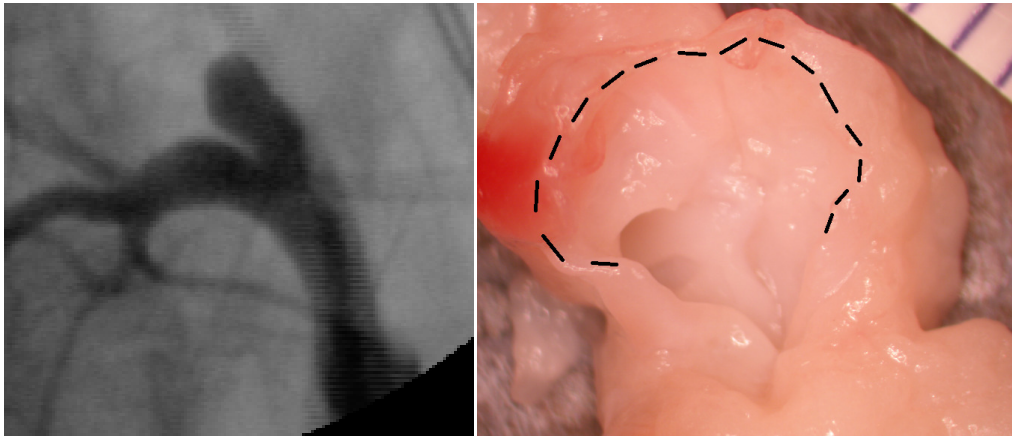


Figure C-15. Rabbit 041. The aneurysm was devoid of thrombus or inflamed tissue at 11 days. The dashed black line outlines the aneurysm.



Figure C-16. Rabbit 042. The aneurysm was largely devoid of thrombus or inflamed tissue at 26 days. The small bit of inflamed tissue at the distal tip of the aneurysm didn't appear to reduce the overall volume of the aneurysm significantly.

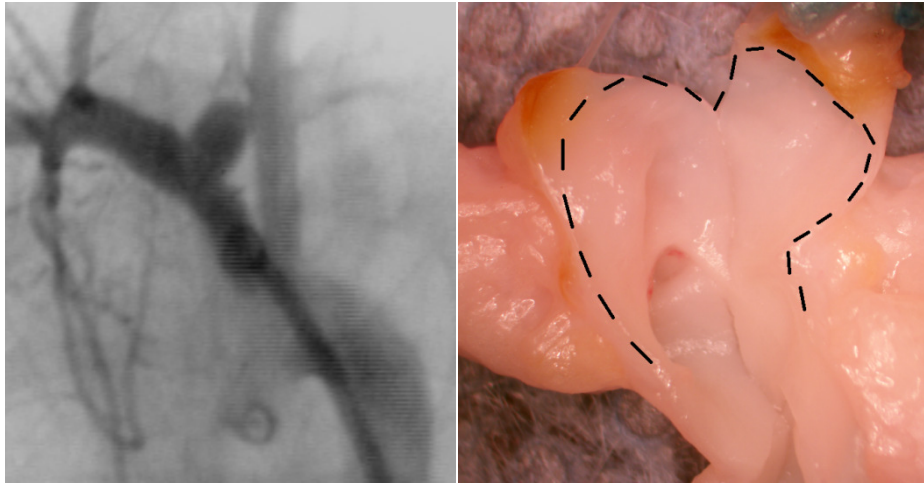


Figure C-17. Rabbit 043. The aneurysm was devoid of thrombus or inflamed tissue at 30 days. The dashed black line outlines the aneurysm.